Continuum QCD approaches to the 3D structure of the nucleon

Michael Riberdy

université PARIS-SACLAY

Continuum QCD approaches to the 3D structure of the nucleon

Approches continues de QCD et structure 3D des hadrons

Thèse de doctorat de l'université Paris-Saclay

École doctorale n576 Particules, Hadrons, Énergie, Noyau, Instrumentation, Imagerie, Cosmos et Simulation (PHENIICS)
Spécialité de doctorat : Physique nucléaire
Graduate School : Physique, Référent : Faculté des sciences d'Orsay

Thèse préparée au **Département de Physique Nucléaire** (Université Paris-Saclay, CEA) sous la direction de **Cédric MEZRAG**, Ingénieur-Chercheur au CEA et la codirection de **Hervé MOUTARDE**, directeur de recherche au CEA

Thèse soutenue à Paris-Saclay, le 04 juillet 2024, par

Michael RIBERDY

Composition du jury

Membres du jury avec voix délibérative

Benoît BLOSSIER Directeur de Recherche, CNRS, IJCLab, Université Paris-Saclay	Président
Barbara PASQUINI Professeur des Universités, Pavia U. and INFN, Pavia, Italie	Rapporteur & Examinatrice
Jakub WAGNER Directeur de Recherche, Warsaw national center for nuclear research, Pologne	Rapporteur & Examinateur
Jose RODRIGUEZ QUINTERO Professeur des Universités, Huelva U., Espagne	Examinateur
Renaud BOUSSARIE Chargé de recherche, CPHT, Ecole Polytechnique	Examinateur

THESE DE DOCTORAT
NNT : 2024UPASP043

université PARIS-SACLAY

ÉCOLE DOCTORALE
Particules, hadrons, énergie et noyau : instrumentation, imagerie, cosmos et simulation (PHENIICS)

Titre: Approches continues de QCD et structure 3D des hadrons
Mots clés: Distribution de Partons Généralisées, Fonctions d'onde du cône de lumière, Chromodynamique quantique, Processus exclusifs, Équations de Dyson-Schwinger, Moment angulaire orbital des quarks

Résumé: La plupart de la masse visible de l'univers est contenue dans les nucléons. Cependant, l'origine de cette masse reste mystérieuse, la portion issue du mécanisme de Higgs dans les schémas de renormalisation standards ne correspondant qu'à quelques pourcents de la masse totale. La réponse est à chercher dans la dynamique de l'interaction forte, décrite par la théorie de la chromodynamique quantique (QCD) en termes de quarks et de gluons. Ainsi, l'interaction entre quarks et gluons est responsable de l'émergence des propriétés connues et mesurées des hadrons comme leur masse ou leur spin. Il existe aujourd'hui une forte dynamique à la fois théorique et expérimentale pour chercher à déterminer la structure 3D des hadrons en terme de quarks et gluons. D'un point de vue théorique, les outils classiques de théorie quantique des champs, à savoir le développement perturbatif, ne permettent pas d'étudier les propriétés émergentes des hadrons. Ces dernières sont intrinsèquement non-perturbatives. Le but de cette thèse est de développer et d'utiliser un formalisme non-perturbatif en partant des équations de Dyson-Schwinger et de Bethe-Salpeter pour déterminer la structure 3D des hadrons, en particulier du nucléon. On utilisera différentes hypothèses dynamiques, afin d'obtenir une cartographie 3D de la charge, de la masse et des effets de moment angulaire orbital. Une confrontation des résultats obtenus avec les données expérimentales sera menée de concert avec les autres membres de LSN.

Title: Continuum QCD approaches to the 3D structure of the nucleon
Keywords: Generalized Parton Distributions, Lightfront Wave Functions, Quantum Chromodynamics, Exclusive processes, Dyson-Schwinger equations, Quarks orbital angular momentum

Abstract: Most of the visible mass of the universe is contained in nucleons. However, the origin of this mass remains mysterious, with the portion from the Higgs mechanism in standard renormalization schemes corresponding to only a few percent of the total mass. The answer is to be found in the dynamics of strong interaction, described by the theory of quantum chromodynamics (QCD) in terms of quarks and gluons. Thus, the interaction between quarks and gluons is responsible for the emergence of known and measured properties of hadrons such as their masses or spins. There is now a strong theoretical and experimental dynamic to determine the 3D structure of hadrons in terms of quarks and gluons. From a theoretical point of view, the classical tools of quantum field theory, namely perturbative expansion, do not allow the study of the emerging properties of hadrons. The latter are inherently non- disruptive. The aim of this thesis is to develop and use a non-perturbative formalism based on the Dyson-Schwinger and Bethe-Salpeter equations to determine the 3D structure of hadrons, in particular the nucleon. Different dynamic assumptions will be used to obtain a 3D mapping of the charge, mass and orbital angular momentum effects. A comparison of the results obtained with the experimental data will be carried out in collaboration with the other LSN members.

1 - Acknowledgements

I acknowledge and appreciate firstly the extreme patience, care, academic prowess, and curiosity of my advisor Cédric Mezrag, who has helped me through every step of this process even before I arrived in France. Thank you for all of your support, Cédric.
In addition, I am thankful for the warm environment sustained by C.M., my other advisor Hervé Moutarde, and Valerio Bertone. Discussions in weekly meetings with all three have pushed my personal development and curiosity more than they know.
I also thank Paweł Sznajder and Jorge Segovia, with whom helpful discussions and useful work have been performed for their support during my time here in Saclay. Further, I thank Hervé Dutrieux, whose sense of humor and prolificity have illuminated my understanding of this subject and of myself, and whose thoughtfulness continues to surprise me. In the same vein I thank Jose Manuel, whose incredible work ethic puts most to shame and whose friendly nature makes him an indispensable colleague and friend with whom time spent is never wasted.
There are so many individuals whose regular interactions with me have made the lab environment an interesting and stimulating place. An inexhaustive list of whom is given by Rémi, Aurore, Elie, Samy, Virgil, Abigail, Francesco, Jerome.
Outside of the lab environment, my time here has been illuminated by individuals such as Paul, Daniel, Kenta, Louis, Jan, Adrian, Rémi, Pablo, Skip, Paca. Thank you for the wonderful time we've spent together.
Thank you to my three friends from home who have stuck with me during all of my time here. Alex, Katie, Sonya, your presence in my life has been wonderful during the last few years of long distance separation. I hope to see you soon.
Thank you to Carlos, and Adriana, and most importantly Sofía, whose support for me during the last two years has been extremely important for my growth as a person. Thank you for treating me so well.
There are only three people left to thank: Mom, Dad, and Stephen. Your interest in my time spent here and your support of my pursuits has only made me enjoy my time here and miss being home with you. I miss you.

Contents

2 - Introduction

In this chapter's first section, preliminary experimental clues for the non-elementarity of the nucleon (a collective word for protons and neutrons) will be discussed. In the second, Quantum Chromodynamics (QCD), the theory of the corresponding interior particles, will be introduced. In the third and fourth sections, experimental processes used to probe the interior nature of the nucleon will be delineated, along with the properties of the objects used to describe the corresponding nuclear structure being probed. In the final section, descriptions of these objects via methods based on discrete models of spacetime, will be explored as a primer for the second chapter on the use of data produced via such methods.

2.1 . Nonelementarity of the Nucleon

2.1.1 . Experimental Clues for Nonelementarity

Fundamental particles, those which are not composed of smaller constituents, exhibit point-like (spatial) charge distributions. In practice, this means that regardless of the situation in which a measurement of such a particle's charge distribution occurs, the same point-like result should be observed. However, experiments lead by R. Hofstadter at Hansen Experimental Physics Laboratory (HEPL) in the 1950s measuring the charge distributions of various nuclei allowed for the extrapolation of data to the conclusion that the spatial distribution of the charge of the nucleon varies with respect to the momentum transfer between the probe and the target of the experiment [1]. This was the first landmark evidence for the non-elementarity of the nucleon.
Other evidence of nucleon non-elementarity came from measurement of the proton magnetic moment. The magnetic moment of any elementary spin $\frac{1}{2}$ particle is a function of natural constants and the mass of the particle ([2]) given by $\frac{e\hbar}{2m}$, with e the elementary charge, $\hbar$ the reduced Plank's constant, and m the mass of the nucleon in question. However, measurements of the proton magnetic moment at Stanford Linear Accelerator Center (SLAC) in the 1950s confirmed the proton moment to deviate from the value expected by assuming its elementarity by a factor of 2.79284734463(82) [3]. Given this experimental evidence for the non-elementarity of the nucleon, physicists began to postulate the properties of possible constituents.

2.1.2 . PreQCD Explanations

In the 1960s, Gell-Mann proposed a constituent quark model of the nucleon and various other baryons in order to explain a large spectrum of mass,

spin, and charge values [4]. In order to do so, Gell-Mann introduced three flavors of spin $\frac{1}{2}$ fermions (quarks) called "up" (u), "down" (d) and "strange" (s), with the u quark possessing an electric charge of $\frac{2}{3}$, and the d and s quarks an electric charge of $-\frac{1}{3}$. In this model, the quark spin vectors were constrained to (anti)align so as to reproduce the spin of the baryons which they constituted. However, the existence the particle consisting of three u quarks, named the Δ^{++} due to its total $+2$ charge, was particularly problematic as it required three quarks of the same flavor to remain in the same state, whereas the exclusion principle for fermions, which precludes such a state, was already well understood at the time. As a consequence, [5]&[6] introduced independently a new "color" gauge group, SU(3), in order to provide an additional quantum number to the model. This property, called "color charge", was set to take on three distinct values. By postulating that each of the three u quarks in the Δ^{++} takes on one of these three distinct values of color charge, the exclusion principle could be satisfied. However, the new gauge group introduced (SU(3)), being non-Abelian, would have far reaching consequences on the scale dependence of the newly formed theory of the strong force, QCD.

2.2 . QCD

2.2.1 . QCD and QED Lagrangians

The Lagrangian (density) of Quantum Electrodynamics (QED) is given by ([7])

$$\mathcal{L}_{\text{QED}} = \bar{\psi}_i(i\gamma^\mu D_\mu^{\text{QED}} - m)_{ij}\psi_j - \frac{1}{4}F^{\mu\nu}F_{\mu\nu}, \tag{2.1}$$

where γ^μ denotes the Dirac matrices, ψ represents a bispinor field of spin-1/2 particles (e.g., electron–positron field), and $\bar{\psi} \equiv \psi^\dagger\gamma^0$ its Dirac adjoint. $D_\mu \equiv \partial_\mu + ieA_\mu$ is the gauge covariant derivative, where e represents the coupling constant, the electric charge of the bispinor field. A_μ denotes the covariant four-potential of the electromagnetic field. The symbol m signifies the mass of the electron or positron. $F_{\mu\nu} = \partial_\mu A_\nu - \partial_\nu A_\mu$ denotes the electromagnetic field tensor, the curvature of the gauge field.
The Lagrangian density of QCD describes the dynamics of quarks and gluons. It is given by

$$\mathcal{L}_{\text{QCD}} = \bar{\psi}_i(i\gamma^\mu D_\mu^{\text{QCD}} - m)_{ij}\psi_j - \frac{1}{4}G_a^{\mu\nu}G^a_{\mu\nu}, \tag{2.2}$$

where γ^μ still denotes the Dirac matrices. Here, ψ represents a bispinor field of spin-1/2 quarks (i.e., up, down, strange), and $\bar{\psi} \equiv \psi^\dagger\gamma^0$ denotes its Dirac adjoint. The QCD gauge covariant derivative, $D_\mu \equiv \partial_\mu + ig_sT_aA^a_\mu$, includes

the strong coupling constant g_s representing the strength of the strong interaction, and A^a_μ denotes the gluon field, which is the covariant four-potential of the color force, associated with the SU(3) gauge symmetry of QCD. T_a represents the generators of the SU(3) group. The symbol m denotes the quark mass. The term $G^a_{\mu\nu} = \partial_\mu A^a_\nu - \partial_\nu A^a_\mu + g_s f_{abc} A^b_\mu A^c_\nu$ represents the gluon field tensor, where f_{abc} are the structure constants of the SU(3) group.

2.2.2 . Scale Dependence

Given these two theories of distinct gauge groups, what conclusions may be made about their behaviors at different energy scales? More specifically, how might the energy of an interaction in each theory affect the strengths of their respective couplings e/g_s, or, as they are usually discussed in the context of scale dependence, $\alpha_{\text{QED}} \equiv \frac{e^2}{4\pi}$ and $\alpha_s \equiv \frac{g_s^2}{4\pi}$? The answer to this question is encoded in the β function of each theory, which determines the dependence on the energy scale μ of α via a differential equation in the coupling and μ of the form

$$\beta(e; g_s) \equiv \mu \frac{d(e; g_s)}{d\mu}. \tag{2.3}$$

In practice, the β function of each theory may be approximated in perturbation theory. As a consequence of the Abelianity of its U(1) gauge group, the resulting behavior of $\alpha(\mu)$ is such that the coupling increases with μ. In fact, the one loop behavior of the QED β function is given by ([8])

$$\beta(\alpha) = \frac{2\alpha^2}{3\pi}. \tag{2.4}$$

At some finite energy scale, including all orders of perturbation theory, the QED coupling α_{QED} function diverges to $+\infty$, signifying infinite interaction strength. This phenomenon is called "the presence of the QED Landau pole". However, the behavior of the QCD β function is quite different. In [9] and [10], it is shown that non-Abelian QFTs may possess negative β functions. The QCD β function is given by

$$\beta(\alpha_s) = -(11 - \frac{2n_f}{3})\frac{\alpha_s^2}{2\pi}, \tag{2.5}$$

which results in the approximate behavior

$$\alpha_{\text{s}}(\mu) \approx \frac{\beta_0}{\ln(\mu/\Lambda)}, \tag{2.6}$$

where β_0 is a constant, Λ is the location of the QCD Landau pole, and n_f is the number of quark flavors, present in the corresponding perturbative QCD (pQCD). As a result, the coupling decreases as the energy scale μ increases at high energy scales, and diverges at the Landau pole. Consequently, we

say that quarks undergo "asymptotic freedom" at high energies (UV), as their behavior asymptotically approaches that of free particles as $\mu \to \infty$. Conversely, at low energies (IR), the coupling is quite large and even diverges at the Landau pole, resulting in what is called "confinement". Given this range of behaviors, it has been long suggested that only color neutral states are physically isolable, a property which is named "color confinement". While color confinement has not been proven, only color neutral states have been observed. When QCD bound states are ripped into pieces via high energy interactions, the resulting pieces end up color neutral as the (anti)quark-quark potentials become so great during the separation process (at "large" distances) that new particles are created and partnered with those pieces such that only color neutral bound states remain.

2.3 . Deep Inelastic Scattering

2.3.1 . The Diagram

In order to compare experimental results with theoretical predictions, it is necessary to interface the two. What form, then, should theoretical predictions take in order to be compared to experiment? On the experimental side, interactions are initiated, their results are measured, and the relative probabilities of such results are tabulated. These probabilities may be easily used to calculate what are called "cross sections". Cross sections may be expressed as the norm squared of sums of amplitudes of various interactions. Amplitudes, in turn, may be expressed via various methods. One such method is perturbation theory. After defining the Lagrangian density of the theory in which one would like to perform computations, one may define the path integral of the theory in order to express amplitudes of a given order in perturbation theory. That is, one may express amplitudes in terms of functional derivatives of the generating functional of the theory with respect to the source fields J, as

$$\begin{aligned} \mathcal{A}^{p_{j\in\{1,\ldots,n\}}} &= \prod_{j=1}^{n}\Big(\frac{\delta^{p_j}}{\delta J_j^{p_j}}\Big) Z[J_{i\in\{1,\ldots,n\}}] \\ &\equiv \prod_{j=1}^{n}\Big(\frac{\delta^{p_j}}{\delta J_j^{p_j}}\Big) \int \Big(\prod_{i=1}^{n} \mathrm{d}\phi_i\Big) e^{iS(\phi_{i\in\{1,\ldots,n\}})+\sum_{j=1}^{n} J_j\phi_j}, \end{aligned} \tag{2.7}$$

where $\mathcal{A}^{p_{j\in\{1,\ldots,n\}}}$ is the amplitude one would like to calculate, S is expressed as a spacetime integral over the Lagrangian density of the theory in a given configuration of the fields $\phi_{i\in\{1,\ldots,n\}}$, $\int\Big(\prod_{i=1}^{n}\mathrm{d}\phi_i\Big)$ expresses an integral over all possible field configurations, and the $J_{i\in\{1,\ldots,n\}}$ are named the source fields. In perturbation theory one expands the exponential as a formal power series in the coupling appearing in the definition of the Lagrangian density. For a

sufficiently small coupling, computation of the first few terms may often be used to predict experimental results.
In QED, one may use the coupling e for such an expansion at scales sufficiently low for the coupling to be low enough for such an expansion to be useful. Admittedly, at some large energy scale the QED coupling will diverge, making such an expansion useless. However, this scale is likely higher than the Planck scale [11]. The QED Landau pole is therefore of no practical concern given the energy scales involved in modern experimentation.
In QCD, on the other hand, the divergent behavior occurs at the relatively low energy scale Λ_{QCD}, a perturbatively estimable quantity which determines where pQCD is precisely useless. Therefore, purely pQCD will not yield useful results at the energy scales at which the dynamics of QCD should be understood if one would like to explore nucleon substructure. However, before deciding how to tackle this problem, one should clearly understand the successes and limitations of perturbation theory in QCD by determining when it is appropriate to use, and when it breaks down.

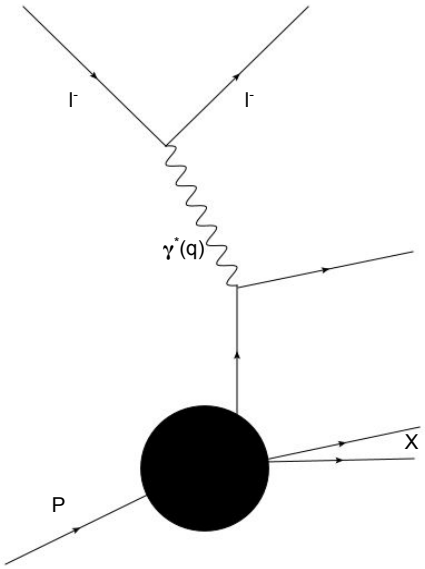

Figure 2.1: A Feynman-like diagram of DIS is shown. On the top left, an incoming lepton l^- emits a virtual photon $\gamma^*(q)$ ($Q^2 = -q^2$), resulting in an outgoing lepton l^-. Further, γ^* is absorbed by the active quark of momentum k of the incoming nucleon of momentum P. Said active quark is permanently separated from the nucleon, whose remaining pieces form an arbitrary product named X.

As a seminal example, let us consider Deeply Inelastic Scattering (DIS) of a nucleon target employing an electron probe (See Fig. 2.1). In this process, the so-called "active" quark of momentum fraction x of an incoming nucleon

of momentum p interacts with an electron probe of momentum k via the exchange of a virtual photon of four momentum q ($Q^2 \equiv -q^2$). In the final state one finds the electron probe of momentum $k' = k - q$ as well as any number of QCD bound states created as the active quark is ripped away from the nucleon via the interaction. As is convention, we denote these final state contents (apart from the final state electron) as X. We define the Bjorken variable ([12])

$$x_{\text{Bj}} \equiv \frac{Q^2}{2p \cdot q}. \tag{2.8}$$

One way to view this is to define the very useful coordinate system called lightcone coordinates, writing for a general four-vector v

$$v = (v^+ \equiv \frac{v^0 + v^3}{\sqrt{2}}, \vec{v}_\perp \equiv (v_1, v_2), v^- \equiv \frac{v^0 - v^3}{\sqrt{2}}), \tag{2.9}$$

and to subsequently define two lightcone vectors

$$p = (1, \vec{0}_\perp, 0), \tag{2.10}$$

$$n = (0, \vec{0}_\perp, 1), \tag{2.11}$$

which point in the $+$ and $-$ directions respectively.
We can now directly write down the expression for the differential cross section $d\sigma$ as

$$d\sigma \equiv \frac{d^3k' e^4}{2|\vec{k'}^2|16\pi^3(p+k)^2Q^4} L^{\mu\nu}(k,k') W_{\mu\nu}(p,q), \tag{2.12}$$

where L is the so-called "Leptonic Tensor", which encodes perturbative information regarding the leptonic part of the cross section and W is the hadronic contribution, and where the cross section is differential in 3 and not 4 dimensions of the variable k because we have chosen to work at fixed lightcone time, corresponding to having completely integrated away the minus component of k [13].
One way of expressing the hadronic tensor is via a decomposition of a current matrix element into

$$W_{\mu\nu} \equiv (\frac{q_\mu q_\nu}{q^2} - g_{\mu\nu})F_1(x,Q^2) + (p_\mu - q_\mu \frac{p\cdot q}{q^2})(p_\nu - q_\nu \frac{p\cdot q}{q^2})F_2(x,Q^2), \tag{2.13}$$

with the $F_{1,2}$ expressible in terms of convolutions of perturbatively calculable coefficient functions C^f and the quark in nucleon PDFs $q^f(x,Q^2,\alpha)$, which is related to the probability of "finding" a quark of flavor f in the unpolarized nucleon carrying a given fraction of the nucleon's momentum $0 \leq x \leq 1$ at a given value of Q^2 and at a given strong coupling α_s which depends on the renormalization scale μ. That is,

$$F_i = \sum_f \int_0^1 \mathrm{d}y C_i^f(\frac{x}{y}, \frac{Q^2}{\mu^2}, \alpha_s) q^f(y, Q^2, \alpha_s) + \mathcal{O}(\frac{M^2}{Q^2}), \tag{2.14}$$

where $M^2 << Q^2$ is the hadron mass. Here, the Cs do not depend on the long distance, low energy behavior of the composite hadronic system. However, at higher orders in the strong coupling, the Cs receive logarithmic corrections in Q^2, which is one of the milestone predictions of QCD [14].

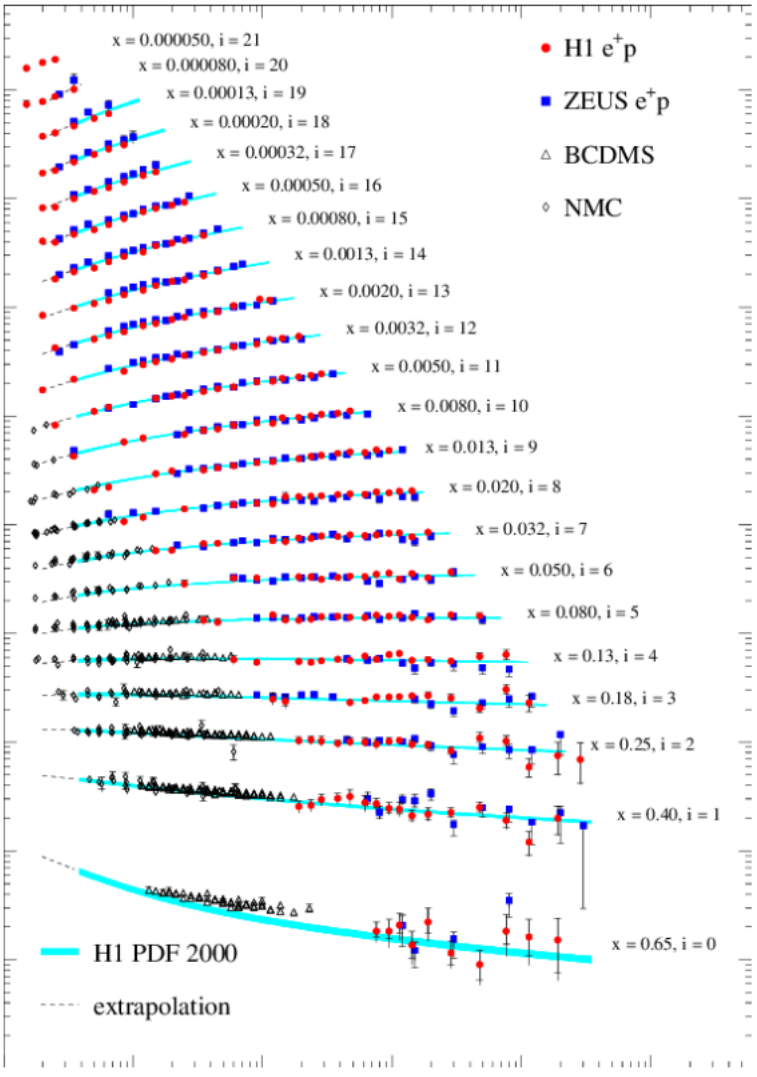

Figure 2.2: Shown is a summary of the F_2 (defined in Eq. (2.34)) structure function measurements by the H1 [15], [16] and ZEUS [17] collaborations at HERA and also by fixed target experiments BCDMS [18] and NMC [19] as shown in [14].

In contrast with the C, however, the PDFs q (see Eq. (2.50)) do not depend on the short distance, high energy behavior of the interaction between the electron probe and the active quark. The idea that one can separate a cross section into independent parts due to the difference in the scales on which

they depend, only needing to convolute them over internal variables in order to predict said cross section, is called factorization and has been proven to all orders for DIS in [20] via careful diagrammatic power counting, as well as via other methods. In practice, what this means is that the behavior of any process which involves a given species-in-species PDF, up to a process dependent kernel, is dictated by the universal behavior of said PDF. This concept of universality has allowed for the community to focus on computing a set of universal objects, whose determination in one context will allow for predictions in experimental processes not yet measured. However, corresponding to their value, universal objects are difficult to extract from experimental data as the convolution involved in computing cross sections may contain a singular kernel, preventing direct inversion of the convolution to yield predictions for the forms of such universal objects. This is the case with objects to be introduced later in this document, but the kernel connecting the PDF to the DIS cross section is not singular. Rather, it features a sum over quark flavors, making flavor separation extremely difficult.

Motivated by DIS measurements at SLAC, the European Muon Collaboration (EMC) [21] performed measurements relating to nucleon structure, resulting in the so-called spin crisis. While it was expected that the nucleon spin would receive by far its largest contribution from QCD bound states in which the three valence quark spins were (anti)aligned to create a total spin of $\pm\frac{1}{2}$, it was found that these states contributed only 20-25% of the nucleon spin. This discovery forced the community to begin to consider unexpectedly substantial contributions from the infinite number of QCD states, called generally Fock states in QFT, which match the quantum numbers of the nucleon, including not only the three nucleonic valence quarks but also contributions from potentially infinitely many gluons and quark-antiquark pairs and combinations thereof. And though not a "crisis" today, the proton spin crisis inspired investigation of states including quarks and gluons of various values of Orbital Angular Momentum (OAM), which Generalized Parton Distributions (GPDs), the subject of this chapter's next section, are used to formalize and investigate.

2.4 . Generalized Parton Distributions

2.4.1 . Deeply Virtual Compton Scattering & Deeply Virtual Meson Production

An important experimental process in the study of distributions even more complicated than the PDF is that of Deeply Virtual Compton Scattering (DVCS) ([22]), (see Fig. 2.4) in which an incoming leptonic probe interacts with a nucleonic target. This contrasts DIS, in which the nucleonic target is in general broken into arbitrary pieces, making DIS an inclusive process, DVCS features

an unbroken nucleon in the final state, along with a second, final state photon and lepton. This second photon, being real, is detected, allowing for the reconstruction of much of the kinematics of the associated partonic interaction, letting one probe the partonic substructure of the nucleonic target. A closely related experimental process is that of Deeply Virtual Meson Production (DVMP) (See Fig. 2.5), in which a meson is produced in the final state. Of these two cases, one aspect unique to DVCS is that of the Bethe Heitler interference term. In addition to the DVCS term, which describes the amplitude of the process shown in Fig. 2.4, contributions to the total measured scattering cross section from the Bethe-Heitler (BH) (see Fig. 2.3) process are present, and actually dominate the statistics of modern DVCS measurements [23].
Further, much as in the case of DIS, factorization for DVCS and DVMP have been proven for some time [24, 25, 26, 27]. Due to the exclusivity of DVCS in which the nucleon is not broken, factorization in the DVCS case occurs at the level of the DVCS amplitude rather than at the level of the cross section. What kinds of contributions have been factorized, once again up to a convolution, then?
Unlike in the inclusive DIS, the exclusive processes DVCS and DVMP involve a more complicated soft part which is in general off-diagonal in momentum space. That is, there is a non-zero momentum transfer between the probe and the target. In this case, this new object entering the game is called a GPD, whose properties will be delineated in the following subsection. The unpolarized nucleon GPDs (H and E) to be discussed here are given in terms of the matrix element

$$\begin{aligned} & \frac{1}{2}\int \frac{\mathrm{d}z^-}{2\pi} e^{ixP^+z^-} \langle P'|\bar{q}^f(-\frac{z^-}{2})\gamma^+ q^f(\frac{z^-}{2})|P\rangle \\ = \quad & \frac{1}{2P^+}\left(H^f(x,\xi,t)\bar{u}(P')\gamma^+\bar{u}(P) + E^f(x,\xi,t)u(P')\frac{i\sigma^{+\nu}\Delta_\nu}{2M}u(P)\right), \end{aligned} \tag{2.15}$$

where we have introduced the momentum difference

$$\Delta \equiv P' - P, \tag{2.16}$$

and

$$t \equiv \Delta^2. \tag{2.17}$$

Further, the average nucleon momentum is given by

$$\bar{P} \equiv \frac{P' + P}{2}, \tag{2.18}$$

and the average active quark momentum is correspondingly given by

$$\bar{k} \equiv \frac{k' + k}{2}. \tag{2.19}$$

Using these definitions the average quark momentum fraction is defined as

$$x \equiv \frac{\bar{k}^+}{\bar{P}^+}, \tag{2.20}$$

and the lightcone "kick" imparted on this active parton is parametrized by

$$\xi \equiv \frac{\bar{\Delta}^+}{2\bar{P}^+}. \tag{2.21}$$

Here we have fixed the gauge as $A^{a+} = 0$, referred to as lightcone gauge. For more details, see the following section on definitions and properties related to GPDs. Further, the quark field operators in the nucleon GPD matrix element definition provided in Eq. (2.15), to be specified in a later chapter, are defined at zero lightcone time ($z^+ = 0$) and also occur on the lightcone with no transverse component $\vec{z}_\perp = \vec{0}_\perp$.
The two unpolarized nucleon GPDs H and E are relevant here in part because they are "leading twist" (leading order in $Q^{-1} \equiv (Q^2)^{-\frac{1}{2}}$). Twist, ($\tau$) discussed in the appendix (see Sec. 8.4) in the context of experimental processes such as DIS, DVCS, and DVMP refers to the suppression via $(Q^{-1})^{\tau-2}$ corresponding to a given term in a tensorial parametrization of a general matrix element, such as the one defined in the following section's Eq. (2.24), of which the GPDs H and E are the leading contributions [28].

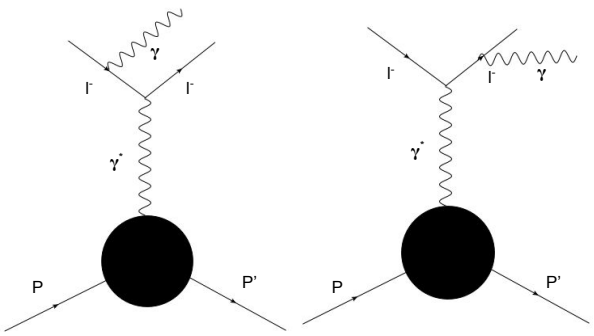

Figure 2.3: A Feynman-like diagram of the Bethe-Heitler process is shown. The lepton probe and the nucleonic target interact via a photon exchange, and the second photon is emitted by the incoming (outgoing) (anti)lepton. Thus, the CFF of the nucleon in question is not probed.

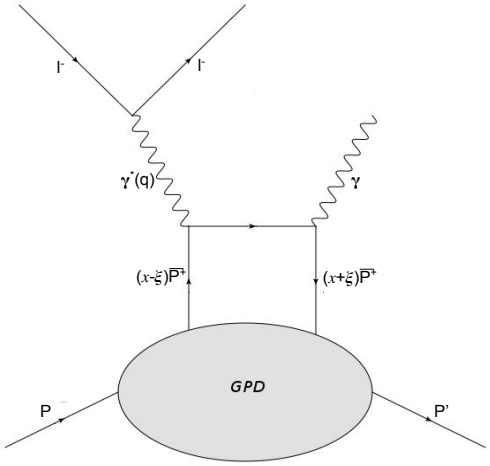

Figure 2.4: A leading order (LO) pQCD Feynman-like diagram of DVCS is shown. On the top left, an incoming lepton l^- emits a virtual photon $\gamma^*(q)$ ($Q^2 = -q^2$), resulting in an l^-. γ^* is absorbed by the active quark of momentum k of the incoming nucleon P, which then emits another photon $\gamma(q')$, resulting in an active quark of momentum k' of an outgoing nucleon of momentum P'.

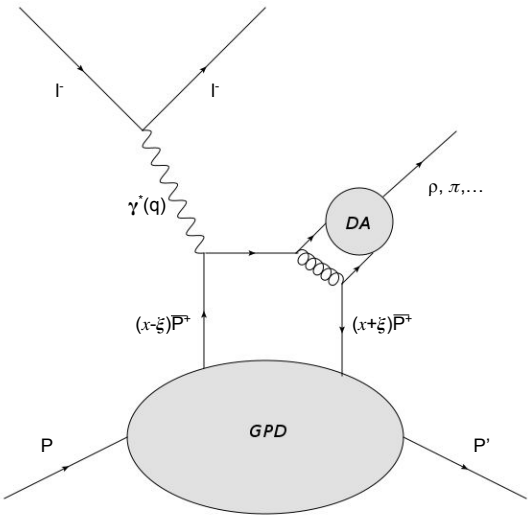

Figure 2.5: A leading order (LO) pQCD Feynman-like diagram of DVMP is shown. On the top left, an incoming lepton l^- emits a virtual photon $\gamma^*(q)$ ($Q^2 = -q^2$), resulting in an outgoing lepton l^-. γ^* is absorbed by the active quark of momentum k of the incoming nucleon P, resulting in a gluon exchange and creation of an outgoing meson and a final state active quark of momentum k' of an outgoing nucleon of momentum P'.

This is an example of one of the common themes of matrix element treatment in quantum field theories (QFTs). We write down the matrix element

we would like to compute, and then write down a convenient tensorial basis using all of the structures available with the same Lorentz transformation, Dirac, and CPT properties as the matrix element. On the lightcone there is an additional final round of this game. One can further decompose the tensorial structures used in one's matrix element parametrization into structures of definite twist, as mentioned in the previous paragraph. Why make such a twist decomposition? By studying the arguments of factorization proofs, one realizes that factorization is often particularly valid in the limit that the hard scale of the process (the virtuality Q^2 in this case) is much larger than the involved masses and any other relevant energy scales. As a consequence, one may take advantage of this behavior by writing one's matrix element in terms of structures with definite twist, such that one might prioritize the computation of term(s) with the lowest twist, knowing all the while that it is precisely those terms which will contribute the most to one's matrix element at high virtuality.

In addition to the GPD contribution, the DVMP amplitude, involving the creation of a QCD bound state (meson) from a quark-antiquark pair, also involves a soft part describing such a meson formation, referred to as a Distribution Amplitude (DA), which we will not treat here.

How do GPDs enter the expression for the amplitude of DVCS in the relevant experimental cross section? As previously mentioned, they enter via a convolution in the longitudinal momentum fraction. That is, for a given contributing GPD $\in \{H(x,\xi,t), E(x,\xi,t)\}$ the corresponding convoluted function, referred to as the corresponding Compton Form Factor (CFF), is given by [29]

$$\mathrm{CFF}_i^f(\xi,t) = \int_{-1}^{1} \mathrm{d}x \mathrm{GPD}^f(x,\xi,t) 2x e_f^2 ((\xi - i\varepsilon)^2 - x^2)^{-1}. \tag{2.22}$$

Here, this LO kernel is not dependent on the scale Q^2. However, as in the case of the PDF (see Eq. (2.14)), at higher orders in α_s this kernel will receive scale dependent corrections in the form of logarithms $\ln(Q^2)$. The CFFs, along with their polarized counterparts derived from the polarized nucleon GPDs to be discussed in Ch. 4, are then used directly in the expression for the cross section. The interested reader can find more details in [24, 25].

In the case of DVMP, we do not enter all of the details, but merely state that the nucleon GPD contributes in analogous way due to the analogous factorizations of the corresponding soft parts of the DVCS and DVMP amplitudes. This takes advantage of the property that the GPD, like the PDF, is a universal object in the sense that once one has proven factorization for a given process in which the GPD contributes, one has automatically shown that the contributing GPD is precisely the same nucleonic structure function as that which contributes to DVCS and DVMP as elaborated here. Like in the case of PDFs, universality makes GPDs highly valuable objects for experimental prediction.

Now that we have understood the relevant context for GPD physics, let us take the opportunity to discuss their properties as well as related quantities.

2.4.2 . GPD Properties and Related Objects

A general quark operator matrix element is here defined as ([30, 31, 32])

$$\begin{aligned} & W_f(x,\vec{\bar{k}}_\perp,\xi,t;\mu) \qquad (2.23)\\ \equiv\ & N_W \int dz d^2\vec{z}_\perp e^{i\bar{k}^+z^-} e^{i\vec{\bar{k}}_\perp\cdot\vec{z}_\perp} \langle P';h'|\bar{q}_f(-\frac{z}{2})\Gamma\mathfrak{W}(-\frac{z}{2},\frac{z}{2})q_f(\frac{z}{2})|P;h\rangle, \end{aligned}$$

where $z^+ = 0$ and N_W is a normalization constant, and μ is an often omitted renormalization scale on which this and all other distributions discussed here depend implicitly, q is a quark field operator with $\bar{q}$ it's conjugate, both of which are defined in the third chapter (Ch. 4). f is the flavor index of the quark, and color and Dirac indices have been suppressed. The ket (bra) $|P(');h(')\rangle(^\dagger)$ represents the incoming (outgoing) nucleon state of momentum $P(')$ and helicity $h(') = \pm\frac{1}{2}$, where † represents Hermitian conjugation, where helicity is proportional to the overlap of a particle's spin vector and it's momentum vector. Γ is a Dirac algebra element which will be used to project onto various twist structures, and the Wilson line included to preserve gauge invariance, $\mathfrak{W}$, is to be defined in the less general case of the GPD below.
The W function defined in Eq. (2.23) is often referred to as the Fourier transform with respect to $\vec{\Delta}_\perp$ of a Wigner distribution in analogy with the Wigner distributions defined in quantum mechanics. Corresponding to the 5 dimensional structure of this object, it is difficult to compute and work with.
In this thesis, we work instead with the three dimensional GPDs ([33]), which can be viewed as Wigner distributions with the $\bar{k}_\perp$ dependence integrated away, or $z_\perp = 0$, which are given in terms of the amplitudes ([34],[35])

$$\begin{aligned} & \mathcal{H}^f_{h'h}(x,\xi,t) \qquad (2.24)\\ \equiv\ & \frac{1}{2\sqrt{1-\xi^2}} \sum_c \int \frac{dz^-}{2\pi} e^{i\bar{x}\bar{p}^+z^-} \langle P',h'|\bar{q}^c_f(-\frac{z}{2})\mathfrak{W}(-\frac{z}{2},\frac{z}{2})\gamma^+ q^c_f(\frac{z}{2})|P,h\rangle, \qquad (2.25) \end{aligned}$$

where $\Gamma = \gamma^+$ has been chosen to project the matrix element onto its leading twist (twist two) components and where $\mathfrak{W}(-\frac{z}{2},\frac{z}{2})$, now a $-$ direction Wilson line, is defined as

$$\begin{aligned} \mathfrak{W}(-\frac{z}{2},\frac{z}{2}) &= \mathsf{P}\, e^{-ig\int_{-\frac{z}{2}}^{\frac{z}{2}} dy^- A^+(0,y^-,0_T)}, & (2.26)\\ A^+ &\equiv A^{a+}T^a, & (2.27) \end{aligned}$$

where P represents path ordering. As mentioned in the previous subsection, it is convention to discuss such matrix elements in the language of the GPDs

H and E, given the decomposition

$$\begin{aligned} & \frac{1}{2}\int \frac{\mathrm{d}z^-}{2\pi} e^{ixP^+z^-}\langle P'|\bar{q}^f(-\frac{z^-}{2})\gamma^+ q^f(\frac{z^-}{2})|P\rangle, \\ = \quad & \frac{1}{2P^+}\Big(H^f(x,\xi,t)\bar{u}(P')\gamma^+u(P) + E^f(x,\xi,t)u(P')\frac{i\sigma^{+\nu}\Delta_\nu}{2M}u(P)\Big), \end{aligned} \tag{2.28}$$

and for gluons

$$\begin{aligned} & 2\int \frac{\mathrm{d}z^-}{2\pi}\langle P'|G^{+\mu}(-\frac{z}{2})G^+_\mu(\frac{z}{2})|P\rangle_{z^+=|\vec{z}_\perp|=0} \\ = \quad & \Big(H^g(x,\xi,t)\bar{u}(P')\gamma^+u(P) + E^g(x,\xi,t)u(P')\frac{i\sigma^{+\mu}\Delta_\mu}{2M}u(P)\Big). \end{aligned} \tag{2.29}$$

Inverting the relationship established in Eqs. (2.15) & (2.24), one may also express the GPDs in terms of the helicity dependent amplitudes $\mathcal{H}^f_{\pm+}$

$$H^f(x,\xi,t) = \mathcal{H}^f_{++} + \frac{\xi^2 2m|\vec{\Delta}_\perp|}{(\Delta_1+i\Delta_2)\sqrt{1-\xi^2}\sqrt{\frac{4\xi^2m^2}{\xi^2-1}-t}}\mathcal{H}^f_{-+} \tag{2.30}$$

$$E^f(x,\xi,t) = \frac{2m|\vec{\Delta}_\perp|\sqrt{1-\xi^2}}{(\Delta_1+i\Delta_2)\sqrt{\frac{4\xi^2m^2}{\xi^2-1}-t}}\mathcal{H}^f_{-+}. \tag{2.31}$$

When $|x| > |\xi|$ and $x < 0$, the left part of the Dokshitzer–Gribov– –Lipatov–Altarelli–Parisi (DGLAP) ([36],[37],[38]) region, an antiquark is probed, and when $|x| > |\xi|$ and $x > 0$, the right part of the DGLAP region, a quark is probed (see Fig. 2.6).

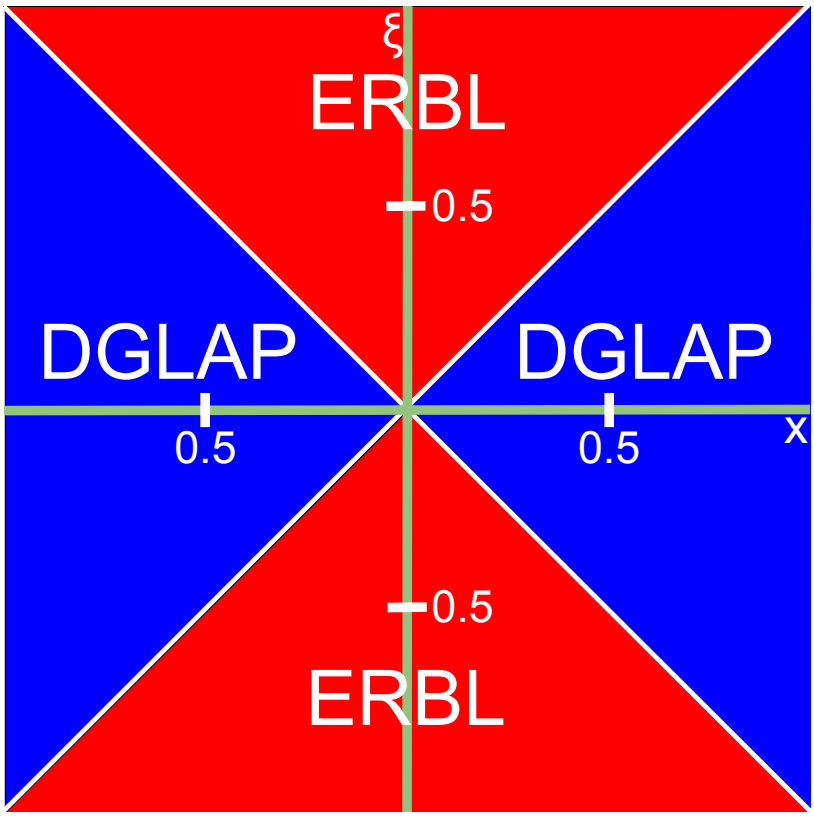

Figure 2.6: The DGLAP and ERBL ([39],[40]) regions are shown in the x, ξ plane.

Further, when $|\xi| > |x|$, the Efremov-Radyushkin-Brodsky-Lepage (ERBL) region, a quark-antiquark pair is probed.
GPDs must obey various constraints. In particular, the imposition of time reversal symmetry implies even parity of spin $\frac{1}{2}$ GPDs with respect to ξ. In fact, due to Lorentz invariance and time reversal symmetry one can show that the GPD's Mellin moments with respect to x must obey the polynomiality property, which may be stated as ([41, 42])

$$\int_{-1}^{1} \mathrm{d}x x^n H^f(x,\xi,t) = \sum_{i=0}^{[\frac{n}{2}]} \xi^{2i} A^f_{n,2i}(t) + \mathrm{mod}(n,2) C_n(t) \xi^{n+1}, \tag{2.32}$$

which, as mentioned, may be derived from Lorentz invariance as shown in [22, 43, 26] and where $[\frac{n}{2}]$ represents the floor function applied to $\frac{n}{2}$ and $\mathrm{mod}(n,2)$ is the remainder of the division of n by 2.
This property can be ensured via the use of the so-called Double Distributions (DDs). It can be shown that, writing a GPD as the Radon transform of non-pathological functions F and D as

$$H^f(x,\xi,t) = \int \mathrm{d}\Omega \Big(F^f(\beta,\alpha,t) + \xi\delta(\beta) D^f(\alpha,t) \Big), \tag{2.33}$$

where $\mathrm{d}\Omega = \mathrm{d}\beta\mathrm{d}\alpha\delta(x-\beta-\alpha\xi)$ and $|\alpha|+|\beta|\leq 1$, where the function D of the final term, called the "D-term", is odd with respect to α [44]. Taking the specific example of the polynomiality property in the $n=0$ case, we find the definitions of the Dirac and Pauli Electromagnetic Form Factors (EFFs) which depend only on the squared momentum transfer Mandelstam t:

$$\begin{aligned} F_1^f(t) &\equiv \int_{-1}^{1} dx H^f(x,\xi,t), \\ F_2^f(t) &\equiv \int_{-1}^{1} dx E^f(x,\xi,t). \end{aligned} \tag{2.34}$$

The nucleon EFFs are then expressed in terms of the quark ones as

$$\begin{aligned} F_i^{P,N;p}(t) &= \frac{2n_u^{P,N}}{3}F_i^{p,u}(t) - \frac{n_d^{P,N}}{3}F_i^{p,d}(t) \\ & n_u^P = 2, \quad n_d^P = 1, \quad n_u^N = 1, \quad n_d^N = 2. \end{aligned} \tag{2.35}$$

Further, one non-relativistic definition of the EM charge radius is given in terms of the FFs as

$$\langle (r_E)^2 \rangle = 6\hbar^2 \sum_f \partial_t \Big(c_f n_f (F_1(t) + \frac{t}{4M_N^2}F_2(t)) \Big)|_{t=0}. \tag{2.36}$$

where the c_f are the corresponding charges. Other definitions are certainly possible, however. Averaging the $n=1$ cases of the GPDs H and E and taking the limit $t\to 0$ gives the total angular momentum contribution to the proton spin of a quark flavor f as (or for gluons labeled by g)

$$\begin{aligned} J^f &= \frac{1}{2}\int \mathrm{d}x x \Big(H^f(x,\xi,0) + E^f(x,\xi,0) \Big) \\ J^g &= \frac{1}{2}\int \mathrm{d}x \Big(H^g(x,\xi,0) + E^g(x,\xi,0) \Big), \end{aligned} \tag{2.37}$$

which is known as Ji's sum rule [29].
This relation may also be reflected in terms of some elements of the decomposition of the following matrix element of the energy momentum tensor (EMT), given by [45, 46]:

$$\begin{aligned} \langle P'|T_a^{\{\mu\nu\}}(0)|P\rangle &= \bar{u}(P')\Big(\frac{P^\mu\gamma^\nu + P^\nu\gamma^\mu}{M}A^a(t) + \frac{i(\bar{P}^\mu\sigma^{\nu\rho} + \bar{P}^\mu\sigma^{\nu\rho})\Delta_\rho}{4M}B_q(t) \\ &+ \frac{\Delta^\mu\Delta^\nu - \eta^{\mu\nu}\Delta^2}{M}C^a(t) + M\eta^{\mu\nu}\bar{C}^a(t)\Big)u(P), \end{aligned} \tag{2.38}$$

where the index a may be a quark flavor f or g representing the corresponding gluon contributions, C and $\bar{C}$ are related to the stress and shear forces of the EMT [47, 48, 49, 50] and the form factor C is related to the previously

established DD D-term. Some of the objects defined here are constrained by angular momentum conservation ([29, 51, 52, 53])

$$\sum_f A^f(0) + A^g(0) = 1 \tag{2.39}$$

$$\sum_f B^f(0) + B^g(0) = 0 \tag{2.40}$$

$$\sum_f \bar{C}^f(t) + \bar{C}^g(t) = 0 \tag{2.41}$$

where $\sum_f$ denotes summation over the considered quark flavors. They are connected to GPDs as particular examples of the previously discussed Mellin moments:

$$\int_{-1}^{1} \mathrm{d}x\, x H^f(x,\xi,t) = A^f(t) + 4\xi^2 C^f(t), \tag{2.42}$$

$$\int_{-1}^{1} \mathrm{d}x\, x E^f(x,\xi,t) = B^f(t) - 4\xi^2 C^f(t). \tag{2.43}$$

The total angular momentum carried by each quark flavor J^f is given by ([29])

$$J^f = \frac{1}{2}(A^f(0) + B^f(0)), \tag{2.44}$$

which is a restatement of the Ji sum rule in the quark case, as promised.
If instead of integrating out the x dependence one Fourier transforms the matrix elements given in Eq. (2.15), one recovers the so-called Impact Parameter Distributions (IPDs), which are given by ([54])

$$\mathcal{I}_{++}(x,\xi,\vec{b}) = \frac{1}{4\pi}\int_0^\infty d(\vec{\mathbb{D}}^2) J_0\Big(|\vec{\mathbb{D}}||\vec{b}|\Big)(H - \frac{\xi^2}{1-\xi^2}E) \tag{2.45}$$

$$\mathcal{I}_{-+}(x,\xi,\vec{b}) = \frac{1}{4\pi}\frac{b^2 - ib^1}{|\vec{b}|}\int_0^\infty d(\vec{\mathbb{D}}^2) J_1\Big(|\vec{\mathbb{D}}||\vec{b}|\Big)\frac{|\vec{\mathbb{D}}|}{2m}E, \tag{2.46}$$

where b, referred to as the impact parameter, is a spatial vector Fourier conjugate to the momentum

$$\vec{\mathbb{D}} = \frac{\vec{P}'}{1-\xi} - \frac{\vec{P}}{1+\xi} \tag{2.47}$$

$$\lim_{\xi\to 0}\vec{\mathbb{D}} = \vec{\Delta}. \tag{2.48}$$

These are the so-called "skewed IPDs". If the skewness is taken to zero, the "normal" IPDs, which offer a 3D probabilistic interpretation in mixed position (transverse) and momentum (longitudinal) space, are recovered [55].

If instead of Fourier transforming with respect to $\vec{\Delta}_\perp$ one does so with respect to x, one recovers the Ioffe-time distributions in terms of the Fourier conjugate of x, $\nu = \bar{P}^+ z^-$ as ([56, 57])

$$\text{GPD}(\nu, \xi, t) = \int \text{d}x e^{ix\nu} \text{GPD}(x, \xi, t), \tag{2.49}$$

where GPD$\in \{H, E\}$.
One other simplification of the GPD is to the PDF in the "forward limit", where the momentum difference between the incoming and outgoing states is set to 0. This is given by

$$H^f(x, 0, 0) = q^f(x)\Theta(x) - \bar{q}^f(-x)\Theta(-x), \tag{2.50}$$

for the quark flavor f. The PDF is employed in one of the "positivity" properties of the GPD. Positivity refers to a set of conditions GPDs must satisfy in the DGLAP region, one of which is given in [34] as

$$|H^f(x, \xi, t) - \frac{\xi^2}{1-\xi^2} E^f(x, \xi, t)| \leq \sqrt{q^f(\frac{x+\xi}{1-\xi}) q^f(\frac{x-\xi}{1-\xi}) \frac{1}{1-\xi^2}}. \tag{2.51}$$

2.5 . Introduction to the Lattice

As discussed earlier in this chapter, quantum field theoretic calculation of cross sections requires writing down amplitudes which describe all possible ways in which an interaction might occur. The part of the previous sentence doing the heavy listing is the phrase "all possible". From the perspective of a perturbation theorist, a functional definition of this phrase can be derived by considering that one should, order by order in the coupling, expand the path integral of the QFT with which they work, computing at each order more precise contributions to the quantity they desire. Neglecting the fact that this doesn't work to arbitrarily high precision even in theory as the perturbation series involved eventually diverges, it is a nice, procedural understanding of how to handle the path integral. However, when perturbation theory is not a viable possibility, i.e., when it breaks down as in QCD, other methods may be used.
One such method is that of the lattice simulation. Lattice field theory is a method of computing quantities on a finite box of countably many discrete spacetime points. In addition to being finite, and therefore computable, modern lattice calculations in QED and QCD, theories which are defined in Minkowski space, are defined on the lattice rather in Euclidean space, that is, with a positive definite metric. Such Euclidean calculations of the results of Minkowskian theories is achieved by extending theories defined in Minkowski space to "imaginary time", thereby introducing an additional $-$ sign into the

metric and making it positive definite (up, possibly, to a phase). In general, integrals in imaginary time may be related to their real time counterparts using contour integration, but this becomes a messy game as such a "Wick rotation" requires intimate knowledge of the singular structure of the integrand (moments of the exponential of the action) in the complex plane [58]. If it is indeed so difficult to perform physically relevant computations in imaginary time, what practical reason could exist to willingly endure such pain? The exponential of the action, forming a complicated part of the integrand involved in path integral computations of amplitudes in QFTs, is oscillatory in the sense that the imaginary unit i multiplies the action when time is taken to be real. When time is taken imaginary, the integration measure used to compute the action introduces an additional complex unit, therefore making the action exponential real. As a result, correlations computed on an Euclidean lattice are characterized by exponential decay instead of oscillatory behavior. Therefore, with a sufficiently large lattice, one is able to estimate correlation functions.

However, if one wants to make physical predictions one should ideally make them using quantities which are independent of the size of a finite box and the spacing between its points. What lattice practitioners, who do not work in such ideal situations, do to remedy this situation is "extrapolate to the continuum". This may be achieved by computing the same physical quantity using different lattices of various sizes and lattice spacings, and using the set of corresponding results to extrapolate towards the continuum.

In GPD computations, the situation is even worse. GPDs and related objects are defined on the lightcone. However, vectors pointing in light-like directions ($v^2 = 0$) collapse to points in Euclidean space unless one is willing to work with complex coordinates, whose entry in the lattice game would trigger severe complications. Therefore, in addition to being required to extrapolate all results to the continuum, those lattice practitioners computing distributions defined at lightcone distances are limited to computations of similar distributions defined off of the lightcone, and matching them to the lightcone. Worse, it is not necessarily the case that the prescription used to go to the continuum commutes with that used to go to the lightcone [59]. As a result, getting a handle on lightcone distributions on the lattice is no trivial task and all of the associated limits must be carefully handled. In the following subsection of this chapter we will discuss two such formalisms and touch upon their comparisons to experiment.

2.5.1 . Pseudo and Quasi Formalisms

Pseudo-GPDs are derived through Fourier transforms of Ioffe-time-dependent distributions onto space-like intervals and provide a generalized framework for GPDs. By being defined as Fourier transforms of generalizations of Ioffe-

time-dependent distributions they ensure a covariant definition of the average momentum fraction x, and their support is naturally constrained within $-1 \leq x \leq 1$ due to the properties of the associated diagrams [60].
Quasi-GPDs are defined as Fourier transforms of matrix elements employing longitudinal separations $z = z_3$ on the lattice [61]. As a consequence, the pseudo formalism employs a generalization of the lightcone matrix elements used to define various distributions, while the quasi formalism exchanges lightcone distances for space-like ones and, by taking an increasing limit of the average nucleon momentum, approximate the lightcone counterparts of quantities defined at light-like separations.
In Fig. 2.7, a comparison of Pseudo-PDF results to various experimental PDF extractions is shown. In the valence region ($0.2 \leq x \leq 0.6$) there is some disagreement between the set of experimental PDF extractions and the lattice Pseudo-PDF shown in purple, however, this discrepancy is rather small and is due to a lack of understanding of systematic effects.
Correspondingly, in Fig. 2.8, a lattice Quasi-PDF computation is compared to a separate experimental PDF extraction. The relatively large disagreement when compared to that mentioned in the pseudo case above is due to an even greater lack of control of systematic uncertainties. Taking a further look at purely quasi results, in Fig. 2.9 two quasi-GPDs as well as a corresponding quasi-PDF are shown. Importantly, the presented GPDs are discontinuous on the line $x = \xi$ which contributes to an undefined DVCS amplitude via undefined CFFs as one can see from Eq. (2.22).
For this reason, the mock lattice data explained and employed in the following chapter is based on Pseudo-PDF data, as we will see.

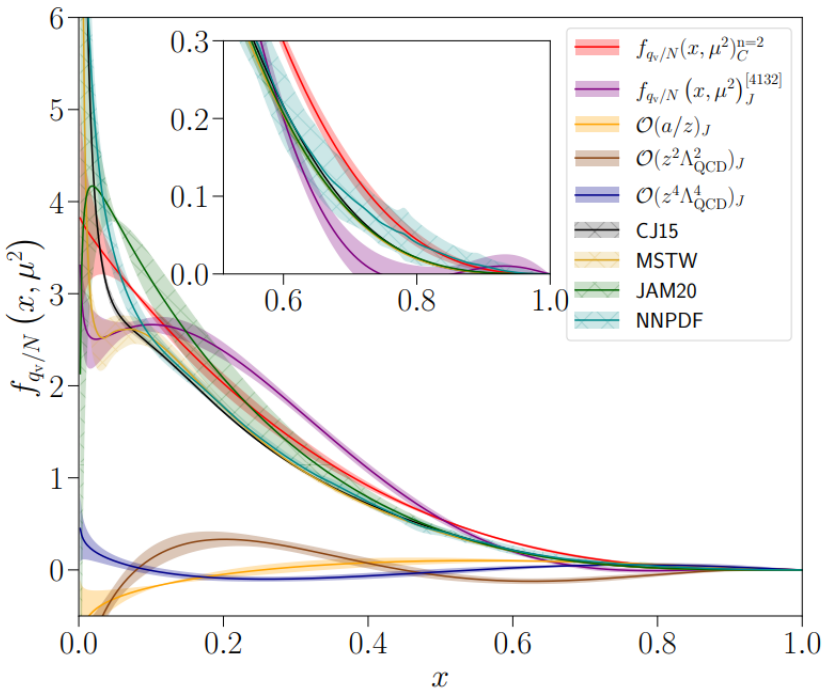

Figure 2.7: Here is shown Fig. 18b from [62] comparing experimental Next to Leading Order (NLO) PDF extractions from JLab and Fermilab data [63] (CJ15, grey/black), a global analysis based NLO PDF determination [64] (MSTW, yellow), a Next to Next to Leading Order (NNLO) PDF from a joint PDF and FF determination via Monte Carlo analysis of high-energy lepton-lepton, lepton-hadron and hadron-hadron scattering data [65], (JAM20, green), a NNLO PDF determined from a global analysis of Tevatron, Large Hadron Collider beauty (LHCb), A Toroidal LHC Apparatus (ATLAS), and Compact Muon Solenoid (CMS) data [66] (NNPDF, teal), a phenomenological PDF model [62] ($f_{q_v,N}(x,\mu^2)_C^{n=2}$, red), a valence quark leading twist lattice Pseudo-PDF [62], ($f_{q_v,N}(x,\mu^2)_J^{[4132]}$, purple), and three corresponding subleading twist lattice Pseudo-PDF analyses ($\mathcal{O}(a/z)_J$, yellow), ($\mathcal{O}(z^2\Lambda^2_{\rm QCD})_J$, brown), ($\mathcal{O}(z^4\Lambda^4_{\rm QCD})_J$, blue), as well as the corresponding 3σ bands All shown curves are PDFs of quarks in the nucleon.

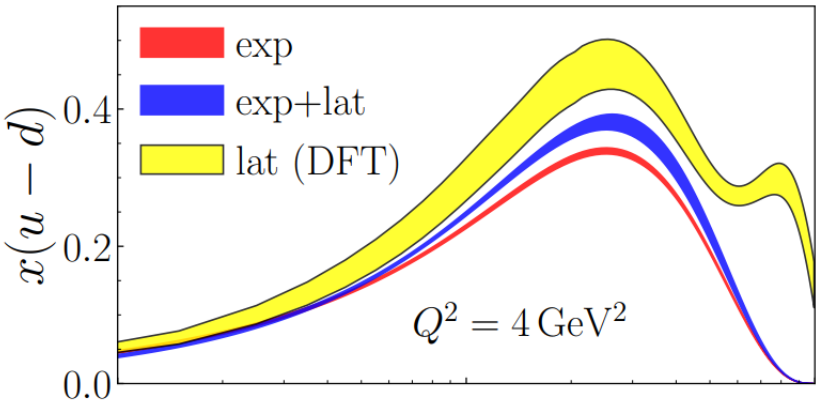

Figure 2.8: A comparison of $x(u-d)$ where u, d represent the u, d quark PDFs as a function of x as extracted from (fit to) a range of experimental data (red), a (fit of) quasi-PDF lattice data (yellow) and a joint fit of the two data sets (blue), each including the corresponding 3σ bands is shown in Fig. 1 of [67]. All shown curves are PDFs of quarks in the nucleon.

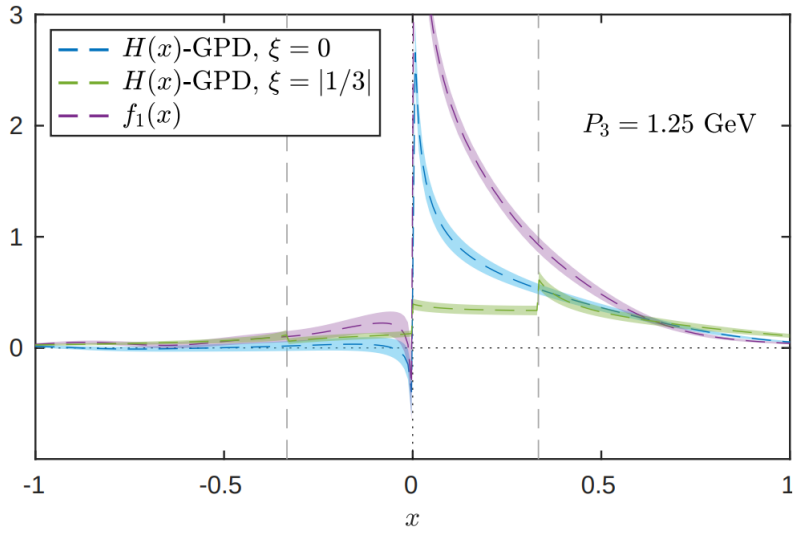

Figure 2.9: Fig. 3 of [68]. The GPD H for $\xi = 0$ (blue) and $\xi = |\frac{1}{3}|$ (green), along with the unpolarized PDF (violet) for $P_z = 1.25$ GeV, are shown [68], as well as each of the corresponding 3σ bands. The region between the vertical dashed lines denotes the ERBL region (see Fig. 2.6). There is a clear discontinuity of in H at $x = \xi$. All shown curves are given in the quark in the nucleon case.

3 - Reweighting

In a continuous effort to discriminate amongst the infinitude of candidate GPDs in an unbiased way while simultaneously ensuring that all such candidate functions satisfy all of the properties of GPDs discussed in the previous chapter (see Subsec. 2.4.2), there have been efforts to model GPDs using Artificial Neural Networks (ANNs). One such case conducted by some of my colleagues is that of [69], in which Goloskokov-Kroll (GK) [70, 71, 72, 73] GPD pseudodata was used to train a set of ANNs whose architecture ensures the satisfaction by all produced candidate functions of most GPD properties. To analyze the impact of further discrimination amongst the produced candidate functions via the introduction of lattice data, mock lattice data which varies systematically with respect to its compatibility with the set of candidate functions was introduced. In this chapter's first two sections, the configuration of the ANNs used for generation of the GPD candidates is described. In the third section, the input data and statistical methods used in the analysis are discussed. In the fourth and fifth, the motivation of the use of the mock lattice QCD data, its generation, and the method of using it to discriminate amongst the candidate GPD replicas is delineated. In the subsequent two sections, the results of such discrimination, called reweighting, are discussed. In the final section, the chapter will be concluded.

3.1 . Artificial Neural Networks

Neural networks are made up of layers of nodes. Feed forward neural networks are those neural networks in which there exist connections only between nodes of adjacent layers (Fig. 3.1). In feed forward ANNs, the output of each node j in layer $i > 1$ (where $i = 1$ represents the input layer), is denoted as $n_{i,j}$, is calculated as

$$n_{i,j} = a_{i,j}(\sum_{k=1}^{N_{i-1}} w_{i,j,k} \cdot n_{i-1,k} + b_{i,j}) \tag{3.1}$$

where $w_{i,j,k}$ is the weight between the kth node in layer $i-1$ and the jth node in layer i, and $b_{i,j}$ is the bias parameter for node j in layer i. N_{i-1} is the number of nodes in the previous layer ($i-1$), and $a_{i,j}$ is an activation function. In the context of ANNs, there exist universal approximation theorems which guarantee that given a sufficiently large network, regardless of its width or depth, it can accurately approximate any continuous function defined on a compact set [74].
The activation functions used are often step functions or sigmoid functions.

The sigmoid is defined as

$$a_{i,j}(p) = (1 + e^{-p})^{-1}, \tag{3.2}$$

which interpolates between 0 as $p \to -\infty$ and 1 as $p \to \infty$.
One important aspect which differs greatly between the description of common ANNs and those employed in the study described here is that of the form of the argument to the activation functions. Due to the constraint of the reproduction of the forward limit (Eq. (2.50)), the arguments to the activation functions feature nonlinearity in the input DD arguments α and β. Further, modeling directly in DD space allows automatic fulfillment of the polynomiality property of GPDs (Eq. (2.33)).
Explicitly, the neurons of the network's single hidden layer perform output

$$\begin{aligned} n_{2,k} \quad = \quad & (a_{2,k}(b_{2,k} + w_{2,1,k}|\beta| + w_{2,2,k}\alpha/(1-|\beta|)) \\ & -a_{2,k}(b_{2,k} + w_{2,1,k}|\beta| + w_{2,2,k})) \\ & +(a_{2,k}(b_{2,k} - w_{2,1,k}|\beta| - w_{2,2,k}\alpha/(1-|\beta|)) \\ & -a_{2,k}(b_{2,k} - w_{2,1,k}|\beta| - w_{2,2,k})), \end{aligned} \tag{3.3}$$

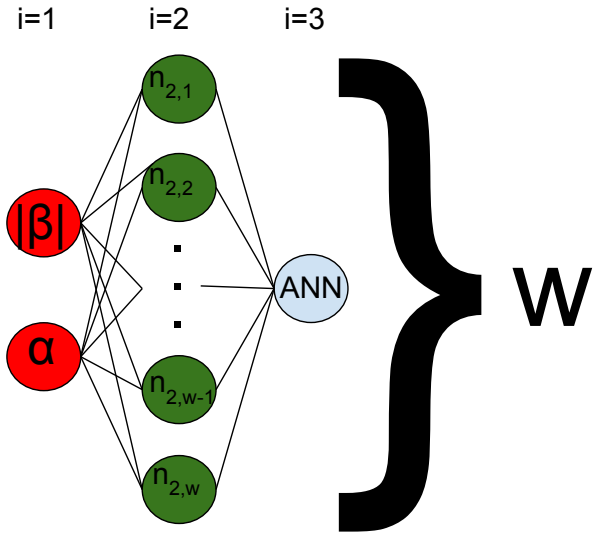

Figure 3.1: A diagram of a three layer neural network including the input and output layers, as well as one hidden layer, is shown from [69]. The DD arguments α and β are received in the input layer and the output layer consists of a single node.

where the $b_{2,k}$ are biases and the $\omega_{1;2,1,k}$ are weights, all of which are free parameters. The functional form $\alpha/(1-|\beta|)$ has been chosen in order to

ensure that the resulting DD vanish at the boundary $|\alpha| + |\beta| = 1$ in order to avoid singular behavior apart from at the point $x = \xi = 0$. The output layer, made up of a sole neuron, has the output

$$\sum_k = \omega_{2,k,1} n_{2,k} \tag{3.4}$$

which notably lacks bias parameters, and employs a purely linear activation function. Three extractions of GPDs using pseudo-data generated with the GK model were performed using such ANNs, a diagram of which is presented in Fig. 3.1. In the first test case, training was done on a dataset where $x \neq \xi$, aimed to reproduce GPD models like GK, and unlike GK this test's model included a D-term contribution to be discussed in the following section (Sec. 3.2). Further, the positivity constraint (Eq. (2.51)) was not enforced as it would have also required simultaneous fit of the GPD E.
In the second test case, only $x = \xi$ data were used, showcasing the capacity for reconstruction of GPDs from processes like DVCS described at LO. The positivity constraint was not enforced in this test, and no D-terms was included. Extremely large uncertainties resulted except for on the $\xi = x$ line (see Fig. 3.2). This highlighted the importance of the inclusion of shadow distribution contributions, which are those GPDs whose contributions to the DVCS amplitude are yielded null as they are eigenvectors of eigenvalue zero of the DVCS kernel [75].

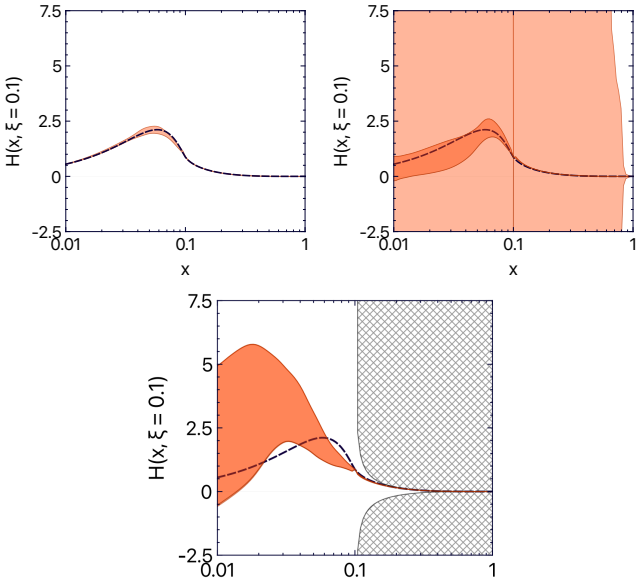

Figure 3.2: From [69], with $\xi = 0.1$. Top left panel: The ANN model is shown to reproduce GK data. Top right panel: The lack of constraint from positivity (2.51) (where the GPD E is taken to be zero) results in extremely large uncertainty. Bottom panel: Enforcing positivity, while killing most of the replicas generated, results in much less extreme values of uncertainty.

In the third test case, the same conditions as in the second one were employed, but the positivity inequality was enforced to show its impact on reducing uncertainties, which was quite large.
What can be surmised from these three cases? In the first case, the artificial neural network (ANN) model successfully replicates the GK data, demonstrating its capability. However, in the second case, the absence of constraint from positivity, as represented by equation (2.51) with the GPD E assumed to be zero, leads to a notable issue: an exceedingly high level of uncertainty. Conversely, in the third case, a potential remedy emerges: by enforcing positivity, albeit at the expense of discarding the majority of generated replicas, the extreme values of uncertainty are significantly reduced. This approach effectively addresses the problem of excessively high uncertainty, offering a more balanced outcome.
In this analysis, the minimization procedure, which involved constraining free parameters, was conducted using a genetic algorithm [76]. The genetic algorithm operated iteratively, evaluating multiple sets of free parameters (referred to as "candidates" in the literature) simultaneously against a fitness function. Following evaluation, the best candidates—those characterized by the highest values of the fitness function—were subjected to crossover in the hope of producing even better candidates for subsequent iterations. Crossover was followed by mutation, where a number of free parameters were ran-

domly altered, significantly reducing the risk of converging to a local minimum. It is noted that since the fitness function was simultaneously evaluated for all candidates in a given iteration of the genetic algorithm, multithreaded computing could be employed to enhance minimization performance.
As observed in other analyses using effectively nonparametric models, regularization had to be employed to avoid biased results caused by overfitting. If regularization was not applied, the training data tended to be described extremely precisely by an (ANN), resulting in minimal variance. However, this precision did not necessarily translate into equally accurate descriptions of other data or predictive power. Generally, bias could manifest due to excessive focus on describing the training data, leading to poor representation of general trends. Many types of regularization methods exist, and the selection of a particular method typically depends on the specific problem under consideration. In this analysis, the dropout method [77] was utilized. In this method, a predefined fraction of neurons (in this case, 10%) was randomly dropped in each iteration of the minimization algorithm (referred to here as the genetic algorithm). This resulted in some neurons becoming inactive and not processing signals, while the output of other neurons was correspondingly scaled to compensate for the loss. Effectively, each iteration probed a different architecture of the ANN, preventing fixation on details solely characterizing the training sample.

3.2 . GPD Modeling with ANNs

The current chapter of the thesis focuses only on results related to the GPD $H(x,\xi,t)$ where t is set to zero in order to focus solely on the $x-\xi$ plane. The reader is reminded how such a GPD may be represented in terms of the Radon transform of a DD as in Eq. (2.33). The ANN models described here and in [69] model the DDs corresponding to the GPD H. Specifically, the odd combination $H^{q(+)}(x,\xi,0) = H^q(x,\xi,0) - H^q(-x,\xi,0)$, the sea quark GPD, will be studied.
To achieve a satisfactory flexibility and reproduction of known limits, this DD model is written as the sum of three terms as

$$(1-x^2)F_C(\beta,\alpha) + (x^2-\xi^2)F_S(\beta,\alpha) + \xi F_D(\beta,\alpha), \tag{3.5}$$

with F_C intended to reproduce the forward limit (Eq. (2.50)) and flexibly model on the $x=\xi$ line, F_S intended to reproduce the uncertainty inherent to deconvolution with a singular perturbative kernel with an explicit lack of contribution both in the forward limit and at $x=\xi$, and F_D designed to model the D-term, as discussed in Eq. (2.33),

$$F_C(\beta,\alpha) = f(\beta)h_C(\beta,\alpha)\frac{1}{1-\beta^2}. \tag{3.6}$$

Introduced in the study is the equation (3.6), where $F_C(\beta,\alpha)$ is defined, ensuring the proper reduction to the forward limit and providing the necessary flexibility to model the $x = \xi$ line, which holds particular relevance for the current GPD phenomenology due to the access provided to this kinematic region via CFFs (see Subsec. 2.4.1). The prefactor $(1-x^2)$ of $F_C(\beta,\alpha)$ in (3.5), combined with $1/(1-\beta^2)$ in (3.6), facilitates the fulfillment of the positivity constraint (2.51). Denoted by $f(\beta)$, the forward limit represents the unpolarised PDF for the GPD H, while $h_C(\beta,\alpha)$ is a profile function given in the study by:

$$h_C(\beta,\alpha) = \frac{\mathrm{ANN}_C(|\beta|,\alpha)}{\int_{-1+|\beta|}^{1-|\beta|} \mathrm{d}\alpha \mathrm{ANN}_C(|\beta|,\alpha)}. \tag{3.7}$$

The neural network $\mathrm{ANN}_C(|\beta|,\alpha)$, even with respect to both β and α variables due to a special design of the activation function and the use of the absolute value, vanishes at the edge of the support region $|\beta|+|\alpha|=1$. The evenness in β maintains the resulting GPD as an odd function of x, relevant for the phenomenology of DVCS, while the evenness in α is mandatory for the time reversal property, ensuring invariance under $\xi \to -\xi$ exchange. Normalization by the integral over α, achievable analytically, enforces the proper forward limit, while the rest of the model typically trains to reproduce the diagonal $x = \xi$ at LO probed by amplitudes of processes like DVCS, TCS, and DVMP. Additionally, due to the tight constraints on the term $F_C(\beta,\alpha)$, necessitated by the reproduction of both $\xi = 0$ and $x = \xi$ lines, an additional term $F_S(\beta,\alpha)$ is introduced. This term explicitly vanishes on these lines, not contributing to the fit of $F_C(\beta,\alpha)$ on the phenomenological inputs. Instead, $(x^2-\xi^2)F_S(\beta,\alpha)$ aims to reproduce the deconvolution uncertainty of exclusive processes, corresponding to a LO shadow distribution as defined and studied in [75]. F_S as follows:

$$F_S(\beta,\alpha) = f(\beta) h_S(\beta,\alpha), \tag{3.8}$$

where:

$$\begin{aligned} h_S(\beta,\alpha)/N_S = &\frac{\mathrm{ANN}_S(|\beta|,\alpha)}{\int_{-1+|\beta|}^{1-|\beta|} \mathrm{d}\alpha \mathrm{ANN}_S(|\beta|,\alpha)} \\ &- \frac{\mathrm{ANN}_{S'}(|\beta|,\alpha)}{\int_{-1+|\beta|}^{1-|\beta|} \mathrm{d}\alpha \mathrm{ANN}_{S'}(|\beta|,\alpha)}. \end{aligned} \tag{3.9}$$

During training, efforts focused on maximizing the N_S normalization factor in (3.9) within positivity limits to leverage maximal flexibility. By writing $h_S(\beta,\alpha)$

as the difference of two profile functions characterized by $\mathrm{ANN}_S(|\beta|,\alpha)$ and $\mathrm{ANN}_{S'}(|\beta|,\alpha)$, one ensures $F_S(\beta,\alpha)$ adds no contribution to the forward limit, while the $f(\beta)$ factor helps enforce positivity.
Lastly, $F_D(\beta,\alpha)$ provides the additional flexibility necessary to model the D-term, which, as mentioned previously, is a degree of freedom of GPDs associated with the final terms in ξ^{n+1} in (2.32), crucial in characterizing partonic matter [78, 48, 44, 47]. It is given by:

$$F_D(\beta,\alpha) = \delta(\beta)D(\alpha), \tag{3.10}$$

and

$$D(\alpha) = (1-\alpha^2)\sum_{\substack{i=1\\ \text{odd}}}^{N} d_i C_i^{\frac{3}{2}}(\alpha), \tag{3.11}$$

where d_i are coefficients of the expansion of the D-term into Gegenbauer polynomials, and where $N = 5$ is an arbitrary truncation parameter.

3.3 . Experimental Data and Uncertainty Estimation

For the purpose of a proof of concept via the implementation of the network architectured to be employed for GPD modeling, it was incumbent upon the author's colleagues to use reliable experimental data in whichever kinematic ranges they preferred in the $x-\xi$ plane. As a result, GK pseudodata was used, as opposed to proper experimental data. The GK model will be explained and explored in this section's first subsection. In the second, a statistical technique for estimating the standard deviation when one is unsure how to usefully define outliers of a data set, known as Median Absolute Deviation (MAD), will be explained as it is the basis of the statistical analysis of this impact study.

3.3.1 . GK Pseudodata

The GK pseudo-experimental data used for the ANN GPD modeling (replica generation) performed as a precursor to the impact study regarding lattice data explained in this thesis was generated based on the following model.
The GK model, originally published as a phenomenological ansatz for the approximation of cross sections in the context of DVMP, has been widely successful in terms of its capacity to reproduce experimentally measured DVMP cross sections low x and high photon virtuality Q^2 [70, 71, 72, 73], (see Fig. 2.5). Much like the processes of DIS and DVCS, the DVMP cross section can be factorized into a hard process which is calculable order by order in perturbation theory, and the GPD of the nucleon (in this case) [72, 71]. However, there is a third amplitude involved in DVMP resulting most directly in meson production referred to as a DA. This DA must be convolved properly with

the nucleon GPD and the corresponding perturbative kernel in order to accurately represent the process shown in the diagram Fig. 2.5.
This thesis will not discuss further the DA and its properties. Rather, as discussed in the previous chapter in the contexts of DIS and DVCS, we merely point out that a proof of factorization of DVMP exists [27]. Given the universality of GPDs discussed in the same section, the GPD ansatz employed in the GK model has been applied to other processes such as DVCS [79].
This ansatz was created in DD space in order to preserve the polynomiality property of the GPD [71, 72, 73]. Correspondingly, this pseudodata is limited by GK's previously discussed kinematic modeling assumptions.

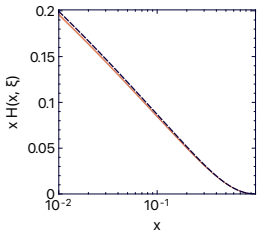

Figure 3.3: The ANN modeling, fitted to GK pseudodata, is compared to said pseudodata as a test of reproducibility at $Q^2 = 4$ GeV^2. When constraining the ANN model with 400 points assessed using the GK model [71, 72, 73] for sea quarks in the $x \neq \xi$ scenario, without enforcing positivity, all three contributions ($F_C(\beta, \alpha), F_S(\beta, \alpha), F_D(\beta, \alpha)$) are incorporated in the presentation of results. Fig. directly from [69].

Fig. 3.3 provides an example of how well the behavior of the used GK pseudo-data is reproduced by the ANN models described in Secs. 3.1 & 3.2.

3.3.2 . MAD

Call this median of a data set X indexed by i $m_X = \text{Median}(X_i)$. A well understood reason for employing the median, as opposed to the mean or other values, as an estimator of a data set's central value is its lack of sensitivity to extreme values, which one may consider outliers.

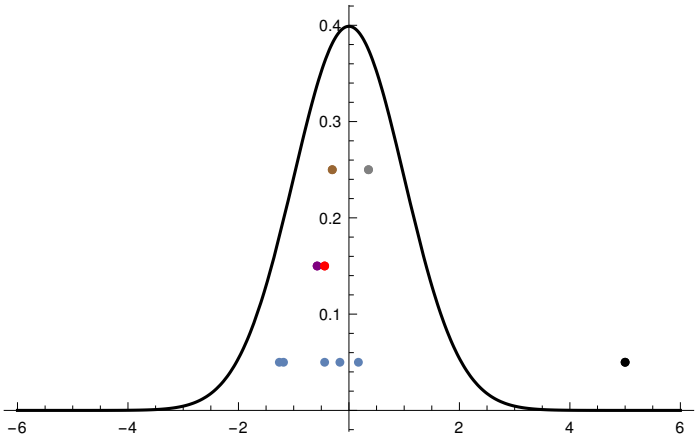

Figure 3.4: A simple example of the resistance of the median to outliers whose effect on the corresponding mean is greatly exaggerated is shown. The blue points have been sampled from the underlying standard normal distribution shown in black. The introduced black point is present at a distance of $5\sigma = 5$ from the central value of the distribution. In purple is the mean of the set of blue points only, and in red is their median. In gray, the mean of the set of blue points and the black point is shown, while in brown is their median. The vertical coordinates of all points are of no significance and only serve for visual ease of comprehension.

As an example, consider Fig. 3.4. Sampled from the shown standard normal distribution whose mean and median are both 0 are 5 points shown in blue. The vertical coordinates of all shown points are assigned only for ease of viewing and carry no significance. The mean of this sample is shown in purple, and the corresponding median is shown in red. As one expects, there is no major difference between these two estimators of central value given the significant clustering of the data near the center of the distribution. Upon the inclusion of the black point, five standard deviations from the central value of the distribution, the resulting mean of the group of 6 points is shown in gray, whereas their median is given in brown. While the median of these 6 points is relatively resistant to the addition of the 6th point, which one might consider an outlier, the means including and excluding this point are significantly distinct. In this clear cut example, exclusion of the outlier shown in black for any further analysis of the data set would be reasonable. However, it is not always clear how to define outliers in general. How should one decide which points should be excluded from further analysis of an arbitrary data set? In lieu of answering this question directly, let's take a look at the following scenario. Later, an explicit example regarding the trouble of defining outliers in the case of the replica set will be provided.
Given a "small" set of data values, X_i one knows first of all how to establish the median value of such values. In general, one may ask why the mean and

the median of X may widely vary with respect to one another based on the underlying distribution governing the data set X. X may contain asymmetries, etc. which contribute to this difference. As such, one may decide to estimate the central value of X using a modified definition of "mean", which takes into account most but not all of the data set X, excluding points which contribute the most to the deviation of the mean from the median m_X. These excluded points are named "outliers". What remains unclear during this explanation of the origin of the idea of outliers, however, is how to precisely determine which points should be considered as such. To illustrate this point, one might imagine constructing various subsets of X, all of whose means reproduce well the median value m_X. Which such subset should one choose for the rest of their analysis? To avoid the arbitrariness inherent to this question, one may simply use the median m_X directly as their estimation of the central value of X. However, when it comes to estimating higher moments of the distribution underling X, such as the standard deviation, one is seemingly forced to decide whether or not to include only a subset of X which reproduces a more representative estimation of such moments at the cost of inclusion of arbitrariness, or to instead deal with a nonarbitrary estimator which poorly reproduces the underlying distribution of X. An assumption inherent in this discussion is that of prior intuition regarding the shape of the underlying distribution governing the sample set X, which from here on we choose to be a normal distribution, which notably has zero statistical skewness (unrelated to the skewness ξ of the GPDs discussed in this thesis). In light of this assumption and the desire to avoid defining outliers, we turn to the MAD estimator of standard deviation, which, as its name suggests, estimates the standard deviation of a sample distribution as the median of the set of absolute deviations of the data set from its central value. We will hereon use the median m_X of X as the corresponding central value estimator. The MAD estimation of the standard deviation of X, is given by [80]

$$\hat{\sigma} \approx 1.4826 * \text{Median}(|X_i - m_X|). \tag{3.12}$$

The presented factor of 1.4826 is derived from the earlier stated assumption that the underlying distribution of the data set is normal.
Understanding now that such a robust second moment estimator may be defined in analogy with the median, one might be tempted to explore analogous definitions for higher moments related to the statistical skewness, kurtosis, etc.. However, given our assumption of a normal distribution for all data sets presented in this work, this thesis will not employ any such definitions. Rather, consider once more the simple example presented in Fig. 3.4. Visualised in addition this time are the spreads of the data sets calculated using the standard deviation and the MAD estimator of standard deviation, shown in Fig. 3.5.

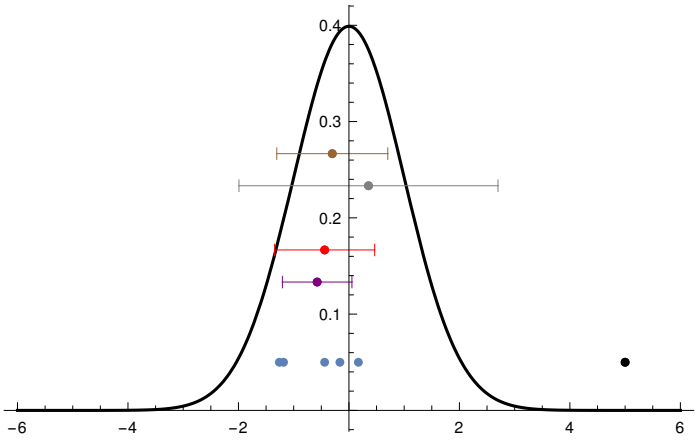

Figure 3.5: A continuation of the example shown in Fig. 3.4 of the resistance of the median to outliers whose effect on the corresponding mean is greatly exaggerated is shown. In addition, each mean is outfitted with error bars denoting the corresponding standard deviation and each median with the corresponding MAD estimated standard deviation. The blue points have been sampled from the underlying standard normal distribution shown in black. The introduced black point is present at a distance of $5\sigma = 5$ from the central value of the distribution. In purple is the mean of the set of blue points only, and in red is their median. In gray, the mean of the set of blue points and the black point is shown, while in brown is their median. The vertical coordinates of all points are of no significance and only serve for visual ease of comprehension.

What is most striking about this example is that the standard deviation including all 6 points (shown in gray) is so much larger than that of the set of only blue points (shown in purple). The corresponding spread change using the MAD estimator without the black point (shown in red) and with the black point (shown in brown) is expectedly robust with respect to this inclusion. However, observe also that while robust, the MAD estimator provides an inflated assessment of the spread of the blue points with respect to the traditional standard deviation. The difference is however a cheap price for the avoidance of outlier definition.

3.4 . Mock Lattice QCD Data Generation

Now understanding both the origin of the GPD replicas (candidate functions) and an important statistical estimator to be employed later in this chapter, it is necessary to take a look at the reasoning for which and method by which mock lattice data has been generated for the forthcoming impact study of its discriminating effect with respect to the ANN GPD replicas. These two points will be respectively delineated in the following subsections.

3.4.1 . Precision and Correlation

The choice to use mock lattice data for this impact study is informed by two key points. The first of these reasons is a lack of access to lattice data. The second, which is an advantage rather than a disadvantage of using mock data, is the ability to systematically control the agreement of the mock data with the set of GPD replicas considered. This systematic control was achieved via the use of parameters controlling the precision and the correlation of the mock lattice data.

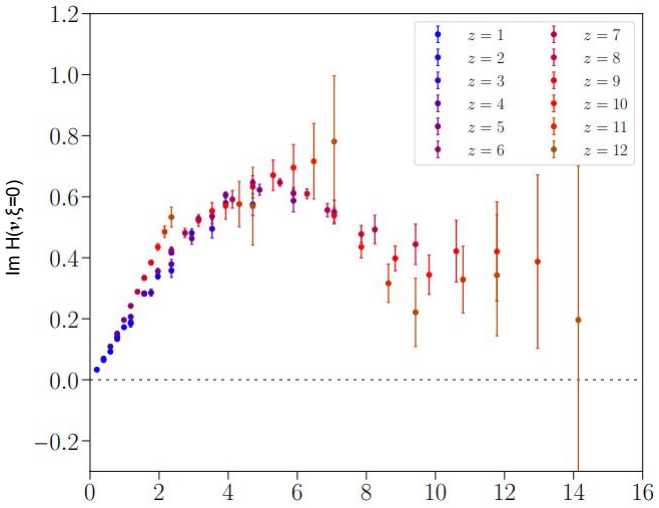

Figure 3.6: An example of realistic lattice data from [62](Fig. 4) is shown.

Based on actual lattice studies such as [62] one draws the conclusion that current state of the art lattice GPD extractions are not equally facilitated in all kinematic ranges. Taking a look at Fig. 3.6 in this reference, lattice data is plotted as a function of Ioffe time $\nu = P \cdot z$, the Fourier conjugate of the momentum fraction x. Indeed, lattice GPD data is presented in general in Ioffe time space in various references as such calculations occur on an Euclidean spacetime lattice, and not in momentum space. However, it is worth noting that the lattice data after which the mock lattice data generated in this study was modeled was not matched to the lightcone, but, as is the case with all lattice data, exists along some Euclidean direction, as was discussed in Subsec. 2.5.1. Therefore a proper study comparing replica to mock lattice data would not have taken place on the lightcone, but off the lightcone.HERE Euclidean replicas are obtained via the convolution of the lightcone one by a matching kernel. This kernel was neglected as in perturbative QCD it is unity up to corrections involving the renormalization scale μ at hand, which was also neglected in the previously described ANN models. Therefore, all calculations in this thesis comparing and combining ANN GPD replicas to mock lattice data are performed in Ioffe time space. As the ANN fitted singlet GPD,

H, of the nucleon is that which is treated here, its odd parity in the longitudinal momentum fraction x allows the limitation of the corresponding Ioffe time studies to the imaginary part of H. That is,

$$H(\nu, \xi, t = 0) = \int_{-1}^{1} dx e^{i\nu x} H^{q(+)}(x, \xi, t = 0), \tag{3.13}$$

where the real part $\Re H(\nu, \xi)$ vanishes by parity. We choose for the rest of this chapter for $H(x, \xi)$ and its Fourier transform $H(\nu, \xi)$ to be distinguished only by their arguments.
As can be seen in the previously referenced Fig. 4b from [62], at Ioffe time values greater than $\nu = 10$ the signal quickly becomes dominated by noise and compatible with 0. In order to systematically produce mock lattice data in line with this characteristic of current state of the art lattice data, we chose to write down a function of Ioffe time which saturates to 5% error at $\nu = 0$, and 100% at $\nu = 10$ using an exponential interpolation between these two points to determine the behavior of the relative errors in the corresponding $0 \leq \nu \leq 10$ range. The most general exponential function given these endpoint constraints is given by

$$g(\nu; b, s = 5\%, \nu_{\max} = 10) = \frac{s(b^{\nu} - b^{\nu_{\max}}) + 1 - b^{\nu}}{1 - b^{\nu_{\max}}}, \tag{3.14}$$

where the parameter b, the base of this exponential function, determines the intermediate behavior of this interpolating function. As $b \to 1$, the corresponding behavior of g becomes linear, whereas as $b \to \infty$, g approaches a shifted and scaled step function in the given range. That is

$$\lim_{b \to 1^+} g(\nu; b, s = 5\%, \nu_{\max} = 10) = \frac{1 - 0.05}{10}\nu + 0.05 \tag{3.15}$$

$$\lim_{b \to \infty} g(\nu; b, s = 5\%, \nu_{\max} = 10) = 0.95\Theta(\nu - 10) + 0.05, \tag{3.16}$$

for $0 \leq \nu \leq 10$, where

$$\Theta(\nu) = 0 \quad , \quad \nu < 0 \tag{3.17}$$

$$\Theta(\nu) = 1 \quad , \quad 0 \leq \nu \tag{3.18}$$

In practice, the precision associated with mock lattice data points generated at "low" Ioffe times increases quickly when b is "low" ($b \to 1$) and slowly when b is "high". As such, we have chosen two values of $b = 1.1, 2$ corresponding to low and high precision mock lattice data generation respectively, which are shown in Fig. 3.7.

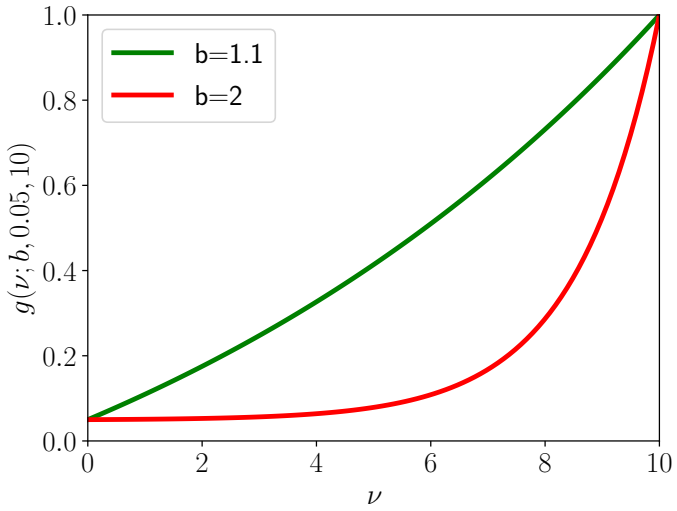

Figure 3.7: The function $g(\nu; b, s = 5\%, \nu_{\max} = 10)$ is shown for $b = 1.1$ in green and for $b = 2$ in red .

Now that our systematic control over the precision of the mock lattice data to be produced has been explained, it is important to determine what the corresponding central values should be. In practice, one never expects realistic lattice data to coincide exactly with the central values of replicas fitted from experimental data. What is important, rather, is that our produced data coincide more or less within their corresponding precisions with the central values of the replica set as a function of Ioffe time. Therefore, we choose to randomly distribute the set of mock lattice data points around the replica band's central value using the relative precision function g.
The used procedure is then as follows. Firstly, a set of Ioffe time values ν_i are chosen corresponding roughly to the density of points provided in the Fig. 4b [62]. At each such value ν_i, the central value of the replica band $\bar{\mu}_i$ is computed. Then, a single point is sampled from a multidimensional normal distribution whose central values are given by the $\bar{\mu}_i$ and whose corresponding standard deviations are given by $g(\nu_i; b, u = 10, v = 0.05)\bar{\mu}_i$. The coordinates of this point, called $\bar{\mu}_i^{\text{Latt.}}$, then serve as the central values of the generated mock lattice data, and the corresponding errors are given once more by $\sigma_i^{\text{Latt.}} = g(\nu_i b, u = 10, v = 0.05)\bar{\mu}_i$.
This method therefore generates mock lattice data which is in general compatible with the (central value of the) band of replicas within the precision generated by the function g. However, it is important to note that thus far, the data generation treats all mock lattice data points as uncorrelated. Decorrelation of realistic lattice data, while probable when regarding data from distinct lattice collaborations, is unlikely when referring to that of any single collaboration. To take this into account in our impact study, therefore, we have cho-

sen to generate mock lattice data in three distinct Ioffe time regions, wherein intracollaboration correlation is set to $0 \leq c < 1$, and intercollaboration correlation is set to zero. Effectively, this means that the correlation matrix of the multidimensional Gaussian distribution from which the mock lattice data is sampled takes on a block diagonal form, where each block of the correlation matrix C, C_j, is of the form

$$C_{j;i,i'} = \Big(c + (1-c)\delta_{i,i'}\Big)\sigma_i\sigma_{i'}, \tag{3.19}$$

where j is an index labeling the various blocks and the i, i' are indices corresponding to the Ioffe time values v_i included in said jth block. In the jth block, the correlation matrix $C_{j;i,i'}$ is constructed such that the diagonal terms are given by the corresponding variances assigned to the mock lattice data points. The off-diagonal terms are proportional to the correlation parameter c, which is multiplied by the product of the corresponding pair of standard deviations.

Note that a correlation value of $c = 1$ is not permitted as it corresponds to a singular correlation matrix (see Eq. (3.20)). This singularity is a problem both for the calculation of the χ^2 values of each of the replica points as discussed in the following section of this chapter, and due to the nature of the expression for the multidimensional correlated normal distribution employed in the data generation procedure defined above. Explicitly, this distribution is given in terms of the full $N \times N$ correlation matrix C as

$$(2\pi)^{-\frac{N}{2}}(\det(C))^{-\frac{1}{2}}e^{-\frac{1}{2}\sum_{1\leq\kappa,\rho\leq N}(y-\mu^{\text{Latt.}})_\kappa(C^{-1})_{\kappa,\rho}(y-\mu^{\text{Latt.}})_\rho}, \tag{3.20}$$

where the independent variables are given by y [81].

In reality, the correlation matrices of lattice data are more complicated than that used to generate our mock lattice data here. Such correlation matrices are not constant with respect to the Ioffe time distances between different pairs of points, nor are they constant with respect to the GPD skewness ξ. As such, one way to perform studies more refined than that presented explicit here would be to include such complicated correlations. Further, it would be excellent for lattice practitioners to publish their correlation matrices along with their lattice results, as without such matrices inclusion of lattice data in any kind of global fit or analysis yields conclusions with very limited scope.

Looking forward to the remainder of this chapter, it is important to specify the three "blocks" in which mock lattice data will be produced. They are given by

- $0.2 \leq \nu_i \leq 2$, $\Delta\nu = 0.2$
- $2.2 \leq \nu_i \leq 4$, $\Delta\nu = 0.2$
- $4.4 \leq \nu_i \leq 6$, $\Delta\nu = 0.4$,

where $\Delta\nu$ is the distance along the Ioffe time axis between points. Given that the use of three blocks is intended to reproduce the effects of the use of lattice data of three collaborations, it is worth noting that in practice the kinematic ranges of actual lattice data would overlap. These non-overlapping blocks have been chosen as a mere matter of simplicity as the analysis described here does not require the mock lattice data subsets be kinematically nonoverlapping. These blocks have been purposely chosen at relatively small Ioffe time values in order to reproduce most accurately the kinds of ν ranges for which GPD lattice results are most often presented in the current state of the art, and are therefore the most informative ranges to use for an impact study such as this [82]. Further, the relative sparsity of the chosen values in the block of highest Ioffe time values has been chosen to reflect such sparsity in previous lattice results.
Fig. 3.8 illustrates a mock lattice dataset (depicted as orange points) overlaid with the replicas generated by our GPD model. The four panels showcase the impact of different combinations of the correlation coefficient c and the noise parameter b. Higher values of c amplify the influence of one central value on the selection of others within a specific block in ν, while increasing the parameter b leads to a dataset more closely concentrated around the maximum likelihood of the GPD model.

3.5 . Bayesian Reweighting

With a method for generating systematically controlled mock lattice data in terms of both

- its precision and adherence to the set of GPD replicas and
- the correlation between all such generated data in hand. It is now possible to influence the associated uncertainty of the replica band using such mock lattice data in order to assess the potential discriminating ability of lattice data.

In the study discussed here, we chose to use a Bayesian reweighting procedure employing the mock lattice data as a prior, with the intention of investigating the resulting uncertainty of the set of GPD replicas without needing to perform costly refits. It is important to note that so far the discussion has largely ignored the skewness of the GPD despite its inclusion in the replica generation process, in order to focus on analysis in x and ν. In the final sections of this chapter, discussions of skewness will play an important role as a lack of positivity constraint on the GPD in the ERBL region has resulted in less coherence of the replica band in the ERBL region. In this section, however, it is first necessary to outline the Bayesian reweighting procedure employed in

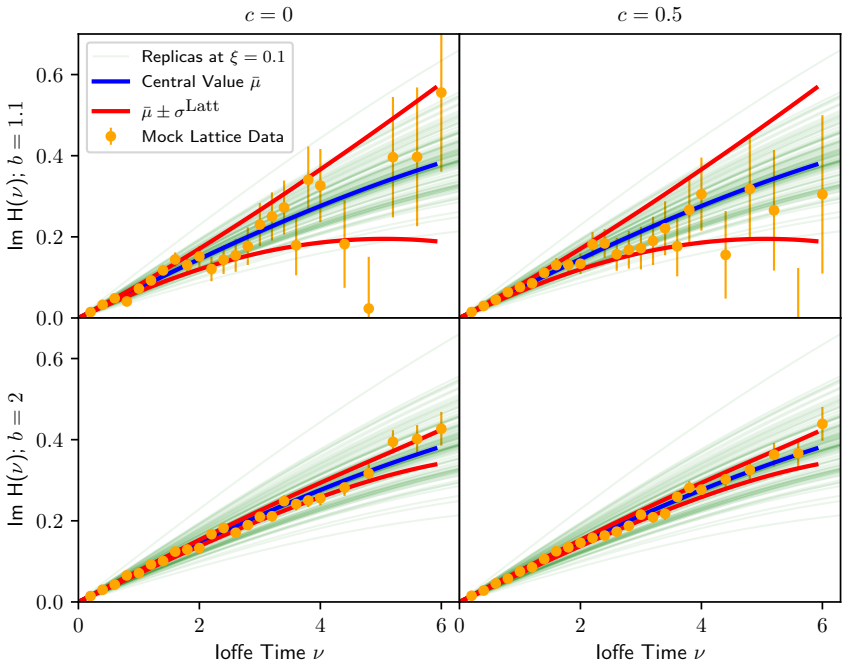

Figure 3.8: Shown are the ensemble of GPD replicas spanning Ioffe times from $\nu = 0$ to $\nu = 6$ at $\xi = 0.1$ (indicated in green), along with their median (in blue) and the 1σ band (in red), which corresponds to $b = 1.1$ (top) and $b = 2$ (bottom). Additionally, the mock lattice data set generated accordingly with $c = 0$ (left) and $c = 0.5$ (right) is depicted in orange.

our analysis in order to allow such skewness related discussions to take place. In the rest of this section the precise procedure used will be delineated.

3.5.1 . Procedure

The goal of this section is to arrive at an understanding of how the mock lattice data, whose generation procedure was outlined in the previous section, has been combined with the GPD replica set at a given value of the skewness ξ. We assume here that a set of mock lattice data points with central values $\mu_i^{\text{Latt.}}$ and errors $\sigma_i^{\text{Latt.}}$ have been produced using the given procedure at a given base of precision value $b \in \{1.1, 2\}$ and using a particular value of $c \in \{0, 0.5\}$. We would eventually like to assign a relative priority value to each of the replicas with respect to the generated corresponding mock lattice data, so we define first a value of χ_k^2, where k indexes R, the set of N replicas. We therefore write

$$\chi_k^2 \quad = \quad \sum_{\text{blocks}} \sum_{i,i'} (\mu_i^{\text{Latt.}} - R_k(\nu_i)) \Big(C^{-1}\Big)_{i,i'} (\mu_{i'}^{\text{Latt.}} - R_k(\nu_{i'})). \qquad (3.21)$$

We then choose to prescribe each replica R_k a corresponding weight from the normalized set of corresponding weights given by

$$\omega_k = \frac{(\chi^2_k)^{\frac{N-1}{2}} e^{-\frac{\chi^2_k}{2}}}{\sum_{k'} (\chi^2_{k'})^{\frac{N-1}{2}} e^{-\frac{\chi^2_{k'}}{2}}}, \tag{3.22}$$

whose functional form avoids 1. that a weight of 1 be assigned to a replica which corresponds with the central value of the replica set and a weight of 0 be assigned to all of the others, which ensures that the standard distribution of the replica set be non-zero, while 2. assigning smaller weights to replicas in less agreement with the mock lattice data [83].
One can further characterize the effective fraction of replicas R that align with the new dataset by defining:

$$\tau \equiv \frac{\exp(-\sum_k \omega_k \ln(\omega_k))}{N}, \tag{3.23}$$

where the exponentiated value represents the Shannon entropy of the weight set [84]. Being a function purely of the set of weights, τ is equal in momentum and position spaces, and therefore the most global metric used here of discrimination among the replica set.
Each weight ω_k has now been properly defined to assess the relative agreement of the corresponding replica R_k with mock lattice data generated from the entire set of replicas. How might this prioritization now be employed to provide uncertainty reduction on the band of replicas? In order to accomplish this task, we choose to define a set of (re)weighted statistics. That is, we define the reweighted median of the replica set to be our representation of a reweighted central value. This reweighted median is defined as follows. At each Ioffe time value ν' the replica values $R_k(\nu')$ are (re)ordered such that $R_{k'}(\nu') \leq R_{k'+1}(\nu')$. We say that $\bar{\mu}_\omega(\nu') = R_{l'}(\nu')$ is the reweighted median of the set of N_{rep} replica values $R_k(\nu')$ given the weight set $\omega_{k'}$ once we find the value of l' such that

$$\sum_{1 \leq k'}^{l'-1} \omega_{k'} \leq \frac{1}{2} \quad \& \quad \sum_{l'+1 \leq k'}^{N_{\text{rep}}} \omega_{k'} \leq \frac{1}{2}. \tag{3.24}$$

Note that in all expressions concerning the definition of this reweighted median, the fact that it is defined in Ioffe time is not explicitly used other than to specify the set of replica values whose reweighted central value we wish to calculate. We can therefore perform an identical procedure in x space, and this is indeed how we establish the replica bundle's reweighted median as a function of x as well. This is possible as the set of weights is robust with respect to Fourier transformation due to its linearity, and in this sense we are able to assess uncertainty reduction resulting from the outlined reweighting

procedure in both spaces.
The corresponding reweighted standard deviation of the replica set is defined in both spaces in an analogous sense as follows. At a given value of $\hat{\nu}$ the replica absolute deviations from the reweighted median $\bar{\mu}_\omega(\hat{\nu})$, $|\bar{\mu}_\omega(\hat{\nu}) - R_k(\hat{\nu})|$ are (re)ordered such that $|\bar{\mu}_\omega(\hat{\nu}) - R_{\hat{k}}(\hat{\nu})| \leq |\bar{\mu}_\omega(\hat{\nu}) - R_{\hat{k}+1}(\hat{\nu})|$. We say that $\bar{\sigma}_\omega = 1.4826 * |\bar{\mu}_\omega(\hat{\nu}) - R_{\hat{l}}(\hat{\nu})|$ is the reweighted MAD estimator of the set of N_{rep} replica absolute deviations from the reweighted median $\bar{\mu}_\omega(\hat{\nu})$, $|\bar{\mu}_\omega(\hat{\nu}) - R_k(\hat{\nu})|$ once we find the value of $\hat{l}$ such that

$$\sum_{1\leq\hat{k}}^{\hat{l}-1} \omega_{\hat{k}} \leq \frac{1}{2} \quad \& \quad \sum_{\hat{l}+1\leq\hat{k}}^{N_{\text{rep}}} \omega_{\hat{k}} \leq \frac{1}{2} \tag{3.25}$$

where once again the robustness of the weights with respect to Fourier transformation may be exploited to define an analogous quantity in momentum space, and we assume a normal distribution of the replica set around the reweighted central value. This imposition of normal statistics is only an assumption in the sense that we assume the Bayesian reweighting procedure ought to result in such a distribution. In addition, note that in the case $\nu' = \hat{\nu}$, $l' \neq \hat{l}$ and $R_{l'} \neq R_{\hat{l}}$ in general as the reordering of the replicas k' in terms of their values at ν' is in general not equivalent to the reordering of the replicas' absolute deviations from the median $\hat{k}$ at $\hat{\nu} = \nu'$.
We then go on to define an analogous function also defined in both spaces which is intended to assess the uncertainty reduction via the Bayesian procedure at the local level as

$$\Sigma(y) \equiv \frac{\bar{\sigma}_\omega(y)}{\bar{\sigma}(y)}, \tag{3.26}$$

with $y \in \{\nu, x\}$. We also define the average value of Σ in each space as a global measure of uncertainty retainment after reweighting, where in x space it is defined on a logarithmic scale in mere correspondence with the our logarithmic plotting convention in momentum space to be viewed in the remaining sections of this chapter as

$$r_\nu = \frac{1}{\nu_{\max} - \nu_{\min}} \int_{\nu_{\min}}^{\nu_{\max}} d\nu \Sigma(\nu), \tag{3.27}$$

$$r_{\ln x} = \frac{1}{\ln(x_{\max}/x_{\min})} \int_{x_{\min}}^{x_{\max}} \frac{dx}{x} \Sigma(x). \tag{3.28}$$

These final three objects are referred to here as "retainments of uncertainty" as they are precisely multiplicative quantifications of the relative amount of uncertainty of the reweighted replica band with respect to that of the unweighted replica bands. As they approach 0, one may interpret that the reweighting procedure has erased all of the corresponding uncertainty, and as they grow to 1 one may conclude that the effect of the inclusion of mock lattice data has had a minimal effect on their uncertainty band.

3.5.2 . Three σ Outlier Rejection

As promised, an example of why defining outliers is a messy business will be given in this subsection. Consider Fig. 3.9. The set of GPD "Cleaned" (defined shortly) replicas is shown in a particular kinematic region. In addition, the central value, 1σ, and 3σ bands of the replica set are shown under the name "Cleaned", which refers to the rejection of replicas. The process of rejection was performed as follows. Firstly, at each considered value of Ioffe time (not shown), the central value and standard deviation were computed in the traditional way. Secondly, if any replicas were outside of the 3σ band at any point in Ioffe time, they were identified as potential outliers. Thirdly, the replica with the highest cumulative quadrature-summed standard deviation of those potential outliers was discarded. After each discarding, this process was repeated until there were no more potential outliers defined in some iteration of the second step. The remaining replicas are called the "Cleaned" replica set. Another set of bands, entitled "Reweighted", were defined and computed using a Bayesian reweighting process to be explained later in Sec. 3.5. Importantly, the low x behavior of the cleaned replica $\sigma, 3\sigma$ bands is concerning, as while the set of replicas mostly tightens towards the x axis as x decreases, the spread of these bands increases. In particular, this is an effect of the equal prioritization of all replicas in Ioffe time space, which prioritizes replicas which in x space may or may not lend themselves to properly describing the behavior of the majority of the replica set due to the presence of outliers. Given this situation, it was quickly decided that there was a need to use estimations of spread robust with respect to outlier inclusion or exclusion so that defining outlier replicas at all would not be necessary.

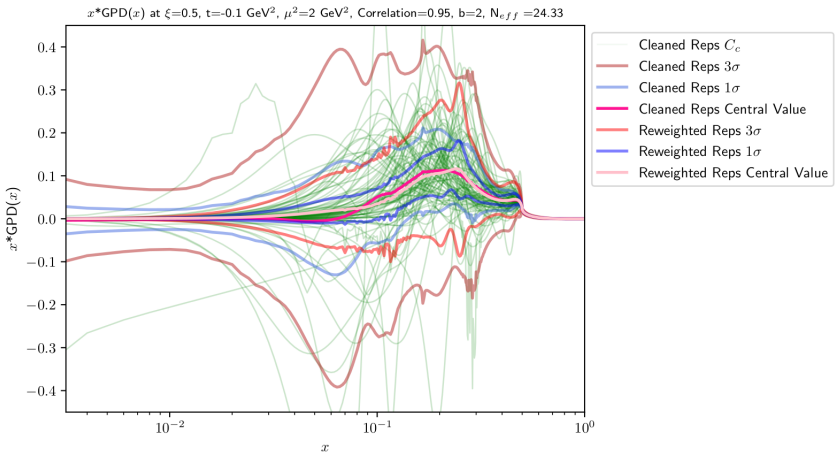

Figure 3.9: An example of the use of the local 3σ rule for outlier determination is shown. "Cleaned" replicas, central values, and σ, $\mu \pm 3\sigma$ bands are shown. "Reweighted" central values and σ, $\mu \pm 3\sigma$ bands are shown as well.

3.6 . Monokinematic Reweighting

In this section we will take a look at the results of the reweighting procedure on the statistics of the replica band at two different values of the skewness. One such value, $\xi = 0.1$, lying close to the forward limit of skewness $\xi = 0$, features large amounts of DGLAP support, and therefore a high resulting replica set coherence. The other, $\xi = 0.5$, a midrange skewness featuring therefore much less DGLAP support and thus via positivity Fig. 3.10, displays a correspondingly small degree of coherence. A comparison of the replica sets at these two skewness values as well as to that of $\xi = 0.9$, an even more extreme case, is provided in Fig. 3.10.

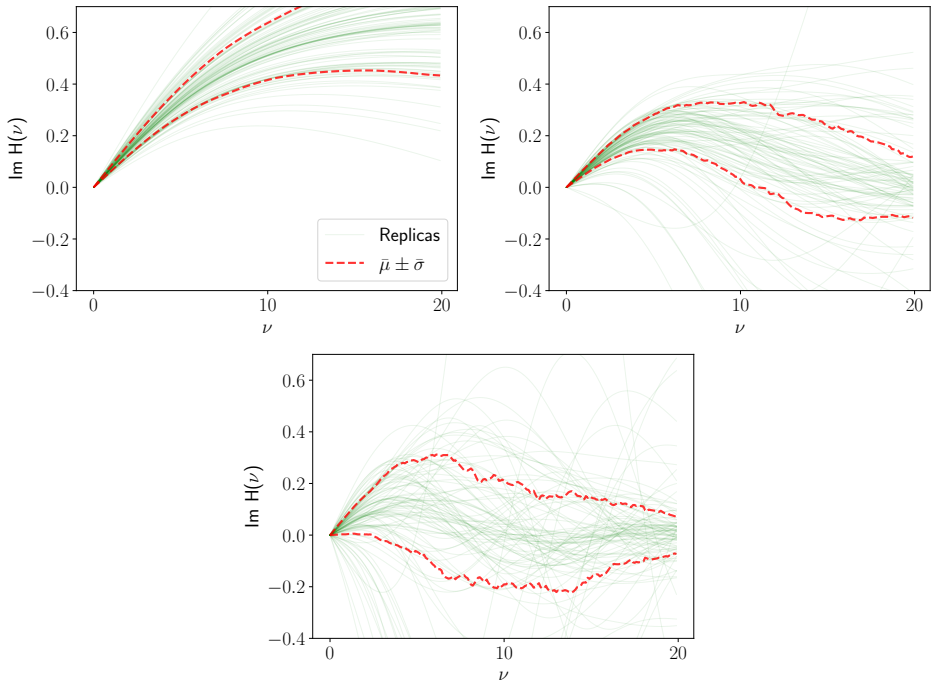

Figure 3.10: The set of GPD replicas $\Im H(\nu, \xi, t = 0)$ between Ioffe times $\nu = 0$ and $\nu = 20$ at $\xi = 0.1$ (top), $\xi = 0.5$ (middle), $\xi = 0.9$ (bottom) and their corresponding one standard deviation bands. Due to waning support $x > \xi$ as ξ increases, the replicas become less constrained by positivity, oscillate more heavily, and decohere. Where $\Im(z)$ is the imaginary part of a complex number z.

One should keep in mind that these results are intended to direct future lattice studies by exploring the possible discriminability of such replica sets using realistic lattice data of various qualities and internal correlations whose true characteristics are bound to be more complicated than the mock data shown here, and that in the following section we will also introduce varia-

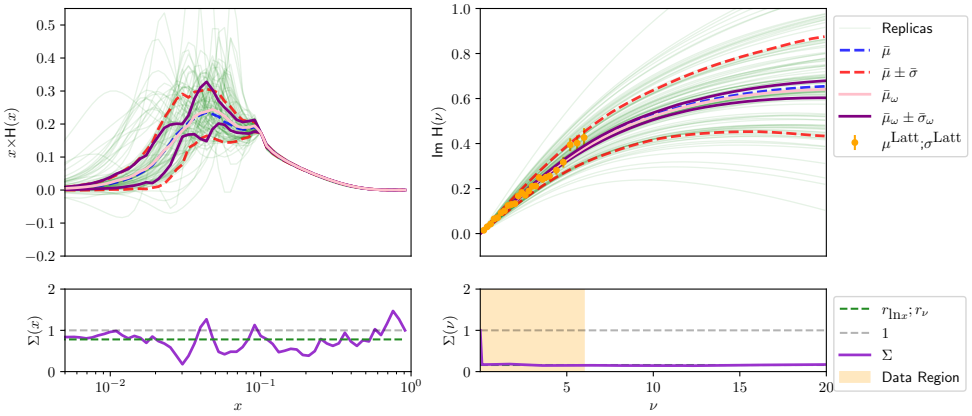

Figure 3.11: Upper plots: The collection of GPD replicas at $\xi = 0.1$, represented in both momentum space (green, left) and Ioffe times space (green, right), displaying their central value (blue-dashed), one standard deviation band (red-dashed), as well as the reweighted central value (pink-solid) and reweighted one standard deviation band (purple-solid). The mock lattice data was produced using $b = 2$ (high precision) and $c = 0$ (no correlation) at $\xi = 0.1$ (orange-dotted, right). Lower plots: Depicting the ratio of reweighted to initial uncertainty (purple-solid), the average uncertainty retention in both x ($r_{\ln x} = 0.78$) and ν ($r_\nu = 0.16$) (green-dashed), and the interval within which the lattice data was generated, from $\nu = 0$ to $\nu = 6$ (orange-shade, right). The corresponding effective fraction of replicas retained after reweighting is denoted by $\tau = 0.3$.

tions of the quantity of mock lattice data across multiple values of the skewness. Therefore, let us draw the attention of the reader in particular to the uncertainty reductions resulting both in the regions in which the mock lattice data is introduced and also those present over the entire Ioffe time regions displayed in the figures. The distinction between the effects of reweighting using data placed realistically in the low lying Ioffe time region on the statistics in the same region and those in the higher ν region, keeping in mind that the higher Ioffe time region corresponds to the highly oscillatory behavior of the GPD replicas in momentum space, should be kept in mind during the discussion and will be invoked throughout. The tools of Bayesian reweighting are now applied using a GPD model fitted on phenomenological inputs as a prior, and mock data as the new information. In monokinematic reweighting, mock data is added at a single value of ξ, and its impact on the GPD extraction at the same value is measured. It's noted that as b increases, the generated mock lattice data gets closer to the most likely output of the prior model on average. With increasing c, the mock lattice data consistently remains above or below the central value of the prior model.

Results for $b = 2$ (high precision), $c = 0$ (uncorrelated data), and $\xi = 0.1$

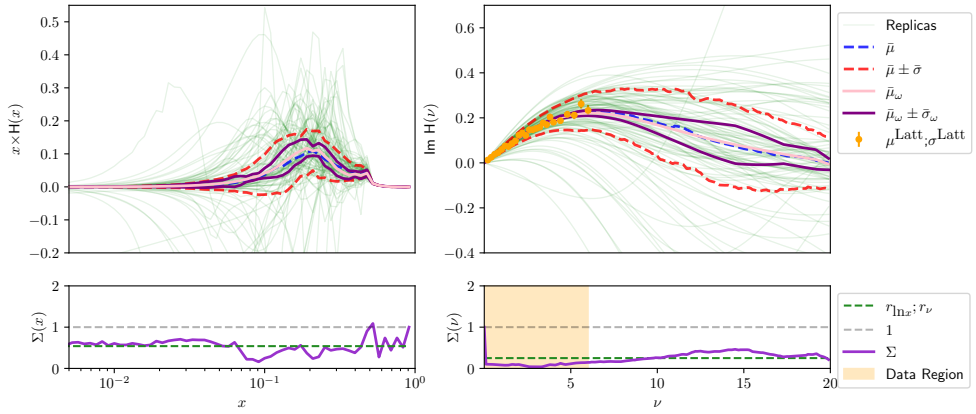

Figure 3.12: Same caption as Fig. 3.11 up to the fact that the GPD is shown at $\xi = 0.5$, with mock data added at $\xi = 0.5$ and similarly $b = 2$ (high precision) and $c = 0$ (no correlation). The average uncertainty retainments are $r_{\ln x} = 0.54$ and $r_\nu = 0.25$, $\tau = 0.11$.

are shown in Fig. 3.11, while Fig. 3.12 presents the results for $\xi = 0.5$ under the same parameters. The effect of reweighting in Ioffe time is significant, leading to a large reduction in uncertainty, which extends beyond the range of the data. However, fluctuations are more pronounced at $\xi = 0.5$ due to lesser coherence of the replica bundle. The average uncertainty retainment in Ioffe time is $r_\nu = 0.16$ at $\xi = 0.1$ and $r_\nu = 0.25$ at $\xi = 0.5$.
On the other hand, the reduction of uncertainty in momentum space is less remarkable, with a larger reduction observed at $\xi = 0.5$ compared to $\xi = 0.1$. Retainment of uncertainty remains high at $\xi = 0.1$, while it decreases at $\xi = 0.5$. This discrepancy illustrates the inversion problem discussed earlier. The origin of the large coherence at $\xi = 0.1$ in momentum space is the tight positivity constraint on the GPD, particularly for $x > 0.1$. This constraint limits the model's flexibility in this region, making reweighting less effective in momentum space.
To compare the effect of reweighting at various ξ values, Fig. 3.16 shows the effective fraction of surviving replicas τ and the uncertainty retainment in Ioffe time and momentum space as functions of ξ. The reduction of uncertainty is consistently better in Ioffe time compared to momentum space due to the imputation problem. However, using better and uncorrelated data ($b = 2, c = 0$) results in a more significant reduction of uncertainty in Ioffe time than in other configurations.
Please note that in general it is possible that at some point $\Sigma(\nu; x) > 1$. This seems to suggest that on the local level the introduction of mock lattice data actually increases the uncertainty associated with the replica set. How might adding information increase uncertainty? In cases in which such a breach of

1 occurs, either it is not in the kinematic region in which mock lattice data has been used to assign weights to the replicas (see Sec. 3.7), or it takes place in momentum space where no mock lattice data was introduced (Fig. 3.11). A replica set coherent at a given skewness in a given Ioffe time range is not guaranteed to be as coherent at all values of skewness and Ioffe time ranges. Therefore, the prioritization of the replicas via the introduction of mock lattice data in one kinematic region may prioritize most highly some replicas which deviate significantly from the replica band in another kinematic region, resulting in an apparent loss of precision in the second region. However, this is no reason to abandon reweighting as a method for data incorporation. As a proof of this claim, consider that the computed values of $r_{\nu;\Lambda_N x}$, the global metrics of uncertainty retainment, never surpass 1. This suggests that even when presented with local gains of uncertainty, global uncertainty is reduced via the introduction of additional information i.e. lattice data. This effect may also be due to the lack of statistics in terms of replica numbers. With such a small number of replicas, it may be too easy to prioritize too few of them, allowing small decoherent fluctuations outside of the region of data introduction.

3.7 . Multikinematic Reweighting

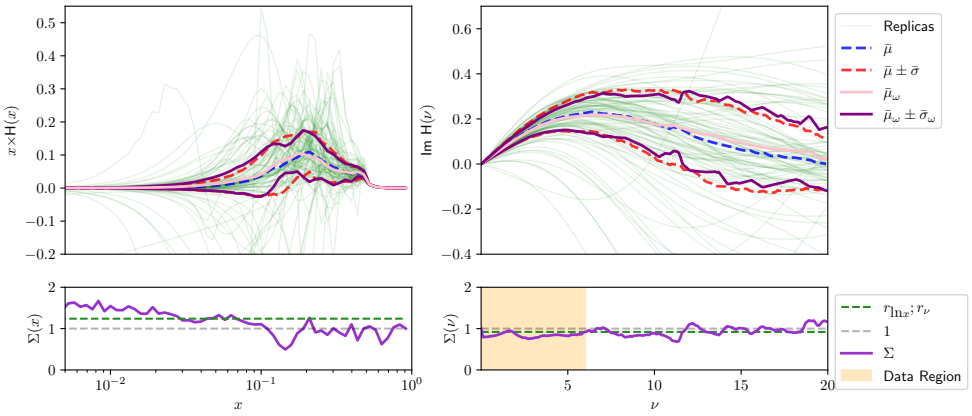

Figure 3.13: Same caption as Fig. 3.11 up to the fact that the GPD is shown at $\xi = 0.5$, with mock data added at $\xi = 0.1$, $b = 1.1$ (low precision) and $c = 0.5$ (correlated data). The average uncertainty retainments are $r_{\ln x} = 1.15$ and $r_\nu = 0.93$, $\tau = 0.83$.

Now that we have seen the effects of reweighting at a single skewness at both low and midrange skewness, it is time to move on to an exploration of the compensatory effect of the inclusion of additional mock lattice data from various values of skewness with respect to the waning discriminability at mid

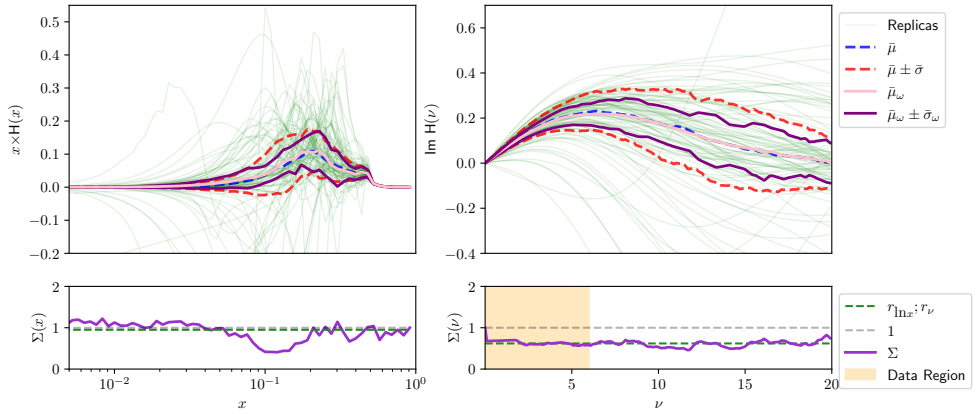

Figure 3.14: Same caption as Fig. 3.11 up to the fact that the GPD is shown at $\xi = 0.5$, with mock data added at $\xi = \{0.1, 0.2, 0.3\}$, $b = 1.1$ (low precision) and $c = 0.5$ (correlated data). The average uncertainty retainments are $r_{\ln x} = 1.0$ and $r_\nu = 0.82$, $\tau = 0.77$.

range skewness. The goal of this section is to compare, therefore, the uncertainty retainments due to various amounts of mock lattice data at low to mid skewness levels $\xi \in \{0.1\}$, $\xi \in \{0.1, 0.2, 0.3\}$, $\xi \in \{0.1, 0.2, 0.3, 0.4, 0.5\}$ to that seen in the previous section at purely midrange skewness. We will find that large amounts of relatively imprecise, highly correlated mock lattice data reproduce the uncertainty reductions corresponding to low amounts of precise, correlated data at purely midrange skewness. This will form a basis for the study's conclusionary recommendations to lattice QCD practitioners regarding the most useful yield based on kinematic choices, and will fuel a conclusionary discussion regarding optimization on the replica generation side. The impact of reweighting on other ξ values is explored. Fig. 3.13 shows the result of reweighting where data is added at $\xi = 0.1$ but observed at $\xi = 0.5$, with $b = 1.1$ (low precision) and $c = 0.5$ (correlated data). With large uncertainties, reweighting does not significantly reduce uncertainty in Ioffe time at $\xi = 0.5$ ($r_\nu = 0.93$) and even increases uncertainty in momentum space ($r_{\ln x} = 1.15$) by smearing the distribution. Adding data for $\xi \in \{0.1, 0.2, 0.3\}$ while keeping $b = 1.1$ and $c = 0.5$ decreases uncertainty retainment at $\xi = 0.5$ to $r_\nu = 0.82$ and $r_x = 1.0$ (Fig. 3.14). Further adding data for $\xi \in \{0.1, 0.2, 0.3, 0.4, 0.5\}$ tightens uncertainty retainment at $\xi = 0.5$ to $r_\nu = 0.65$ and $r_x = 0.75$ (Fig. 3.15). However, this is not better than direct $b = 2$, $c = 0.5$ reweighting at $\xi = 0.5$, resulting in $r_\nu = 0.58$ and $r_x = 0.64$. This shows that adding data at one ξ value has minimal effect on other higher ξ values within the GPD model.

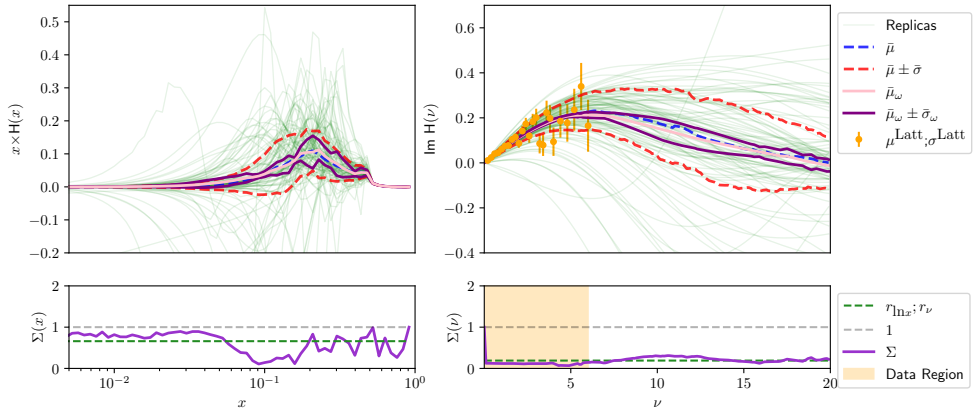

Figure 3.15: Same caption as figures 3.11 up to the fact that the GPD is shown at $\xi = 0.5$, with mock data added at $\xi = \{0.1, 0.2, 0.3, 0.4, 0.5\}$, $b = 1.1$ (low precision) and $c = 0.5$ (correlated data). The average uncertainty retainments are $r_{\ln x} = 0.75$ and $r_\nu = 0.65$, $\tau = 0.57$.

	Data			Results		
ξ_{Used}	Precision	Correlation	ξ_{Shown}	τ	r_ν	$r_{\ln x}$
0.1	Low	Low	0.1 / 0.5	0.47	0.25 / 0.92	0.82 / 1.24
0.1	Low	High	0.1 / 0.5	0.83	0.85 / 0.93	1.02 / 1.15
0.1	High	Low	0.1 / 0.5	0.30	0.16 / 0.90	0.78 / 1.08
0.1	High	High	0.1 / 0.5	0.46	0.23 / 0.91	0.82 / 1.23
0.5	Low	Low	0.5	0.36	0.44	0.67
0.5	Low	High	0.5	0.52	0.58	0.64
0.5	High	Low	0.5	0.11	0.25	0.54
0.5	High	High	0.5	0.37	0.51	0.77
0.1 0.2 0.3	Low	Low	0.5	0.30	0.62	0.95
0.1 0.2 0.3	Low	High	0.5	0.77	0.82	1.00
0.1 0.2 0.3	High	Low	0.5	0.10	0.34	0.54
0.1 0.2 0.3	High	High	0.5	0.30	0.61	0.73
0.1 0.2 0.3 0.4 0.5	Low	Low	0.5	0.16	0.19	0.66
0.1 0.2 0.3 0.4 0.5	Low	High	0.5	0.57	0.65	0.75
0.1 0.2 0.3 0.4 0.5	High	Low	0.5	0.03	0.13	0.45
0.1 0.2 0.3 0.4 0.5	High	High	0.5	0.18	0.25	0.77

Table 3.1: Results as dependent on the reweighting parameters. Low Correlation: $c = 0$, High Correlation: $c = 0.5$, Low Precision: $b = 1.1$, High Precision: $b = 2$. $r_{\ln x}$: Average uncertainty retainment in x, r_ν: Average uncertainty retainment in ν, τ: Effective fraction of replicas retained post-reweighting.

Fig. 3.16 illustrates the comparison of reweighting effects at various values of ξ by presenting the effective fraction of retained replicas τ and the preservation of uncertainty in both Ioffe time and momentum space. As ξ increases, indicating a higher degree of replica bundle decoherence, τ dimin-

ishes rapidly. Beyond $\xi > 0.7$, a complete refit appears necessary due to insufficient statistics. Notably, we consistently observe a greater reduction in uncertainty in Ioffe time compared to momentum space, as anticipated due to the imputation issue. When utilizing improved and uncorrelated data ($b = 2$, $c = 0$), there is generally a marked decrease in uncertainty in Ioffe time compared to other configurations, though this improvement is not mirrored in momentum space. Notably, for $b = 1.1$ (low precision), uncertainty in momentum space decreases with larger ξ values. The erratic behavior of uncertainty for $b = 2$ can be attributed to the small value of τ, rendering results unreliable at higher ξ values, thus emphasizing the restrictive nature of the new data compared to the prior model.

3.8 . Conclusion

We conducted a study examining how mock lattice QCD data, with moderate values of ξ, affects a GPD model. This model, based on machine learning techniques, is fitted to the forward limit and diagonal $x = \xi$ of the phenomenological GK model, which encapsulates typical experimental information on GPDs. We also impose a positivity constraint, significantly restricting the model's freedom in the $x > \xi$ region.

Our findings indicate that uncertainties in our model are largely autocorrelated in the small Ioffe-time region at small ξ. Consequently, lattice data only minimally reduces uncertainty in momentum space. The reduction in uncertainty in momentum space is consistently lower than that in Ioffe time space due to the challenge of relating the two representations of GPDs, known as the inverse problem.

Moreover, adding data at low ξ values minimally impacts GPD at higher ξ values, particularly when neglecting t-dependence. However, the use of lattice data at non-zero t is expected to increase the impact of reweighting once ANN modeling is performed in the non-zero t region.

In addition, taking a look at Fig. 3.16, one sees that at mid-range skewness, the effective fraction of replicas retained after the reweighting process τ is roughly equal in the low correlation low precision and high correlation high precision cases. This suggests a trade off between these two parameters in the sense that it implies that for a given value of one there is a value of the other which allows for a Bayesian reweighting's ability to discriminate among replicas in an equally effective way. This compensatory relationship between precision and skewness to produce similar results at the level of reweighting may be exploited by lattice practitioners in their decisions as to how to focus their computational resources.

We employ a Bayesian method to combine experimental and lattice knowledge on GPDs, which proves effective when lattice data aligns well with the

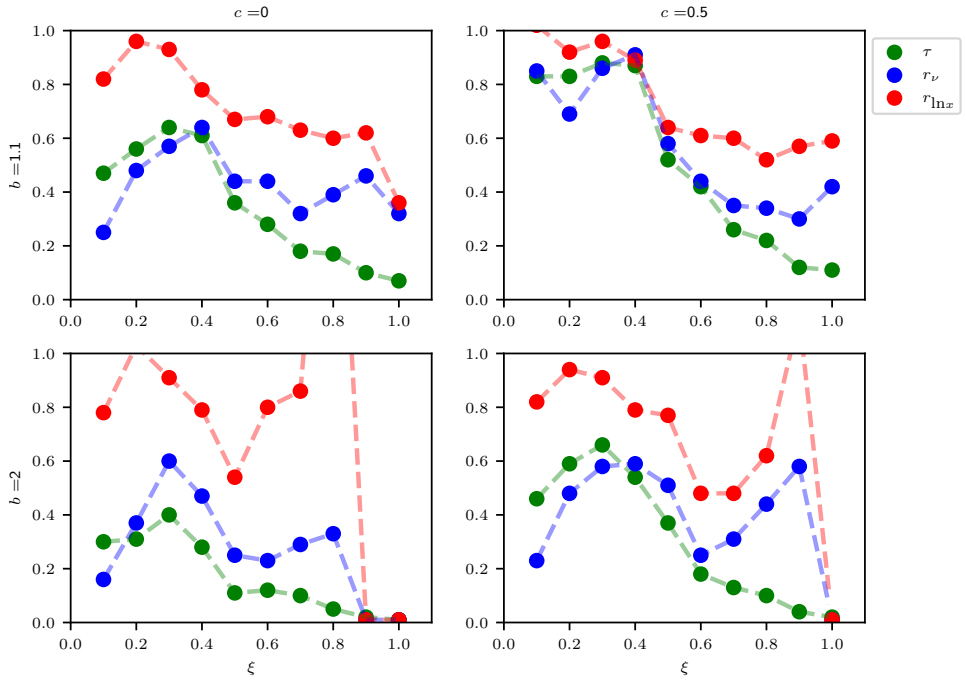

Figure 3.16: The effective fraction of replicas retained following reweighting τ (illustrated by the green curve), preservation of uncertainty in Ioffe time (shown by the blue curve), and in momentum space (represented by the red curve) for various combinations of high and low noise (designated as $b = 1.1$ and 2 respectively) and low and high correlation (indicated as $c = 0$ and 0.5 respectively).

prior model and from which one can expect a 40% uncertainty at mid-range skewness. However, our study underscores the importance of addressing correlations within lattice data for a joint extraction, as real lattice data often exhibit high degrees of correlation and systematic effects that require careful management to prevent biases in uncertainty assessment.

4 - Continuum Techniques

This chapter involves a change of focus with respect to the previous topic. Although this thesis will continue to treat nucleon GPDs, the remaining information will pertain to continuum techniques and modeling. This chapter analyzes GPDs as matrix elements which can be expanded in terms of overlaps of other functions, LFWFs, to which the following chapter will be devoted. The outline is as follows. The first section contains a delineation of the relationships between the nucleonic states involved in Eq. (2.15) and amplitudes defined on the light front. In the second, the characterization of such amplitudes in terms of quark OAM will be discussed. Finally, the representation of GPDs in terms of such amplitudes will be explained.

4.1 . Fock Expansion of the Nucleonic States and Light Front Wave Functions

The matrix elements involved in Eq. (2.15) contain nucleonic state vectors and a quark field operator. The easier of the two with which to deal is the quark field operator, whose algebraic properties are understood (see Sec. 4.1.1). The more complicated substructure includes the nucleonic bra and ket, each of which represents a state which is in principle a linear combination of an infinite number of states whose quantum numbers match that of the nucleon. By writing down systematic truncations of these linear combinations explicitly, one may manipulate the resulting sum of matrix elements, gaining a physical intuition of which pairs of incoming and outgoing states survive the quark bilinear operator. In this section such an expansion is justified in the first subsection, and the implications of the corresponding truncation are discussed in the second.

4.1.1 . Nucleonic States

We start with a Fock expansion of the nucleonic state ([85])

$$|P;h\rangle = \sum_{n=3}^{\infty}\sum_{s=1}^{S_n}\int \mathcal{D}_n\varphi_{n,s}(x_1,\vec{k}_{1\perp};x_2,\vec{k}_{2\perp};...;x_n,\vec{k}_{n\perp})|\mathfrak{D}_{1,s},\mathfrak{D}_{2,s},...,\mathfrak{D}_{n,s}\rangle, \tag{4.1}$$

where

- n corresponds to the number of particles in each state whose minimum value of 3 corresponds to the three valence quarks of the nucleon,
- s indexes all states with particle number n, with a maximum value S_n which depends on n,

- $\varphi_{n,s}$ is an expansion coefficient named a Light Front Wave Function (LFWF) depending on the momenta and quantum numbers of the partons involved in the state to which it corresponds which are not constrained by the equal lightcone time required for this expansion, and
- the $\mathfrak{D}_{n,s}$ represent the quantum numbers of all such partons including momentum,
- the momentum conserving integration measure $\mathcal{D}_n \propto \left(\prod_{i=1}^{n} dx_i d^2\vec{k}_{i\perp}\right)\left(\delta(1-\sum_{i=1}^{n} x_i)\delta^2(\sum_i \vec{k}_{i\perp})\right)$, up to a normalization constant to be discussed in the next chapter,
- and the limits of the x_i integration are 0 to 1, and the integration with respect to $\vec{k}_{i\perp}$ is over the entire $\mathbb{R}^2$.

This kind of sum takes place over, as previously discussed, all Fock states with quantum numbers α compatible with those of the nucleonic state, which is an infinite number of states with no upper boundary on the associated particle number. In addition, the coefficient functions $\varphi_{n,s}$ cannot depend on the full 4-momenta of the partons as the $-$ component of each parton momentum has already been integrated out. To see this, require that the lightcone time z^+, the Fourier conjugate of k_i^-, has been set to zero, equivalent to integrating over k_i^-.
Written in a less precise, more practical way, this sum can be expanded as

$$|P;h\rangle = \sum_{\hat{s}\in qqq}\int \mathcal{D}_3\varphi_{\hat{s}}|\hat{\mathfrak{D}}_{\hat{s}}\rangle + \sum_{\hat{s}\in qqqg}\int \mathcal{D}_4\varphi_{\hat{s}}|\hat{\mathfrak{D}}_{\hat{s}}\rangle + \sum_{\hat{s}\in qqq\bar{q}}\int \mathcal{D}_5\varphi_{\hat{s}}|\hat{\mathfrak{D}}_{\hat{s}}\rangle, +... \tag{4.2}$$

where the hats ($\hat{}$) identify each of the variables as a symbolic version of it's precise counterpart in Eq. (4.1). This way of writing down the Fock expansion of the nucleonic state $|P;h\rangle$ makes explicit that the infinitude of contributing states includes the three valence quarks (qqq), as well arbitrarily many gluons (g) and quark-antiquark pairs ($q\bar{q}$). To construct practical models for computing GPDs and related distributions such as those presented in Subsec. 2.4.2 of this thesis one may choose to truncate this sum by particle number. In fact, that is what will be done here.
However, such a truncation is a matter of practicality. Plugging directly the illustrational expansion given in Eq. (4.2) into a matrix element of the quark bilinear operator $\hat{O}_{\bar{q}q} \equiv \bar{q}_f^c(-\frac{z}{2})\gamma^+ q_f^c(\frac{z}{2})$ of Eq. (2.24), where we decide momentarily to omit the corresponding integrals over all momenta, yields

$$\langle P';h'|\hat{O}_{\bar{q}q}|P;h\rangle = \sum_{\mathfrak{c},\mathfrak{c}'\in\mathbb{N}}\sum_{\hat{s}\in c}\sum_{\hat{s}'\in c'} \varphi^*_{\hat{s}'}\varphi_{\hat{s}}\langle\hat{\mathfrak{D}}_{\hat{s}'}|\hat{O}_{\bar{q}q}|\hat{\mathfrak{D}}_{\hat{s}}\rangle, \tag{4.3}$$

where the $\mathfrak{c}(')$ run over all infinitely many particle configuration contributions $\mathbb{N}$.
The quark field operators are defined as

$$q^c_{\alpha,f}(z^-,z_\perp) = \int \frac{\mathrm{d}k^+}{2k^+}\frac{\mathrm{d}^{(2)}k_\perp}{(2\pi)^3}\theta(k^+)\sum_\lambda (b^c_{\lambda,f}(k^+,k_\perp)u_{\alpha,\lambda}(k^+,k_\perp) \times e^{-i(k^+z^- - k_\perp z_\perp)} + d^{c,\dagger}_{\lambda,f}(k^+,k_\perp)v_{\alpha,\lambda}(k^+,k_\perp)e^{i(k^+z^- - k_\perp z_\perp)}, \tag{4.4}$$

where u and v are lightcone spinors and b and d are the annihilation operators respectively for a quark and an antiquark. α (suppressed in this discussion) is a Dirac index, f a flavor index and c a color one, while quark light-front helicity is denoted with λ. The creation (b) and annihilation (d) operators fulfill the following anticommutation relations:

$$\begin{aligned}\{b^c_{\lambda,f}(k^+,k_\perp), b^{c',\dagger}_{\lambda',f'}(k^{+\prime},k'_\perp)\} &= \{d^c_{\lambda,f}(k^+,k_\perp), d^{c',\dagger}_{\lambda',f'}(k^{+\prime},k'_\perp)\} \\ &= 16\pi^3 k^+\delta(k^+-k^{+\prime})\delta^{(2)}(k_\perp-k'_\perp)\delta_{ff'}\delta_{cc'}\delta_{\lambda\lambda'},\end{aligned} \tag{4.5}$$

where we remind the reader that $\lambda \in \{\pm\frac{1}{2}\}$ is a helicity, c a color index, and f a flavor index. They act on the vacuum as (in the direction of [34], we ignore here possible complications related to zero-modes.)

$$\begin{aligned}|q;k^+,k_\perp,\lambda,c,f\rangle &= b^{c\dagger}_{\lambda,f}(k^+,k_\perp)|0\rangle, \\ |\bar{q};k^+,k_\perp,\lambda,c,f\rangle &= d^{c\dagger}_{\lambda,f}(k^+,k_\perp)|0\rangle,\end{aligned} \tag{4.6}$$

and $\bar{q} \equiv q^\dagger\gamma^0$.
Now that it is clear at the level of particle number and species which QCD Fock states contribute to matrix elements such as Eqs. (2.24) & (2.15), an issue with Fock space truncation is apparent. Even setting the gluon number to zero as will be done in the remainder of this thesis, the bilocal quark operator $\hat{O}_{\bar{q}q}$ may create a quark-antiquark pair. If the incoming state is a three-quark one, the outgoing state may be a five particle one. The required outgoing states whose contributions are necessary for consistent modeling of the three-quark state $|qqq\rangle$ are then given by $|qqq\rangle$ and $|qqq\bar{q}\rangle$. Carrying on the logic, one soon realizes that in order to model the contributions of three-quark Fock contributions to hadronic states one needs to involve an untenable infinite number of Fock states. This infinite set of ever increasing quantities of contributions is often referred to as an "infinite tower of states" and is impractical for modeling purposes [34].
However, not all hope is gone. By limiting the computation to a particular kinematic region in which the operator $\hat{O}_{\bar{q}q}$ is limited only to quark annihilation and creation, that is, no antiquark bilinear, this infinite tower can be scaled systematically. In the following subsection (Subsec. 4.1.2) it will be shown how to do precisely that before settling on only the lowest, three-quark contributions for the remainder of this thesis.

4.1.2 . Truncation of the Fock space and Limitation to the DGLAP Region

In the DGLAP region, one can consistently choose to truncate the Fock space used to expand the nucleonic states, as has been chosen to be the case in the remainder of this thesis. This choice can be made because, as stated explicitly in the previous chapter, a quark (antiquark) will be probed in the right (left) region. However, in the ERBL region such a consistent truncation cannot be made of the Fock states involved, as the corresponding probed parton is a quark-antiquark pair. As illustrated in the previous subsection (Subsec.), quark-antiquark pair creation or annihilation in the context of a two field interpolation operator requires an infinite tower of states to be treated consistently at the level of Fock expansion contributions. For this reason, the ERBL region is not treated in the remainder of this work.
This thesis will stick to the very first term in Eq. (4.3). That is, the approximation

$$\begin{aligned} |P;h\rangle &\approx \sum_{n=3}^{\infty}\delta_{n,3}\sum_{s=1}^{S_n}\int \mathcal{D}_n\varphi_{n,s}(x_1,\vec{k}_{1\perp};x_2,\vec{k}_{2\perp};...;x_n,\vec{k}_{n\perp}) \\ &\quad \times|\mathfrak{D}_{1,s},\mathfrak{D}_{2,s},...,\mathfrak{D}_{n,s}\rangle \qquad (4.7) \\ &= \sum_{s=1}^{S_3}\int \mathcal{D}_3\varphi_{3,s}(x_1,\vec{k}_{1\perp};x_2,\vec{k}_{2\perp};x_3,\vec{k}_{3\perp})|\mathfrak{D}_{1,s},\mathfrak{D}_{2,s},\mathfrak{D}_{3,s}\rangle, \qquad (4.8) \end{aligned}$$

will be employed. This is a "valence" quark approximation to the nucleonic Fock expansion. In the proceeding section of this chapter (Subsec. 4.1.1), finer questions about the states and combinations thereof will be presented. As mentioned in the first chapter there has been some successful pioneering work completed which extends DGLAP results into the ERBL region in the case on the pion using finite element methods, DDs, and the inverse Radon transform [86, 87, 88, 89]. Such is the intention behind part of this thesis, which studies the nucleon in the DGLAP region such that an ERBL extension might be performed.

4.2 . LFWF characterization and OAM

As discussed in the previous chapter, LFWFs capture the full momentum space content corresponding to Fock states in the expansion of a quantum field theoretic state. Further, by characterizing all LFWFs contributing to a given hadronic state one may compute parton distributions, transition amplitudes, expectation values, etc. as the LFWFs fully characterize the hadronic state in question, making them an extremely valuable tool for modeling such objects [34]. Corresponding to their high value they are indubitably difficult to consistently compute. Given the uncountably infinite quantity of normaliz-

able functional forms which LFWFs may take a priori, one must find a method for discrimination in a large functional space, i.e. modeling. In the next chapter a full characterization of the modeling used to compute LFWFs in this thesis will be given. For now, it suffices to admit that one fundamental aspect of such modeling is its dependence on the computation of matrix elements characterizing the overlaps of various Fock states with the nucleon state in question. But before one can dream of computing such matrix elements, and therefore LFWFs, in such a model, one must characterize their relationships in a consistent way.
In this section's first subsection, the matrix element to be used to access the LFWF contributions to the nucleon will be introduced. In the second, said matrix element will be parametrized. In the third and fourth subsections, such parametrization will be explored. In the fifth, the three-quark Fock states contributing to the nucleonic state will be given.

4.2.1 . The Matrix Element

We will now build a matrix element which will be used to consistently characterize the set of three-quark Fock states contributing to the nucleonic state $|P;h\rangle$. Without loss of generality we will consider here only the value $h=+\frac{1}{2}$ as corresponding states for $h=-\frac{1}{2}$ can be easily obtained from the results. For the sake of simplicity, we now write $|P\rangle$, where dependence on h is implicit.
Let us write down an operator creating a general color neutral three-quark state.

$$\epsilon^{c_1,c_2,c_3}\bar{q}^{+}_{f_1,c_1,\alpha_1}(z_1)\bar{q}^{+}_{f_2,c_2,\alpha_2}(z_2)\bar{q}^{+}_{f_3,c_3,\alpha_3}(z_2), \tag{4.9}$$

$z_r=(z_r^+=0,\vec{z}_{r\perp},z_r^-)$ where $\vec{z}_{r\perp}$ is a vector transverse to the lightcone, ϵ^{c_1,c_2,c_3} is the completely antisymmetric Levi-Civita tensor in color space with the convention $\epsilon^{1,2,3}\equiv 1$, the α are Dirac indices, and we have used the leading twist ($+$) components of the spinor parts of the quark operators, which are defined by

$$\bar{q}^{\pm}_{f,c,\beta}\equiv\frac{1}{2}\left(\gamma^{\mp}\gamma^{\pm}\right)_{\beta,\beta'}\bar{q}_{f,c,\beta'}. \tag{4.10}$$

Notice that the Dirac indices of the three involved quark field operators are open. This is key for two reasons. Firstly, it will allow for transparency during the process of parametrizing the matrix elements in a Dirac basis whose terms will be chosen based on constraints via Lorentz symmetry. That is, all terms in the sum of said parametrization will be required to carry such indices. Secondly, and as a consequence, it will allow for the use of a diverse set of Dirac structures onto which this matrix element may be projected via tracing. Each choice of Dirac structure will (anti)align the quark helicities in a manner which can be used to consistently compute contributions from each

quark helicity configuration. As we will see in the final section of this chapter, due to conservation of angular momentum, each quark helicity configuration corresponds to a particular value of quark OAM (qOAM). By writing the nucleon GPDs as a sum of overlaps of nucleonic states of definite and diverse qOAM, the relative contributions of these states to the overall nucleon spin will be elucidated. Further, the spatial shapes of these distinct states will be of particular interest, and may inform our understanding of the relative contributions of these states to the shape of the nucleon.
With this parametrization of the set of operators creating the states whose contributions to the nucleon state we wish to investigate in hand, we can now write down the matrix element to be parametrized in momentum space as

$$\frac{f_N}{4} N_\sigma \mathcal{M}_{\alpha,\sigma} \equiv N_F \Big(\prod_{r=1}^{3} \int \mathrm{d}z_r^- \mathrm{d}^2 \vec{z}_{r\perp} e^{i(z_r^- k_r^+ - \vec{z}_{r\perp}\cdot\vec{k}_{r\perp})}\Big) \tag{4.11}$$
$$\langle 0|\epsilon^{c_1,c_2,c_3} q^+_{f_1=u,c_1,\alpha_1}(z_1) q^+_{f_2=u,c_2,\alpha_2}(z_2) q^+_{f_3=d,c_3,\alpha_3}(z_3)|P\rangle,$$

where f_N is a normalization constant, N_F is a normalization constant corresponding to the involved 3D Fourier transform, and in expressions such as these the label α is a Dirac multiindex of the three-quark helicities $\alpha \equiv \{\alpha_1, \alpha_2, \alpha_3\}$. For any choice of quark helicities, which will be controlled by projection on a Dirac basis as explained later in this chapter, this matrix element represents none other than the overlap of the resulting state with the nucleonic one. However, it is as of now unclear how exactly each such overlap will be computed. Let us therefore move on to the parametrization of this matrix element in terms of all of the available Dirac and Lorentz structures which transform as this matrix element does. In doing so, we will set the stage for the modeling of LFWFs in the following chapter.

4.2.2 . Matrix Element Parametrizations

Given that LFWFs are the coefficients in a Fock expansion of hadronic states on the light front, each LFWF should be related to the inner product of the Fock state to which it corresponds with the full hadronic state. To consistently compute a combination of three-quark in nucleon LFWFs this and the following sections follow and elaborate upon methods established in [90]. In this subsection one of the usual tricks of matrix element decomposition is employed. The matrix element to be parametrized will be introduced, a full list of tensorial structures which Lorentz transforms like the matrix element available is given and condensed into a basis. Finally, the LFWFs will be given in terms of the linear combinations of the coefficients of basis tensors in the parametrization.

4.2.3 . Tensorial Basis

We now explore a set of tensorial structures from the literature [90]. As is done in [91], the nucleon momentum may be decomposed in terms two of light-like vectors n and p as

$$P^\mu = p^\mu + n^\mu \frac{M_N^2}{2p \cdot n}. \tag{4.12}$$

In addition to these vectors which define the lightcone, we have access to two of three transverse components of the quark momenta, where the third can be rewritten in terms of the other two and the nucleon momentum due to momentum conservation. Their plus components are proportional to the nucleon momentum's plus component, and their minus components have been integrated away. They must carry purely transverse indices $i, j \in \{1, 2\}$. Further, on the Dirac side we have access to γ matrices, γ_5, the leading twist component of the nucleon spinner N, the Dirac slashed lightcone vectors $\not{p}$, $\not{n}$, and the charge conjugation matrix $C \equiv i\gamma^2\gamma^0$. Employing the index μ as a Lorentz index we now write down a twelve element tensorial basis $T^{\mathfrak{t}}_\alpha$ ($1 \leq \mathfrak{t} \leq 12$) for the matrix element $\mathcal{M}_\alpha$ with the same CPT properties

$$\begin{aligned}
T_\alpha \quad = \quad & \Big\{ -(C\not{p})_{\alpha_1\alpha_2}(\gamma_5 N^+)_{\alpha_3}, \\
& \frac{1}{4}(C\not{p})_{\alpha_1\alpha_2}(\gamma_5\gamma^i N^+)_{\alpha_3}(k_1^i + k_2^i \hat{E}_{\mathbb{S}_3}), \\
& (C\not{p})_{\alpha_1\alpha_2}\epsilon^{ij}k_1^i k_2^j N^+_{\alpha_3}, \\
& -(C\not{p}\gamma_5)_{\alpha_1\alpha_2}N^+_{\alpha_3}, \\
& -\frac{1}{4}(C\not{p}\gamma_5)_{\alpha_1\alpha_2}(\gamma^i N^+)_{\alpha_3}(k_1^i - k_2^i \hat{E}_{\mathbb{S}_3}), \\
& (C\not{p}\gamma_5)_{\alpha_1\alpha_2}\epsilon^{ij}k_1^i k_2^j(\gamma_5 N^+)_{\alpha_3}, \\
& \frac{1}{32}(n_\mu\sigma^{\mu i}C)_{\alpha_1\alpha_2}(\gamma^i\gamma_5 N^+)_{\alpha_3}, \\
& \frac{1}{8}(n_\mu\sigma^{\mu i}C)_{\alpha_1\alpha_2}(\gamma_5 N^+)_{\alpha_3}(k_1^i + k_2^i \hat{E}_{\mathbb{S}_3}), \\
& \frac{1}{8}(n_\mu\sigma^{\mu i}C)_{\alpha_1\alpha_2}N^+_{\alpha_3}\epsilon^{ij}(k_1^j + k_2^j \hat{E}_{\mathbb{S}_3}), \\
& \frac{1}{32}(n_\mu\sigma^{\mu i}C)_{\alpha_1\alpha_2}(\gamma^j\gamma_5 N^+)_{\alpha_3}|\epsilon^{ij}|(k_1^i k_1^j + k_2^i k_2^j \hat{E}_{\mathbb{S}_3}), \\
& \frac{1}{32}(n_\mu\sigma^{\mu i}C)_{\alpha_1\alpha_2}|\epsilon^{ij}|k_1^i k_2^j(\gamma^j\gamma_5 N^+)_{\alpha_3}, \\
& \frac{1}{32}(n_\mu\sigma^{\mu i}C)_{\alpha_1\alpha_2}(k_1^i k_2^j - k_2^i k_1^j)(\gamma^j\gamma_5 N^+)_{\alpha_3}\Big\},
\end{aligned} \tag{4.13}$$

where $|\epsilon^{ij}| = \delta_{i,3-j}$ is a coefficient dependent on i and j, and is not a contracted tensor, and where $\hat{E}_{\mathbb{S}_3}$ exchanges the first two argument of a function coming directly afterwards. $\mathbb{S}$ is defined as the set of permutations of $\int_3$ and

denoted by

$$\begin{aligned} \mathbb{S}_1 &\equiv \{1,2,3\} \qquad & \mathbb{S}_2 &\equiv \{1,3,2\} \\ \mathbb{S}_3 &\equiv \{2,1,3\} \qquad & \mathbb{S}_4 &\equiv \{2,3,1\} \\ \mathbb{S}_5 &\equiv \{3,1,2\} \qquad & \mathbb{S}_6 &\equiv \{3,2,1\}. \end{aligned} \tag{4.14}$$

Unless otherwise specified, the argument exchange operators $\hat{E}_{\mathbb{S}_n}$ exchange momentum degrees of freedom. Now let us project these objects according to all possible helicites of the quarks. That is, in order to find out how such tensorial structures simplify when contributing to the matrix element defined in Eq. (4.11). We project it using a helicity projector (Eq. (4.23)) for each quark operator. We use the relations

$$[\mathcal{P}^\lambda, \gamma_5] = 0 \tag{4.15}$$

$$\mathcal{P}^\lambda \gamma_5 = 2\lambda \mathcal{P}^\lambda \quad |\lambda \in \{\pm\frac{1}{2}\}\,, \tag{4.16}$$

$$\mathcal{P}^\lambda s^+ \equiv s^+_\lambda\,, \tag{4.17}$$

$$\gamma_5 s^+_\lambda = 2\lambda s^+_\lambda\,, \tag{4.18}$$

$$\mathcal{P}^\lambda \gamma^i = \gamma^i \mathcal{P}^{-\lambda}\,, \tag{4.19}$$

$$\mathcal{P}^{\lambda_1} C \not{p} \mathcal{P}^{\lambda_2} = \delta_{\lambda_1,-\lambda_2} \mathcal{P}^{\lambda_1} \not{p} C\,, \tag{4.20}$$

$$\mathcal{P}^{\lambda_1} C \not{p} \gamma_5 \mathcal{P}^{\lambda_2} = (-2\lambda_1)\delta_{\lambda_1,-\lambda_2} \mathcal{P}^{\lambda_1} \not{p} C\,, \tag{4.21}$$

$$\mathcal{P}^{\lambda_1} \sigma^{\mu\nu} C \mathcal{P}^{\lambda_2} = \delta_{\lambda_1,\lambda_2} \mathcal{P}^{\lambda_1} \sigma^{\mu\nu} C, \tag{4.22}$$

where s is a spinor and where

$$q^\lambda_{f,c,\beta} \equiv \Big(\frac{1+(-1)^{\lambda-\frac{1}{2}}\gamma_5}{2}\Big)_{\beta\beta'} q_{f,c,\beta'} \equiv \mathcal{P}^\lambda_{\beta\beta'} q_{f,c,\beta'}, \tag{4.23}$$

defines the helicity projection operator. In fact, it is truly a chirality projection operator which is extended to a helicity projection operator in the infinite

momentum frame even for massive particles. We then write

$$
\begin{aligned}
\hat{T}^{\lambda}_{\alpha} &\equiv \Big(\prod_{l=1}^{3}\mathcal{P}^{\lambda_l}_{\alpha_l\alpha'_l}\Big)T_{\alpha'} \qquad (4.24)\\
&= \Big\{ -\delta_{\lambda_1,-\lambda_2}(\mathcal{P}^{\lambda_1}C\not{p})_{\alpha_1\alpha_2}(2\lambda_3 N^{+}_{\lambda_3})_{\alpha_3},\\
&\quad \frac{1}{4}\delta_{\lambda_1,-\lambda_2}(\mathcal{P}^{\lambda_1}C\not{p})_{\alpha_1\alpha_2}(-2\lambda_3\gamma^i N^{+}_{-\lambda_3})_{\alpha_3}(k_1^i+k_2^i\hat{E}_{\mathbb{S}_3}),\\
&\quad \delta_{\lambda_1,-\lambda_2}(\mathcal{P}^{\lambda_1}C\not{p})_{\alpha_1\alpha_2}\epsilon^{ij}k_1^i k_2^j N^{+}_{\lambda_3;\alpha_3},\\
&\quad 2\lambda_1\delta_{\lambda_1,-\lambda_2}(\mathcal{P}^{\lambda_1}C\not{p})_{\alpha_1\alpha_2}N^{+}_{\lambda_3;\alpha_3}\\
&\quad \frac{1}{4}(2\lambda_1)\delta_{\lambda_1,-\lambda_2}(\mathcal{P}^{\lambda_1}C\not{p})_{\alpha_1\alpha_2}(\gamma^i N^{+}_{-\lambda_3})_{\alpha_3}(k_1^i-k_2^i\hat{E}_{\mathbb{S}_3}),\\
&\quad -2\lambda_1\delta_{\lambda_1,-\lambda_2}(\mathcal{P}^{\lambda_1}C\not{p})_{\alpha_1\alpha_2}\epsilon^{ij}k_1^i k_2^j 2\lambda_3 N^{+}_{\lambda_3;\alpha_3},\\
&\quad \frac{1}{32}\delta_{\lambda_1,\lambda_2}(n_\mu\mathcal{P}^{\lambda_1}\sigma^{\mu i}C)_{\alpha_1\alpha_2}(-2\lambda_3)(\gamma^i N^{+}_{-\lambda_3})_{\alpha_3},\\
&\quad \frac{1}{8}\delta_{\lambda_1,\lambda_2}(n_\mu\mathcal{P}^{\lambda_1}\sigma^{\mu i}C)_{\alpha_1\alpha_2}2\lambda_3 N^{+}_{\lambda_3;\alpha_3}(k_1^i+k_2^i\hat{E}_{\mathbb{S}_3}),\\
&\quad \frac{1}{8}\delta_{\lambda_1,\lambda_2}(n_\mu\mathcal{P}^{\lambda_1}\sigma^{\mu i}C)_{\alpha_1\alpha_2}N^{+}_{\lambda_3;\alpha_3}\epsilon^{ij}(k_1^j+k_2^j\hat{E}_{\mathbb{S}_3}),\\
&\quad \frac{1}{32}\delta_{\lambda_1,\lambda_2}(n_\mu\mathcal{P}^{\lambda_1}\sigma^{\mu i}C)_{\alpha_1\alpha_2}(-2\lambda_3)(\gamma^j N^{+}_{-\lambda_3})_{\alpha_3}|\epsilon^{ij}|(k_1^i k_1^j+k_2^i k_2^j\hat{E}_{\mathbb{S}_3}),\\
&\quad \frac{1}{32}\delta_{\lambda_1,\lambda_2}(n_\mu\mathcal{P}^{\lambda_1}\sigma^{\mu i}C)_{\alpha_1\alpha_2}|\epsilon^{ij}|k_1^i k_2^j(-2\lambda_3)(\gamma^j N^{+}_{-\lambda_3})_{\alpha_3},\\
&\quad \frac{1}{32}\delta_{\lambda_1,\lambda_2}(n_\mu\mathcal{P}^{\lambda_1}\sigma^{\mu i}C)_{\alpha_1\alpha_2}(k_1^i k_2^j-k_2^i k_1^j)(-2\lambda_3)(\gamma^j N^{+}_{-\lambda_3})_{\alpha_3}\Big\}.
\end{aligned}
$$

To clarify, in the following chapter we will introduce a method for modeling of the matrix element defined in Eq. (4.11). In this section, we will shortly write the helicity projection of said matrix element as a linear combination of the elements of the projected basis given above. Therefore, it will be useful to catalog here a set of projectors to be used to isolate the coefficients of that linear combination. We choose to do so in the form of a set of Dirac traces. We will list these projectors in turn, and by cataloging them here, we

will illuminate the connection between this basis and qOAM.

$$
\begin{aligned}
\hat{T}^{\lambda}_{\alpha} R^{1}_{\alpha} &\equiv \hat{T}^{\lambda}_{\alpha}(|N^{+}_{\lambda_3}|^2 n\cdot p)^{-1} 2(\not{n}C)_{\alpha_2\alpha_1} N^{+}_{\alpha_3} \\
&= \delta_{\lambda_1,-\lambda_2}\{2\lambda_3, 0, -\epsilon^{ij}k_1^i k_2^j, -2\lambda_1, 0, 4\lambda_1\lambda_3\epsilon^{ij}k_1^i k_2^j, \\
&\quad 0,0,0,0,0,0\} \\
\hat{T}^{\lambda}_{\alpha} R^{2}_{\alpha} &\equiv \hat{T}^{\lambda}_{\alpha}(|N^{+}_{-\lambda_3}|^2 n\cdot p)^{-1} 2(\not{n}C)_{\alpha_2\alpha_1}(\gamma^s N^{+})_{\alpha_3} \\
&= \delta_{\lambda_1,-\lambda_2}\{0, 2\lambda_3(k_1^s + k_2^s \hat{E}_{\mathbb{S}_3}), 0, 0, -2\lambda_1(k_1^s - k_2^s\hat{E}_{\mathbb{S}_3}), 0, \\
&\quad 0,0,0,0,0,0\} \\
\hat{T}^{\lambda}_{\alpha} R^{3}_{\alpha} &\equiv \hat{T}^{\lambda}_{\alpha}(|N^{+}_{\lambda_3}|^2 n\cdot p)^{-1} 2(ip_\nu C\sigma^{\nu r})_{\alpha_2\alpha_1} N^{+}_{\alpha_3} \\
&= \delta_{\lambda_1,\lambda_2}(\delta_{i,r} - 2i\lambda_1\epsilon^{ir})\{0,0,0,0,0,0, \\
&\quad 0, 2\lambda_3, 2\lambda_1, 0, 0, 0\}(k_1^j + k_2^j \hat{E}_{\mathbb{S}_3}) \\
\hat{T}^{\lambda}_{\alpha} R^{4}_{\alpha} &\equiv \hat{T}^{\lambda}_{\alpha}(|N^{+}_{-\lambda_3}|^2 n\cdot p)^{-1} 2(ip_\nu\sigma^{\nu r}C)_{\alpha_2\alpha_1}(\gamma^s N^{+}_{-\lambda_3})_{\alpha_3} \\
&= \delta_{\lambda_1,\lambda_2}(\delta_{i,r} - 2i\lambda_1\epsilon^{ir}) \\
&\quad 2\lambda_3\{0,0,0,0,0,0, \\
&\quad \delta_{i,s}, 0, 0, |\epsilon^{is}|(k_1^i k_1^s + k_2^i k_2^s \hat{E}_{\mathbb{S}_3}), |\epsilon^{is}| k_1^i k_2^s, \epsilon^{is} k_1^i k_2^s\},
\end{aligned}
\tag{4.25}
$$

where r and s are transverse indices, and we have defined the projectors $R_{\alpha}^{g\in\{1,2,3,4\}}$. In practice, these trace formulae, in combination with the unique momentum-dependent structures associated with the non-zero elements of each set, allow one to identify the contribution of each individual structure defined in Eq. (4.13) to any model of the matrix element defined in Eq. (4.11).

4.2.4 . Symmetric Constraints

The set of twelve tensorial structures is given in Eq. (4.13) represent a basis for the expansion of the three-quark matrix element defined in Eq. (4.11) at leading twist. In the previous subsection, Dirac tracing against appropriately chosen tensorial structures has illuminated one way to identify these individual structure's contributions for example, when modeling such a matrix element, in Eq. (4.25). In this work, we treat quark flavor as labels only, in the sense that we work in the isospin limit, treating u and d quarks as possessing the same mass. Further, the exchange of the two u quarks, due to their flavor symmetry, must leave the matrix element unchanged. As a consequence, the full list of tensorial structures enumerated without this limit in mind actually admits a set of simplifications at the level of the coefficient functions which will appear in the expansion.
Taking a look at the contribution identification trace formulas presented in Eqs. (4.25), let's identify sets of tensorial structures with related momentum-dependent coefficients. The indices of the structure sets are

1. 1: 1, 4, 7
2. $\epsilon^{ij}k_1^i k_2^j$: 3, 6, 12

3. $(k_1^i \pm k_2^i \hat{E}_{\mathbb{S}_3})$: 2, 5, 8, 9

4. $|\epsilon^{ij}| k_a^i k_b^j$: 10, 11

with $a, b \in \{1, 2\}$. Now it becomes clear why this basis has been chosen. The first two bullets point in the preceding list corresponds to zero units of projected qOAM, the second to two units in opposing directions, the third to one unit, and the fourth to two units in the same direction.
Now we take a proper look at the symmetries of the matrix elements. Symmetry under the exchange of the u quarks is defined as

$$\mathcal{M}_{\alpha,\sigma}(\kappa) \equiv \mathcal{M}_{\alpha,\sigma}(\kappa_{\mathbb{S}_3}), \tag{4.26}$$

and isospin symmetry imposes

$$0 \equiv \sum_{w \in \{1,4,5\}} \mathcal{M}_{\alpha,\sigma}^{f_{\mathbb{S}_w}}, \tag{4.27}$$

where the generally omitted flavor labels of the matrix element have been restored for illustrational purposes. The relation given in Eq. (4.27) is due to a group theoretical three-quark (valence) expansion of the proton state in terms of total quark helicity $\lambda_\Sigma = h = \pm\frac{1}{2}$ ([92])

$$\begin{aligned} |P;h\rangle = \frac{1}{\sqrt{18}}(\quad & 2|u^h u^h d^{-h}\rangle + 2|d^{-h} u^h u^h\rangle + 2|u^h d^{-h} u^h\rangle \\ & -|u^h u^{-h} d^h\rangle - |d^h u^{-h} u^h\rangle - |u^h d^h u^{-h}\rangle \\ & -|u^{-h} u^h d^h\rangle - |d^h u^h u^{-h}\rangle - |u^{-h} d^h u^h\rangle, \end{aligned} \tag{4.28}$$

which is symmetric under the exchange of any two of the quarks. This expression's overlap with any expression of the form

$$\sum_{w \in \{1,4,5\}} |q_{f_1}^{\lambda} q_{f_2}^{\pm\lambda} q_{f_3}^{\mp\lambda}\rangle^{f_{\mathbb{S}_w}}, \tag{4.29}$$

is zero, as one may easily verify. The key insight here is that these conditions (Eqs. (4.26) & (4.27)) apply even when the matrix element is helicity projected (Eq. (4.24)) although they do not continue to apply when individual contributions are selected by a trace (Eq. (4.25)). This is due to the difference between these two projections. The trace projection is basis-specific as the set of projectors R was chosen with respect to the projected basis defined in Eq. (4.24), whereas the form of the quark helicity projectors (Eq. (4.23)) does not depend on any choice of basis.
Let us finally define the parametrization of the matrix element defined in Eq. (4.11) and its helicity projected counterpart as

$$\begin{aligned} \frac{f_N}{4} N_\sigma \mathcal{M}_{\alpha,\sigma} &\equiv \sum_{\mathfrak{t}=1}^{12} T_\alpha^{\mathfrak{t}} \phi^{\mathfrak{t}}(\kappa) \\ \frac{f_N}{4} N_\sigma \hat{\mathcal{M}}_{\alpha,\sigma}^{\lambda} &\equiv \sum_{\mathfrak{t}=1}^{12} \hat{T}_\alpha^{\lambda\mathfrak{t}} \phi^{\mathfrak{t}}(\kappa), \end{aligned} \tag{4.30}$$

where we have defined the momentum dependent basis coefficient functions $\phi^{\mathfrak{t}}(\kappa)$.
Using the Fierz identity, a way of decomposing products of Dirac spinor outer products in a Dirac matrix basis with coefficients which are functions of inner products of those spinors as outlined in [93], one may identify from the helicity projected parametrization provided in Eq. (4.30) in addition to the isospin symmetry constraint specified in Eq. (4.27) that

$$\begin{aligned}
0 &= (\hat{E}_{\mathbb{S}_2} + \hat{E}_{\mathbb{S}_4})(2\lambda_3\phi^1 - 2\lambda_1\phi^4) - 2\lambda_3\phi^7 \\
0 &= i(\hat{E}_{\mathbb{S}_2} - \hat{E}_{\mathbb{S}_4})(\phi^3 - 4\lambda_1\lambda_3\phi^6) - 2\lambda_3\phi^{12} \\
0 &= (1 + \hat{E}_{\mathbb{S}_2} - \hat{E}_{\mathbb{S}_5} - \hat{E}_{\mathbb{S}_6})(2\lambda_3\phi^8 + 2\lambda_1\phi^9) \\
0 &= 2\lambda_3\phi^8 - 2\lambda_1\phi^9 - \hat{E}_{\mathbb{S}_5} 4\lambda_1\phi^5 - \hat{E}_{\mathbb{S}_6}(2\lambda_3\phi^2 - 2\lambda_1\phi^5) \\
0 &= \phi^{11} + (\hat{E}_{\mathbb{S}_5} + \hat{E}_{\mathbb{S}_4} - \hat{E}_{\mathbb{S}_1} - \hat{E}_{\mathbb{S}_3})\phi^{10}.
\end{aligned} \tag{4.31}$$

Each of these statements implies that there is a smaller set of amplitudes to be chosen, which form an isospin symmetric, u-quark symmetric basis for the full set of amplitudes. Still following the discussion outlined in the work [90], we define

$$\psi^{1,w} \equiv \phi^1 + w\phi^4 \tag{4.32}$$
$$\psi^{2,w} \equiv \phi^3 + w\phi^6 \tag{4.33}$$
$$\psi^{3,w} \equiv \phi^2 + w\phi^5 \tag{4.34}$$
$$(1 - \hat{E}_{\mathbb{S}_2})\psi^5 \equiv \frac{1}{2}(\phi^8 + \phi^9) \tag{4.35}$$
$$\psi^6 \equiv \frac{1}{2}\phi^{10}, \tag{4.36}$$

with $w \equiv -4\lambda_1\lambda_3 = \pm 1$ such that we may write the set of inverted relations

$$
\begin{aligned}
\phi_1 &= \frac{1}{2}(\psi^{1,w} + \psi^{1,-w}) \\
\phi_2 &= \frac{1}{2}(\psi^{3,w} + \psi^{3,-w}) \\
\phi_3 &= \frac{1}{2}(\psi^{2,w} + \psi^{2,-w}) \\
\phi_4 &= \frac{q}{2}(\psi^{1,w} - \psi^{1,-w}) \\
\phi_5 &= \frac{q}{2}(\psi^{3,w} - \psi^{3,-w}) \\
\phi_6 &= \frac{w}{2}(\psi^{2,w} - \psi^{2,-w}) \\
\phi^7 &= (\hat{E}_{\mathbb{S}_2} + \hat{E}_{\mathbb{S}_4})\psi^{1,w} \\
\phi^8 &= (1 - \hat{E}_{\mathbb{S}_2})\psi^5 + \frac{2\lambda_3}{2}(\hat{E}_{\mathbb{S}_6}\psi^{3,-w} + \hat{E}_{\mathbb{S}_5}\frac{w}{2}(\psi^{3,w} - \psi^{3,-w})) \\
\phi^9 &= (1 - \hat{E}_{\mathbb{S}_2})\psi^5 - \frac{2\lambda_3}{2}(\hat{E}_{\mathbb{S}_6}\psi^{3,-w} + \hat{E}_{\mathbb{S}_5}\frac{w}{2}(\psi^{3,w} - \psi^{3,-w})) \\
\phi^{10} &= 2\psi^6 \\
\phi^{11} &= 2(\hat{E}_{\mathbb{S}_1} + \hat{E}_{\mathbb{S}_3} - \hat{E}_{\mathbb{S}_5} - \hat{E}_{\mathbb{S}_4})\psi^6 \\
\phi^{12} &= 2\lambda_3 i(\hat{E}_{\mathbb{S}_2} - \hat{E}_{\mathbb{S}_4})\psi^{2,w}.
\end{aligned}
\tag{4.37}
$$

The lack here of an amplitude named ψ^4 is due to an adherence of our notation to the notation of [90], which performs this aspect of the analysis in the slightly more limited case of a strictly spin up nucleon. In our notation the equivalent amplitude is denoted as $\psi^{3,-1}$.

We can now write down the helicity projected matrix element defined in (4.30) in terms of the ψ basis. To clarify the presentation of this matrix element, we contract with a helicity h projected nucleon spinor as well in order to make manifest the contributions of the two spin states $h = \pm\frac{1}{2}$. The matrix element now reads

$$
\begin{aligned}
&\frac{f_N}{4} N_{h;\sigma} \hat{\mathcal{M}}^{\lambda}_{\alpha,\sigma} \\
= \; & -2\lambda_3\delta_{\lambda_3,h}\hat{T}^{\lambda,1}_{\alpha}\psi^{1,w} + \delta_{\lambda_3,-h}\hat{T}^{\lambda,7}_{\alpha}(\hat{E}_{\mathbb{S}_2} + \hat{E}_{\mathbb{S}_4})\psi^{1,w} \\
& + \delta_{\lambda_3,h}\hat{T}^{\lambda,3}_{\alpha}\psi^{2,w} + 2\lambda_3 i\delta_{\lambda_3,-h}\hat{T}^{\lambda,12}_{\alpha}(\hat{E}_{\mathbb{S}_2} - \hat{E}_{\mathbb{S}_4})\psi^{2,w} \\
& + \frac{1}{2}(\delta_{\lambda_3,-h}(-2\lambda_3\hat{T}^{\lambda,2}_{\alpha} - 2\lambda_1\hat{T}^{\lambda,5}_{\alpha}) - \frac{2\lambda_1}{2}\delta_{\lambda_3,h}(\hat{T}^{\lambda,8}_{\alpha}\hat{E}_{\mathbb{S}_5} - \hat{T}^{\lambda,9}_{\alpha}\hat{E}_{\mathbb{S}_6}))\psi^{3,w} \\
& + \frac{1}{2}(\delta_{\lambda_3,-h}(-2\lambda_3\hat{T}^{\lambda,2}_{\alpha} + 2\lambda_1\hat{T}^{\lambda,5}_{\alpha}) - \frac{2\lambda_1}{2}\delta_{\lambda_3,h}(\hat{T}^{\lambda,8}_{\alpha}\hat{E}_{\mathbb{S}_5} + \hat{T}^{\lambda,9}_{\alpha}\hat{E}_{\mathbb{S}_6}))\psi^{3,-w} \\
& + \frac{2\lambda_3}{2}\delta_{\lambda_3,h}(\hat{T}^{\lambda,8}_{\alpha} - \hat{T}^{\lambda,9}_{\alpha})\hat{E}_{\mathbb{S}_6}\psi^{3,-w} + \delta_{\lambda_3,h}(\hat{T}^{\lambda,8}_{\alpha} + \hat{T}^{\lambda,9}_{\alpha})(1 - \hat{E}_{\mathbb{S}_2})\psi^5 \\
& + 2\delta_{\lambda_3,-h}(\hat{T}^{\lambda,10}_{\alpha} + \hat{T}^{\lambda,11}_{\alpha}(\hat{E}_{\mathbb{S}_1} + \hat{E}_{\mathbb{S}_3} - \hat{E}_{\mathbb{S}_5} - \hat{E}_{\mathbb{S}_4}))\psi^6.
\end{aligned}
\tag{4.38}
$$

Taking a look at this matrix element, a few comments are in order.

Firstly, the full amplitude ψ^5 is never used. The projector $1 - \hat{E}_{\mathbb{S}_2}$ eliminates

the contribution to it which is even under the exchange of arguments 2 and 3.
Secondly, the inversion relations given in Eqs. (4.37) for $\phi^{7,8,9,12}$ appear contradictory in the sense that the functions $\psi^{\mathfrak{s}}$ are $\lambda_{1,3}$ independent, and yet they are apparently related to each other via $\lambda_{1,3}$ dependent coefficients in the isospin limit. For example, let us take a look at the first the relations provided in the Eqs. (4.31)

$$\begin{aligned} 0 &= (\hat{E}_{\mathbb{S}_2} + \hat{E}_{\mathbb{S}_4})(2\lambda_3\phi^1 - 2\lambda_1\phi^4) - 2\lambda_3\phi^7 \\ &\rightarrow \phi^7 = (\hat{E}_{\mathbb{S}_2} + \hat{E}_{\mathbb{S}_4})(\phi^1 + q\phi^4). \end{aligned}$$

This relation is indeed intended to be presented as true whether $q = +1$ or $q = -1$. How is this possible? The solution to this puzzle is to recognize that the imposition of isospin symmetry and the consequent reduction of the set of independently contributing amplitudes $\phi^{\mathfrak{t}}$ has been performed here only once our matrix element of interest has been fully projected onto quark helicities. That is, we have used the second of Eqs. (4.30) to impose isospin symmetry, and as a consequence the resulting relations in terms of the auxiliary functions ϕ maintain manifest dependence on the quark helicities.
To see this a different way, take a look at the set tensorial basis defined in Eq. (4.13). These basis elements, yet to be projected onto the three-quark helicities, are by definition linearly independent. Therefore, their coefficients cannot be related in linear combinations except among identical structures via imposition of the symmetry conditions provided in Eq. (4.27) and Eq. (4.26). Therefore, when we write an expression here such as those given in the Eqs. (4.31) it is to be understood that such simplifying relationships are given in the context of a particular set of quark helicity projections and change according to such projections.
To isolate each of the eight amplitudes $\psi^{\mathfrak{s}}$ defined in Eqs. (4.32) we can use the corresponding trace formulas given by

$$\begin{aligned} \frac{f_N}{4} N_\sigma \hat{\mathcal{M}}^{\frac{1}{2},-\frac{1}{2},\lambda_3}_{\alpha,\sigma} R^1_\alpha &= \frac{p\cdot n}{2} |N^+_{\lambda_3}|^2 (2\lambda_3 \psi^{1,-2\lambda_3} - \epsilon^{ij} k_1^i k_2^j \psi^{2,-2\lambda_3}) \\ \frac{f_N}{4} N_\sigma \hat{\mathcal{M}}^{\frac{1}{2},-\frac{1}{2},\lambda_3}_{\alpha,\sigma} R^2_\alpha &= \frac{p\cdot n}{2} |N^+_{\lambda_3}|^2 2\lambda_3 (k_1^s \psi^{3,-2\lambda_3} + k_2^s \hat{E}_{\mathbb{S}_3} \psi^{3,2\lambda_3}) \\ \frac{f_N}{4} N_\sigma (\hat{\mathcal{M}}^{\frac{1}{2},\frac{1}{2},\lambda_3}_{\alpha,\sigma} + \hat{\mathcal{M}}^{-\frac{1}{2},-\frac{1}{2},\lambda_3}_{\alpha,\sigma}) R^3_\alpha &= \frac{p\cdot n}{2} |N^+_{\lambda_3}|^2 \delta_{i,r} 2\lambda_3 k_1^i (1 - \hat{E}_{\mathbb{S}_2}) \psi^5 + ... \\ \frac{f_N}{4} N_\sigma (\hat{\mathcal{M}}^{\frac{1}{2},\frac{1}{2},\lambda_3}_{\alpha,\sigma} + \hat{\mathcal{M}}^{-\frac{1}{2},-\frac{1}{2},\lambda_3}_{\alpha,\sigma}) R^4_\alpha &= \frac{p\cdot n}{2} |N^+_{\lambda_3}|^2 \delta_{i,r} 2\lambda_3 |\epsilon^{is}| k_1^i k_1^s \psi^6 + ..., \end{aligned} \tag{4.39}$$

where ... denotes similar terms with distinct momentum dependence such that the written term may be readily identified.

4.2.5 . The Fock Basis

Let us restate a modified version of Eq. (4.39) in which we define a new set of helicity projected tensorial structures $\tilde{T}_\alpha^{\lambda,\mathrm{t}}$ such that dependence on the quark and nucleon helicities, the quark momenta, and the functions ψ defined in Eq. (4.32) is made manifest, and all other dependencies are summarized in the $\tilde{T}_\alpha^{\lambda,\mathrm{t}}$. We choose to write

$$
\begin{aligned}
&\frac{f_N}{4} N_{h;\sigma} \hat{\mathcal{M}}^{\lambda}_{\alpha,\sigma} \\
= \;& -2\lambda_3 \delta_{\lambda_1,-\lambda_2}\delta_{\lambda_1,\lambda_3}\delta_{\lambda_3,h}\tilde{T}_\alpha^{\lambda,1}\psi^{1,w} + \delta_{\lambda_1,\lambda_2}\delta_{\lambda_1,-\lambda_3}\delta_{\lambda_3,-h}\tilde{T}_\alpha^{\lambda,7}(\hat{E}_{\mathbb{S}_2}+\hat{E}_{\mathbb{S}_4})\psi^{1,w} \\
&+\delta_{\lambda_1,-\lambda_2}\delta_{\lambda_1,\lambda_3}\delta_{\lambda_3,h}\tilde{T}_\alpha^{\lambda,3}\epsilon^{ij}k_1^i k_2^j\psi^{2,w} \\
&+2\lambda_3 i\delta_{\lambda_1,\lambda_2}\delta_{\lambda_1,-\lambda_3}\delta_{\lambda_3,-h}\tilde{T}_\alpha^{\lambda,12}(k_1^i k_2^j - k_2^i k_1^j)(\hat{E}_{\mathbb{S}_2}-\hat{E}_{\mathbb{S}_4})\psi^{2,w} \\
&+\frac{1}{2}\delta_{\lambda_1,-\lambda_3}\Big(\delta_{\lambda_1,-\lambda_2}\delta_{\lambda_3,-h}(-2\lambda_3\tilde{T}_\alpha^{\lambda,2}(k_1^i+k_2^i\hat{E}_{\mathbb{S}_3}) - 2\lambda_1\tilde{T}_\alpha^{\lambda,5}(k_1^i-k_2^i\hat{E}_{\mathbb{S}_3})) \\
&-\frac{2\lambda_1}{2}\delta_{\lambda_1,\lambda_2}\delta_{\lambda_3,h}(\tilde{T}_\alpha^{\lambda,8}(k_1^i+k_2^i\hat{E}_{\mathbb{S}_3})\hat{E}_{\mathbb{S}_5} - \tilde{T}_\alpha^{\lambda,9}\epsilon^{ij}(k_1^j+k_2^j\hat{E}_{\mathbb{S}_3})\hat{E}_{\mathbb{S}_6})\Big)\psi^{3,w} \\
&+\frac{1}{2}\delta_{\lambda_1,-\lambda_3}\Big(\delta_{\lambda_1,-\lambda_2}\delta_{\lambda_3,-h}(-2\lambda_3\tilde{T}_\alpha^{\lambda,2}(k_1^i+k_2^i\hat{E}_{\mathbb{S}_3}) + 2\lambda_1\tilde{T}_\alpha^{\lambda,5}(k_1^i-k_2^i\hat{E}_{\mathbb{S}_3})) \\
&-\frac{2\lambda_3}{2}\delta_{\lambda_1,\lambda_2}\delta_{\lambda_3,h}(\tilde{T}_\alpha^{\lambda,8}(k_1^i+k_2^i\hat{E}_{\mathbb{S}_3})\hat{E}_{\mathbb{S}_5} + \tilde{T}_\alpha^{\lambda,9}\epsilon^{ij}(k_1^j+k_2^j\hat{E}_{\mathbb{S}_3})\hat{E}_{\mathbb{S}_6})\Big)\psi^{3,-w} \\
&+\frac{2\lambda_3}{2}\delta_{\lambda_1,\lambda_2}\delta_{\lambda_1,-\lambda_3}\delta_{\lambda_3,h}(\tilde{T}_\alpha^{\lambda,8}(k_1^i+k_2^i\hat{E}_{\mathbb{S}_3}) - \tilde{T}_\alpha^{\lambda,9}\epsilon^{ij}(k_1^j+k_2^j\hat{E}_{\mathbb{S}_3}))\hat{E}_{\mathbb{S}_6}\psi^{3,-w} \\
&+\delta_{\lambda_1,\lambda_2}\delta_{\lambda_1,\lambda_3}\delta_{\lambda_3,h}(\tilde{T}_\alpha^{\lambda,8}(k_1^i+k_2^i\hat{E}_{\mathbb{S}_3}) + \tilde{T}_\alpha^{\lambda,9}\epsilon^{ij}(k_1^j+k_2^j\hat{E}_{\mathbb{S}_3}))(1-\hat{E}_{\mathbb{S}_2})\psi^{5} \\
&+2(-2\lambda_3)\delta_{\lambda_1,\lambda_2}\delta_{\lambda_1,\lambda_3}\delta_{\lambda_3,-h}(\tilde{T}_\alpha^{\lambda,10}|\epsilon^{ij}|(k_1^i k_1^j + k_2^i k_2^j) \\
&+\tilde{T}_\alpha^{\lambda,11}|\epsilon^{ij}|k_1^i k_2^j(\hat{E}_{\mathbb{S}_1}+\hat{E}_{\mathbb{S}_3}-\hat{E}_{\mathbb{S}_5}-\hat{E}_{\mathbb{S}_4}))\psi^{6},
\end{aligned}
\tag{4.40}
$$

where any apparent instances of a lack of summation over i, j is due to a lack of display of these indices in the corresponding objects $\tilde{T}_\alpha^{\lambda,\mathrm{t}}$ to avoid further clutter.
We therefore write down all contributing Fock states in terms of the functions ψ and quark field operators acting on the vacuum and categorize them in terms of their quark helicities, nucleon helicities, and consequent qOAM in Tab. 4.1

$\sum_d c_d \psi^d$	$\|\text{Fock}\rangle$	Ψ_{h,λ_Σ}	qOAM
$-(k_1^x + ik_1^y)\psi^5$	$\|u^{-\frac{1}{2}}u^{-\frac{1}{2}}d^{-\frac{1}{2}}\rangle - \|u^{-\frac{1}{2}}d^{-\frac{1}{2}}u^{-\frac{1}{2}}\rangle$	$\Psi_{-\frac{1}{2},-\frac{3}{2}}$	1
$(k_1^x + ik_1^y)(k_3^x + ik_3^y)\psi^6$	$\|u^{-\frac{1}{2}}u^{-\frac{1}{2}}d^{-\frac{1}{2}}\rangle - \|u^{-\frac{1}{2}}d^{-\frac{1}{2}}u^{-\frac{1}{2}}\rangle$	$\Psi_{\frac{1}{2},-\frac{3}{2}}$	2
$-\psi^{1,-1} + i(k_1^x k_2^y - k_1^y k_2^x)\psi^{2,-1}$	$\|u^{-\frac{1}{2}}u^{+\frac{1}{2}}d^{-\frac{1}{2}}\rangle - \|u^{-\frac{1}{2}}d^{-\frac{1}{2}}u^{+\frac{1}{2}}\rangle$	$\Psi_{-\frac{1}{2},-\frac{1}{2}}$	0
$(k_1^x + ik_1^y)\psi^{3,-1} + (k_2^x + ik_2^y)\hat{E}_{\mathbb{S}_3}\psi^{3,1}$	$\|u^{+\frac{1}{2}}u^{-\frac{1}{2}}d^{-\frac{1}{2}}\rangle - \|u^{+\frac{1}{2}}d^{-\frac{1}{2}}u^{-\frac{1}{2}}\rangle$	$\Psi_{\frac{1}{2},-\frac{1}{2}}$	1
$(k_1^x - ik_1^y)\psi^{3,-1} + (k_2^x - ik_2^y)\hat{E}_{\mathbb{S}_3}\psi^{3,1}$	$\|u^{-\frac{1}{2}}u^{+\frac{1}{2}}d^{+\frac{1}{2}}\rangle - \|u^{-\frac{1}{2}}d^{+\frac{1}{2}}u^{+\frac{1}{2}}\rangle$	$\Psi_{-\frac{1}{2},\frac{1}{2}}$	-1
$\psi^{1,-1} + i(k_1^x k_2^y - k_1^y k_2^x)\psi^{2,-1}$	$\|u^{+\frac{1}{2}}u^{-\frac{1}{2}}d^{+\frac{1}{2}}\rangle - \|u^{+\frac{1}{2}}d^{+\frac{1}{2}}u^{-\frac{1}{2}}\rangle$	$\Psi_{\frac{1}{2},\frac{1}{2}}$	0
$-(k_1^x - ik_1^y)(k_3^x - ik_3^y)\psi^6$	$\|u^{+\frac{1}{2}}u^{+\frac{1}{2}}d^{+\frac{1}{2}}\rangle - \|u^{+\frac{1}{2}}d^{+\frac{1}{2}}u^{+\frac{1}{2}}\rangle$	$\Psi_{-\frac{1}{2},\frac{3}{2}}$	-2
$-(k_1^x - ik_1^y)\psi^5$	$\|u^{+\frac{1}{2}}u^{+\frac{1}{2}}d^{+\frac{1}{2}}\rangle - \|u^{+\frac{1}{2}}d^{+\frac{1}{2}}u^{+\frac{1}{2}}\rangle$	$\Psi_{\frac{1}{2},\frac{3}{2}}$	-1

Table 4.1: The LFWFs Ψ_{h,λ_Σ} are defined as momentum dependent coefficients of the Fock expansion of a nucleonic state and are categorized in terms of the nucleon helicity h and the total three-quark (z) helicity projection λ_Σ of the Fock states to which they correspond. Conservation of OAM allows for deduction of the corresponding total qOAM values, which are shown in the third column and are given by $h - \lambda_\Sigma$.

where we have defined the implicitly labeled LFWFs $\Psi_{h,\lambda_\Sigma}(\kappa)$ which implicitly carry all of the flavor, color, and helicity labels of the Fock state corresponding to $\Psi_{h,\lambda_\Sigma}(\kappa)$ in addition to its momentum dependence.

A few comments are in order. Firstly, how were such Fock states computed? Comparing Tab. 4.1 to Eq. (4.40) which makes manifest the contributions to the matrix element defined in Eq. (4.11) in terms of the full set of quark and nucleon helicity (anti)alignment configurations, one can identify a drastic simplification merely in the number of terms present? Why so? For the Fock components of qOAM value $\pm\frac{1}{2}$, there are three contributing Fock states corresponding to the three-quark helicity configurations associated with such a total value (i.e. $\pm\frac{1}{2} = \pm(\frac{1}{2} + \frac{1}{2} - \frac{1}{2}) = \pm(\frac{1}{2} - \frac{1}{2} + \frac{1}{2}) = \pm(-\frac{1}{2} + \frac{1}{2} + \frac{1}{2})$). The corresponding Fock components presented in Tab. 4.1 are sums of the corresponding states.

A second, subtler point implicit in the previous, and mentioned earlier in this sections is that of the antisymmetric momentum-dependent structures featured in the matrix element decomposition, such as $\epsilon^{ij}k_1^i k_2^j$. These structures contribute no projected qOAM, but do correspond to two opposing units of qOAM, each one on a distinct quark. As a result, even if not explicitly stated, discussion regarding individual qOAM contributions here implicitly reference *total* qOAM contributions corresponding to given LFWF contributions.

4.3 . Overlap Representation of GPDs

Given that the remainder of this thesis will be focused on the contributions of three-quark states to GPDs and related objects, it is important to characterize precisely which pairs of states will contribute. In the subsection of this section, the formula describing the kinds of pairs of three-quark Fock states which will contribute, called the overlap representation of GPDs, will be presented.

4.3.1 . Overlap Formula

In order to understand in a relatively transparent manner the requirements for Fock contributions to GPDs, let us take a look at the GPD matrix element-based definition given in the first chapter (2.15). Let us consider GPDs in the context of DVCS, only to extend the resulting formulae to other experimental processes via GPD universality. In DVCS, the involved quark bilinear operator, physically motivated by the change in momentum received by the active quark via its joint interaction with both the virtual initial photon and its on shell final state counterpart, imparts in general a non-zero momentum difference on the joint nucleonic system by modifying the momentum of only the active quark. Therefore, the remaining two quarks should exhibit identical momenta and other quantum numbers before and after the interaction. However, for the chiral even GPDs considered in this work, the initial and final state momenta of the active quark should reflect precisely the difference imparted by the interaction with the photon-electron probe system. All quantum numbers of the active quark must otherwise be unchanged. The momentum equivalence presented here for the inactive quarks is of course the case in any given frame, so this thesis will work with three frames, following the work in [34]. These three frames are incoming (hadron in) in which the z direction is that of the incoming nucleon's motion, outgoing (hadron out) in which the z direction is that of the outgoing nucleon's motion, and the so-called "symmetric frame" in which the momentum transfer is evenly distributed among the incoming and outgoing nucleonic states i.e.: $\vec{0} = \vec{\bar{P}}_\perp = \vec{P}_\perp + \frac{\vec{\Delta}_\perp}{2} = \vec{P}'_\perp - \frac{\vec{\Delta}_\perp}{2}$. In the symmetric frame the z direction is that of the nucleon's average momentum. The associated symmetric frame variables are labeled as

$$(\bar{x}_i \quad , \quad \vec{\bar{k}}_{i\perp}), \tag{4.41}$$

$$(\bar{x}_j \mp \frac{\xi}{2} \quad , \quad \vec{\bar{k}}_{j\perp} \mp \frac{\vec{\Delta}_\perp}{2}), \tag{4.42}$$

where the index i always labels spectator parton-related quantities and j those of the active parton, and where the $-$ signs correspond to the incoming state, whereas the $+$ signs correspond to the outgoing state (See Fig. 4.1).

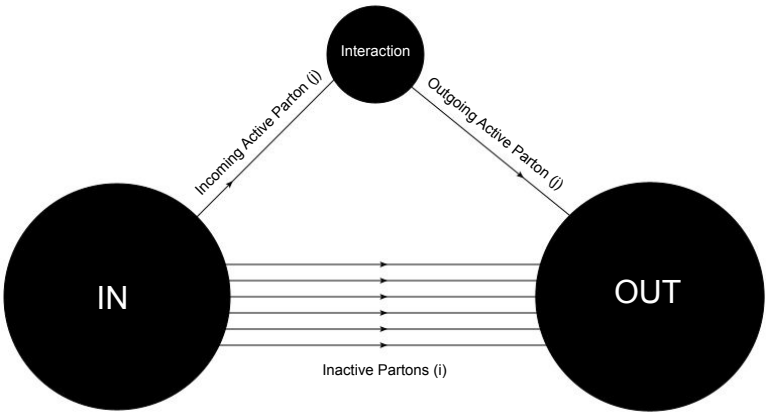

Figure 4.1: Here a general schematic for the incoming and outgoing states, and the corresponding transitional interaction is shown.

In the incoming frame the quark longitudinal momentum fractions and transverse momenta are given in terms of their counterpoints in the symmetric momentum frame as well as the skewness ξ, and $\vec{\Delta}_\perp$ as

$$\begin{aligned} x_i &\equiv \frac{\bar{x}}{1-\xi}, \qquad \vec{k}_{i\perp} \equiv \vec{\bar{k}}_{i\perp} + \frac{\bar{x}}{1-\xi}\frac{\vec{\Delta}_\perp}{2} \\ x_j &\equiv \frac{\bar{x}_j + \xi}{1-\xi}, \qquad \vec{k}_{j\perp} \equiv \vec{\bar{k}}_{j\perp} - \frac{1-\bar{x}}{1-\xi}\frac{\vec{\Delta}_\perp}{2}. \end{aligned} \tag{4.43}$$

The corresponding outgoing frame variables are given in terms of the same basis as

$$\begin{aligned} x'_i &\equiv \frac{\bar{x}}{1+\xi}, \qquad \vec{k}'_{i\perp} \equiv \vec{\bar{k}}_{i\perp} - \frac{\bar{x}}{1+\xi}\frac{\vec{\Delta}_\perp}{2} \\ x'_j &\equiv \frac{\bar{x}_j - \xi}{1+\xi}, \qquad \vec{k}'_{j\perp} \equiv \vec{\bar{k}}_{j\perp} + \frac{1-\bar{x}}{1+\xi}\frac{\vec{\Delta}_\perp}{2}, \end{aligned} \tag{4.44}$$

where we remind the reader that our convention for ξ is opposite in sign with respect to the definition given in [34]. We also define a shorthand for denotation of the quark momenta as

$$\kappa_l = (x_l, \vec{k}_{l\perp}), \tag{4.45}$$

we also define

$$\delta(\kappa_l - \kappa_{l'}) = \delta(x_l - x_{l'})\delta^2(\vec{k}_{l\perp} - \vec{k}_{l'\perp}), \tag{4.46}$$

and the integration measure

$$d\kappa_l \equiv dx_l d^2\vec{k}_{l\perp}. \tag{4.47}$$

Now it is necessary to provide a proper definition of the quantum numbers $\mathfrak{D}_{n,s}$ introduced as a catch-all in Eq. (4.1). They are nothing but the momenta,

helicities, colors, and flavors of the quarks in question we select using the index $l \in \{1,2,3\}$ as κ_l, λ_l, c_l, and f_l, respectively, whose collective labels are correspondingly given by $\kappa = (\kappa_1, \kappa_2, \kappa_3)$, $\lambda = (\lambda_1, \lambda_2, \lambda_3)$, $c = (c_1, c_2, c_3)$, $f = (f_1, f_2, f_3)$. The collective label for a given quark's quantum numbers is defined as $\mathcal{Q}_l \equiv (\kappa_l, \lambda_l, c_l, f_l)$ such that one may write

$$\delta^{\mathcal{Q}_{l'}}_{\mathcal{Q}_l} = \delta(\kappa_l - \kappa_{l'})\delta^{\lambda_{l'}}_{\lambda_l}\delta^{c_{l'}}_{c_l}\delta^{f_{l'}}_{f_l}, \tag{4.48}$$

and

$$\mathcal{Q}^{\kappa} = \kappa, \quad \mathcal{Q}^{\lambda} = \lambda, \quad \mathcal{Q}^{c} = c, \quad \mathcal{Q}^{f} = f. \tag{4.49}$$

We also define the collective $\mathcal{Q} = (\mathcal{Q}_1, \mathcal{Q}_2, \mathcal{Q}_3)$ and write

$$\delta^{\mathcal{Q}'}_{\mathcal{Q}} \equiv \prod_{l=1}^{3} \delta^{\mathcal{Q}'_l}_{\mathcal{Q}_l}, \tag{4.50}$$

and then denote the corresponding "reshuffling" of the collective labels' (λ, f, c, and $\mathcal{Q}$) elements (using $\mathcal{Q}$ as an example) according to $\mathbb{S}$ as

$$(\hat{\mathbb{S}}_{\mathbb{A}}(\mathcal{Q}))_l = \mathcal{Q}_{\mathbb{S}_{\mathbb{A},l}}. \tag{4.51}$$

As such, we give the nucleonic Fock expansion

$$|P;h\rangle = \sum\!\!\!\!\!\!\int_{\mathcal{Q}} \varphi_{\mathcal{Q};h}|\mathcal{Q}\rangle, \tag{4.52}$$

where

$$\sum\!\!\!\!\!\!\int_{\mathcal{Q}} \equiv \int \mathcal{D}_3 \prod_{l=1}^{3} \Big(\sum_{\mathcal{Q}_l^{\lambda}}^{\in\{-\frac{1}{2},\frac{1}{2}\}} \sum_{\mathcal{Q}_l^{c}} \sum_{\mathcal{Q}_l^{f}} \Big) \epsilon^{\mathcal{Q}^c}, \tag{4.53}$$

where ϵ^{ijk} is the completely antisymmetric Levi-Civita tensor, $\varphi_{\mathcal{Q};h}$ is the LFWF labeled by the indices of the Fock state to which it corresponds, which is given by the ordered product

$$|\mathcal{Q}\rangle \equiv \Big(\prod_{l=1}^{3} q^{\mathcal{Q}_l^{\lambda}}_{\mathcal{Q}_l^{f},\mathcal{Q}_l^{c}}(\mathcal{Q}_l^{\kappa}) \Big)|0\rangle \equiv q_{\mathcal{Q}}|0\rangle, \tag{4.54}$$

where we have implicitly defined the three-quark field operator $q_{\mathcal{Q}}$, and employed helicity projected quark operators $\mathcal{P}^{\lambda}$.
Though generally Dirac indices ($\beta(')$) are suppressed in this subsection. We have now built all of the tools to write down the overlap formula for the helicity dependent amplitude defined in Eq. (2.24). We will also include the polarization index $\mathbb{P} \in \{0,1\}$. For $\mathbb{P} = 0$ recover the unpolarized amplitudes

defined in Eq. (2.24). For $\mathbb{P}=1$ we find their polarized counterparts as defined in the appendix Sec. 8.3. We write

$$
\begin{aligned}
&\mathcal{H}^{\hat{f},\mathbb{P}}_{h'h}(\bar{x},\xi,t)\\
\equiv\;& \frac{1}{2\sqrt{1-\xi^2}}\sum_{\hat{c}}\int\frac{dz^-}{2\pi}e^{i\bar{x}\bar{p}^+z^-}\langle P',h'|\bar{q}^{\hat{c}}_{\hat{f}}(-\frac{z}{2})\gamma^+(\gamma_5)^{\mathbb{P}}q^{\hat{c}}_{\hat{f}}(\frac{z}{2})|P,h\rangle\\
=\;& \frac{1}{2\sqrt{1-\xi^2}}\sum_{\hat{c}}\int\frac{dz^-}{2\pi}e^{i\bar{x}\bar{p}^+z^-}\sum_{\mathbb{A}=1}^{6}\sum\!\!\!\!\!\!\int_{\mathcal{Q}'}\sum\!\!\!\!\!\!\int_{\mathcal{Q}}\varphi^*_{\hat{\mathbb{S}}_{\mathbb{A}}(\mathcal{Q}');h'}\varphi_{\mathcal{Q};h}\\
&\times\langle\hat{\mathbb{S}}_{\mathbb{A}}(\mathcal{Q}')|\bar{q}^{\hat{c}}_{\hat{f}}(-\frac{z}{2})\gamma^+(\gamma_5)^{\mathbb{P}}q^{\hat{c}}_{\hat{f}}(\frac{z}{2})|\mathcal{Q}\rangle\\
=\;& \frac{1}{2\sqrt{1-\xi^2}}\sum_{\mathbb{A}=1}^{6}\sum\!\!\!\!\!\!\int_{\mathcal{Q}',\mathcal{Q}}\delta^{\mathcal{Q}}_{\hat{\mathbb{S}}_{\mathbb{A}}(\mathcal{Q}')}\int\mathcal{D}'_3\mathcal{D}_3\varphi^*_{\hat{\mathbb{S}}_{\mathbb{A}}(\mathcal{Q}');h'}\varphi_{\mathcal{Q};h}\sum_{\bar{l}=1}^{3}\delta^{\hat{f}}_{f_{\bar{l}}}\delta(x_l-\bar{x})(\text{sign}(\lambda_l))^{\mathbb{P}}\\
\equiv\;& \mathcal{O}^{\hat{f},\mathbb{P}}\Big[\varphi_{\hat{\mathbb{S}}_{\mathbb{A}}(\mathcal{Q}');h'},\varphi_{\mathcal{Q};h}\Big](\bar{x},\xi,t),
\end{aligned}
\tag{4.55}
$$

where the computation between the second and third lines has been performed using the corresponding commutation relations of the creation and annihilation relations provided.
In the final line of Eq. (4.55), the notation $\mathcal{O}(\varphi',\varphi)$ has been used to represent this overlap, but also to emphasize an analogy with atomic orbitals. In the following chapter the analogy will become clearer as we will characterize a basis of functions φ of definite qOAM. Indeed, the remaining chapters of this thesis are intended ultimately to develop a method of using LFWFs to examine the effects of diverse qOAM states on the "shape" of the nucleons by investigating precisely how such states contribute to nucleonic structure functions such as GPDs.

4.3.2 . Master Overlap Formula: GPDs and Subresults

The reader is reminded that the GPDs are given in terms of the helicity dependent amplitudes $\mathcal{H}$ as [34]

$$
H^{\hat{f},\mathbb{P}} = \mathcal{H}^{\hat{f},\mathbb{P}}_{\frac{1}{2},\frac{1}{2}}+\frac{\xi^{2-\mathbb{P}}2M_N|\vec{\Delta}_\perp|}{(\Delta_1+i\Delta_2)\sqrt{1-\xi^2}\sqrt{\frac{4\xi^2m^2}{\xi^2-1}-t}}\mathcal{H}^{\hat{f},\mathbb{P}}_{-\frac{1}{2},\frac{1}{2}} \tag{4.56}
$$

$$
E^{\hat{f},\mathbb{P}} = \frac{2M_N|\vec{\Delta}_\perp|\sqrt{1-\xi^2}}{\xi^{\mathbb{P}}(\Delta_1+i\Delta_2)\sqrt{\frac{4\xi^2M_N^2}{\xi^2-1}-t}}\mathcal{H}^{\hat{f},\mathbb{P}}_{-\frac{1}{2},\frac{1}{2}}. \tag{4.57}
$$

In terms of definite qOAM, one has

$$
\begin{aligned}
\mathcal{H}^{\hat{f},\mathbb{P}}_{\frac{1}{2},\frac{1}{2}} = \;& \Big(\mathcal{O}^{\hat{f},\mathbb{P}}(\Psi_{\frac{1}{2},\frac{1}{2}},\Psi_{\frac{1}{2},\frac{1}{2}})+\mathcal{O}^{\hat{f},\mathbb{P}}(\Psi_{\frac{1}{2},-\frac{1}{2}},\Psi_{\frac{1}{2},-\frac{1}{2}})\\
&+\mathcal{O}^{\hat{f},\mathbb{P}}(\Psi_{\frac{1}{2},\frac{3}{2}},\Psi_{\frac{1}{2},\frac{3}{2}})+\mathcal{O}^{\hat{f},\mathbb{P}}(\Psi_{\frac{1}{2},-\frac{3}{2}},\Psi_{\frac{1}{2},-\frac{3}{2}})\Big)
\end{aligned}
\tag{4.58}
$$

$$
\mathcal{H}^{\hat{f},\mathbb{P}}_{-\frac{1}{2},\frac{1}{2}} = \Big(\mathcal{O}^{\hat{f},\mathbb{P}}(\Psi_{-\frac{1}{2},-\frac{3}{2}},\Psi_{\frac{1}{2},\frac{3}{2}})+\mathcal{O}^{\hat{f},\mathbb{P}}(\Psi_{-\frac{1}{2},\frac{3}{2}},\Psi_{\frac{1}{2},-\frac{3}{2}})\Big). \tag{4.59}
$$

One sees from this that the helicity conserving ($h_N = h'_N$) function $\mathcal{H}^{\hat{f},\mathbb{P}}_{\frac{1}{2},\frac{1}{2}}$ receives contributions from qOAM zero (first term), one (second and third terms), and two (fourth term) whereas the helicity flip ($h_N = -h'_N$) function $\mathcal{H}^{\hat{f},\mathbb{P}}_{-\frac{1}{2},\frac{1}{2}}$ receives contributions only from qOAM one (first term) and two (second term). As the GPD E is a function of only one of these (the helicity flip function $\mathcal{H}^{\hat{f},\mathbb{P}}_{-\frac{1}{2},\frac{1}{2}}$) it receives no qOAM zero contributions. Calculation of the nucleon PDFs yields

$$\begin{aligned} f^{\hat{f},\mathbb{P}}(x_{\mathsf{BJ}}) &= H^{\hat{f},\mathbb{P}}|_{t=\xi=0} = \\ &\Big(\mathcal{O}^{\hat{f},\mathbb{P}}(\Psi_{\frac{1}{2},\frac{1}{2}},\Psi_{\frac{1}{2},\frac{1}{2}}) + \mathcal{O}^{\hat{f},\mathbb{P}}(\Psi_{\frac{1}{2},-\frac{1}{2}},\Psi_{\frac{1}{2},-\frac{1}{2}}) \\ &+\mathcal{O}^{\hat{f},\mathbb{P}}(\Psi_{\frac{1}{2},\frac{3}{2}},\Psi_{\frac{1}{2},\frac{3}{2}}) + \mathcal{O}^{\hat{f},\mathbb{P}}(\Psi_{\frac{1}{2},-\frac{3}{2}},\Psi_{\frac{1}{2},-\frac{3}{2}})\Big)|_{t=\xi=0}, \end{aligned} \tag{4.60}$$

where the incoming and outgoing momenta are now identical. For the convenience of the reader the appendix section Sec. 8.5 contains expressions for the FFs and the EM radius expectation values in terms of the overlaps $\mathbb{O}$. Now that we have expressed all of the quantities which interest us in terms of the LFWF basis and it is completely manifest which contributions correspond to each value of qOAM, it is now expedient to build the LFWFs in a particular model. While doing so, we will discuss some previous work on LFWFs, including those which employ a point-like diquark, and illustrate how and why this thesis's use of a non-point-like diquark provides access to a more complete set of contributions than those obtained in the case point-like diquark based models.

4.4 . An Example: Calculation of $\mathcal{O}^{u,0}(\Psi_{1,\frac{1}{2}},\Psi_{1,\frac{1}{2}})$

We start with the general expression specified to the case at hand

$$\begin{aligned} &\mathcal{O}^{u,0}(\Psi_{1,\frac{1}{2}},\Psi_{1,\frac{1}{2}}) \\ \equiv\ &\frac{1}{2\sqrt{1-\xi^2}}\sum_{\mathbb{A}=1}^{6}\sum_{\mathcal{Q}',\mathcal{Q}}\delta^{\mathcal{Q}}_{\hat{\mathbb{S}}_{\mathbb{A}}(\mathcal{Q}')}\int \mathcal{D}'_3\mathcal{D}_3\Psi^*_{1,1;\hat{\mathbb{S}}_{\mathbb{A}}(\mathcal{Q}');h'}\Psi_{1,1;\mathcal{Q};h}\sum_{\bar{l}=1}^{3}\delta^{\hat{f}}_{f_{\bar{l}}}\delta(x_l-\bar{x}), \end{aligned} \tag{4.61}$$

and cite the corresponding Fock element, decomposing it into its two terms

$$\Psi_{1,\frac{1}{2}}(|u^{+\frac{1}{2}}u^{-\frac{1}{2}}d^{+\frac{1}{2}}\rangle - |u^{+\frac{1}{2}}d^{+\frac{1}{2}}u^{-\frac{1}{2}}\rangle) = T_1 + T_2. \tag{4.62}$$

We then list all of the possible permutations $\mathbb{S}$:

$$\begin{aligned} &\mathbb{S}_1 \equiv \{1,2,3\} \qquad &&\mathbb{S}_2 \equiv \{1,3,2\} \\ &\mathbb{S}_3 \equiv \{2,1,3\} \qquad &&\mathbb{S}_4 \equiv \{2,3,1\} \\ &\mathbb{S}_5 \equiv \{3,1,2\} \qquad &&\mathbb{S}_6 \equiv \{3,2,1\}. \end{aligned} \tag{4.63}$$

We arrive at (where the active quark variables are shown by the Dirac δ in each term in the sum):

$$
\begin{aligned}
&\mathcal{O}^{u,0}(\Psi_{1,\frac{1}{2}},\Psi_{1,\frac{1}{2}}) = \frac{1}{2}\int[\mathcal{D}\bar{\kappa}]\\
&\Big(2\Psi^*_{1,\frac{1}{2}}(\frac{\bar{x}_1+\xi}{1+\xi},\vec{\bar{k}}_{1\perp}+\frac{1-\bar{x}_1}{1+\xi}\frac{\vec{\Delta}_\perp}{2};\frac{\bar{x}_2}{1+\xi},\\
&\vec{\bar{k}}_{2\perp}-\frac{\bar{x}_2}{1+\xi}\frac{\vec{\Delta}_\perp}{2};\frac{\bar{x}_3}{1+\xi},\vec{\bar{k}}_{3\perp}-\frac{\bar{x}_3}{1+\xi}\frac{\vec{\Delta}_\perp}{2})\\
&\times\Psi_{1,\frac{1}{2}}(\frac{\bar{x}_1-\xi}{1-\xi},\vec{\bar{k}}_{1\perp}-\frac{1-\bar{x}_1}{1-\xi}\frac{\vec{\Delta}_\perp}{2};\frac{\bar{x}_2}{1-\xi},\\
&\vec{\bar{k}}_{2\perp}+\frac{\bar{x}_2}{1-\xi}\frac{\vec{\Delta}_\perp}{2};\frac{\bar{x}_3}{1-\xi},\vec{\bar{k}}_{3\perp}+\frac{\bar{x}_3}{1-\xi}\frac{\vec{\Delta}_\perp}{2})\delta(x-\bar{x}_1)\\
&+\Psi^*_{1,\frac{1}{2}}(\frac{\bar{x}_1}{1+\xi},\vec{\bar{k}}_{1\perp}-\frac{\bar{x}_1}{1+\xi}\frac{\vec{\Delta}_\perp}{2};\frac{\bar{x}_2+\xi}{1+\xi},\\
&\vec{\bar{k}}_{2\perp}+\frac{1-\bar{x}_2}{1+\xi}\frac{\vec{\Delta}_\perp}{2};\frac{\bar{x}_3}{1+\xi},\vec{\bar{k}}_{3\perp}-\frac{\bar{x}_3}{1+\xi}\frac{\vec{\Delta}_\perp}{2})\\
&\times\Psi_{1,\frac{1}{2}}(\frac{\bar{x}_1}{1-\xi},\vec{\bar{k}}_{1\perp}+\frac{\bar{x}_1}{1-\xi}\frac{\vec{\Delta}_\perp}{2};\frac{\bar{x}_2-\xi}{1-\xi},\\
&\vec{\bar{k}}_{2\perp}-\frac{1-\bar{x}_2}{1-\xi}\frac{\vec{\Delta}_\perp}{2};\frac{\bar{x}_3}{1-\xi},\vec{\bar{k}}_{3\perp}+\frac{\bar{x}_3}{1-\xi}\frac{\vec{\Delta}_\perp}{2})\delta(x-\bar{x}_2)\\
&+\Psi^*_{1,\frac{1}{2}}(\frac{\bar{x}_1}{1+\xi},\vec{\bar{k}}_{1\perp}-\frac{\bar{x}_1}{1+\xi}\frac{\vec{\Delta}_\perp}{2};\frac{\bar{x}_2}{1+\xi},\\
&\vec{\bar{k}}_{2\perp}-\frac{\bar{x}_2}{1+\xi}\frac{\vec{\Delta}_\perp}{2};\frac{\bar{x}_3+\xi}{1+\xi},\vec{\bar{k}}_{3\perp}+\frac{1-\bar{x}_3}{1+\xi}\frac{\vec{\Delta}_\perp}{2})\\
&\times\Psi_{1,\frac{1}{2}}(\frac{\bar{x}_1}{1-\xi},\vec{\bar{k}}_{1\perp}+\frac{\bar{x}_1}{1-\xi}\frac{\vec{\Delta}_\perp}{2};\frac{\bar{x}_2}{1-\xi},\\
&\vec{\bar{k}}_{2\perp}+\frac{\bar{x}_2}{1-\xi}\frac{\vec{\Delta}_\perp}{2};\frac{\bar{x}_3-\xi}{1-\xi},\vec{\bar{k}}_{3\perp}-\frac{1-\bar{x}_3}{1-\xi}\frac{\vec{\Delta}_\perp}{2})\delta(x-\bar{x}_3)\\
&+\Psi^*_{1,\frac{1}{2}}(\frac{\bar{x}_3}{1+\xi},\vec{\bar{k}}_{3\perp}-\frac{\bar{x}_3}{1+\xi}\frac{\vec{\Delta}_\perp}{2};\frac{\bar{x}_2}{1+\xi},\\
&\vec{\bar{k}}_{2\perp}-\frac{\bar{x}_2}{1+\xi}\frac{\vec{\Delta}_\perp}{2};\frac{\bar{x}_1+\xi}{1+\xi},\vec{\bar{k}}_{1\perp}+\frac{1-\bar{x}_1}{1+\xi}\frac{\vec{\Delta}_\perp}{2})\\
&\times\Psi_{1,\frac{1}{2}}(\frac{\bar{x}_1-\xi}{1-\xi},\vec{\bar{k}}_{1\perp}-\frac{1-\bar{x}_1}{1-\xi}\frac{\vec{\Delta}_\perp}{2};\frac{\bar{x}_2}{1-\xi},\\
&\vec{\bar{k}}_{2\perp}+\frac{\bar{x}_2}{1-\xi}\frac{\vec{\Delta}_\perp}{2};\frac{\bar{x}_3}{1-\xi},\vec{\bar{k}}_{3\perp}+\frac{\bar{x}_3}{1-\xi}\frac{\vec{\Delta}_\perp}{2})\delta(x-\bar{x}_1)\\
&+\Psi^*_{1,\frac{1}{2}}(\frac{\bar{x}_3+\xi}{1+\xi},\vec{\bar{k}}_{3\perp}+\frac{1-\bar{x}_3}{1+\xi}\frac{\vec{\Delta}_\perp}{2};\frac{\bar{x}_2}{1+\xi},\\
&\vec{\bar{k}}_{2\perp}-\frac{\bar{x}_2}{1+\xi}\frac{\vec{\Delta}_\perp}{2};\frac{\bar{x}_1}{1+\xi},\vec{\bar{k}}_{1\perp}-\frac{\bar{x}_1}{1+\xi}\frac{\vec{\Delta}_\perp}{2})\\
&\times\Psi_{1,\frac{1}{2}}(\frac{\bar{x}_1}{1-\xi},\vec{\bar{k}}_{1\perp}+\frac{\bar{x}_1}{1-\xi}\frac{\vec{\Delta}_\perp}{2};\frac{\bar{x}_2}{1-\xi},\\
&\vec{\bar{k}}_{2\perp}+\frac{\bar{x}_2}{1-\xi}\frac{\vec{\Delta}_\perp}{2};\frac{\bar{x}_3-\xi}{1-\xi},\vec{\bar{k}}_{3\perp}-\frac{1-\bar{x}_3}{1-\xi}\frac{\vec{\Delta}_\perp}{2})\delta(x-\bar{x}_3)\Big).
\end{aligned}
\tag{4.64}
$$

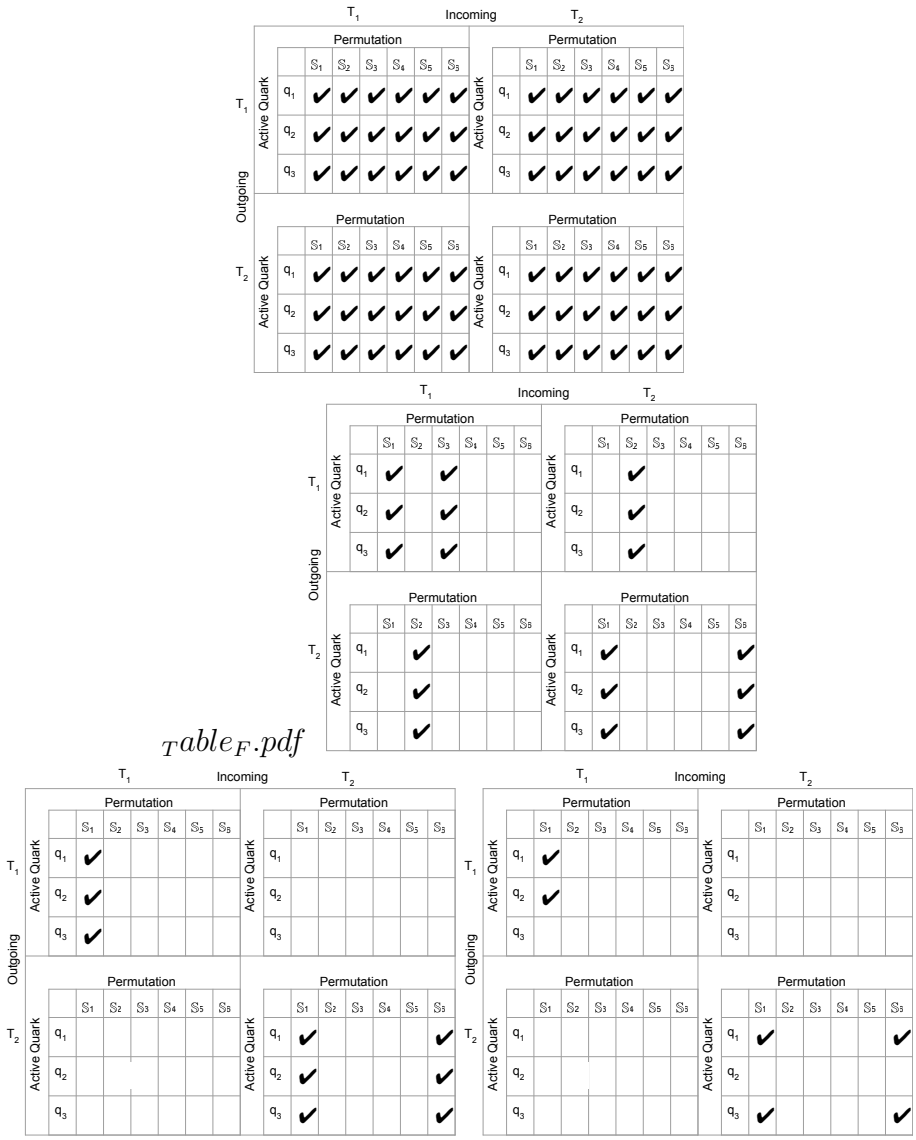

Figure 4.2: A demonstration of how we first consider all possible options for active quark flavor and permutation (first panel), then filter by flavor (second panel), all quark helicities (third panel), and active flavor (fourth panel) using the corresponding Kronecker deltas. At this point all dependence on color, flavor, and quark helicity have been considered, leaving only the momentum dependence.

In Fig. 4.2, the overlap selection process unfolds in a sequence of panels, each refining the considerations for active quark flavor and permutation. Initially, in the first panel, all conceivable options for active quark flavor and permutation are explored. Subsequently, in the second panel, filtration by flavor ensues, followed by an assessment of all quark helicities in the third panel. Finally, the fourth panel refines the selection further by focusing on ac-

tive flavor, employing corresponding Kronecker deltas for each step. Through this iterative process, all dependencies on color, flavor, and quark helicity are meticulously accounted for, culminating in the isolation of momentum dependence as the sole remaining consideration.

5 - LFWF Modeling

Starting from the goal of computing nucleon GPDs and related subresults, the latter half of this thesis has traced backwards, seeking to characterize the nucleonic states present in the matrix element definition of GPDs via a Fock expansion at equal lightcone time, in turn characterizing the coefficients in this expansion, LFWFs, in terms of matrix elements involving the contributions of individual Fock states to nucleonic states. Now it is time to start from a model of such matrix elements to construct LFWFs and build up to GPDs, FFs, PDFs, and the EM radius. In the first section of this chapter the quark-diquark model used to model this three-body system is presented. In the following two sections a discussion presenting the Euclidean model employed, as well as the method of Mellin of moments used to extend Euclidean results to the lightcone, are presented. Finally, an example LFWF is presented and plotted.

5.1 . The Quark-Diquark Model

One aspect differentiating this work from previous discussions of quark-diquark correlation based models of the nucleon is this work's treatment of the diquark as a two body quark system. That is, the diquark is not treated here as point-like. While simplifying the problem extensively from a three-body to a two-body system, the point-like diquark approach kills any p-wave correlations internal to the diquark, thus forcing one's decomposition of GPDs into distinct qOAM state transitions to be an incomplete picture, even at the valence level. A review of some important works regarding the point-like diquark will be given, along with a short motivation, in the following two sections. What maintains this work, then, as one regarding quark-diquark correlations is the use of the tensorial structures associated with the quark-diquark amplitude, which will be presented along with the corresponding diagrams in the final two subsections of this section.

5.1.1 . Motivation

The standard way to extract information about bound states in Quantum Field Theory is often by relying on the pole structure of N-point functions. In the case of baryons, the quark 6-point function (5.1) is of particular interest, where T represents the standard time-ordered product.

$$G(x_1, x_2, x_3, y_1, y_2, y_3) = \langle 0|\mathrm{T}\{q(x_1)q(x_2)q(x_3)\bar{q}(y_1)\bar{q}(y_2)\bar{q}(y_3)\}|0\rangle. \quad (5.1)$$

Its Fourier transform yields:

$$\tilde{G}(p_1,p_2,p_3,q_1,q_2,q_3) = \int \prod_{j=1}^{3} \mathrm{d}x_j \mathrm{d}y_j e^{ip_j x_j} e^{iq_j y_j} G(x_1,x_2,x_3,y_1,y_2,y_3). \quad (5.2)$$

Introducing $P = \sum_i p_i$ and $Q = \sum_i q_i$, the Green function $\tilde{G}$ can be simplified when $P \to Q$ and $P^2 \to M^2$ where M represents the nucleon mass, as shown in equation (5.3). The residue at the pole, χ, serves as the Faddeev wave function, as defined in equation (5.4).

$$\tilde{G}(p_1,p_2,p_3,q_1,q_2,q_3) \underset{\substack{P\to Q \\ P^2\to M^2}}{\sim} \frac{\chi(p_1,p_2,p_3)\bar{\chi}(q_1,q_2,q_3)}{P^2-M^2}. \quad (5.3)$$

The Euclidean space Faddeev wave function χ is defined in terms of matrix element in coordinate space as

$$\begin{aligned} \langle 0|T\{q(z_1)q(z_2)q(z_3)\}|P,\lambda\rangle &= \frac{1}{4} f_N N_\sigma(P,\lambda) \int \prod_{j=1}^{3} \mathrm{d}^{(4)}k_j e^{-ik_j z_j} \quad (5.4) \\ &\quad \delta^{(4)}(P - \sum_j k_j)\chi_\sigma(k_1,k_2,k_3). \end{aligned}$$

Following references [94, 95], the transposition operator ^{T} is used on one of the quark fields, simplifying the three-spinor algebra into the standard 4×4 Dirac structure and the direct product of a Dirac spinor. χ_σ can be computed using relativistic-three body bound state Bethe-Salpeter equations [96], sometimes called Faddeev equations. Equation (5.5) presents the solution for χ, involving various irreducible kernels. Defining G_0, the disconnected product of three dressed quark propagators, χ is the solution of

$$\chi = G_0 K \chi \quad \text{with} \quad K = K^{(3)} + \sum_{i=1}^{3} (K_i^{(2)} \otimes S_i^{-1}), \quad (5.5)$$

where $K^{(2)}$ and $K^{(3)}$ are respectively the two and three quarks irreducible kernels, i labels the quark not participating to the two-particle kernel, the first equation represents the integral convolution of G_0, K, and χ, and S_i is the propagator of the ith quark (see Fig. 5.1).

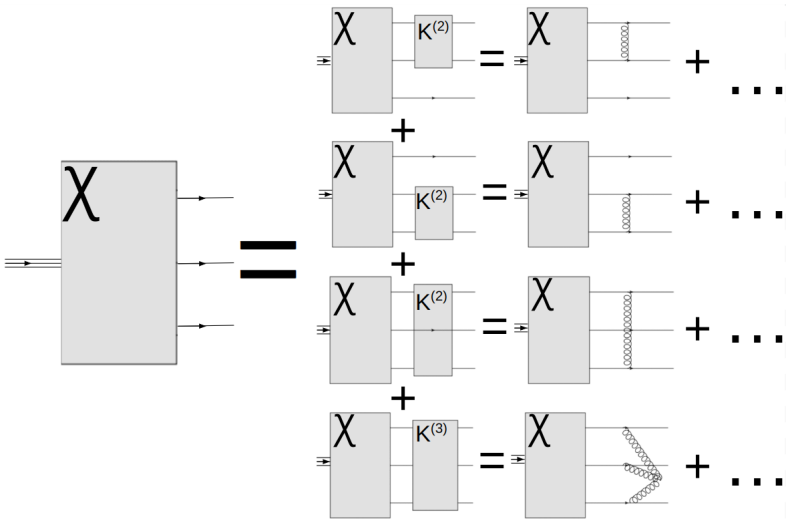

Figure 5.1: The Faddeev kernel for three quarks (left) is a sum of contributions of the three two-quark kernels $K^{(2)}$ (right, first three panels) and the three-quark kernel $K^{(3)}$ (right, bottom panel), where "..." signifies corrections due to higher order interactions.

The two-quark irreducible kernel $K^{(2)}$ contributes at lower order in α_s than the three-quark irreducible $K^{(3)}$ as $K^{(3)}$ contributions vanish by symmetry at the first order in α_s at which $K^{(2)}$ provides non-zero contributions. Additionally, solving the kernel $K^{(2)}$ results in diquark poles in the scattering kernel for three quarks, indicating the accuracy of the diquark approximation [97]. The Bethe-Salpeter wave function formalism provides advantages when studying hadron properties. First, it allows the exploitation of a fully covariant formalism, and thus, the utilization of standard QFT tools. Furthermore, it allows the differentiation between characteristics of the quark and gluon interaction entering the two-body kernel K and observables. Although successful in describing hadron electromagnetic and transition form factors, the formalism has drawbacks, such as difficulty in evaluating systematic uncertainties arising from the choice of the kernel. Recent improvements in the meson sector include the availability of more refined kernels [98, 99, 100, 101]. Additionally, it's worth mentioning that the Faddeev wave function does not represent a "true" wave function in the Quantum Mechanical sense, as it is not associated with probability amplitudes. To recover a probabilistic interpretation, projection of the fully-covariant Faddeev wave function onto the light front is necessary, as explained in the next section.

5.1.2 . The Point-Like diquark

As previously stated, two-quark interactions appear at a lower order in the strong coupling than three-quark interactions at the level of the Faddeev kernel used to solve for the three body fully covariant Faddeev amplitude of

the nucleon. Observing this and wishing to work with simpler toy models in which exact expressions for various amplitudes involved in nucleonic amplitudes can be computed directly using a Lagrangian approach, some have investigated scalar diquark models involving a fundamental scalar field coupled to a quark field (For an inexhaustive set of discussion of this topic in the literature is can be found for example in [102, 103, 104, 105, 106, 107]). This simplicity is the primary motivation for studying such models, but by assuming a point-like scalar diquark field and thereby erasing the contributions of the internal degrees of freedom of the scalar diquark correlations, one immediately kills any p-wave correlations internal to the diquark. Further, when comparing to the other dominant contribution of two body diquarks, the axial vector diquark, one sees that the positing of a fundamental diquark field removes some p-wave contributions from the picture as well. In this work we work with a scalar diquark truly formed of two dynamical bodies, and thus restore p-wave contributions internal to the diquark with respect to any such point-like models. In essence, this is another simplification in that, instead of the singular two body problem present in the point-like diquark models we work with two simultaneous two body problems, one "inside" of the other. This "middle of the road" level simplification of the full three body problem, while more complicated than the point-like toy models, provides access to contributions of quark states of diverse values of qOAM. In addition, it allows for solutions of the Faddeev equation to be propagated directly to the level of three-quark GPDs, a development which in point-like diquark methods is impossible. In the rest of this chapter we will develop such contributions in the Euclidean space model to be elucidated in the following section.

5.1.3 . Diagrams

Considering the three quarks of the nucleon system which we consider in this thesis, there are correspondingly 3 ways of choosing two quarks to form a diquark. We can visualize these three ways using the following three corresponding diagrams:

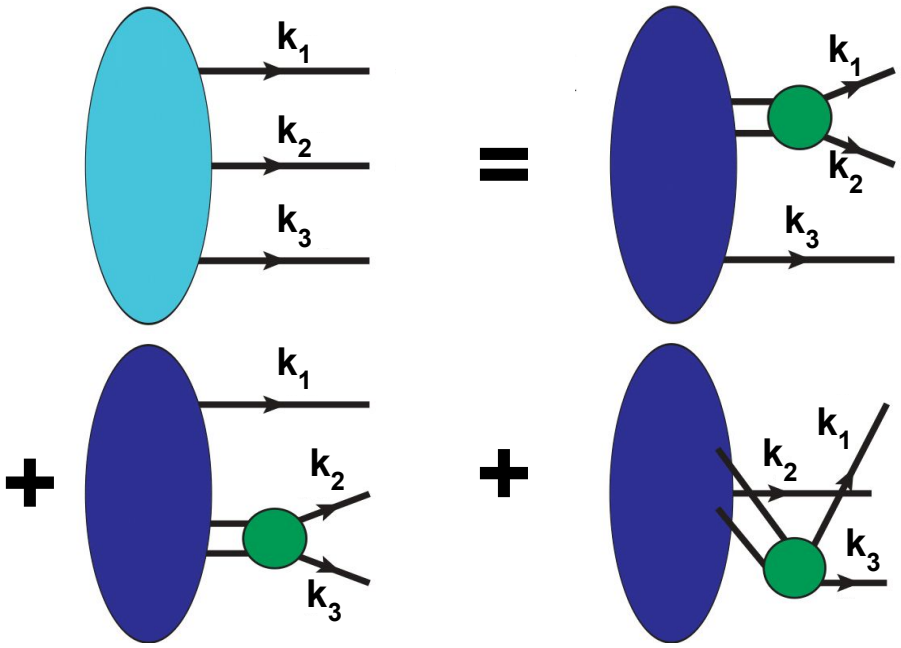

Figure 5.2: At the top left, an expression of the full Faddeev amplitude, is written in the diquark approximation as a sum over the three basis diagrams each involving a unique diquark correlation allowed at leading Fock (three valence quarks only), which are shown on the right and on the bottom. The top right diagram, involving a two u diquark, only contributes significantly when considering axial-vector diquark correlations as there is no way to form a scalar diquark correlation from two quarks of identical flavor.

As mentioned previously in this chapter, all four of the four possible diquark correlations which one may posit are not equally probable. The scalar and axial vector diquark correlations are the most probable [108]. In the following section, the set of tensorial structures available for the diquark amplitude will be given for those two cases only. However, as a matter of conducting a proof of concept study, only the simplest structure in the scalar diquark case will be considered. The methods presented, however, are intended to be readily generalizable to the remaining tensorial structures. In fact, some Mathematica code to do just that has been developed during this thesis. In this subsection, it suffices to admit that, due to the Pauli exclusion principle, a scalar diquark correlation containing two quarks of the same flavor is not permitted. As such, the diagram including the diquark formed by two u quarks will no longer be considered. It is worth noting that this diquark is relevant in the case of the axial vector diquark, however, as it is of spin parity $J^P = 1^+$ [108].

5.1.4 . Tensorial Structures

In expressing the set of possible tensorial structures which may contribute to diquark correlations, it is necessary to choose a basis. This is because, for each set of tensorial structures one can imagine which transform like the corresponding amplitude, one can choose an arbitrary set of linearly independent linear combinations of such structures as another basis. Naturally, we have chosen a basis which comes directly from the literature.
From [109] we explain that the quark-diquark Faddeev amplitudes are computed using the following setup. The Faddeev amplitude representing the nucleon is given by

$$\Psi_N = \Psi_1 + \Psi_2 + \Psi_3, \tag{5.6}$$

where the subscripts denote the bystander quark, (the quark which does not participate in the diquark), all three of which are related to one another by exchanging corresponding indices. The nucleon, possessing spin and isospin $1/2$, is a combination of scalar and axial-vector diquark correlations, the latter of which we mention only for completeness as we will not model it here. That is

$$\Psi_y(k_{1,2,3}, \alpha_{1,2,3}, \tau_{1,2,3}) = \mathcal{N}_y^{0^+} + \mathcal{N}_y^{1^+}, \quad y \in \{1,2,3\} \tag{5.7}$$

with $(k_{1,2,3}, \alpha_{1,2,3}, \tau_{1,2,3})$ representing the momentum, spin, and isospin labels of the constituent quarks, and $P = k_1 + k_2 + k_3$ representing the total momentum of the system. This example scalar diquark component is expressed as:

$$\mathcal{N}_1^{0^+}(k_{1,2,3}, \alpha_{1,2,3}, \tau_{1,2,3}) \quad = \quad [\Gamma^{0^+}(q;K)]^{\tau_2\tau_3}_{\alpha_2\alpha_3}\, \Delta^{0^+}(K)\, [\mathcal{A}^{0^+}(l;P)u(P)]^{\tau_1}_{\alpha_1}, \tag{5.8}$$

where the spinor satisfies the Euclidean Dirac equation

$$(i\gamma \cdot P + M)\, u(P) = 0 = \bar{u}(P)\, (i\gamma \cdot P + M), \tag{5.9}$$

with M being the mass obtained by solving the Faddeev equation. Here, $K_{\{ij\}} = k_i + k_j$, $q_{[ij]} = k_i - k_j$, $l_{\{ij\}y} := (-K_{ij} + 2k_y)/3$, Δ^{0^+} represents the pseudoparticle propagator for the scalar diquark formed from quarks 1 and 2, and Γ^{0^+} is the Bethe-Salpeter Amplitude (BSA) of the scalar diquark. K, q, and l the diquark momentum, the diquark's internal momentum difference, and the remaining momentum dependence respectively have been chosen as our momentum basis in part because of the nice property that in Euclidean space they are real, which will be elaborated further later in this chapter. Further, they are imparted with the subscript labels $\{ij\}$, $[ij]$, and $\{ij\}y$ respectively in order to allow for all possible ways of forming a diquark out of the three quarks available. Furthermore, $\mathcal{A}$, a 4×4 Dirac matrix, is

the BSA of the quark-diquark system. Ensuring that $\mathcal{A}^{0^+}(l;P)$ represents a positive energy nucleon implies

$$\mathcal{A}^{0^+}(l;P) = \sum_{n=1}^{2} c_{\mathcal{A}}^{0^+;n}(l;P)\; T_{\mathcal{A}}^{0^+;n}(l;P)\,, \tag{5.10}$$

$$T_{\mathcal{A}}^{0^+;1}(l;P) = 1, \quad T_{\mathcal{A}}^{0^+;2}(l;P) = (i\gamma\cdot l - l\cdot\hat{P}\,) \tag{5.11}$$

where $(I_{\rm D})_{rs} = \delta_{rs}$, $\hat{\ell}^2 = 1$, $\hat{P}^2 = -1$. In the nucleon rest frame, $s_{1,2}$ describe, respectively, the upper, lower component of the bound-state nucleon's spinor.

5.2 . The Euclidean Model

Although the objects this thesis seeks to compute exist on the lightcone, the tensorial structures presented, as well as the rest of the associated computation, will take place in Euclidean spacetime. Fundamentally, this is because the solutions to the Faddeev equations used were computed in Euclidean space. A three-body relativistic equation of state, the Faddeev equation gives rise to solutions named Faddeev amplitudes.

5.2.1 . Issues with Going to the Lightcone

To continue quantities defined in Minkowski space with the metric $\eta_{\mu\nu} = \delta_{\mu,0}\delta_{\nu,0} - \sum_{i=1}^{3}\delta_{\mu,i}\delta_{\nu,i}$ into Euclidean space one requires an entirely positive definite or negative definite metric. As a consequence we choose to perform such a continuation by defining $l_{4;E} \equiv -il_{0;M}$ and writing previously Minkowski vectors as Euclidean vectors using such a convention as

$$l_M = (l_{0;M}, \vec{l}) \to l_E = (\vec{l}, l_{4;E} = -il_{0;M}) \tag{5.12}$$

where M and E are subscripts labeling Minkowskian and Euclidean vectors respectively, and which we will often drop when facilitated by context clues for ease of legibility.
This kind of coordinate transformation is often called a "Wick rotation", and is used in lattice field theory as well as in continuum techniques due to its tendency to send Minkowskian propagators with poles on the real axis in momentum space integrands to Euclidean propagators with poles off the real axis in the complex plane as

$$S_M(k_M) = \frac{f_M(k_M)}{k_M^2 - \mu^2} \to S_E(k_E) = \frac{f_E(k_E)}{k_E^2 + \mu^2}, \tag{5.13}$$

where the subscripts M and E label Minkowskian and Euclidean objects, respectively, whereas to avoid confusion the propagator mass is given by μ, and

$f_{M;E}$ represents a general propagator numerator which depends on the spin of the excitation in question.
Some have employed Euclidean space techniques to solve the Faddeev equation, rather than solve it directly in Minkowski space to avoid once again poles on the real axis in momentum space [110, 111]. However, once such a solution is computed numerically, Wick rotating in the opposite direction to recover Minkowskian results from Euclidean ones is a highly nontrivial task. This is due to conceivably hidden pole structures in the complex plane.

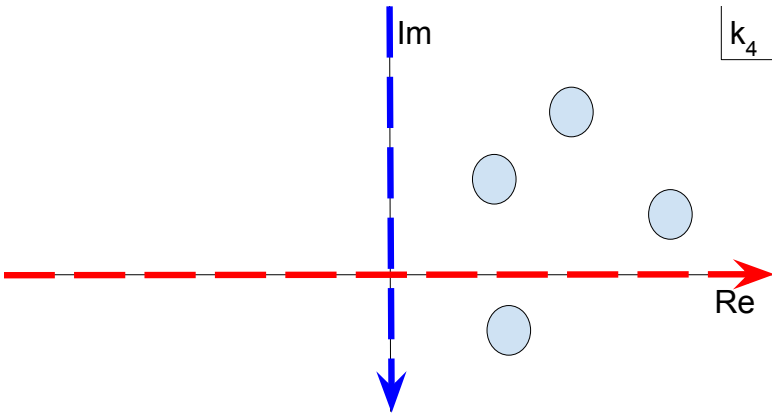

Figure 5.3: One contour of integration which may be used to relate the integral over the real axis and that over the imaginary axis is shown. Points representing possible problematic pole locations are shown as well. If these poles are not present (i.e. the function is analytic inside and on the integration contour), then no such problems arise.

As shown in Fig. 5.3, Wick rotation relates integration over the real and imaginary axes by closing a contour in the complex plane at infinity in two quadrants of the complex plane. Integration along the contour is divided into four pieces. I_1 and I_3 represent the contributions to the integral I from the real and imaginary axes, respectively. I_2 and I_4 represent the contributions to the integral I from the quarter-circle terms (which are taken with infinite radius R, corresponding to $I_{1;3}$ representing integrations over entire axes) which vanish if the integrand decreases towards zero as the radius R goes to infinity. When the integrand is analytic everywhere in the complex plane, one can relate the two resulting integrals as

$$I = \lim_{R\to\infty} \sum_{i=1}^{4} I_i = \lim_{R\to\infty} \sum_{j=1}^{2} I_{2j-1} = 0. \tag{5.14}$$

However, if the integrand possesses poles in the two quadrants in question, one must modify the previous relation of the two integrals using the residue

theorem as

$$I = \lim_{R\to\infty} \sum_{i=1}^{4} I_i = \lim_{R\to\infty} \sum_{j=1}^{2} I_{2j-1} = \text{Residue Contribution.} \tag{5.15}$$

The situation in the presence of branch cuts or other singular or pathological behaviors is even more complicated and we do not enter the details here. However, the bottom line is that with a mere numerical solution in Euclidean space, i.e. without an algebraic functional form in hand, one simply cannot compute the corresponding Minkowskian result, even numerically, as one is unaware of the pole structure in the quadrants in which the contributions $I_{2;4}$ are computed.
This issue is compounded when considering the previously introduced lightcone coordinates. The $\pm$ coordinates of a vector in lightcone coordinates correspond to the extents of that vector as projected onto two light-like vectors, say p and n. That is

$$l_M = l^+ n + l^- p + \sum_{i=1}^{2} l_i \hat{e}_i, \tag{5.16}$$

where the $\hat{e}_i$ is a basis vector for the ith transverse direction. The important point here is that the lightcone basis vectors p and n, being light-like, square to 0, which does not change when going to Euclidean space. However, whereas in Minkowski space one has access to infinitely many vectors of norm 0, Euclidean space possesses only a single vector, the zero vector, unless one is willing to go to complex coordinates which we do not enter here and, numerically, would require modeling in higher dimensions. As a consequence, any practical Euclidean space numerical methods employed in the state of the art today will face such an issue of "going to the lightcone", in the sense that results computed numerically in Euclidean space, such as solutions to the Faddeev equation, cannot be directly brought to the lightcone, as full reconstruction of the behavior of such an amplitude in a two dimensional subspace from its value at a single point requires access to information impossible to contain at such a single point [111].

5.3 . Mellin Reconstruction

Given the previously stated issues with going to the lightcone directly from a computation performed in Euclidean space, it will be necessary to be clever when attempting to set the lightcone time arguments of our Faddeev amplitude expressions to zero. That is, we want to transform Faddeev amplitudes into LFWFs, amplitudes defined on the lightcone, by performing integration

with respect to some parameters. In Minkowski space we would like to compute

$$\Psi(x_1, \vec{k}_{1\perp}; x_2, \vec{k}_{2\perp}) = N \int \mathrm{d}k^-_{1;M} \mathrm{d}k^-_{2;M} \chi(k_{1;M}, k_{2;M}), \tag{5.17}$$

for some normalization N. Given that we work instead in Euclidean space, we use a trick. We write down a kernel allowing us to trade x dependence for m dependence, referred to as a Mellin moment computation of order m. Because of momentum conservation, only two momentum fractions x_i out of the possible three are independent. There, to reconstruct on the lightcone, we perform such a transform in both the 1 and 2 momentum variables [112]. This is performed in order to exploit Mellin moment uniqueness to avoid messy contour integration. The Mellin moment of order m of the function f is given by

$$\int \mathrm{d}x x^m f(x), \tag{5.18}$$

where the integration bounds are $0 \leq x \leq 1$. Digressing further, in non-pathological cases two functions all of whose Mellin moments are identical are equivalent [113]. That is

$$\begin{aligned} \int \mathrm{d}x x^m f(x) &= \int \mathrm{d}x x^m g(x), \quad \forall m \in \mathbb{N} \\ \Rightarrow f(x) &= g(x). \end{aligned} \tag{5.19}$$

For a given longitudinal momentum fraction x_i, expressing this as a momentum fraction according to Eq. (2.20) and rewriting in terms of the Euclidean variables, it can be expressed as

$$x_i^{m_i} \equiv \frac{(k_{E;i} \cdot n_E)^{m_i}}{(P_E \cdot n_E)^{m_i}}, \tag{5.20}$$

where it is simply necessary to know that the nilpotent vector $n_E^2 = 0$ projects vectors onto their $+$ lightcone components. In the next subsection of this section, the uniqueness of Mellin moments will be stated. This will allow us to reconstruct the $x_{1,2}$ dependence of the LFWFs via the relation

$$\begin{aligned} &\int_0^1 \mathrm{d}x_1 \int_0^{1-x_1} \mathrm{d}x_2 x_1^{m_1} x_2^{m_2} \Psi(x_1, \vec{k}_{1\perp}; x_2, \vec{k}_{2\perp}) \\ \equiv\ &\text{Normalization} \int \mathrm{d}k^3_{1;E} \mathrm{d}k^4_{1;E} \mathrm{d}k^3_{2;E} \mathrm{d}k^4_{2;E} \frac{(k_{E;1} \cdot n_E)^{m_1}}{(P_E \cdot n_E)^{m_1}} \frac{(k_{E;2} \cdot n_E)^{m_2}}{(P_E \cdot n_E)^{m_2}} \\ &\mathrm{Tr}_{\text{Dirac}} \Big\{ \Gamma_{\text{Proj.}} \chi(k_{1;E}, k_{2;E}) \Big\}, \end{aligned} \tag{5.21}$$

which is the Mellin moment reconstruction employed in [112, 112], and where $\Gamma_{\text{Proj.}}$ is a Dirac structure designed to project out the relevant contribution. In the following subsection we will then discuss how this method can be used to reconstruct the x dependence from the Euclidean Faddeev amplitudes.

5.3.1 . Identification of Mellin Variables

We demonstrate the computation of the fundamental contributions to the six light front wave functions mentioned previously by employing a Euclidean quark-diquark correlation model of the nucleon. Our approach involves the introduction of tensorial structures, which we then contract to obtain an entity that transforms akin to our target matrix element. Subsequently, we determine the Mellin moments of this entity on the lightcone concerning its longitudinal momenta. By projecting the resultant tensorial structures, we extract their contributions to the (LFWFs). Let's define the quark propagator as:

$$S(p) = \big[-i\gamma\cdot p + M_q\big] D_{M_q}(p^2), \tag{5.22}$$

$$D_M(s) = \frac{1}{s+M^2}, \tag{5.23}$$

and a Nakanishi ([114]) representation of the diquark vertex using the basis l and q given below:

$$\eta_0\Gamma^0_\mu C^\dagger = i\gamma_5\int_{-1}^{1}\mathrm{d}z\rho_\nu(z)D_{\Lambda_q}(q_z), \tag{5.24}$$

where ρ_ν is a polynomial [115] and we define

$$q_z = q+\frac{z}{2}(\frac{2}{3}P-\ell)., \tag{5.25}$$

We also define the diquark propagator in terms of the diquark momentum K and a Nakanishi representation of the quark-diquark correlation s_1 as follows:

$$\Delta^{0+}(K) = \frac{1}{K^2+\widetilde{M^2}}, \tag{5.26}$$

$$s_1 = i\eta\int_{-1}^{+1}\mathrm{d}z,\tilde{\rho}(z)[\frac{1}{(\ell_z^2+\Lambda_N^2)}]^3, \tag{5.27}$$

$$\tag{5.28}$$

where $\tilde{\rho}(z)$ is a distinct polynomial, and

$$P \equiv (0,0,0,iM_N) = \sum_{i=1}^{3}k_i \tag{5.29}$$

$$k_i \equiv \frac{P}{3}+\ell = \frac{K}{2}+\frac{3\ell}{2} \tag{5.30}$$

$$k_j \equiv \frac{P}{3}-\frac{\ell}{2}+q = \frac{K}{2}+q \tag{5.31}$$

$$k_k \equiv \frac{P}{3}-\frac{\ell}{2}-q = \frac{K}{2}-q, \tag{5.32}$$

where we now use a positive-definite metric and where we have omitted quark number indices on K, q, and ℓ. Next, we decompose the Faddeev wave

function into three diquark contributions. To work with a general example, we will perform this computation in the case that quark 1 is not included in the diquark, that is the diagram-dependent indices i, j, k labeling the three quarks in Eq. (5.32) given by $i = 1$, $j = 2$, $k = 3$. The corresponding projected Faddeev amplitude is given by:

$$\chi^{\uparrow,\downarrow,\uparrow}_{\alpha_3;\sigma} = S(k_2)_{\alpha_2\alpha_2'}[\Gamma^0(q,K)]_{\alpha_2'\alpha_3'}S(k_3)_{\alpha_3\alpha_3'}\Delta_0 S^T(k_1)_{\alpha)_1'\alpha_1}\mathcal{S}_{\alpha_1',\sigma}. \tag{5.33}$$

The projected wave function in the scalar case is expressed as:

$$\begin{aligned}\chi^{h_1,h_2,h_3}_{\alpha_1\alpha_2\alpha_3;\sigma} = \quad & (\not{n}L^{\uparrow}_{\alpha_3'\alpha_3}S_{\alpha_3\lambda}(k_3)\Gamma^{0T}_{\lambda\lambda'}S^T_{\lambda'\alpha_2}(k_2) \\ & \times(L^{\downarrow}\not{n}^T(C^\dagger)^T L^{\uparrow})_{\alpha_2\alpha_1}S_{\alpha_1\alpha_1'}(k_1)\mathcal{S}_{\alpha_1'\sigma}\Delta(k_2+k_3).\end{aligned} \tag{5.34}$$

To extract the leading twist operator part of this matrix, we project on γ^ν as follows:

$$\begin{aligned}&\frac{1}{4}\gamma_\nu \mathrm{Tr}[\gamma^\nu \not{n}L^{\uparrow}S(k_3)\Gamma^{0T}S^T(k_2)(L^{\downarrow}\not{n}^T(C^\dagger)^T L^{\uparrow}S(k_1)\mathcal{S}]\Delta(k_2+k_3) \\ &= \frac{1}{4}\gamma_\nu \mathrm{Tr}[(2n^\nu - \not{n}\gamma^\nu)S(p_3)\Gamma^{0T}S^T(k_2)(L^{\downarrow}C(-)\not{n}L^{\uparrow}\sigma_S(k_1)]s_1(\ell,P)\Delta(k_2+k_3) \\ &= \frac{1}{2}\gamma_\nu n^\nu \mathrm{Tr}[S(k_3)\Gamma^{0T}S^T(k_2)L^{\downarrow}C^\dagger\not{n}L^{\uparrow}]\sigma_S(k_1)s_1(\ell,P)\Delta(k_2+k_3) \\ &= \frac{1}{4}\gamma_\nu \mathrm{Tr}[S(k_3)\Gamma^{0T}S^T(k_2)L^{\downarrow}C^\dagger\not{n}L^{\uparrow}]\mathrm{Tr}[\gamma^\nu\not{n}L^{\uparrow}S(k_1)s_1(\ell,P)]\Delta(k_2+k_3)\end{aligned}$$
. (5.35)

Consequently, we obtain a trace dependent on the internal diquark constituent and a trace on the remaining quark and nucleon quark-diquark Bethe-Salpeter Amplitude.
Let's start evaluating the trace associated with the diquark:

$$\begin{aligned}&\mathrm{Tr}[C^\dagger\not{n}\frac{1+\gamma_5}{2}(-i\gamma\cdot(\frac{(\frac{2}{3}P-\ell)}{2}-q)+M)i\gamma_5 \\ &\times C^\dagger(-i\gamma\cdot(q+\frac{\frac{2}{3}P-\ell}{2})+M)^T(\frac{1-\gamma_5}{2})]\end{aligned} \tag{5.36}$$

$$= \quad 2M(\frac{2}{3}P-\ell)\cdot n = 2MK\cdot n, \tag{5.37}$$

where we utilized:

$$C^\dagger\gamma_\mu^T C = -\gamma_\mu, \tag{5.38}$$

with $C^\dagger = C^T = -C$. Next, let's handle the denominator and introduce the Feynman parameters u, v, and y, leading to the following expression: with

$$\beta = u - v + yz. \tag{5.39}$$

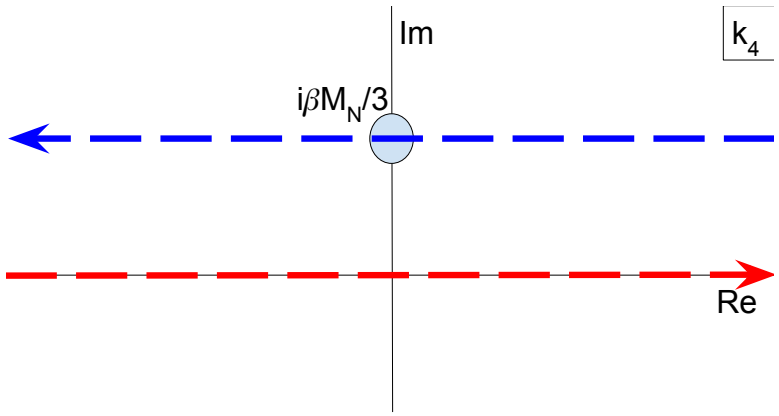

Figure 5.4: The contour of integration is intended to be understood as closed at infinity on the left and right. The resulting shift off of the real axis as explained in Subsec. 5.2.1 is valid provided that there are no other poles (controlled by the masses and Nakanishi Λ parameters) in the strip between the red and blue arrows.

Given that $P = (0, 0, 0, iM_N)$, we analyze the integral in the complex plane of q_4 before shifting it (see Fig. 5.4). We introduce:

$$k'_4 = \bar{k_4} + i\beta\frac{M_N}{3}, \tag{5.40}$$

with $\bar{k}_4 = q_4 - \frac{\beta}{2}\ell$ real. This results in:

$$\begin{array}{rcl} \Re(k'^2_4) & = & \bar{k}^2_4 - \beta^2\frac{M_N^2}{9} \\ \Im(k'^2_4) & = & 2\bar{k}_4\beta\frac{M_N}{3}, \end{array} \tag{5.41}$$

where $\Re(z)$ is the real part of an arbitrary complex number z. We search for poles in the k'_4 complex plane, which occur if and only if:

$$\begin{array}{rcl} \bar{k}^2_4 - \beta^2\frac{M_N^2}{9} + (u+v)M^2 + y\Lambda_q^2 + (u+v+yz^2-\beta^2)\frac{\ell^2-\frac{4}{9}M_N^2}{4} & = & 0 \\ 2\bar{k}_4\beta\frac{M_N}{3} + (u+v+yz^2-\beta^2)\frac{\ell_4-\frac{4}{3}M_N}{4} & = & 0. \end{array} \tag{5.42}$$

It is noted that $(u + v + yz^2 - \beta^2)$ is always positive:

$$\begin{array}{rl} & u+v+yz^2-\beta^2 \\ = & u(1-u)+v(1-v)+z^2(1-u-v)(u+v) \\ & -(2u(1-u-v)z - 2(u+(1-u-v)z)v) \\ = & u(1-u)(1-z)^2 + v(1-v)(1+z)^2 + 2uv(1-z^2) > 0. \end{array} \tag{5.43}$$

The condition for the real part, in the most extreme case of $\ell = 0$, yields:

$$\bar{k}^2_4 + (u+v)M^2 + y\Lambda_q^2 - (u+v+yz^2)\frac{M_N^2}{9} = 0. \tag{5.44}$$

Thus, for M and Λ_q larger than $M_N/3$, the condition is never satisfied and no poles cross the integration line of k_4'. Hence, we assume this condition for this example calculation. The complex conjugate poles remain on either side of the k_4' line, allowing us to close the contour through the real axis, resulting in a real integral. We introduce $\bar{\beta} = \frac{1-\beta}{2}$ such that $0 < \bar{\beta} < 1$. As $n^2 = 0$, the only non-zero contribution is from $(K \cdot n)^{m_2}$, leading to:

$$\begin{aligned} I &= \frac{(K\cdot n)^{m_2+1}}{(P\cdot n)^{m_2}} \frac{2\pi}{(2\pi)^2} \int_{-1}^{1} \mathrm{d}z \int \mathrm{d}\bar{\beta}\mathrm{d}u\mathrm{d}v \frac{4M}{1-u-v} \rho_\nu(z)(1-u-v)^{\nu-1} \\ &\times \frac{1}{2}\frac{\Gamma(2+\nu)\Gamma(\nu+1)}{\Gamma(\nu+2)\Gamma(\nu)} \bar{\beta}^{m_2} \Big((q_\perp - \frac{1-2\bar{\beta}}{2}\ell_\perp)^2 + (u+v)M^2 + y\Lambda_q^2 \\ &+ (u+v+(1-u-v)z^2 - (1-2\bar{\beta})^2) \frac{(\frac{2}{3}P-\ell)^2}{4} \Big)^{-(\nu+1)}. \end{aligned} \tag{5.45}$$

A this point, defining $\bar{u} = 1-u$, we can then define an effective mass M_{eff}^2 and effective momentum $q_\perp^{\text{eff}}$ such that:

$$\begin{aligned} M_{\text{eff}}^2 &= 4\frac{(1-\bar{u}+v)M^2 + (\bar{u}-v)\Lambda_q^2}{(1-\bar{u}+v+(\bar{u}-v)z^2 - (1-2\bar{\beta})^2)} \\ &= \frac{(1-\bar{u}+v)M^2 + (\bar{u}-v)\Lambda_q^2}{(\bar{\beta}(v(\bar{\beta}-2)+\bar{\beta}) + \bar{u}(v-\bar{\beta}^2))}(\bar{u}-v), \end{aligned} \tag{5.46}$$

$$(q_\perp^{\text{eff}})^2 = 4\frac{(q_\perp - \frac{1-2\bar{\beta}}{2}\ell_\perp)^2}{(u+v+yz^2-\beta^2)} = \frac{(q_\perp - \frac{1-2\bar{\beta}}{2}\ell_\perp)^2}{(\bar{\beta}(v(\bar{\beta}-2)+\bar{\beta}) + \bar{u}(v-\bar{\beta}^2))}(\bar{u}-v), \tag{5.47}$$

and the previous integrals can be written as:

$$\begin{aligned} I &= \frac{1}{(2\pi)}\frac{(K\cdot n)^{m_2+1}}{(P\cdot n)^{m_2}} \int_{-1}^{1} \mathrm{d}z \int \mathrm{d}\bar{\beta}\mathrm{d}\bar{u}\mathrm{d}v \rho_\nu(z_\nu)(\bar{u}-v)^{2\nu-1} 2M \frac{\Gamma(1+\nu)}{\Gamma(\nu)} \\ &\times [(\bar{\beta}(v(\bar{\beta}-2)+\bar{\beta}) + \bar{u}(v-\bar{\beta}^2)]^{-\nu-1} [M_{eff}^2 + K^2]^{-\nu-1} \bar{\beta}^{m_2}. \end{aligned} \tag{5.48}$$

We then continue

$$\frac{1}{4}\mathrm{Tr}[\not{n}\frac{1+\gamma_5}{2}(-i(P-K)\cdot\gamma + M)\gamma^\mu]\gamma_\mu = \frac{1}{2}M\not{n}. \tag{5.49}$$

We can apply the same Feynman parametrization technique as previously.

$$
\begin{aligned}
&(P\cdot n)^{-m_1}\int_{-1}^{1}\mathrm{d}\tilde{z}\int[\mathrm{d}a_i]\frac{i}{2}M^2\not{n}(k_1\cdot n)^{m_1}\tilde{\rho}(\tilde{z})[(2/3P-\ell)^2+\widetilde{M}^2]^{-1}\\
&\times[(\ell-\frac{1+3\tilde{z}}{6}P)^2+\Lambda_N^2]^{-\sigma}[(\ell+P/3)^2+M^2]^{-1}\\
&\times[M_{\text{eff}}^2+(q_\perp^{\text{eff}})^2+(2/3P-\ell)^2]^{-(\nu+1)}
\end{aligned}
\tag{5.50}
$$

$$
\begin{aligned}
=\;&(P\cdot n)^{-m_1}\int_{-1}^{1}\mathrm{d}\tilde{z}\int[\mathrm{d}a_i]\frac{i}{2}M^2\not{n}(k_1\cdot n)^{m_1}\tilde{\rho}a_2^{\sigma-1}a_4^{\nu}\delta(1-a_1-a_2-a_3-a_4)\\
&\times\frac{\Gamma(\sigma+3+\nu)}{\Gamma(\sigma)\Gamma(\nu+1)}\Big((\ell-\alpha\frac{P}{3})^2+a_1M^2+a_2\Lambda_N^2+a_3\widetilde{M}^2+a_4(M_{eff}^2+(q_\perp^{\text{eff}})^2)\\
&+(a_1+a_2(\frac{1+3\tilde{z}}{2})^2+4a_3+4a_4-\alpha^2)\frac{P^2}{9}\Big)^{-(\sigma+3+\nu)},\\
=\;&(P\cdot n)^{-m_1}\int_{-1}^{1}\mathrm{d}\tilde{z}\int[\mathrm{d}a_i]\frac{i}{2}M^2\not{n}(k_1\cdot n)^{m_1}\tilde{\rho}a_2^{\sigma-1}a_4^{\nu}\delta(1-a_1-a_2-a_3-a_4)\\
&\times\frac{\Gamma(\sigma+3+\nu)}{\Gamma(\sigma)\Gamma(\nu+1)}\Big((\ell-\alpha\frac{P}{3})^2+M_N^2(a_1(\frac{M^2}{M_N^2}-\frac{1}{9})+a_2(\frac{\Lambda_N^2}{M_N^2}-\frac{(1+3\tilde{z})^2}{36})\\
&+a_3(\frac{\widetilde{M}^2}{M_N^2}-\frac{4}{9})+a_4(\frac{M_{eff}^2+(q_\perp^{\text{eff}})^2}{M_N^2}-\frac{4}{9})+\frac{\alpha^2}{9})\Big)^{-(\sigma+3+\nu)},
\end{aligned}
\tag{5.51}
$$

with $[\mathrm{d}a_i]=\mathrm{d}a_1\mathrm{d}a_2\mathrm{d}a_3\mathrm{d}a_4$ and we make the change of variables $\alpha=-a_1+a_2\frac{1+3\tilde{z}}{2}+2a_3+2a_4$. Just like in the case of the scalar diquark, we are now facing an integral in the ℓ_4 complex plane. In analogy with the previous case, mass ratios such that:

$$
\begin{aligned}
&(\frac{M^2}{M_N^2}-\frac{1}{9})>0, \qquad (\frac{\Lambda_N^2}{M_N^2}-\frac{(1+3z)^2}{36})>0,\\
&\frac{\widetilde{M}^2}{M_N^2}-\frac{4}{9})>0, \qquad (\frac{M_{eff}^2}{M_{N^2}}-\frac{4}{9})>0,
\end{aligned}
\tag{5.52}
$$

would guarantee the absence of poles. Only the last one cannot be tuned anymore and requires further study. We investigate the most extreme case by setting $\vec{k}_{1,2\perp}=\vec{0}_\perp$.

$$
M_{eff}^2=\frac{(\bar{u}-v)(1-\bar{u}+v)M^2+(\bar{u}-v)\Lambda_q^2)}{v\bar{\beta}(\bar{\beta}-2)+\bar{u}(v-\bar{\beta}^2)+\bar{\beta}^2}.
\tag{5.53}
$$

$$
\begin{aligned}
\frac{\partial M_{eff}^2}{\partial\bar{u}}&=\frac{(v-\bar{\beta})^2M^2+(\bar{u}-v)(\Lambda_q^2-M^2)(2\bar{\beta}^2+\bar{u}(v-\bar{\beta}^2+v\bar{\beta}^2-4v\bar{\beta}+v^2)}{[v\bar{\beta}(\bar{\beta}-2)+\bar{u}(v-\bar{\beta}^2)+\bar{\beta}^2]^2}\\
&=((v-\bar{\beta})^2M^2+(\bar{u}-v)(\Lambda_q^2-M^2))[(\bar{\beta}(1-\bar{u})+(\bar{\beta}-v))(\bar{\beta}-v)
\end{aligned}
\tag{5.54}
$$

$$
\begin{aligned}
&+v(\bar{u}-\bar{\beta})(1-\bar{\beta})][v\bar{\beta}(\bar{\beta}-2)+\bar{u}(v-\bar{\beta}^2)+\bar{\beta}^2]^{-2}\\
&>0 \quad \text{for} \quad \Lambda_q^2\geq M^2.
\end{aligned}
\tag{5.55}
$$

Computing the gradient, one realizes that the minimum value is obtained for either $\bar{u}$ or v equal to $\bar{\beta}$ if we assume $\Lambda_q^2 \geq M^2$. We therefore have for $\bar{u} = \bar{\beta}$:

$$M_{eff}^2 \geq \frac{M^2}{\bar{\beta}(1-\bar{\beta})} + (\bar{\beta} - v)\frac{\Lambda_q^2 - M^2}{\bar{\beta}(1-\bar{\beta})} \geq \frac{4}{9}M_N^2 \quad \text{since} \quad M^2 \geq \frac{1}{9}M_N^2. \tag{5.56}$$

Consequently, the pole structure allows us to close the Cauchy contour on the real axis, and we therefore end up with a real-valued integral. We now introduce $\bar{\alpha} = (1+\alpha)/3$, $\bar{a}_1 = 1 - a_1$ and $a_{34} = a_3 + a_4$. Introducing also:

$$\lambda = \frac{(1+3\tilde{z})^2}{36} = \frac{1}{36}(3(2\frac{(\bar{\alpha} - a_{34})}{\bar{a}_1 - a_{34}} - 1) + 1)^2. \tag{5.57}$$

We obtain in the end:

$$\begin{aligned}
J &= i\not{\pi}\int [df]\frac{M^2}{2}\frac{2\pi}{(2\pi)^2}\tilde{\rho}\rho_\nu \frac{2}{\bar{a}_1 - a_{34}}(\bar{a}_1 - a_{34})^{\sigma-1}(a_{34} - a_3)^\nu \\
&\times \frac{\Gamma(\sigma+3+\nu)}{\Gamma(\sigma)\Gamma(\nu+1)}\frac{1}{2}\frac{\Gamma(\sigma+\nu+2)}{\Gamma(\Gamma(\sigma+\nu+3)}\bar{\alpha}^{m_1}(1-\bar{\alpha})^{m_2+1}\bar{\beta}^{m_2} \\
&\times \Big[\ell_\perp^2 + M_N^2(1-\bar{a}_1)(\frac{M^2}{M_N^2} - \frac{1}{9}) + M_N^2(\bar{a}_1 - a_{34})(\frac{\Lambda_N^2}{M_N^2} - \lambda) \\
&+ a_3 M_N^2(\frac{\widetilde{M}^2}{M_N^2} - \frac{4}{9}) + (a_{34} - a_3)M_N^2(\frac{M_{\text{eff}}^2 + (q_\perp^{\text{eff}})^2}{M_N^2} - \frac{4}{9}) \\
&+ M_N^2(\bar{\alpha} - \frac{1}{3})^2\Big]^{-(\sigma+2+\nu)} \\
&\times [\bar{\beta}(v(\bar{\beta}-2) + \bar{\beta}) + \bar{u}(v - \bar{\beta}^2)]^{-\nu-1}(\bar{u} - v)^{2\nu-1}\frac{\Gamma(\nu+1)}{\Gamma(\nu)}\frac{1}{2\pi}
\end{aligned} \tag{5.58}$$

with:

$$\int [\mathrm{d}f] = \int_0^1 \mathrm{d}\bar{\alpha}\int_0^1 \mathrm{d}\bar{\beta}\int_0^{\bar{\beta}} \mathrm{d}v \int_{\bar{\beta}}^1 \mathrm{d}\bar{u}\int_0^{\bar{\alpha}} \mathrm{d}a_{34}\int_{\bar{\alpha}}^1 \mathrm{d}\bar{a}_1\int_0^{a_{34}} \mathrm{d}a_3. \tag{5.59}$$

The last step is to define $\beta' = (1-\bar{\alpha})\bar{\beta}$, together with $u' = (1-\bar{\alpha})\bar{u}$ and $v' = (1-\bar{\alpha})v$. J then becomes:

$$\begin{aligned}
J &= \frac{i\not{\pi}}{(2\pi)^2}\int [df']\frac{M}{2}\tilde{\rho}\rho_\nu \frac{1}{\bar{a}_1 - a_{34}}(\bar{a}_1 - a_{34})^{\sigma-1}(a_{34} - a_3)^\nu \frac{\Gamma(\sigma+2+\nu)}{\Gamma(\sigma)\Gamma(\nu)} \\
&\times \bar{\alpha}^{m_1}(1-\bar{\alpha})\beta'^{m_2}\Big[\ell_\perp^2 + M_N^2(1-\bar{a}_1)(\frac{M^2}{M_N^2} - \frac{1}{9}) + M_N^2(\bar{a}_1 - a_{34})(\frac{\Lambda_N^2}{M_N^2} - \lambda) \\
&+ a_3 M_N^2(\frac{\widetilde{M}^2}{M_N^2} - \frac{4}{9}) \\
&+ (a_{34} - a_3)M_N^2(\frac{M_{\text{eff}}^2 + (q_\perp^{\text{eff}})^2}{M_N^2} - \frac{4}{9}) + M_N^2(\bar{\alpha} - \frac{1}{3})^2\Big]^{-(\sigma+2+\nu)} \\
&\times [\beta'(v'(\beta' - 2(1-\bar{\alpha})) + \beta'(1-\bar{\alpha})) + u'(v'(1-\bar{\alpha}) - (\beta')^2)]^{-\nu-1} \\
&\times (\bar{u}' - v')^{2\nu-1}(1-\bar{\alpha})^{\nu+1},
\end{aligned} \tag{5.60}$$

with corresponding modifications of $M_{\rm eff}$ and $q_\perp^{\rm eff}$ and with

$$\int [\mathrm{d}f'] = \int_0^1 \mathrm{d}\bar{\alpha} \int_0^{1-\bar{\alpha}} \mathrm{d}\beta' \int_0^{\beta'} \mathrm{d}v' \int_{\beta'}^{1-\bar{\alpha}} \mathrm{d}u' \int_0^{\bar{\alpha}} \mathrm{d}a_{34} \int_{\bar{\alpha}}^1 \mathrm{d}\bar{a}_1 \int_0^{a_{34}} \mathrm{d}a_3. \quad (5.61)$$

Now it is possible to invoke the uniqueness of Mellin moments to identify J with $\psi^1(\kappa)$. We identify

$$\begin{aligned} \int_0^1 \mathrm{d}x_2 \int_0^{1-x_2} \mathrm{d}x_1 x_1^{m_1} x_2^{m_2} \psi^1(\kappa) &= J(m_1, m_2, \vec{k}_{1\perp}, \vec{k}_{2\perp}) \quad (5.62) \\ &\rightarrow \quad x_1 = \bar{\alpha}, \quad x_2 = \beta', \end{aligned}$$

where for clarity we remind the reader that $\kappa_\perp$ (the set of the transverse quark momenta) is subject to the condition $\vec{0}_\perp = \sum_{r=1}^3 \vec{k}_{r\perp}$. This Mellin moment reconstruction method is one of the main tricks used in the literature to reconstruct dependence of amplitudes calculated in Euclidean space to the lightcone at equal lightcone time. One question worth asking in this situation is why we choose to integrate directly using a Dirac Delta to enforce the relationship between x and it's lightcone definition presented in Eq. (10.13). This is a subtle issue which will not be completely explored here. Suffice it to say that reconstructing $x_{1,2}$ dependence in using such a method requires intimate knowledge of the singular structure in the complex plane of the integrand, because the Dirac Delta made to enforce our constraint must contain a complex argument. This requires, for example, an extended definition of the Dirac Delta in the complex plane, which is no trivial task [116]. Some recent and impressive results using similar methods can be found here [111] for the interested reader. We are limited to integrating along a small range of contours parallel to the real axes of the Euclidean variables in this thesis, so we leave this discussion aside. Let us now move on to view some plots of $\psi^{1,-1}$, which are the first numerical results of this half of this thesis.

5.3.2 . LFWF Plots

In this section we show plots of the LFWF $\psi^{1,2;w}$ for various configurations of the transverse momenta in Figs. 5.6, 5.7, 5.8, 5.9, 5.10, 5.11.

$\lvert\vec{q}_\perp\rvert$	$\lvert\vec{l}_\perp\rvert$	θ_{ql}	n	$\lvert\vec{k}_{1\perp}\rvert$	$\lvert\vec{k}_{2\perp}\rvert$	θ_{12}
0	0	U	1	0	0	U
			2	0	0	U
			3	0	0	U
0.1	0	U	1	0	0.01	U
			2	0.01	0	U
			3	0.01	0.01	π
0	0.1	U	1	0.01	0.0025	π
			2	0.0025	$.01$	π
			3	0.0025	0.0025	0
0.1	0.1	0	1	0.01	0.0025	0
			2	0.0225	$.01$	π
			3	0.0025	0.0225	π
0.1	0.1	$\frac{\pi}{2}$	1	0.01	0.0125	2.03444
			2	0.0125	$.01$	2.03444
			3	0.0125	0.0125	2.2143
0.1	0.1	π	1	0.01	0.0225	π
			2	0.0025	$.01$	0
			3	0.0225	0.0225	π

Figure 5.5: Here we present the relationship between the magnitude of the diquark internal transverse momentum q, the magnitude of the transverse momentum l, the angle between them $\theta_{ql} \equiv \cos(\frac{\vec{q}_\perp \cdot \vec{l}_\perp}{|\vec{q}_\perp||\vec{l}_\perp|})$, and the corresponding values of the magnitudes of the tranverse momenta $k_{1,2}$ an the angle between them $\theta_{12} \equiv \cos(\frac{\vec{k}_{1\perp} \cdot \vec{k}_{2\perp}}{|\vec{k}_{1\perp}||\vec{k}_{2\perp}|})$. U, present only when one or both of the corresponding vectors are of magnitude 0, means undefined. n marks the bystander quark. The analytic versions of these relations are provided in the appendix Sec. 8.6. This correspondence depends on which quark is chosen to be the bystander i.e. which quark does not participate in the diquark correlation i.e. the diagram of those presented in Fig. 5.2, which determines which of the $\psi^{1,2;w}$ receives a contribution.

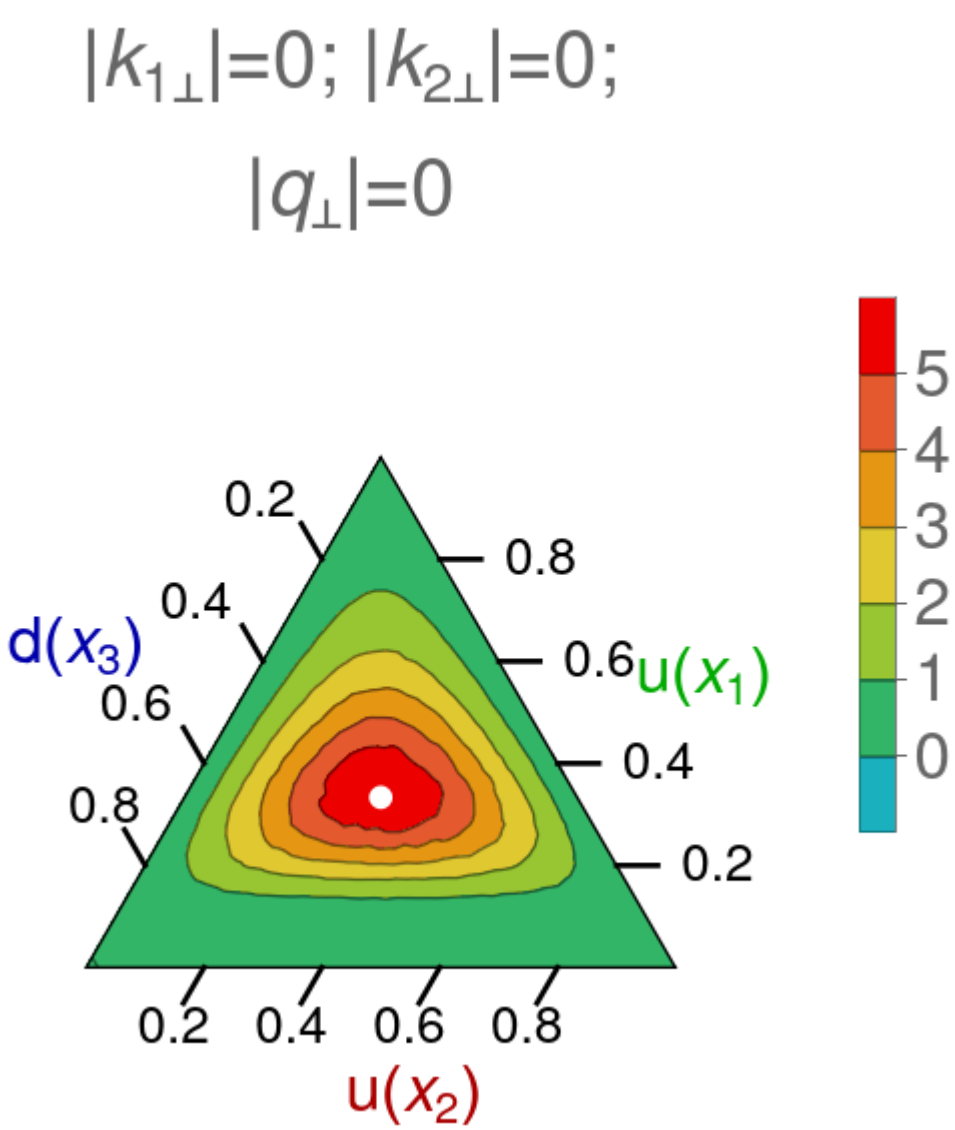

Figure 5.6: Plots of the function $\psi^{1,-1}$ for $|\vec{k}_{1\perp}| = |\vec{k}_{2\perp}| = 0$ is shown. This plot is a contour plot, given on a triangular domain due to the momentum conservational constraint $1 = \sum_{i=1}^{3} x_i$. The normalization has not been set due to any physical constraints, and is consistent among all of the LFWF plots given in this document. The normalization is calculated by computing the largest value of $\psi^{1,-1}$ among all of the computed values, and scaling all plots such that that maximum value becomes 6, in order to align with the color scales of these plots. We remind the reader that the transverse momenta are given in units of the nucleon mass M_N.

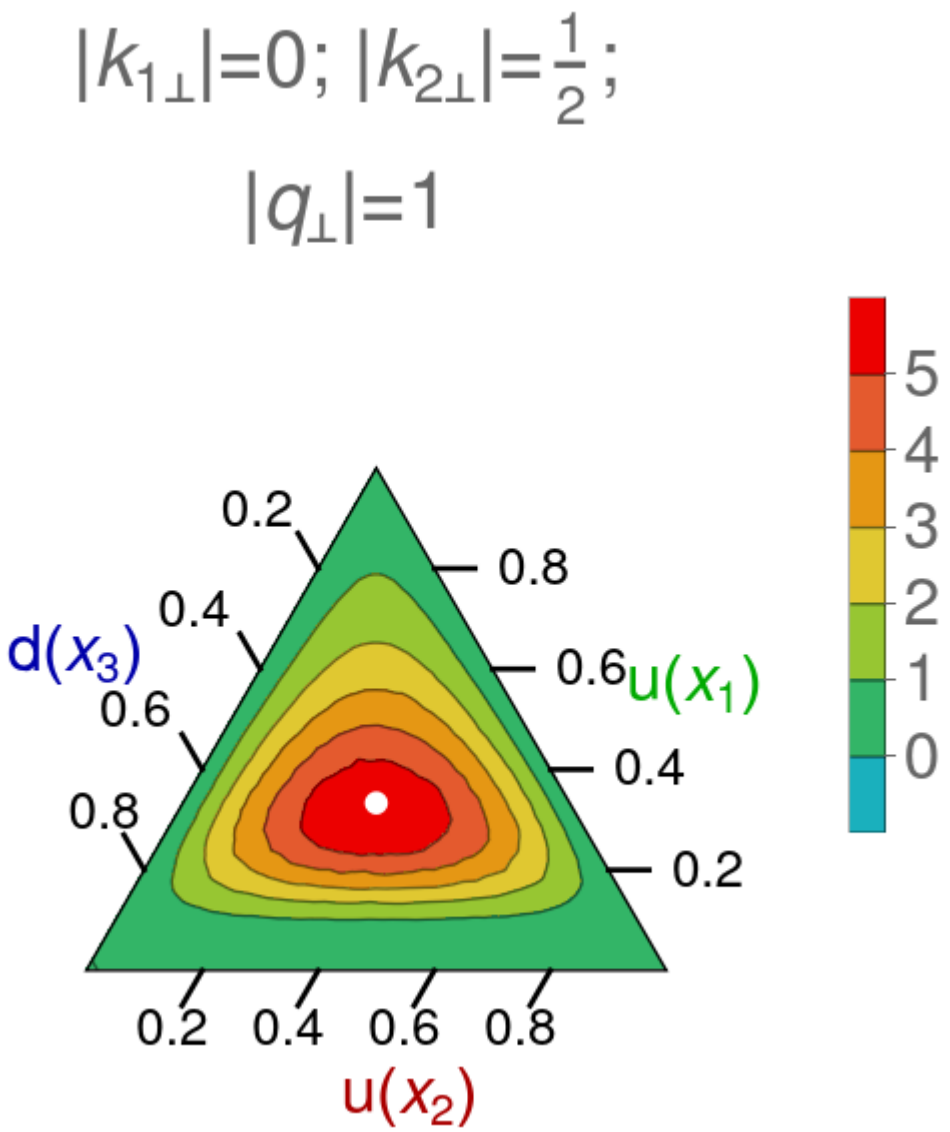

Figure 5.7: Identical to Fig. 5.6 except that $|\vec{k}_{1\perp}| = 0$, $|\vec{k}_{2\perp}| = 0.5$ is shown.

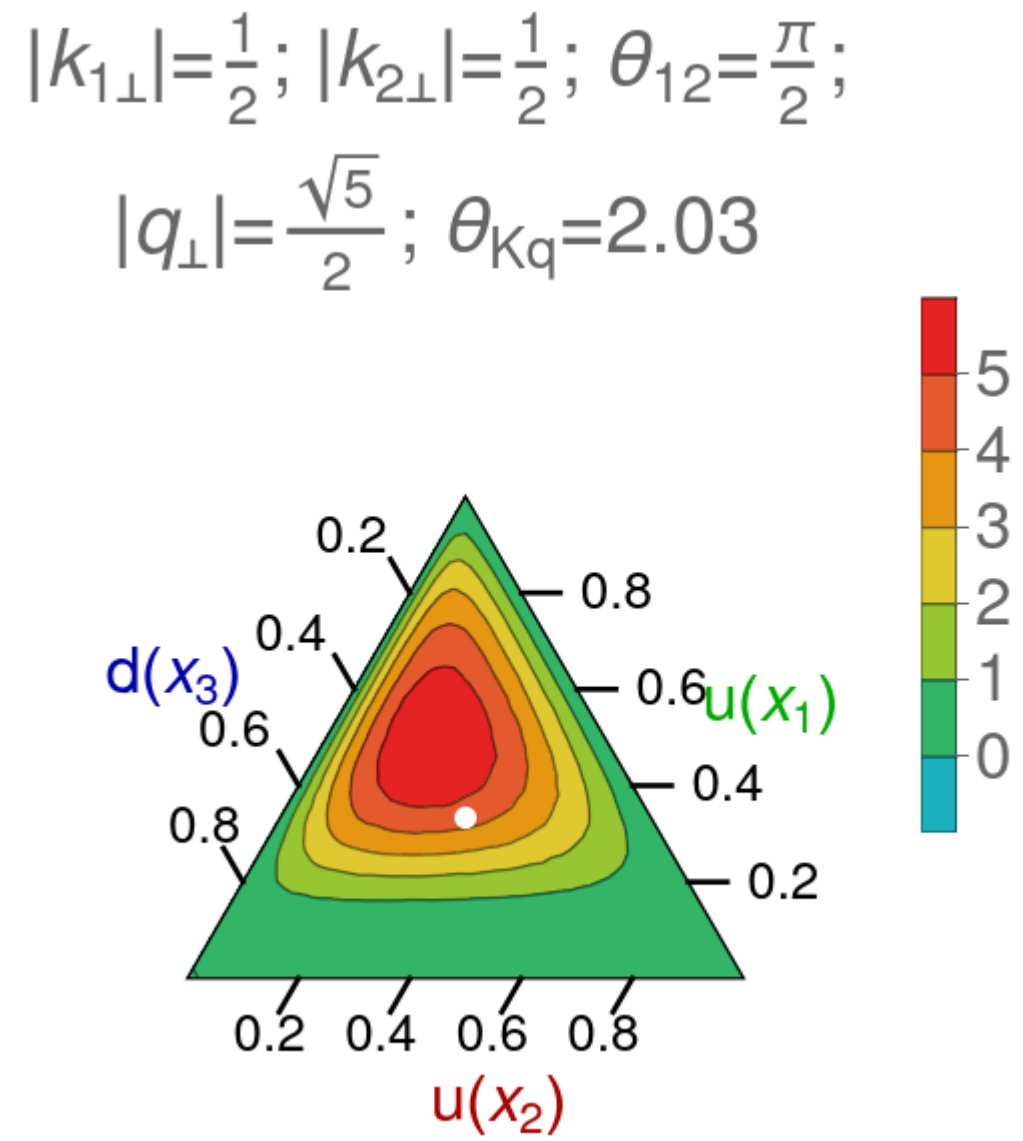

Figure 5.8: Identical to Fig. 5.6 except that $|\vec{k}_{1\perp}| = |\vec{k}_{2\perp}| = 0.5$, $\theta_{12} = 0$ is shown. θ_{Kq} is defined to be the angle between the total and internal diquark momenta, and is called the internal angle of the diquark.

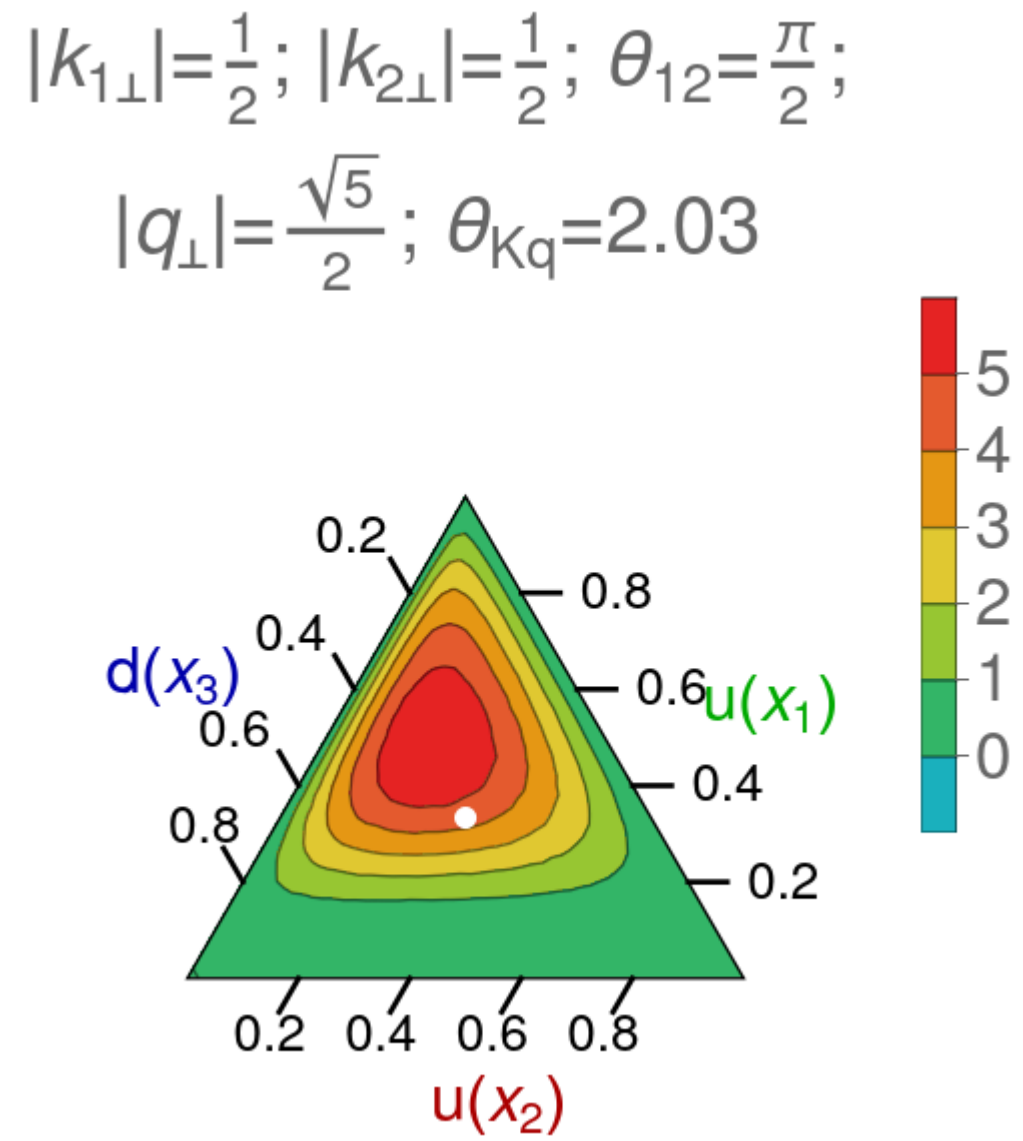

Figure 5.9: Identical to Fig. 5.6 except that $|\vec{k}_{1\perp}| = |\vec{k}_{2\perp}| = 0.5$, $\theta_{12} = \frac{\pi}{2}$ is shown.

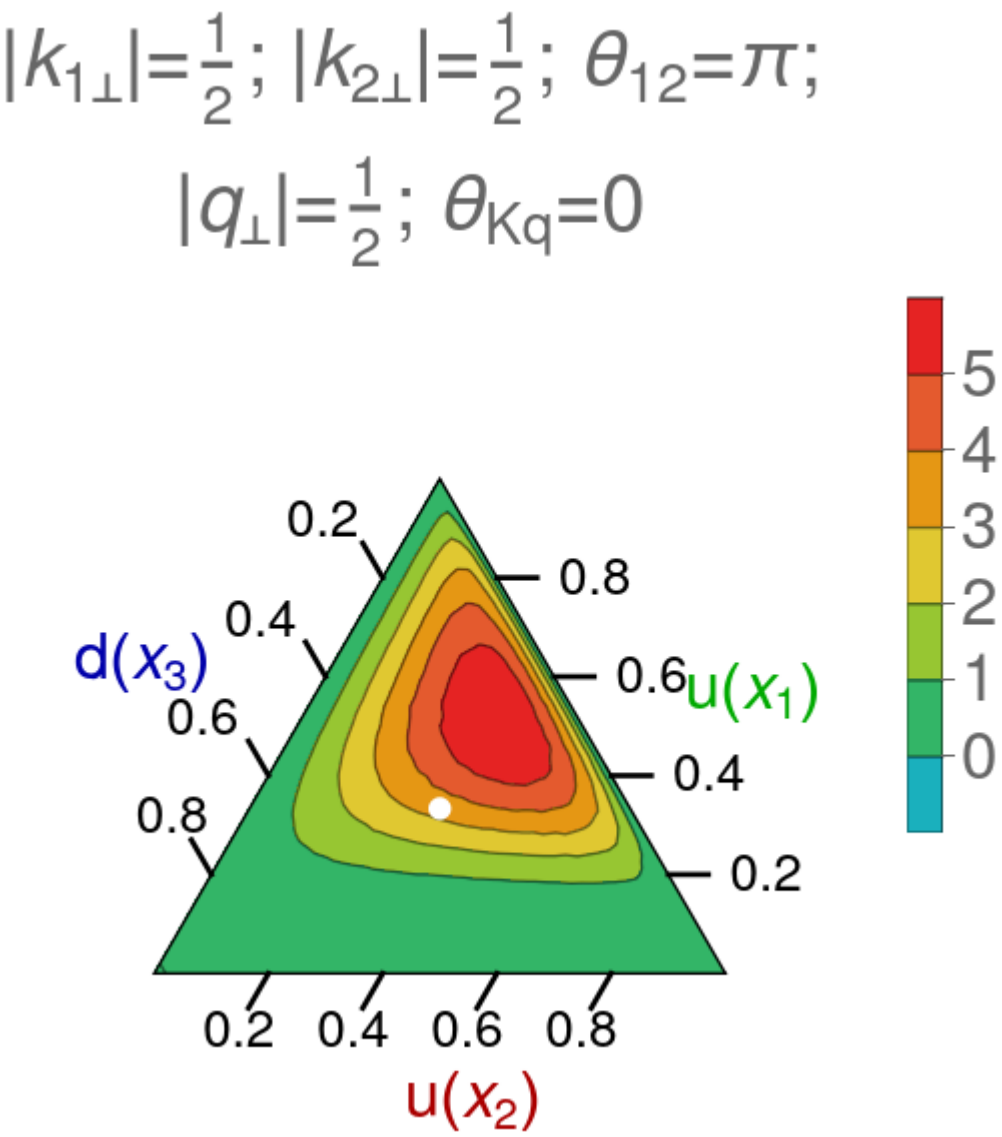

Figure 5.10: Identical to Fig. 5.6 except that $|\vec{k}_{1\perp}| = |\vec{k}_{2\perp}| = 0.5$, $\theta_{12} = \pi$ is shown.

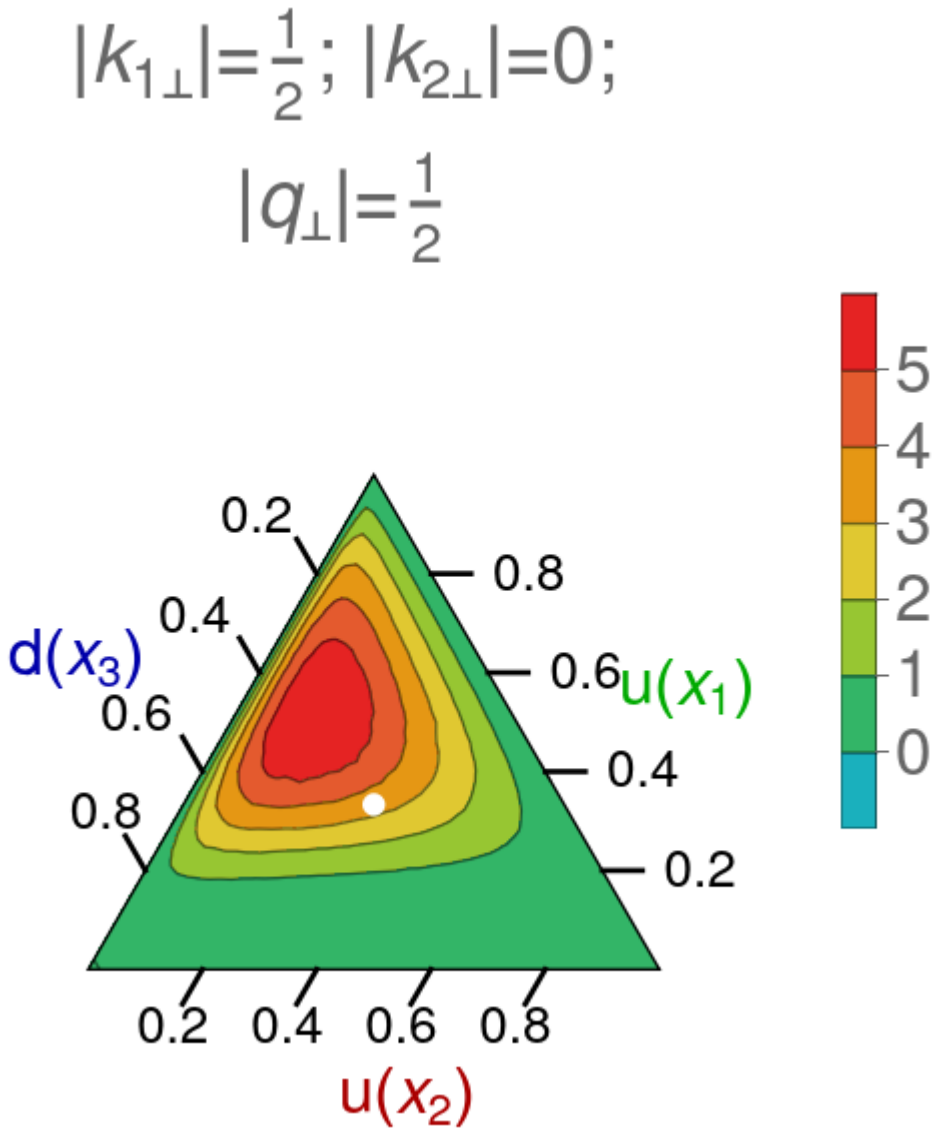

Figure 5.11: Identical to Fig. 5.6 except that $|\vec{k}_\perp| = 0.5$, $|\vec{k}_{2\perp}| = 0$ is shown.

In Fig. 5.6, symmetry between the quark $u2$ and the d quark is relatively clear. That is to say that, neglecting noise, exchanging their axes yields an identical plot. This is also the case in Fig. 5.7, as the internal diquark transverse momentum remains zero. In the remaining plots slight deformations from this symmetry are present and can be understood as due to asymmetry between the contributions of the two non-bystander quarks are no longer interchangeable when their longitudinal momenta are not equal. In particular, the internal angle of the diquark θ_{qK}, when nonzero, results in an asymmetric share of longitudinal momentum of the diquark's constituents. In addition, it is clear that the bystander quark tends to carry the majority of the longitudi-

nal momentum.

6 - Further Results

In this section are shown corresponding PDF plots, as well as those of related distributions. However, these results are not numerically stable at the current moment. This is mostly due to the large dimensionality of the numerical integration necessary to tackle in order to compute the overlap of two LFWFs which are each written as definite integrals over five Feynman parameters. In addition, all of the objects which we would like to compute via the overlap representation of LFWFs (GPDs, FFs, PDFs, IPDs) require the integration over the quark transverse momenta, as can be seen from the definition of the overlaps $\mathcal{O}$ as given in Eq. (4.55). For this second reason, we choose to compute the integrals over the quark transverse momenta analytically. This process will now be demonstrated before we choose to display any further results as well as the difficulties associated with the subsequent multidimensional numerical integration. Afterwards, some further improvements that might be made to improve the computation of more contributions to our distributions of interest as well as any future goals for subsequent studies will be delineated.

6.1 . Preparation for Numerical Integration

In order to compute the contributions of various LFWFs to Wigner distributions and their associated limits we must first compute their overlaps. Let us begin with the contribution to the function $\Psi^{1,-}$ as elucidated in the previous section. We drop here the arrows of the transverse vector notation for legibility. It is proportional to

$$\begin{aligned}\Psi^{1,-} &= \tilde{N}(\nu,\sigma)\int [df]\tilde{\rho}\rho_\nu(\bar{a}_1-a_{34})^{\sigma-2}(a_{34}-a_3)^\nu(1-x_2)^{\nu+2}M_N^{-2(\sigma+2+\nu)}\\ &\times\Big[\frac{\ell_\perp^2}{M_N^2}+(1-\bar{a}_1)(\frac{M^2}{M_N^2}-\frac{1}{9})+(\bar{a}_1-a_{34})(\frac{\Lambda_N^2}{M_N^2}-\lambda)+a_3(\frac{\widetilde{M}^2}{M_N^2}-\frac{4}{9})\\ &+(a_{34}-a_3)(\frac{M_{\text{eff}}^2+(q_\perp^{\text{eff}})^2}{M_N^2}-\frac{4}{9})+(x_2-\frac{1}{3})^2\Big]^{-(\sigma+2+\nu)}\\ &\times[x_1(v'(x_1-2(1-x_2))+x_1(1-x_2))+\bar{u}'(v'(1-x_2)-(x_1)^2)]^{-\nu-1}\\ &(\bar{u}'-v')^{2\nu-1},\end{aligned} \tag{6.1}$$

where $\tilde{N}(\nu,\sigma)$ is a normalization factor depending on ν and σ, the Nakanishi model exponents. To calculate the contribution of this function's overlap with itself to the GPD H when quark 1 is active we first take at a look at the transverse momentum dependent term, combining with a new Feynman

parametrization as

$$\begin{aligned}
&\Big[(1+\frac{a_{34}-a_3}{(x_2-1)^2}x_1^2)k_{1\perp}^2+(a_{34}-a_3)k_{2\perp}^2 \\
&+2\frac{a_{34}-a_3}{-1+x_2}x_1\vec{k}_{1\perp}\cdot\vec{k}_{1\perp}+\hat{M}^2\Big]_{in}^{-(\sigma+2+\nu)}\Big[(1 \\
&+\frac{a_{34}-a_3}{(x_2-1)^2}x_1^2)k_{1\perp}^2+(a_{34}-a_3)k_{2\perp}^2+2\frac{a_{34}-a_3}{-1+x_2}x_1\vec{k}_{1\perp}\cdot\vec{k}_{1\perp} \\
&+\hat{M}^2\Big]_{out}^{-(\sigma+2+\nu)} \\
= &\int_0^1 dh\Big[A_1\bar{k}_{1\perp}^2+A_2\bar{k}_{2\perp}^2+A_3\Delta_\perp^2+A_4\bar{k}_{1\perp}\cdot\bar{k}_{2\perp} \\
&+A_5\bar{k}_{1\perp}\cdot\Delta_\perp+A_6\bar{k}_{2\perp}\cdot\Delta_\perp+A_7]^{-2(\sigma+2+\nu)},
\end{aligned} \tag{6.2}$$

where $\hat{M}$ is a collection of all non-transverse-momentum-dependent terms to be dealt with later and where h is the new Feynman parameter and the coefficients A_{1-6} of the six kinematic combinations resulting from use the definitions of the incoming and outgoing momenta from Eqs. (4.43) and (4.44), as well as the term A_7, are given in Eqs. (8.18). In order to integrate over the transverse quark momenta we first shift them along the real axis by defining

$$\begin{aligned}
\tilde{k}_{1\perp} &\equiv \bar{k}_{1\perp}+\frac{A_4}{2A_1}\bar{k}_{2\perp}+\frac{A_5}{2A_1}\Delta_\perp \\
\tilde{k}_{2\perp} &\equiv \bar{k}_{2\perp}+\tilde{A}_6\Delta_\perp \\
\bar{k}_{1\perp} &= \tilde{k}_{1\perp}-\frac{A_4}{2A_1}\tilde{k}_{2\perp}+(\tilde{A}_6-\frac{A_5}{2A_1})\Delta_\perp \\
\bar{k}_{2\perp} &= \tilde{k}_{2\perp}-\tilde{A}_6\Delta_\perp.
\end{aligned} \tag{6.3}$$

Here we define for convenience

$$\begin{aligned}
\tilde{A}_2 &\equiv A_2-\frac{A_4^2}{4A_1} \\
\tilde{A}_6 &\equiv A_6-\frac{A_4A_5}{2A_1} \\
\tilde{A}_3 &\equiv A_3-\frac{\tilde{A}_6^2}{2\tilde{A}_2}.
\end{aligned} \tag{6.4}$$

The expression now reads

$$\int_0^1 dh\Big[A_1\tilde{k}_{1\perp}^2+\tilde{A}_2\tilde{k}_{2\perp}^2+\tilde{A}_3\Delta_\perp^2+A_7\Big]^{-2(\sigma+2+\nu)}. \tag{6.5}$$

Integrating over both $\tilde{k}_{1,2}$ then gives

$$\begin{aligned}
&\Big[\tilde{N}(\nu,\sigma)\int [df_{in}]\tilde{\rho}\rho_\nu(\bar{a}_1-a_{34})^{\sigma-2}(a_{34}-a_3)^\nu(1-x_2)^{\nu+2} \\
&\times[x_1(v'(x_1-2(1-x_2))+x_1(1-x_2)) \\
&+\bar{u}'(v'(1-x_2)-(x_1)^2)]^{-\nu-1}(\bar{u}'-v')^{2\nu-1}\Big]_{\text{in}} \\
&\Big[\tilde{N}(\nu,\sigma)\int [df_{in}]\tilde{\rho}\rho_\nu(\bar{a}_1-a_{34})^{\sigma-2}(a_{34}-a_3)^\nu(1-x_2)^{\nu+2} \\
&\times[x_1(v'(x_1-2(1-x_2))+x_1(1-x_2)) \\
&+\bar{u}'(v'(1-x_2)-(x_1)^2)]^{-\nu-1}(\bar{u}'-v')^{2\nu-1}\Big]_{\text{out}} \\
&\times\frac{\pi^2}{2}\int_0^1 dh\Big[\tilde{A}_3\Delta_\perp^2+A_7\Big]^{-2(\sigma+1+\nu)}\Big[A_1\tilde{A}_3(\sigma+\nu+1)(3+2\sigma+2\nu)\Big]^{-1}.
\end{aligned} \tag{6.6}$$

Restoring the relevant prefactors then allows us to compute the overlap contribution of $\Psi^{1,-}$. The resulting PDF contributions are shown in Fig. 9.3.

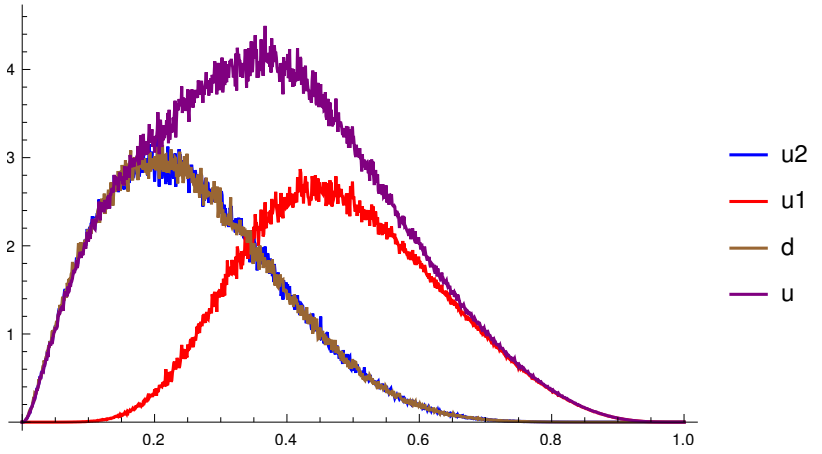

Figure 6.1: The results for the forward limit of $\Psi^{1,-}$ self overlaps (PDFs) are shown. The red curve corresponds to that of the bystander quark $u1$, the blue to the participant quark $u2$, the brown to the participant quark $d(3)$, and the purple to the total u quark contribution. This result has been computed using AMC integration with 1001 points along the x axis, and is extremely noisy. Even so, there is a clearly visibile signal which is not compatible with zero.

6.2 . Difficulties with Numerical Integration

There are two numerical integration methods which we will explain here, both implemented natively in Mathematica. The first is integration in quadrature using the Gauss-Kronrod rule, which is more numerically stable but extremely computationally costly due to the high dimensionality of the inte-

grand, taking more than 20 times as long as the second method to be described below. This method combines Gauss quadrature and Kronrod extension points to estimate definite integrals accurately. Firstly, Gauss quadrature points, points chosen for their accuracy in estimating polynomials up to a certain degree based on corresponding weights which determine their contributions to the integral, are employed within the integration interval to compute an initial integral estimate [117]. Additionally, Kronrod extension points are incorporated to enhance accuracy, particularly for functions with rapid variations or singularities [118]. The integration process then follows an adaptive strategy, where subintervals are initially divided, and estimates using Gauss quadrature and Kronrod extension points are computed. The algorithm recursively subdivides the interval and computes new estimates if the estimated error for a subinterval exceeds a specified tolerance level. This process continues until the estimated error falls below the tolerance level or after a predetermined number of iterations. Finally, contributions from all regions are summed to provide an estimation of the total value of the integral.
The more efficient but less reliable integration method to which we compare quadrature integration is Adaptive Monte Carlo (AMC). AMC integration is a numerical technique used to estimate a definite integral's value by randomly sampling points within the corresponding domain. The integration domain is initially divided into regions, from each of which random points are sampled. At each sample point, the integrand is evaluated, then the average of the function over all such sample points is calculated. This average value is then multiplied by the size of the integration domain in order to estimate the integral. The algorithm repeatedly adjusts the number of sample points and their distribution based on error estimates, focusing more sampling in regions where the integrand varies significantly or where the error is highest, and reducing sampling in regions where the function is relatively flat or where the error is low. This adaptive process is iterative, continuing until the estimated error is found to be below a specified tolerance level or until a maximum number of iterations is achieved. By adjusting the sampling strategy adaptively based on the local behavior of the integrand, AMC integration provides accurate estimates of integrals even for functions with complex behavior.
Taking a look at the Fig. 9.3, it is clear that the function $\Psi^{1,-1}$ contributes to the PDFs of all three quarks. In addition, it contributes symmetrically to u_2 and d, which reflects their participation in the diquark correlation involved in the modeling of this function. In addition, as observed in the auxiliary function $\psi^{1,-1}$ plots above, the large share of longitudinal momentum fraction taken on by the bystander quark is reflected in the large x tail of the bystander quark (red curve).

6.3 . Looking Forward

6.3.1 . Analytic Traces and Mellin Moments

The computation of the Mellin moment integrations as explained in the previous chapter is one of the most technically challenging parts of the entire computation. This is due to the wealth of tensorial structures as presented in Eq. (5.11). Computing the corresponding traces and the consequent integration requires code which may systematically compute vector integrals analytically, extrapolating the trends of various example integrals (low order Mellin moments) to all orders, which is a highly nontrivial task.

6.3.2 . Mass Relationships

As explained in the previous chapter, results presented for the nucleon LFWFs are only valid for particular relationships between the quark masses, the nucleon masses, the diquark correlation mass, and the Nakanishi mass parameters. This is because the integration technique relies on a contour shift in the complex plane, whose validity is dependent on the lack of the presence of poles inside the corresponding contour. This presents the masses and parameters from falling below a minimum value, accounting for which would require computation using residues. Further, it is well known that the quark masses are not constant, but tend to run with the momentum of the corresponding quark in a way shown in Fig. 6.2.

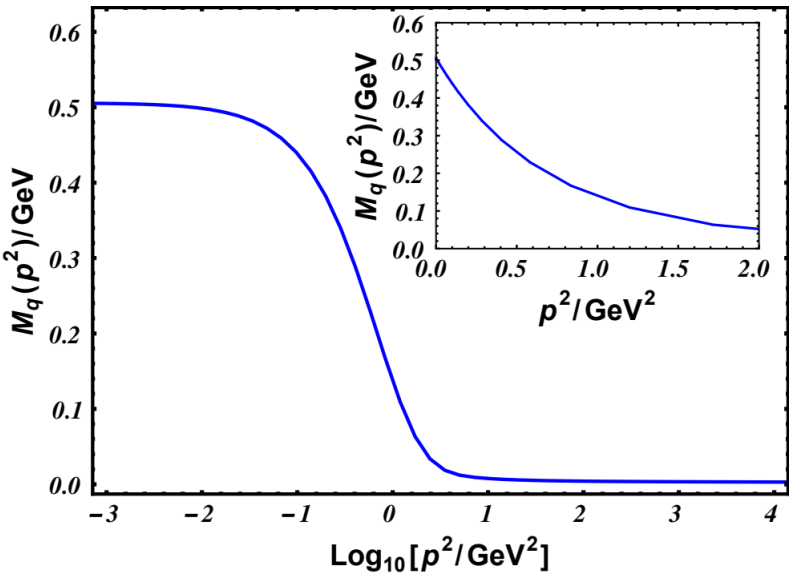

Figure 6.2: An example of the running quark mass is graphed here in a figure from [119].

In order to allow for this running mass behavior, one would need to deal with a denominator with more complicated behavior, contributing in turn to

more complicated contributions to the numerator in the Mellin moment computations. Such computations have been computed directly in the complex plane for example in [111].

6.3.3 . Extension to the ERBL and Comparison to Experiment

Once more contributions at the level of diverse tensorial structures have been computed, it would be necessary to compare the resulting distributions to those extracted from experimental data. In order to do so, it would be necessary at the level of the GPD to extend the results to the ERBL region. A procedure developed by the authors of [86], employing finite element Radon transform inversion, would likely be used to perform such a numerical extension. The numerical extension relies on the polynomiality property given in Eq. (2.32). As a consequence of covariance, we know that the polynomiality propery must hold if the GPD can be written as a the Radon transform of a DD. In fact, in a recent paper it has been shown that merely partial DGLAP knowledge of a GPD is (nearly) enough to construct a unique DD representation, from which the ERBL region contribution of the GPD may be computed [120]. Because the polynomiality property involves integration over the entire x domain at all relevant values of ξ, its satisfaction is only achieved when the GPD model involved is defined over the entire domain of interest, which involves both the DGLAP and ERBL regions. For this reason, [86] features a covariant extension which passes first to DD space.

In order to start with a DGLAP GPD model and arrive at a corresponding DD expression, one needs to compute an inverse Radon transform. One can then covariantly extend uniquely to the ERBL region up to D-term-like contributions.

In [86], the authors use a finite element method for numerical inversion of the Radon transform, an ill-posed problem, in which integrals over "DGLAP lines" in DD space takes place. These DGLAP lines are defined as

$$x_i - \beta - \alpha\xi_i = 0 \tag{6.7}$$

with x_ξ & ξ_i chosen such that $x_i > \xi_i$, ensuring they correspond to the DGLAP condition.

With such numerical results in hand, we would then choose to evolve them to experimental scales for direct comparison to experimental results. In the case of comparison with DVCS data, this would involve convolution with a perturbatively calculable kernel for computation of the CFFs and the resultant cross section.

7 - Concluding Remarks

As discussed in the introductory chapter, the GPDs enter the descriptions of various experimental processes including DVCS and DVMP. Corresponding to this universality, which is ensured by proofs of factorization, GPDs are extremely valuable for experimental predictions. This value is compensated by the difficulty of their extraction from experimental data of these processes, cross sectional data, which is related to the GPDs via obscuring convolutions with perturbatively calculable kernels. For this reason, constraint on the precise functional forms of various GPDs from a practical perspective should involve inputs from lattice QCD computations, continuum techniques, etc. in order to be compared to experiment.
In the second chapter it was explained that by employing a Bayesian reweighting of ANN GPD candidates using lattice data a large uncertainty reduction of the corresponding replica bundle may result. This requires that the correlation of said lattice data be known, as highly correlated data, even albeit precise, simply chooses a single replica, thereby yielding unuseful results in any Ioffe-time region in which such lattice data is introduced. Lattice data may also be chosen/computed in a manner complementary to the shortcomings resulting from the singular structure of the perturbative kernel associated with the experimental data to which the ANNs were fitted, thereby providing access to regions of the space of candidate functions to which the experimental data are insensitive.
In its third chapter, this thesis contains a specification of the overlap representation of polarized and unpolarized DGLAP region GPDs via LFWFs of definite qOAM derived from the decomposition a matrix element characterizing contributions of three-quark Fock states of definite quark helicities in a leading twist tensorial basis to the nucleonic state with definite helicity. This characterization can be thought of in analogy with atomic physics, in which (nonrelativistic) wave functions of distinct angular momentum-related quantum numbers contribute to the total atomic configuration. It is also noteworthy that LFWFs of non-zero qOAM contribute to the GPD H, implying that they contribute even in the forward limit. This means that the polarized PDF is sensitive to contributions of non-zero qOAM, which is striking given that we associate the generalization of the PDF, the GPD, with direct access to qOAM contributions via the Ji sum rules [29]. A simple Faddeev amplitude based model for such LFWFs has been introduced in the fourth chapter, where it has been outlined how they might be computed from a wealth of tensorial structures, along with a simple example computation. These functions may also be used to compute objects apart from GPDs, such as DAs [121],[112], and the corresponding methods may be used to look at aspects of the bary-

onic spectrum [109].
To compare these models to experiment, it will be necessary to first extend the resulting DGLAP GPDs to the ERBL region, and subsequently to evolve the resulting GPDs up to experimental scales, as has been done in the case of the pion [86].
Further, there is much work to do on the modeling side. In this thesis it was already a difficult task to calculate the contributions to the basis LFWFs of only the simplest tensorial structure as a matter of proof of concept. As discussed in the previous chapter, systemization of the incorporation of further tensorial structures is a must for a proper understanding of contributions of qOAM to the nucleon. In addition, more complicated methods of integrating in the complex plane to recover lightcone amplitudes from Faddeev wave functions may be used in conjunction with a running mass, as discussed in the previous chapter.

8 - Appendix

8.1 . Notation and Conventions

8.1.1 . Notation

$$\gamma^{\pm} \equiv \frac{1}{\sqrt{2}}(\gamma^0 \pm \gamma^3). \tag{8.1}$$

8.1.2 . Fourier Convention

$$i\partial^j = k^j, \tag{8.2}$$

$$\tilde{\partial}^j \to \epsilon^{jl}(-i)k^l, \tag{8.3}$$

$$\tilde{\partial}^j\partial^j \to -\epsilon^{jl}k^lk^j, \tag{8.4}$$

8.1.3 . Lightcone Vectors

For any Lorentz vector v

$$(v^+ \equiv \frac{v^0+v^3}{\sqrt{2}}, v^- \equiv \frac{v^0-v^3}{\sqrt{2}}, \vec{v}_\perp), \tag{8.5}$$

8.2 . Identities

8.2.1 . Feynman Parametrization

One may rewrite integrals with many factors in the denominator as integrals of sums over such factors by paying the price of introducing additional integration parameters as

$$\begin{aligned}\frac{1}{A_1^{\alpha_1}\cdots A_n^{\alpha_n}} &= \frac{\Gamma(\alpha_1+\cdots+\alpha_n)}{\Gamma(\alpha_1)\cdots\Gamma(\alpha_n)} \\ &\int_0^1 du_1\cdots\int_0^1 du_n \frac{\delta(1-\sum_{k=1}^n u_k)\; u_1^{\alpha_1-1}\cdots u_n^{\alpha_n-1}}{(\sum_{k=1}^n u_kA_k)^{\sum_{k=1}^n\alpha_k}},\end{aligned} \tag{8.6}$$

where $\Re(\alpha_j) > 0$ and where the smallest possible subset of the complex plane containing all of said quantities A_j must not include 0 [122].

8.3 . Polarized GPDs

We now turn to the polarized skewed quark distributions (marked by $\mathbb{P} = 1$), $\widetilde{H}^q(\bar{x},\xi;t)$ and $\widetilde{E}^q(\bar{x},\xi;t)$, defined by the Fourier transform of the axial vector matrix element ([34])

$$\begin{aligned}\widetilde{\mathcal{H}}^f_{h'h} &\equiv \frac{1}{2\sqrt{1-\xi^2}}\sum_c \int \frac{\bar{z}^-}{2\pi}\, e^{i\,\bar{x}\bar{P}^+z^-}\ \langle P',\lambda'|\bar{p}si^c_q(-\frac{z}{2})\,\gamma^+\gamma_5\psi^c_q(\frac{z}{2})|P,h\rangle \\ &= \frac{\bar{u}(P',h')\gamma^+\gamma_5 u(P,h)}{2\bar{P}^+\sqrt{1-\xi^2}}\ \widetilde{H}^q(\bar{x},\xi;t) \\ &\quad + \frac{\bar{u}(P',h'),\lambda')\Delta^+\gamma_5 u(P,h)}{4m\,\bar{P}^+\sqrt{1-\xi^2}}\ \widetilde{E}^q(\bar{x},\xi;t),\end{aligned} \tag{8.7}$$

$$\widetilde{\mathcal{H}}^f_{++} = \widetilde{\mathcal{H}}^f_{--} = \widetilde{H}^f - \frac{\xi^2}{1-\xi^2}\widetilde{E}^f \tag{8.8}$$

$$\widetilde{\mathcal{H}}^f_{-+} = (\widetilde{\mathcal{H}}^f_{+-})^* = \frac{|\vec{\Delta}_\perp|}{(\Delta_1+i\Delta_2)}\frac{\sqrt{t_0-t}}{2m}\frac{\xi}{\sqrt{1-\xi^2}}\widetilde{E}^f. \tag{8.9}$$

8.4 . Twist

As discussed in the third chapter, there are three linearly independent Dirac algebraic structures whose contribution (as Γ) to the matrix element defined in Eq. (2.24) yields a leading twist structure. They receive contributions from twist $\tau = 2$ GPDs, implying they do not receive suppression with respect to Q. These structures are given by

$$\Gamma = \gamma^+, \gamma^5\gamma^+, \sigma^{+i}, \tag{8.10}$$

where i is a transverse Lorentz index.
However, decompositions have been made for the same matrix element in the case of DVCS for the Dirac structures (see [28])

$$\Gamma = \gamma^\mu, \gamma^5\gamma^\mu, \tag{8.11}$$

where $\mu \in \{0,1,2,3\}$ is a Lorentz index. Because of the range of the index μ, the transverse and $-$ indices are included in such decompositions, and correspondingly higher twist structures enter the game. In [28], such twist $\tau = 3$ structures are enumerated, and receive suppression with respect to $|Q|^{-1}$.

8.5 . Overlap Formulas

Calculating the EFFs one finds

$$
\begin{aligned}
F_1^{\hat{f},\mathbb{P}}(t) &\equiv \int_{-1}^{1} dx H^{\hat{f},\mathbb{P}}(x,0,t) = \int_{-1}^{1} dx \Big(\mathcal{O}^{\hat{f},\mathbb{P}}(\Psi_{\frac{1}{2},\frac{1}{2}}, \Psi_{\frac{1}{2},\frac{1}{2}}) \\
&\quad + \mathcal{O}^{\hat{f},\mathbb{P}}(\Psi_{\frac{1}{2},-\frac{1}{2}}, \Psi_{\frac{1}{2},-\frac{1}{2}}) + \mathcal{O}^{\hat{f},\mathbb{P}}(\Psi_{\frac{1}{2},\frac{3}{2}}, \Psi_{\frac{1}{2},\frac{3}{2}}) \\
&\quad + \mathcal{O}^{\hat{f},\mathbb{P}}(\Psi_{\frac{1}{2},-\frac{3}{2}}, \Psi_{\frac{1}{2},-\frac{3}{2}}) \Big) |_{\xi=0} \qquad (8.12) \\
F_2^{\hat{f},\mathbb{P}}(t) &\equiv \int_{-1}^{1} dx E^{\hat{f},\mathbb{P}}(x,0,t) = \int_{-1}^{1} dx \frac{2M_N |\vec{\Delta}_\perp|}{(\Delta_1 + i\Delta_2)\sqrt{-t}} \\
&\quad \Big(\mathcal{O}^{\hat{f},\mathbb{P}}(\Psi_{-\frac{1}{2},-\frac{3}{2}}, \Psi_{\frac{1}{2},\frac{3}{2}}) \mathcal{O}^{\hat{f},\mathbb{P}}(\Psi_{-\frac{1}{2},\frac{3}{2}}, \Psi_{\frac{1}{2},-\frac{3}{2}}) \Big) |_{\xi=0}. \qquad (8.13)
\end{aligned}
$$

And their squared electric radii are expressed in these terms as

$$
\begin{aligned}
\langle (r_E^{P,N})^2 \rangle &= 6\hbar^2 \partial_t \Big(F_1^{P,N;0}(t) + \frac{t}{4M_N^2} F_2^{P,N;0}(t) \Big)|_{t=0} \qquad (8.14)\\
&= 6\hbar^2 \partial_t \Big(\frac{2n_u^{P,N}}{3} F_1^{0,u}(t) - \frac{n_d^{P,N}}{3} F_1^{0,d}(t) \\
&\quad + \frac{t}{4M_N^2} (\frac{2n_u^{P,N}}{3} F_2^{0,u}(t) - \frac{n_d^{P,N}}{3} F_2^{0,d}(t)) \Big)|_{t=0} \\
&= 4\hbar^2 n_u^{P,N} \partial_t \int_{-1}^{1} dx \Big(\mathcal{O}^{0,u}(\Psi_{\frac{1}{2},\frac{1}{2}}, \Psi_{\frac{1}{2},\frac{1}{2}}) + \mathcal{O}^{0,u}(\Psi_{\frac{1}{2},-\frac{1}{2}}, \Psi_{\frac{1}{2},-\frac{1}{2}}) \\
&\quad + \mathcal{O}^{0,u}(\Psi_{\frac{1}{2},\frac{3}{2}}, \Psi_{\frac{1}{2},\frac{3}{2}}) + \mathcal{O}^{0,u}(\Psi_{\frac{1}{2},-\frac{3}{2}}, \Psi_{\frac{1}{2},-\frac{3}{2}}) \Big)|_{t=\xi=0} \\
&\quad - 2\hbar^2 n_d^{P,N} \partial_t \int_{-1}^{1} dx \Big(\mathcal{O}^{0,d}(\Psi_{\frac{1}{2},\frac{1}{2}}, \Psi_{\frac{1}{2},\frac{1}{2}}) + \mathcal{O}^{0,d}(\Psi_{\frac{1}{2},-\frac{1}{2}}, \Psi_{\frac{1}{2},-\frac{1}{2}}) \\
&\quad + \mathcal{O}^{0,d}(\Psi_{\frac{1}{2},\frac{3}{2}}, \Psi_{\frac{1}{2},\frac{3}{2}}) + \mathcal{O}^{0,d}(\Psi_{\frac{1}{2},-\frac{3}{2}}, \Psi_{\frac{1}{2},-\frac{3}{2}}) \Big)|_{t=\xi=0} \\
&\quad - \frac{2\hbar^2 n_u^{P,N} \sqrt{-t} |\vec{\Delta}_\perp|}{M_N(\Delta_1 + i\Delta_2)} \partial_t \\
&\quad \times \int_{-1}^{1} dx \Big(\mathcal{O}^{0,u}(\Psi_{-\frac{1}{2},-\frac{3}{2}}, \Psi_{\frac{1}{2},\frac{3}{2}}) + \mathcal{O}^{0,u}(\Psi_{-\frac{1}{2},\frac{3}{2}}, \Psi_{\frac{1}{2},-\frac{3}{2}}) \Big)|_{t=\xi=0} \\
&\quad + \frac{\hbar^2 n_d^{P,N} \sqrt{-t} |\vec{\Delta}_\perp|}{M_N(\Delta_1 + i\Delta_2)} \partial_t \\
&\quad \times \int_{-1}^{1} dx \Big(\mathcal{O}^{0,d}(\Psi_{-\frac{1}{2},-\frac{3}{2}}, \Psi_{\frac{1}{2},\frac{3}{2}}) + \mathcal{O}^{0,d}(\Psi_{-\frac{1}{2},\frac{3}{2}}, \Psi_{\frac{1}{2},-\frac{3}{2}}) \Big)|_{t=\xi=0} \\
&\quad + \frac{\hbar^2 n_u^{P,N} |\vec{\Delta}_\perp|}{\sqrt{-t} M_N(\Delta_1 + i\Delta_2)} \\
&\quad \times \int_{-1}^{1} dx \Big(\mathcal{O}^{0,u}(\Psi_{-\frac{1}{2},-\frac{3}{2}}, \Psi_{\frac{1}{2},\frac{3}{2}}) + \mathcal{O}^{0,u}(\Psi_{-\frac{1}{2},\frac{3}{2}}, \Psi_{\frac{1}{2},-\frac{3}{2}}) \Big)|_{t=\xi=0} \\
&\quad - \frac{\hbar^2 n_d^{P,N} |\vec{\Delta}_\perp|}{2\sqrt{-t} M_N(\Delta_1 + i\Delta_2)} \\
&\quad \times \int_{-1}^{1} dx \Big(\mathcal{O}^{0,d}(\Psi_{-\frac{1}{2},-\frac{3}{2}}, \Psi_{\frac{1}{2},\frac{3}{2}}) + \mathcal{O}^{0,d}(\Psi_{-\frac{1}{2},\frac{3}{2}}, \Psi_{\frac{1}{2},-\frac{3}{2}}) \Big)|_{t=\xi=0}.
\end{aligned}
$$

8.6 . Euclidean Modeling Coefficients

We now state the equations used to rewrite dependence on the l, q basis and the k_1, k_2 as a function of which quark does not participate in the diquark,

which is labeled as the nth quark.

$$|\vec{k}_{1\perp}| = \delta_{1,n}\ell^2 + \delta_{2,n}(\frac{\ell^2}{4} + \ell\cdot q + q^2) + \delta_{3,n}(\frac{\ell^2}{4} - \ell\cdot q + q^2) \quad (8.15)$$

$$|\vec{k}_{2\perp}| = \delta_{1,n}(\frac{\ell^2}{4} - \ell\cdot q + q^2) + \delta_{2,n}\ell^2 + \delta_{3,n}(\frac{\ell^2}{4} + \ell\cdot q + q^2) \quad (8.16)$$

$$\theta_{12} = \cos^{-1}(-\frac{(\ell^2 - 2\ell\cdot q)\delta_{1,n}}{\sqrt{\ell^2(\ell^2 - 4\ell\cdot q + 4q^2)}} - \frac{(\ell^2 + 2\ell\cdot q)\delta_{2,n}}{\sqrt{l^4 + 4\ell^2(\ell\cdot q + q^2)}} + \frac{(\ell^2 - 4q^2)\delta_{3,n}}{\sqrt{l^4((\ell^2 + 4q^2)^2 - 16\ell\cdot q^2)}}). \quad (8.17)$$

8.7 . Overlap Coefficients

The coefficients A_{1-7} are provided in their full glory for the case that the active quark is the $u1$ and also that quark $u1$ is the bystander quark. Similarly awful expressions exist for the other choices of active and bystander quark.

The index i (o) labels incoming (outgoing) variables.

$$
\begin{aligned}
A_1 \;=\; & \Big(h(-(-\xi+x_2-1) \\
& ((\xi+x_2-1)(-a_{34i}(x_1^2-\xi^2)^2 a_{34o}(x_1^2-\xi^2)^2+a_{3i}\xi^4 \\
& +a_{3i}x_1^4-2a_{3i}\xi^2 \\
& x_1^2-a_{3o}\xi^4-a_{3o}x_1^4+2a_{3o}\xi^2x_1^2-4\xi^3-4\xi x_1^2+4\xi x_1^2x_2+4\xi^3x_1 \\
& +4\xi x_1+4\xi x_1x_2^2 \\
& -8\xi x_1x_2+4\xi^3x_2)-(\xi-1)v_o'(x_1-\xi) \\
& (\xi+x_1+2x_2-2) \\
& \times(a_{34i}(\xi+x_1)^2-a_{3i}(\xi+x_1)^2 \\
& +(\xi-x_2+1)^2))+(\xi-1)u_o'(-\xi+x_2-1) \\
& \times((\xi-1)v_o'(\xi+x_2-1)-(x_1-\xi)^2)(a_{34i}(\xi+x_1)^2-a_{3i} \\
& (\xi+x_1)^2+(\xi-x_2+1)^2) \\
& +(\xi+1)v_i'(\xi+x_1) \\
& (\xi+x_2-1)(-\xi+x_1+2x_2-2)(a_{34o}(x_1-\xi)^2-a_{3o}(x_1-\xi)^2 \\
& +(\xi+x_2-1)^2))-(h-1)(\xi+1)u_i' \\
& (\xi+x_2-1)((\xi+1)v_i'(-\xi+x_2-1)+(\xi+x_1)^2) \\
& \times(a_{34o}(x_1-\xi)^2-a_{3o}(x_1-\xi)^2+(\xi+x_2-1)^2)-((\xi+x_1) \\
& (\xi+x_2-1)((\xi+1)v_i' \\
& \times(-\xi+x_1+2x_2-2)-(\xi+x_1) \\
& (-\xi+x_2-1))(a_{34o}(x_1-\xi)^2-a_{3o}(x_1-\xi)^2 \\
& +(\xi+x_2-1)^2))\Big)\Big(\\
& ((\xi+1)u_i'((\xi+1)v_i'(-\xi+x_2-1)+(\xi+x_1)^2)-(\xi+x_1) \\
& \times((\xi+1)v_i' \\
& (-\xi+x_1+2x_2-2)-(\xi+x_1)(-\xi+x_2-1)))((\xi-1)u_o' \\
& \times((\xi-1)v_o' \\
& (\xi+x_2-1)-(x_1-\xi)^2)(x_1-\xi)((\xi-1)v_o' \\
& (\xi+x_1+2x_2-2) \\
& +(x_1-\xi)(\xi+x_2-1)))\Big)^{-1},
\end{aligned}
\tag{8.18}
$$

$$
\begin{aligned}
A_2 \;=\;& \Big(h(a_{34i}-a_{3i})(-\xi+x_2-1)^3\Big) \\
&\times\Big((\xi+1)u_i'((\xi+1)v_i'(-\xi+x_2-1)+(\xi+x_1)^2) \\
&-(\xi+x_1)((\xi+1)v_i'(-\xi+x_1+2x_2-2)-(\xi+x_1)(-\xi+x_2-1))\Big)^{-1} \\
&-\Big(a_{34o}(h-1)(\xi+x_2-1)^3\Big) \\
&\times\Big((\xi-1)u_o'((\xi-1)v_o'(\xi+x_2-1)-(x_1-\xi)^2) \\
&+(x_1-\xi)((\xi-1)v_o'(\xi+x_1+2x_2-2)+(x_1-\xi)(\xi+x_2-1))\Big)^{-1} \\
&+\Big(a_{3o}(h-1)(\xi+x_2-1)^3\Big) \\
&\times\Big((\xi-1)u_o'((\xi-1)v_o'(\xi+x_2-1)-(x_1-\xi)^2) \\
&+(x_1-\xi)((\xi-1)v_o'(\xi+x_1+2x_2-2)+(x_1-\xi)(\xi+x_2-1))\Big)^{-1},
\end{aligned}
\tag{8.19}
$$

$$
\begin{aligned}
A_3 \;=\; & \Big((h-1)u_i'(x_2+\xi-1)((x_1+\xi)^2+v_i'(x_2-\xi-1)(\xi+1)) \\
& \times((a_{34o}-a_{3o})x_1^4-2(a_{34o}-a_{3o})(\xi+1)x_1^3+((x_2+\xi-1)^2 \\
& +a_{34o}(2x_2^2+2(\xi-1)x_2+\xi^2+4\xi+1) \\
& -a_{3o}(2x_2^2+2(\xi-1)x_2+\xi^2+4\xi+1))x_1^2 \\
& -2((a_{34o}(\xi+1)-a_{3o}(\xi+1)+1)x_2^2 \\
& +(\xi-1)(a_{34o}(\xi+1)-a_{3o}(\xi+1)+2)x_2 \\
& +(a_{34o}-a_{3o}+1)\xi^2+(a_{34o}-a_{3o}-2)\xi+1)x_1 \\
& +(a_{34o}-a_{3o})x_2^4+a_{34o}\xi^2-a_{3o}\xi^2+\xi^2 \\
& +2(a_{34o}-a_{3o})x_2^3(\xi-1)-2\xi \\
& +2x_2(\xi-1)(a_{34o}\xi-a_{3o}\xi+1) \\
& +x_2^2(a_{34o}(\xi^2+1)-a_{3o}(\xi^2+1)+1)+1)(\xi+1)^3 \\
& +(x_1+\xi)(x_2+\xi-1)(v_i'(x_1+2x_2-\xi-2)(\xi+1) \\
& -(x_2-\xi-1)(x_1+\xi))((a_{34o}-a_{3o})x_1^4 \\
& -2(a_{34o}-a_{3o})(\xi+1)x_1^3+((x_2+\xi-1)^2 \\
& +a_{34o}(2x_2^2+2(\xi-1)x_2+\xi^2+4\xi+1) \\
& -a_{3o}(2x_2^2+2(\xi-1)x_2+\xi^2+4\xi+1))x_1^2 \\
& -2((a_{34o}(\xi+1)-a_{3o}(\xi+1)+1)x_2^2 \\
& +(\xi-1)(a_{34o}(\xi+1)-a_{3o}(\xi+1)+2)x_2 \\
& +(a_{34o}-a_{3o}+1)\xi^2+(a_{34o}-a_{3o}-2)\xi+1)x_1 \\
& +(a_{34o}-a_{3o})x_2^4+a_{34o}\xi^2-a_{3o}\xi^2+\xi^2 \\
& +2(a_{34o}-a_{3o})x_2^3(\xi-1)-2\xi \\
& +2x_2(\xi-1)(a_{34o}\xi-a_{3o}\xi+1)+x_2^2(a_{34o}(\xi^2+1) \\
& -a_{3o}(\xi^2+1)+1)+1)(\xi+1)^2 \\
& -h(u_o'(x_2-\xi-1)(v_o'(\xi-1)(x_2+\xi-1)-(x_1-\xi)^2) \\
& \times((a_{34i}-a_{3i})x_1^4-2(a_{34i}-a_{3i})(x_2-2\xi)x_1^3 \\
& +((a_{34i}-a_{3i}+1)x_2^2 \\
& -2(2a_{34i}\xi-2a_{3i}\xi+\xi+1)x_2 \\
& +(4a_{34i}-4a_{3i}+1)\xi^2+(-2a_{34i}+2a_{3i}+2)\xi+1)x_1^2 \\
& -2(x_2^2-((a_{34i}-a_{3i}+2)\xi+2)x_2 \\
& +(2a_{34i}-2a_{3i}+1)\xi^2+2\xi+1)x_1+x_2^2+a_{34i}\xi^2-a_{3i}\xi^2 \\
& +\xi^2-2x_2-2x_2\xi+2\xi+1)(\xi-1)^3 \\
& +v_i'(x_1+2x_2-\xi-2)(\xi+1)^3(x_1+\xi) \\
& \times(x_2+\xi-1)((a_{34o}-a_{3o})x_1^4 \\
& -2(a_{34o}-a_{3o})(\xi+1)x_1^3+((x_2+\xi-1)^2 \\
& +a_{34o}(2x_2^2+2(\xi-1)x_2+\xi^2+4\xi+1) \\
& -a_{3o}(2x_2^2+2(\xi-1)x_2+\xi^2+4\xi+1))x_1^2
\end{aligned}
\tag{8.20}
$$

$$
\begin{aligned}
&-2((a_{34o}(\xi+1)-a_{3o}(\xi+1)+1)x_2^2\\
&+(\xi-1)(a_{34o}(\xi+1)-a_{3o}(\xi+1)+2)x_2\\
&+(a_{34o}-a_{3o}+1)\xi^2+(a_{34o}-a_{3o}-2)\xi+1)x_1\\
&+(a_{34o}-a_{3o})x_2^4+a_{34o}\xi^2-a_{3o}\xi^2+\xi^2\\
&+2(a_{34o}-a_{3o})x_2^3(\xi-1)-2\xi\\
&+2x_2(\xi-1)(a_{34o}\xi-a_{3o}\xi+1)+x_2^2(a_{34o}(\xi^2+1)\\
&-a_{3o}(\xi^2+1)+1)+1)\\
&+(x_2-\xi-1)(v_o'(x_1-\xi)(\xi-1)^3(x_1\\
&+2x_2+\xi-2)((a_{34i}-a_{3i})x_1^4\\
&-2(a_{34i}-a_{3i})(x_2-2\xi)x_1^3+((a_{34i}-a_{3i}+1)x_2^2\\
&-2(2a_{34i}\xi-2a_{3i}\xi+\xi+1)x_2\\
&+(4a_{34i}-4a_{3i}+1)\xi^2+(-2a_{34i}+2a_{3i}+2)\xi+1)x_1^2\\
&-2(x_2^2-((a_{34i}-a_{3i}+2)\xi+2)x_2\\
&+(2a_{34i}-2a_{3i}+1)\xi^2+2\xi+1)x_1+x_2^2\\
&+a_{34i}\xi^2-a_{3i}\xi^2+\xi^2-2x_2-2x_2\xi+2\xi+1)\\
&\times(x_2+\xi-1)(-a_{34i}\xi^2x_1^6+a_{3i}\xi^2x_1^6-a_{34i}x_1^6\\
&+a_{3i}x_1^6+2a_{34i}\xi x_1^6-2a_{3i}\xi x_1^6-2a_{34i}\xi^3x_1^5\\
&+2a_{3i}\xi^3x_1^5+4a_{34i}\xi^2x_1^5-4a_{3i}\xi^2x_1^5+2a_{34i}x_2\xi^2x_1^5\\
&-2a_{3i}x_2\xi^2x_1^5+2a_{34i}x_2x_1^5-2a_{3i}x_2x_1^5\\
&-2a_{34i}\xi x_1^5+2a_{3i}\xi x_1^5-4a_{34i}x_2\xi x_1^5+4a_{3i}x_2\xi x_1^5\\
&+3a_{34i}\xi^4x_1^4-3a_{3i}\xi^4x_1^4-4a_{34i}\xi^3x_1^4\\
&+4a_{3i}\xi^3x_1^4+4x_2\xi^3x_1^4-a_{34i}x_2^2x_1^4+a_{3i}x_2^2x_1^4\\
&-a_{34i}x_2^2\xi^2x_1^4+a_{3i}x_2^2\xi^2x_1^4-a_{34i}\xi^2x_1^4\\
&+a_{3i}\xi^2x_1^4+2a_{34i}x_2^2\xi x_1^4-2a_{3i}x_2^2\xi x_1^4\\
&+4x_2^2\xi x_1^4+2a_{34i}\xi x_1^4-2a_{3i}\xi x_1^4-4x_2\xi x_1^4+4a_{34i}\xi^5x_1^3\\
&+4a_{3i}\xi^5x_1^3+4\xi^5x_1^3-8a_{34i}\xi^4x_1^3+8a_{3i}\xi^4x_1^3-6a_{34i}x_2\xi^4x_1^3\\
&+6a_{3i}x_2\xi^4x_1^3+2a_{34i}\\
&\times x_2^2\xi^3x_1^3-2a_{3i}x_2^2\xi^3x_1^3+4x_2^2\xi^3x_1^3\\
&+4a_{34i}\xi^3x_1^3-4a_{3i}\xi^3x_1^3+10a_{34i}x_2\xi^3x_1^3\\
&-10a_{3i}x_2\xi^3x_1^3-8\xi^3x_{DF1}^3-4a_{34i}x_2^2\xi^2x_1^3\\
&+4a_{3i}x_2^2\xi^2x_1^3-2a_{34i}x_2\xi^2x_1^3+2a_{3i}x_2\xi^2x_1^3\\
&+2a_{34i}x_2^2\xi x_1^3-2a_{3i}x_2^2\xi x_1^3-4x_2^2\xi x_1^3\\
&-2a_{34i}x_2\xi x_1^3+2a_{3i}x_2\xi x_1^3+4\xi x_1^3-4a_{34i}\xi^6x_1^2\\
&+4a_{3i}\xi^6x_1^2+2a_{34i}\xi^5x_1^2-2a_{3i}\xi^5x_1^2+4a_{34i}x_2\xi^5x_1^2\\
&-4a_{3i}x_2\xi^5x_1^2+4x_2\xi^5x_1^2-8\xi^5x_1^2\\
&-a_{34i}x_2^2\xi^4x_1^2+a_{3i}x_2^2\xi^4x_1^2+7a_{34i}\xi^4x_1^2
\end{aligned}
$$

$$
\begin{aligned}
&-7a_{3i}\xi^4x_1^2 - 4a_{34i}x_2\xi^4x_1^2 + 4a_{3i}x_2\xi^4x_1^2\\
&+2a_{34i}x_2^2\xi^3x_1^2 - 2a_{3i}x_2^2\xi^3x_1^2 - 4x_2^2\xi^3x_1^2\\
&-4a_{34i}\xi^3x_1^2 + 4a_{3i}\xi^3x_1^2 - 4a_{34i}x_2\xi^3x_1^2\\
&+4a_{3i}x_2\xi^3x_1^2 - 16x_2\xi^3x_1^2 + 16\xi^3x_1^2 - a_{34i}x_2^2\xi^2x_1^2\\
&+a_{3i}x_2^2\xi^2x_1^2 - a_{34i}\xi^2x_1^2 + a_{3i}\xi^2x_1^2\\
&+4a_{34i}x_2\xi^2x_1^2 - 4a_{3i}x_2\xi^2x_1^2 - 4x_2^2\xi x_1^2\\
&+12x_2\xi x_1^2 - 8\xi x_1^2 + 4a_{34i}\xi^6x_1 - 4a_{3i}\xi^6x_1 - 6a_{34i}\xi^5x_1\\
&+6a_{3i}\xi^5x_1 - 2a_{34i}x_2\xi^5x_1 + 2a_{3i}x_2\xi^5x_1 - 8x_2\xi^5x_1\\
&+4\xi^5x_1 + 4a_{34i}x_2\xi^4x_1 - 4a_{3i}x_2\xi^4x_1 - 4x_2^2\xi^3x_1\\
&+2a_{34i}\xi^3x_1 - 2a_{3i}\xi^3x_1 - 2a_{34i}x_2\xi^3x_1 + 2a_{3i}x_2\xi^3x_1\\
&+16x_2\xi^3x_1 - 8\xi^3x_1 + 4x_2^2\xi x_1\\
&-8x_2\xi x_1 + 4\xi x_1 - a_{34i}\xi^6 + a_{3i}\xi^6 + 2a_{34i}\xi^5\\
&-2a_{3i}\xi^5 + 4x_2\xi^5 - a_{34i}\xi^4 + a_{3i}\xi^4\\
&+4x_2^2\xi^3 - 4x_2\xi^3 + a_{34o}(\xi+1)^2(x_1+\xi)^2(x_1^2 - (\xi+1)x_1\\
&+x_2^2 + x_2(\xi-1) + \xi)^2\\
&-a_{3o}(\xi+1)^2(x_1+\xi)^2(x_1^2 - (\xi+1)x_1\\
&+x_2^2 + x_2(\xi-1) + \xi)^2))))\Big)\Big(4(\xi^2-1)^2\\
&\times((\xi+x_1)((\xi+1)v_i'(-\xi+x_1+2x_2-2)\\
&-(\xi+x_1)(-\xi+x_2-1)) - (\xi+1)u_i'\\
&\times((\xi+1)v_i'(-\xi+x_2-1) + (\xi+x_1)^2))\\
&\times((\xi-1)u_o'((\xi-1)v_o'(\xi+x_2-1)\\
&-(x_1-\xi)^2) + (x_1-\xi)((\xi-1)v_o'\\
&\times(\xi+x_1+2x_2-2)(x_1-\xi)(\xi+x_2-1)))\Big)^{-1},
\end{aligned}
$$

$$
\begin{aligned}
A_4 \;=\; & \Big(-2(h(a_{34i}-a_{3i})(\xi+x_1)(\xi-x_2+1)^2 \\
& \times((\xi-1)u_o'((\xi-1)v_o'(\xi+x_2-1)-(x_1-\xi)^2) \\
& +(x_1-\xi)((\xi-1)v_o'(\xi+x_1+2x_2-2) \\
& +(x_1-\xi)(\xi+x_2-1))) - a_{34o}(h-1)(x_1-\xi) \\
& \times(\xi+x_2-1)^2((\xi+1)u_i'((\xi+1)v_i'(-\xi+x_2-1) \\
& +(\xi+x_1)^2) - (\xi+x_1)((\xi+1)v_i' \\
& \times(-\xi+x_1+2x_2-2) - (\xi+x_1)(-\xi+x_2-1))) \\
& +a_{3o}(h-1)(x_1-\xi)(\xi+x_2-1)^2 \\
& \times((\xi+1)u_i'((\xi+1)v_i'(-\xi+x_2-1) \\
& +(\xi+x_1)^2) - (\xi+x_1)((\xi+1)v_i'(-\xi+x_1+2x_2-2) \\
& -(\xi+x_1)(-\xi+x_2-1))))\Big) \\
& \times\Big(((\xi+1)u_i'((\xi+1)v_i'(-\xi+x_2-1) \\
& +(\xi+x_1)^2) - (\xi+x_1) \\
& \times((\xi+1)v_i'(-\xi+x_1+2x_2-2) \\
& -(\xi+x_1)(-\xi+x_2-1)))((\xi-1)u_o'((\xi-1)v_o'(\xi+x_2-1) \\
& -(x_1-\xi)^2) + (x_1-\xi)((\xi-1)v_o' \\
& \times(\xi+x_1+2x_2-2) + (x_1-\xi)(\xi+x_2-1)))\Big)^{-1},
\end{aligned}
\tag{8.21}
$$

$$
\begin{aligned}
A_5 \;=\; & \Big((h-1)u_i'(x_2+\xi-1)((x_1+\xi)^2 \\
& +v_i'(x_2-\xi-1)(\xi+1))((a_{34o}-a_{3o})x_1^3 \\
& -(a_{34o}-a_{3o})(2\xi+1)x_1^2+((a_{34o}-a_{3o}+1)x_2^2 \\
& +(a_{34o}-a_{3o}+2)(\xi-1)x_2 \\
& +(a_{34o}-a_{3o}+1)\xi^2+2(a_{34o}-a_{3o}-1)\xi+1)x_1 \\
& -a_{34o}\xi^2+a_{3o}\xi^2-\xi^2+2\xi \\
& -x_2(\xi-1)(a_{34o}\xi-a_{3o}\xi+2) \\
& +x_2^2(-a_{34o}\xi+a_{3o}\xi-1)-1)(\xi+1)^2+(x_1+\xi) \\
& \times(x_2+\xi-1)(v_i'(x_1+2x_2-\xi-2)(\xi+1) \\
& +(x_2-\xi-1)(x_1+\xi))((a_{34o}-a_{3o})x_1^3 \\
& -(a_{34o}-a_{3o})(2\xi+1)x_1^2+((a_{34o}-a_{3o}+1)x_2^2 \\
& +(a_{34o}-a_{3o}+2)(\xi-1)x_2 \\
& +(a_{34o}-a_{3o}+1)\xi^2+2(a_{34o}-a_{3o}-1)\xi+1)x_1 \\
& -a_{34o}\xi^2+a_{3o}\xi^2-\xi^2+2\xi \\
& -x_2(\xi-1)(a_{34o}\xi-a_{3o}\xi+2) \\
& +x_2^2(-a_{34o}\xi+a_{3o}\xi-1)-1)(\xi+1) \\
& -h(u_o'(x_2-\xi-1)(v_o'(\xi-1)(x_2+\xi-1) \\
& -(x_1-\xi)^2)((a_{34i}-a_{3i})x_1^3-(a_{34i}-a_{3i}) \\
& \times(x_2-3\xi)x_1^2+(x_2^2-((a_{34i}-a_{3i}+2)\xi+2)x_2 \\
& +(2a_{34i}-2a_{3i}+1)\xi^2 \\
& +(-a_{34i}+a_{3i}+2)\xi+1)x_1-x_2^2-a_{34i}\xi^2 \\
& +a_{3i}\xi^2-\xi^2+2x_2+2x_2\xi-2\xi-1)(\xi-1)^2 \\
& +v_i'(x_1+2x_2-\xi-2)(\xi+1)^2(x_1+\xi)(x_2 \\
& +\xi-1)((a_{34o}-a_{3o})x_1^3-(a_{34o}-a_{3o}) \\
& \times(2\xi+1)x_1^2+((a_{34o}-a_{3o}+1)x_2^2 \\
& +(a_{34o}-a_{3o}+2)(\xi-1)x_2+(a_{34o}-a_{3o}+1)\xi^2 \\
& +2(a_{34o}-a_{3o}-1)\xi+1)x_1-a_{34o}\xi^2 \\
& +a_{3o}\xi^2-\xi^2+2\xi-x_2(\xi-1)(a_{34o}\xi-a_{3o}\xi+2) \\
& +x_2^2(-a_{34o}\xi+a_{3o}\xi-1)-1) \\
& +(x_2-\xi-1)(v_o'(x_1-\xi)(x_1+2x_2+\xi-2)((a_{34i}-a_{3i})2(x_1^3 \\
& -(a_{34i}-a_{3i})(x_2-3\xi)x_1^2 \\
& +(x_2^2-((a_{34i}-a_{3i}+2)\xi+2)x_2+(2a_{34i}-2a_{3i}+1)\xi^2 \\
& +(-a_{34i}+a_{3i}+2)\xi+1)x_1-x_2^2-a_{34i}\xi^2+a_{3i}\xi^2 \\
& -\xi^2+2x_2+2x_2\xi-2\xi-1)(\xi-1)^2 \\
& +(x_2+\xi-1)((-\xi a_{3i}+a_{3i}+a_{3o}+a_{34i}(\xi-1) \\
& +a_{3o}\xi-a_{34o}(\xi+1))x_1^5
\end{aligned}
\tag{8.22}
$$

$$
\begin{aligned}
&+(-((a_{34i}-a_{3i})(x_2-\xi)(\xi-1))+a_{34o}(\xi+1)\\
&-a_{3o}(\xi+1))x_1^4+(2a_{34o}\xi^3+3a_{3i}\xi^3\\
&-2a_{3o}\xi^3+2a_{34o}\xi^2-2a_{3i}\xi^2-2a_{3o}\xi^2\\
&+2\xi^2-a_{3i}\xi+a_{34i}(-3\xi^3+2\xi^2+\xi)\\
&+x_2^2(\xi a_{3o}+a_{3o}-a_{34o}(\xi+1)-2)\\
&-x_2(\xi-1)(-a_{34i}\xi+a_{3i}\xi+4\xi+a_{34o}(\xi+1)\\
&-a_{3o}(\xi+1)+4)-2)x_1^3+((-a_{34i}+a_{3i}-4)\xi^4\\
&+2(a_{34i}-a_{34o}-a_{3i}+a_{3o})\xi^3\\
&+(-a_{34i}-2a_{34o}+a_{3i}+2a_{3o}+2)\xi^2-x_2(\xi-1)\\
&\times((-a_{34i}+a_{34o}+a_{3i}-a_{3o})\xi^2\\
&+(a_{34o}-a_{3o}-4)\xi-4)+x_2^2(-4\xi^2-a_{34o}(\xi+1)\xi\\
&+a_{3o}(\xi+1)\xi+2)+2)x_1^2\\
&+\xi^2(-a_{34o}\xi^3-2a_{3i}\xi^3+a_{3o}\xi^3-a_{34o}\xi^2\\
&+a_{3i}\xi^2+a_{3o}\xi^2+6\xi^2+a_{3i}\xi\\
&+a_{34i}(2\xi^2-\xi-1)\xi+x_2^2(a_{34o}(\xi+1)-a_{3o}(\xi+1)+2)\\
&+x_2(\xi-1)(-a_{34i}\xi+a_{3i}\xi-4\xi+a_{34o}(\xi+1)\\
&-a_{3o}(\xi+1)-4)-6)x_1\\
&+\xi^2((-a_{34i}+a_{34o}+a_{3i}-a_{3o})\xi^3\\
&+(a_{34i}+a_{34o}-a_{3i}-a_{3o}-2)\xi^2\\
&+x_2(a_{34o}\xi-a_{3o}\xi+4)(\xi^2-1)\\
&+x_2^2(a_{34o}\xi(\xi+1)-a_{3o}\xi(\xi+1)+2)+2))))\Big)\\
&\times\Big((\xi-1)(\xi+1)((\xi+x_1)((\xi+1)v_i'\\
&\times(-\xi+x_1+2x_2-2)-(\xi+x_1)(-\xi+x_2-1))\\
&-(\xi+1)u_i'((\xi+1)v_i'(-\xi+x_2-1)\\
&+(\xi+x_1)^2))((\xi-1)u_o'((\xi-1)v_o'(\xi+x_2-1)\\
&-(x_1-\xi)^2)+(x_1-\xi)((\xi-1)v_o'(\xi+x_1+2x_2-2)\\
&+(x_1-\xi)(\xi+x_2-1)))\Big)^{-1},
\end{aligned}
$$

$$
\begin{aligned}
A_6 \;=\; & \Big(h(\xi-1)(a_{34i}-a_{3i})(\xi-x_2+1)^2 \\
& \times(-\xi+x_1^2+2\xi x_1-x_1x_2)((\xi-1)u_o' \\
& \times((\xi-1)v_o'(\xi+x_2-1)-(x_1-\xi)^2) \\
& +(x_1-\xi)((\xi-1)v_o'(\xi+x_1+2x_2-2) \\
& +(x_1-\xi)(\xi+x_2-1))) \\
& -a_{34o}(h-1)(\xi+1)(\xi+x_2-1)^2 \\
& \times(\xi+x_1^2-(\xi+1)x_1+x_2^2+(\xi-1)x_2) \\
& \times((\xi+1)u_i'((\xi+1)v_i'(-\xi+x_2-1) \\
& +(\xi+x_1)^2)-(\xi+x_1)((\xi+1)v_i' \\
& \times(-\xi+x_1+2x_2-2)-(\xi+x_1)(-\xi+x_2-1))) \\
& +a_{3o}(h-1)(\xi+1)(\xi+x_2-1)^2(\xi+x_1^2 \\
& -(\xi+1)x_1+x_2^2+(\xi-1)x_2)((\xi+1) \\
& \times u_i'((\xi+1)v_i'(-\xi+x_2-1)+(\xi+x_1)^2) \\
& -(\xi+x_1)((\xi+1)v_i' \\
& \times(-\xi+x_1+2x_2-2)-(\xi+x_1) \\
& \times(-\xi+x_2-1)))\Big)\Big((\xi-1)(\xi+1) \\
& \times((\xi+x_1)((\xi+1)v_i'(-\xi+x_1+2x_2-2) \\
& -(\xi+x_1)(-\xi+x_2-1)) \\
& -(\xi+1)u_i'((\xi+1)v_i'(-\xi+x_2-1)+(\xi+x_1)^2)) \\
& \times((\xi-1)u_o'((\xi-1)v_o' \\
& \times(\xi+x_2-1)-(x_1-\xi)^2) \\
& +(x_1-\xi)((\xi-1)v_o'(\xi+x_1+2x_2-2) \\
& +(x_1-\xi)(\xi+x_2-1)))\Big)^{-1},
\end{aligned}
\tag{8.23}
$$

$$
\begin{aligned}
A_7 \;=\;& h((\bar{a}_{1i}-a_{34i})(\Lambda_N^2-(\bar{a}_{1i}(\xi+1) \\
&+2a_{34i}(\xi+1)-3x_2)^2(9(\xi+1)^2(\bar{a}_{1i}-a_{34i})^2)^{-1}) \\
&+(1-\bar{a}_{1i})(M^2-\frac{1}{9})(a_{34i}-a_{3i}) \\
&\times(-((\xi+1)(u_i'-v_i')(\xi-x_2+1)(\lambda_q^2(\xi+1)(u_i'-v_i') \\
&+M^2(\xi-(\xi+1)u_i'+\xi v_i'+v_i'-x_2+1))) \\
&\times((\xi+1)u_i'((\xi+1)v_i'(-\xi+x_2-1) \\
&+(\xi+x_1)^2)-(\xi+x_1)((\xi+x_1)(\xi-x_2+1) \\
&-(\xi+1)v_i'(\xi-x_1-2x_2+2)))^{-1}-\frac{4}{9}) \\
&+a_{3i}(\widetilde{M}^2-\frac{4}{9})+(\frac{x_2}{\xi+1}-\frac{1}{3})^2) \\
&+(1-h)((\bar{a}_{1o}-a_{34o})(\Lambda_N^2-((\bar{a}_{1o}(\xi-1) \\
&+2a_{34o}(\xi-1)+3x_2)^2)(9(\xi-1)^2(\bar{a}_{1o}-a_{34o})^2)^{-1}) \\
&+(1-\bar{a}_{1o})(M^2-\frac{1}{9}) \\
&+(a_{34o}-a_{3o})(((\xi-1)(u_o'-v_o')(\xi+x_2-1) \\
&\times(\lambda_q^2(\xi-1)(u_o'-v_o') \\
&+M^2(\xi-\xi u_o'+u_o'+(\xi-1)v_o'+x_2-1))) \\
&\times((\xi-1)u_o'((\xi-1)v_o'(\xi+x_2-1) \\
&-(x_1-\xi)^2)+(x_1-\xi)((\xi-1)v_o'(\xi+x_1+2x_2-2) \\
&+(x_1-\xi)(\xi+x_2-1)))^{-1} \\
&-\frac{4}{9})+a_{3o}(\widetilde{M}^2-\frac{4}{9})+(\frac{x_2}{1+\xi}-\frac{1}{3})^2),
\end{aligned}
\tag{8.24}
$$

8.8 . Acronyms

- ANN: Artificial Neural Network
- AMC: Adaptive Monte Carlo
- BH: Bethe-Heitler
- BSA: Bethe-Salpeter Amplitude
- CFF: Compton Form Factor
- DA: Distribution Amplitude
- DD: Double Distribution
- DGLAP: Dokshitzer–Gribov–Lipatov–Altarelli–Parisi
- DIS: Deep Inelastic Scattering

- DVCS: Deeply Virtual Compton Scattering
- DVMP: Deeply Virtual Meson Production
- EMC: European Muon Collaboration
- EMT: Energy Momentum Tensor
- ERBL: Efremov-Radyushkin-Brodsky-Lepage
- (E)FF: (Electromagnetic) Form Factor
- GK: Goloskokov-Kroll
- GPD: Generalized Parton Distribution
- HEPL: Hansen Experimental Physics Laboratory
- IPD: Impact Parameter Distribution
- IR: Infrared (Low energy)
- LFWF: Light Front Wave Function
- MAD: Median Absolute Deviation
- (N^j)LO: (Next to)^{j}Leading Order
- (q)OAM: (quark) Orbital Angular Momentum
- PDF: Parton Distribution Function
- (p)QCD: (perturbative) Quantum Chromodynamics
- QFT: Quantum Field Theory
- SLAC: Stanford Linear Accelerator Center
- UV: Ultraviolet (High energy)

8.9 . Abbreviations

- eff: Subscript, "Effective", labels objects related to the remnants of mass and momentum dependence left over after the $q^{3,4}$ dependence
- rep: Subscript, labels objects of or pertaining to GPD replicas i.e. ANN generated candidate GPDs
- Latt.: Superscript, "Lattice", labels statistics of the generated mock lattice data

9 - Résumé détaillé en Français

9.1 . Introduction

In the 1960s, Gell-Mann proposed a quark model to explain a large spectrum of spin and charge values [4]. He introduced three flavors of spin-$\frac{1}{2}$ quarks: "up" (u), "down" (d), and "strange" (s), with charges $\frac{2}{3}$, $-\frac{1}{3}$, and $-\frac{1}{3}$, respectively. Quark spins were constrained to (anti)align to match the baryon spins. The Δ^{++} particle, with three u quarks and a total charge of $+2$, was problematic due to the exclusion principle. To solve this, [5, 6] introduced a "color" gauge group, SU(3), adding a quantum number called "color charge" with three values. This allowed each u quark in the Δ^{++} to have a different color, satisfying the exclusion principle.
The non-Abelian SU(3) gauge group had significant consequences for the strong force, leading to Quantum Chromodynamics (QCD). The Lagrangian density of Quantum Electrodynamics (QED) describes spin-1/2 particles (e.g., electrons) and electromagnetic fields, including terms for the fermionic field ψ, gauge covariant derivative D_μ, electromagnetic field tensor $F_{\mu\nu}$, and fermion mass m. QCD's Lagrangian density describes quarks and gluons, including terms for the quark field ψ, gauge covariant derivative D_μ with strong coupling constant g_s, gluon field tensor $G^a_{\mu\nu}$, and quark mass m. The β functions of QED and QCD determine the scale dependence of their coupling constants. In QED, the coupling increases with energy scale, leading to the Landau pole. In QCD, the coupling decreases at high energies (asymptotic freedom) and increases at low energies, leading to confinement. This implies that only color-neutral states are observable, a property known as color confinement.

9.1.1 . Comparison with Experiment

To compare experimental results with theoretical predictions, theoretical calculations must be structured to match experimental observables. Experimental interactions and their probabilities are tabulated as cross sections, calculated from sums of interaction amplitudes. Perturbation theory is one method to express these amplitudes theoretically. In Quantum Electrodynamics (QED), the coupling constant e allows for useful perturbative expansions at low energy scales, with the QED Landau pole presenting no practical issue for calculations corresponding to current experiments. However, in Quantum Chromodynamics (QCD), the Landau pole occurs at a relatively low energy scale Λ_{QCD}, rendering perturbative QCD (pQCD) ineffective alone for understanding nucleon substructure.
Deeply Inelastic Scattering (DIS) is a process revealing nucleon structure. Factorization, the process of separating the cross section into perturbatively cal-

culable and hard parts and corresponding perturbatively inaccessible soft parts, has been proven for DIS, allowing predictions based on Parton Distribution Functions (PDFs). However, extracting these PDFs from experimental data poses challenges due to the convolution involved which makes the separation of the contributions due to individual quark flavors difficult.
The European Muon Collaboration (EMC) "discovered" the nucleon spin crisis, revealing unexpected contributions to nucleon spin from QCD states beyond valence quarks, inspiring investigations into Generalized Parton Distributions (GPDs) to understand nucleon structure further. Deeply Virtual Compton Scattering (DVCS) and Deeply Virtual Meson Production (DVMP) are experimental processes that allow probing the partonic substructure of nucleonic targets. DVCS involves an incoming leptonic probe interacting with a nucleonic target, resulting in an unbroken nucleon in the final state along with a second, final state photon and lepton. DVMP, on the other hand, produces a meson in the final state in place of DVCS's final state photon. Both processes involve factorization, where contributions from the soft and hard parts of the interaction are separated. The nucleon Generalized Parton Distributions (GPDs), denoted as $H(x, \xi, t)$ and $E(x, \xi, t)$, describe the correlations of the average partonic momentum fraction x for the active parton, the light-cone kick parameter ξ, called the skewness, and the t, the squared momentum transfer of the nucleon in the interaction. They are given in terms of matrix elements involving quark and gluon fields. They satisfy various constraints, such as even parity with respect to ξ and polynomiality properties. These GPDs contribute to Compton Form Factors (CFFs), which are convolutions of GPDs with a kernel function. These CFFs are used in the expression for the experimental cross-section. Furthermore, GPDs are connected to Electromagnetic Form Factors (EFFs), which describe the internal structure of nucleons The total angular momentum carried by quarks is related to the first Mellin moments of the quark GPDs and is known as Ji's sum rule. Additionally, Impact Parameter Distributions (IPDs) and Ioffe-time distributions provide alternative representations of GPDs in position-momentum space and momentum-spatial space, respectively.
In addition, in the coming years, in addition to experimental data we expect lattice QCD to provide useful data.

9.2 . Reweighting

9.2.1 . Artificial Neural Networks

In an ongoing effort to distinguish among the myriad candidate Generalized Parton Distributions (GPDs) in an unbiased manner while ensuring adherence to all necessary theoretical constraints. Artificial Neural Networks (ANNs) have been employed to model GPDs. An example is the work by

Dutrieux et al. [69], where Goloskokov-Kroll (GK) GPD pseudodata was utilized to train ANNs. These ANNs were designed to produce candidate functions satisfying most GPD properties. To assess further discrimination among the candidate functions, mock lattice QCD data, systematically varied for compatibility with the candidate functions, was introduced.
Neural networks consist of layers of nodes. Feed forward neural networks, like the ones used in this study, have connections only between adjacent layers. The output of each node j in layer $i > 1$ is calculated using activation functions and weighted sums of inputs from the previous layer. Universal approximation theorems guarantee that sufficiently large networks can approximate any continuous function on a compact set. Activation functions, often sigmoid functions, interpolate between 0 and 1. Notably, in the ANN models used here, the activation function arguments feature nonlinearity in the input variables α and β to ensure the fulfillment of certain GPD properties.
The ANN's hidden layer neurons perform specific calculations to reproduce certain properties of GPDs. Three extractions of GPDs using pseudo-data generated with the GK model were performed, with different training datasets and constraints. The genetic algorithm was employed for parameter minimization, with regularization used to prevent biased results due to overfitting. Dropout regularization was utilized, randomly dropping a predefined fraction of neurons in each iteration of the minimization algorithm to prevent fixation on training data details. This section focuses on the modeling of the GPD $H(x, \xi, t)$, with t set to zero to examine the $x - \xi$ plane exclusively. Represented in terms of the Radon transform of a Double Distribution (DD), the ANN models discussed here aim to model the DDs corresponding to H. Specifically, the odd combination $H^{q(+)}(x, \xi, 0) = H^q(x, \xi, 0) - H^q(-x, \xi, 0)$, representing the sea quark GPD, is studied. To achieve flexibility and reproduce known limits, the DD model comprises three terms: F_C, F_S, and F_D. F_C is designed to reproduce the forward limit and model the $x = \xi$ line, F_S aims to reproduce deconvolution uncertainty and vanishes at certain lines, and F_D models the D-term. F_C is defined to ensure the proper reduction to the forward limit and flexibility to model the $x = \xi$ line. F_S aims to reproduce deconvolution uncertainty and is written as the difference of two profile functions. Lastly, F_D provides flexibility to model the D-term, crucial in characterizing partonic matter.
Instead of using proper experimental data, Goloskokov-Kroll (GK) pseudodata was employed as a proof of concept for the implementation of the network architecture used in GPD modeling. The GK model, originally developed for DVMP, has been successful in reproducing experimental measurements. The GK pseudodata is limited by the assumptions inherent in the GK model.

9.2.2 . Analysis

Statistical techniques such as Median Absolute Deviation (MAD) are discussed as a method for estimating uncertainty, particularly when defining outliers in the data set is challenging. MAD provides a robust estimation of standard deviation without the need for defining outliers explicitly, making it suitable for analyzing data sets where defining outliers may be arbitrary. The comparison between standard deviation and MAD illustrates the robustness of MAD in estimating the spread of data sets, particularly in the presence of outliers. Now understanding both the origin of the GPD replicas (candidate functions) and an important statistical estimator to be employed later in the corresponding chapter, it is necessary to take a look at the reasoning for which and method by which mock lattice data has been generated for the forthcoming impact study of its discriminating effect with respect to the ANN GPD replicas. These two points are respectively delineated as well.

9.2.3 . Mock Lattice Data

The choice to use mock lattice data for this impact study is informed by two key points. The first of these reasons is a lack of access to lattice data. The second, which is an advantage rather than a disadvantage of using mock data, is the ability to systematically control the agreement of the mock data with the set of GPD replicas considered. This systematic control was achieved via the use of parameters controlling the precision and the correlation of the mock lattice data. Based on actual lattice studies such as the one cited, one draws the conclusion that current state-of-the-art lattice GPD extractions are not equally facilitated in all kinematic ranges. Lattice GPD data is typically presented in Ioffe-time space, as calculations occur on an Euclidean spacetime lattice, rather than in momentum space. However, it is worth noting that the lattice data after which the mock lattice data generated in this study was modeled was not matched to the lightcone, but exists along some Euclidean direction. Therefore, a proper study comparing replica to mock lattice data would not have taken place on the lightcone, but off the lightcone. Therefore, all calculations comparing and combining ANN GPD replicas to mock lattice data are performed in Ioffe-time space. As the ANN fitted singlet GPD, H, of the nucleon is that which is treated here, its odd parity in the longitudinal momentum fraction x allows the limitation of the corresponding Ioffe-time studies to the imaginary part of H. This method generates mock lattice data which is in general compatible with the central value of the band of replicas within the precision generated by the function g. However, thus far, the data generation treats all mock lattice data points as uncorrelated. To take this into account in our impact study, mock lattice data is generated in three distinct Ioffe-time regions, wherein intracollaboration correlation is set to $0 \leq c < 1$, and intercollaboration correlation is set to zero. Fig. 9.1 illustrates a mock lattice dataset overlaid with the replicas generated by our GPD model. With a

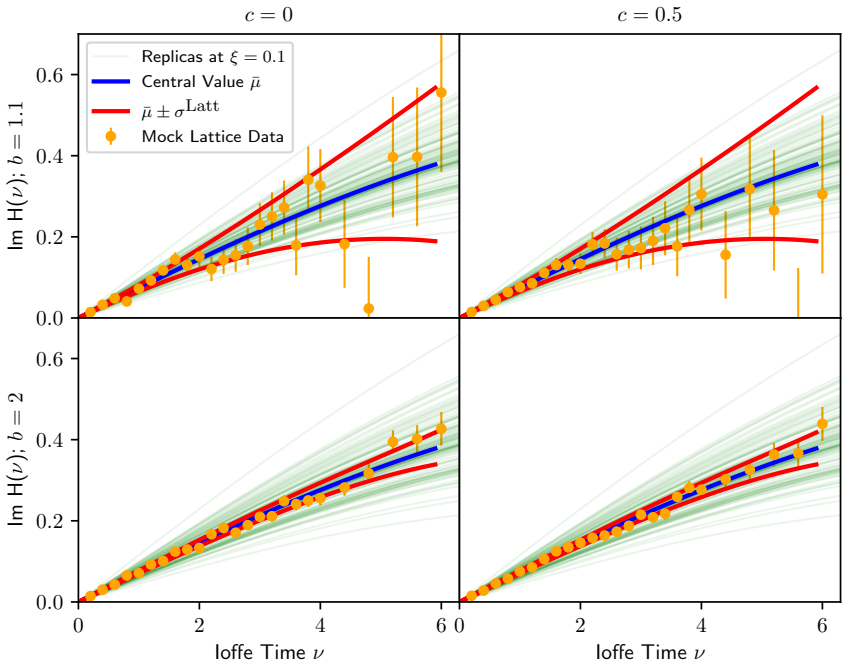

Figure 9.1: Shown are the ensemble of GPD replicas spanning Ioffe times from $\nu = 0$ to $\nu = 6$ at $\xi = 0.1$ (indicated in green), along with their median (in blue) and the 1σ band (in red), which corresponds to $b = 1.1$ (top) and $b = 2$ (bottom). Additionally, the mock lattice data set generated accordingly with $c = 0$ (left) and $c = 0.5$ (right) is depicted in orange.

method for generating systematically controlled mock lattice data in terms of both its precision and adherence to the set of GPD replicas, and the correlation between all such generated data in hand, it is now possible to influence the associated uncertainty of the replica band using such mock lattice data to assess the potential discriminating ability of lattice data. In the study discussed here, a Bayesian reweighting procedure employing the mock lattice data as a prior was chosen, aiming to investigate the resulting uncertainty of the set of GPD replicas without costly refits. So far, the discussion largely ignored the skewness of the GPD, focusing on analysis in x and ν. In the final sections, discussions of skewness will play an important role, necessitating an outline of the Bayesian reweighting procedure employed. The precise procedure delineates the assignment of weights to each replica based on their agreement with the mock lattice data, leading to a reweighted median and standard deviation of the replica set. These quantities provide a measure of uncertainty reduction on the band of replicas.

9.2.4 . Results of Reweighting

	Data			Results		
ξ_{Used}	Precision	Correlation	ξ_{Shown}	τ	r_ν	$r_{\ln x}$
0.1	Low	Low	0.1 / 0.5	0.47	0.25 / 0.92	0.82 / 1.24
0.1	Low	High	0.1 / 0.5	0.83	0.85 / 0.93	1.02 / 1.15
0.1	High	Low	0.1 / 0.5	0.30	0.16 / 0.90	0.78 / 1.08
0.1	High	High	0.1 / 0.5	0.46	0.23 / 0.91	0.82 / 1.23
0.5	Low	Low	0.5	0.36	0.44	0.67
0.5	Low	High	0.5	0.52	0.58	0.64
0.5	High	Low	0.5	0.11	0.25	0.54
0.5	High	High	0.5	0.37	0.51	0.77
0.1 0.2 0.3	Low	Low	0.5	0.30	0.62	0.95
0.1 0.2 0.3	Low	High	0.5	0.77	0.82	1.00
0.1 0.2 0.3	High	Low	0.5	0.10	0.34	0.54
0.1 0.2 0.3	High	High	0.5	0.30	0.61	0.73
0.1 0.2 0.3 0.4 0.5	Low	Low	0.5	0.16	0.19	0.66
0.1 0.2 0.3 0.4 0.5	Low	High	0.5	0.57	0.65	0.75
0.1 0.2 0.3 0.4 0.5	High	Low	0.5	0.03	0.13	0.45
0.1 0.2 0.3 0.4 0.5	High	High	0.5	0.18	0.25	0.77

Table 9.1: Results as dependent on the reweighting parameters. Low Correlation: $c = 0$, High Correlation: $c = 0.5$, Low Precision: $b = 1.1$, High Precision: $b = 2$. $r_{\ln x}$: Average uncertainty retainment in x, r_ν: Average uncertainty retainment in ν, τ: Effective fraction of replicas retained post-reweighting.

We compare the uncertainty retainments resulting from different amounts of mock lattice data at low to mid skewness levels ($\xi \in \{0.1\}$, $\xi \in \{0.1, 0.2, 0.3\}$, $\xi \in \{0.1, 0.2, 0.3, 0.4, 0.5\}$) with those observed in the previous section at purely midrange skewness. The key findings include:

- Reweighting with large uncertainties and low precision ($b = 1.1$) and correlated data ($c = 0.5$) significantly reduces uncertainty in Ioffe-time at $\xi = 0.5$.

- Adding data at $\xi = 0.1$ improves uncertainty retainment at $\xi = 0.5$, but further inclusion of data at $\xi \in \{0.1, 0.2, 0.3\}$ and $\xi \in \{0.1, 0.2, 0.3, 0.4, 0.5\}$ tightens uncertainty retainment at $\xi = 0.5$. However, direct reweighting at $\xi = 0.5$ with $b = 2$ and $c = 0.5$ yields better results.

Furthermore, we present a Tab. (9.1) illustrating the impact of varying levels of noise and correlation on the retention processes. Additionally, we use Fig. 9.2 to compare reweighting effects at various values of ξ by presenting the effective fraction of retained replicas (τ) and the retainment of uncertainty in both Ioffe-time and momentum space.

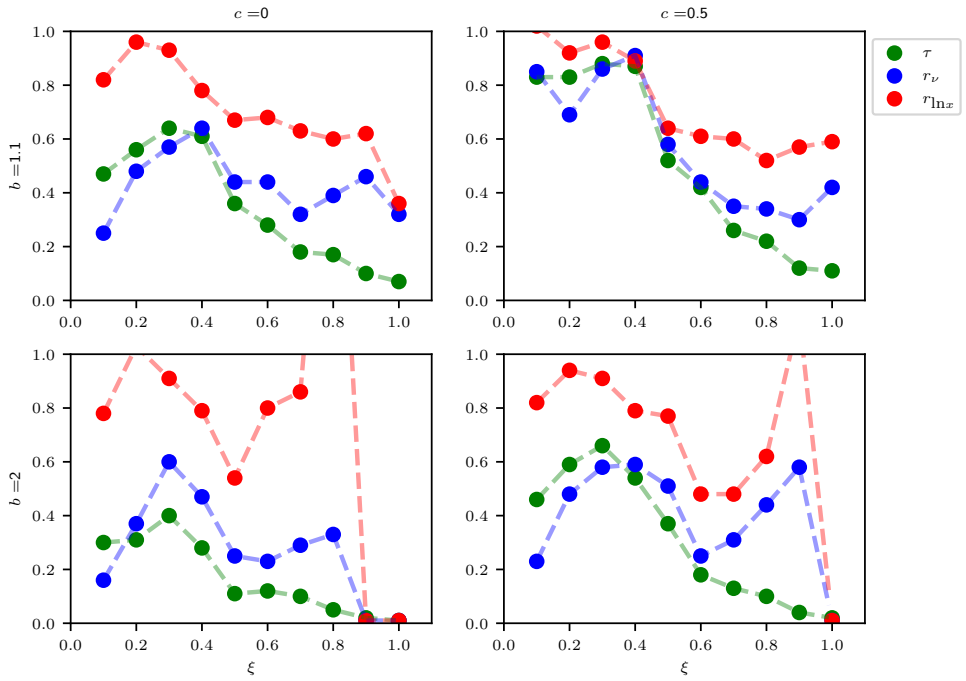

Figure 9.2: The effective fraction of replicas retained following reweighting τ (illustrated by the green curve), preservation of uncertainty in Ioffe time (shown by the blue curve), and in momentum space (represented by the red curve) for various combinations of high and low noise (designated as $b = 1.1$ and 2 respectively) and low and high correlation (indicated as $c = 0$ and 0.5 respectively).

Examining Fig. 9.2, we observe that at mid-range skewness, the effective fraction of retained replicas after reweighting (τ) is roughly equal in both low correlation low precision and high correlation high precision scenarios. This compensatory relationship between precision and correlation could guide lattice practitioners in allocating computational resources effectively.
It is important to note that by employing a Bayesian approach to merge experimental and lattice knowledge on GPDs, proving effective when lattice data aligns well with the prior model, has yielded approximately 40% uncertainty at midrange skewness. Nonetheless, our study underscores the necessity of addressing correlations within lattice data for a joint extraction, as real lattice data often exhibit high degrees of correlation and systematic effects that require careful management to prevent biases in uncertainty assessment.

9.3 . Continuum Techniques for GPD Modeling

The analysis pursued here of generalized parton distributions of nucleons involves expanding matrix elements using light-front wave functions (LFWFs). This approach elucidates the connection between nucleonic states and the amplitudes defined on the light front, offering insights into definite quark orbital angular momentum (OAM) contributions to GPDs and related objects. By examining the Fock expansion of nucleonic states in which LFWFs appear as momentum and quantum number dependent coefficient functions, one can consistently truncate such Fock expansions for practical computations, at the cost of limiting the kinematics of the computation to $|x| < |\xi|$. This allows the representation of GPDs to be expressed in terms of overlaps of LFWFs, including only the contributions from valence quarks.
The matrix element used to characterize the three-quark Fock states contributing to a nucleon state $|P;h\rangle$ (with $h = +\frac{1}{2}$) involves an operator that creates a color-neutral three-quark state. In momentum space, we represent this matrix element in terms of various tensorial structures which we then project onto definite quark helicity projection states, which correspond to definite qOAM values. This tensorial basis' components, imparted with corresponding coefficient functions called auxiliary functions some of whose linear combinations give the Light-Front Wave Functions, then provide a way to extract such LFWFs from a given model for such a matrix element via selective Dirac traces. By reducing the employed tensorial basis into a smaller set of tensors by enforcing u-quark symmetry and isospin symmetry, the LFWFs may be identified as has been done in the literature [90].

9.4 . Overlap Representation of GPDs

To characterize the contributions of three-quark states to Generalized Parton Distributions (GPDs) and related objects, we can take advantage of the overlap representation of GPDs [34]. This approach clarifies which pairs of three-quark Fock states contribute to GPDs by using their overlaps. Before beginning this section we define the convenient lightcone coordinates:

$$v = (v^+ \equiv \frac{v^0 + v^3}{\sqrt{2}}, \vec{v}_\perp \equiv (v_1, v_2), v^- \equiv \frac{v^0 - v^3}{\sqrt{2}}). \tag{9.1}$$

9.4.1 . Overlap Formula

The active quark's initial and final state momenta reflect the momentum transfer due to the interaction with the photon. To see which combinations of incoming and outgoing Fock combinations contribute, let's look at the involved quantum numbers. The collective quantum numbers $\mathcal{Q}_l$ for the lth quark are defined as:

- **Momentum**: $\kappa_l = (x_l, \vec{k}_{l\perp})$,
- **Helicity**: λ_l,
- **Color**: c_l,
- **Flavor**: f_l,

The overlap formula for the helicity dependent amplitude $\mathcal{H}^{\hat{f}}_{h'h}(\bar{x}, \xi, t)$ is given by:

$$\mathcal{H}^{\hat{f}}_{h'h}(x, \xi, t) = \frac{1}{2\sqrt{1-\xi^2}} \sum_{\hat{c}} \int \frac{dz^-}{2\pi} e^{ix\bar{P}^+ z^-} \langle P', h' | \bar{q}^{\hat{c}}_{\hat{f}}(-\frac{z}{2}) \gamma^+ q^{\hat{c}}_{\hat{f}}(\frac{z}{2}) | P, h \rangle \tag{9.2}$$

$$\equiv \mathcal{O}^{\hat{f}} \left[\varphi_{\hat{\mathbb{S}}_{\mathbb{A}}(\mathcal{Q}');h'}, \varphi_{\mathcal{Q};h} \right] (x, \xi, t), \tag{9.3}$$

where $\hat{f}$ is the active quark flavor, $\hat{c}$ is a color index, $P(')$ and $h(')$ are the incoming (outgoing) nucleon momenta and helicities, $z = (z^+ = 0, \vec{z}_\perp = \vec{0}_\perp, z^-)$ is a minus direction spatial vector, $\bar{P}^+$ is the average plus momentum of the nucleon, $\bar{q}^{\hat{c}}_{\hat{f}}(-\frac{z}{2})\gamma^+ q^{\hat{c}}_{\hat{f}}(\frac{z}{2})$ is a bilocal quark field bilinear, and $\hat{\mathbb{S}}_{\mathbb{A}}$ is the $\mathbb{A}$th permutation of the permutation group S_3 over all six of which we sum. Here, $\mathcal{O}^{\hat{f}}[\varphi', \varphi]$ represents the overlap function between the LFWFs of the initial and final states.

9.4.2 . Master Overlap Formula: GPDs and Subresults

The GPDs $H^{\hat{f}}$ and $E^{\hat{f}}$ are expressed in terms of the helicity dependent amplitudes:

$$H^{\hat{f}} = \mathcal{H}^{\hat{f}}_{\frac{1}{2},\frac{1}{2}} + \frac{\xi^2 2M_N|\vec{\Delta}_\perp|}{(\Delta_1 + i\Delta_2)\sqrt{1-\xi^2}\sqrt{\frac{4\xi^2 m^2}{\xi^2-1} - t}}\mathcal{H}^{\hat{f}}_{-\frac{1}{2},\frac{1}{2}} \tag{9.4}$$

$$E^{\hat{f}} = \frac{2M_N|\vec{\Delta}_\perp|\sqrt{1-\xi^2}}{(\Delta_1 + i\Delta_2)\sqrt{\frac{4\xi^2 M_N^2}{\xi^2-1} - t}}\mathcal{H}^{\hat{f}}_{-\frac{1}{2},\frac{1}{2}}, \tag{9.5}$$

We can represent the helicity dependent amplitudes in terms of LFWF overlaps, where our LFWFs Ψ_{h,λ_Σ} are labeled by the corresponding proton helicity h and the total quark helicity projection λ_Σ such that qOAM=$h - \lambda_\Sigma$. In terms of our definite quark orbital angular momentum (qOAM) LFWFs we have:

$$\begin{aligned}\mathcal{H}^{\hat{f}}_{\frac{1}{2},\frac{1}{2}} = \quad & \Big(\mathcal{O}^{\hat{f}}(\Psi_{\frac{1}{2},\frac{1}{2}},\Psi_{\frac{1}{2},\frac{1}{2}}) + \mathcal{O}^{\hat{f}}(\Psi_{\frac{1}{2},-\frac{1}{2}},\Psi_{\frac{1}{2},-\frac{1}{2}}) \\ & + \mathcal{O}^{\hat{f}}(\Psi_{\frac{1}{2},\frac{3}{2}},\Psi_{\frac{1}{2},\frac{3}{2}}) + \mathcal{O}^{\hat{f}}(\Psi_{\frac{1}{2},-\frac{3}{2}},\Psi_{\frac{1}{2},-\frac{3}{2}})\Big)\end{aligned} \tag{9.6}$$

$$\mathcal{H}^{\hat{f}}_{-\frac{1}{2},\frac{1}{2}} = \quad \Big(\mathcal{O}^{\hat{f}}(\Psi_{-\frac{1}{2},-\frac{3}{2}},\Psi_{\frac{1}{2},\frac{3}{2}}) + \mathcal{O}^{\hat{f}}(\Psi_{-\frac{1}{2},\frac{3}{2}},\Psi_{\frac{1}{2},-\frac{3}{2}})\Big). \tag{9.7}$$

While the helicity conserving amplitude receives only diagonal contributions in qOAM, the helicity flip one receives only off-diagonal contributions. This does not violate our expectations, as it means that the helicity flip GPD E, which receives contributions only from the helicity flip amplitude $\mathcal{H}_{-\frac{1}{2},\frac{1}{2}}$, receives only off-diagonal contributions in qOAM. Further, the PDF, which is related to the probability of finding a parton (quark here) of a particular flavor carrying a particular fraction of the longitudinal momentum of the nucleon, is given in the forward limit of the expression for the GPD H as

$$\begin{aligned}f^{\hat{f},\mathbb{P}}(x_{\mathsf{BJ}}) \quad = \quad & H^{\hat{f},\mathbb{P}}|_{t=\xi=0} = \\ & \Big(\mathcal{O}^{\hat{f},\mathbb{P}}(\Psi_{\frac{1}{2},\frac{1}{2}},\Psi_{\frac{1}{2},\frac{1}{2}}) + \mathcal{O}^{\hat{f},\mathbb{P}}(\Psi_{\frac{1}{2},-\frac{1}{2}},\Psi_{\frac{1}{2},-\frac{1}{2}}) \\ & + \mathcal{O}^{\hat{f},\mathbb{P}}(\Psi_{\frac{1}{2},\frac{3}{2}},\Psi_{\frac{1}{2},\frac{3}{2}}) + \mathcal{O}^{\hat{f},\mathbb{P}}(\Psi_{\frac{1}{2},-\frac{3}{2}},\Psi_{\frac{1}{2},-\frac{3}{2}})\Big)|_{t=\xi=0},\end{aligned} \tag{9.8}$$

which, though receiving only diagonal contributions in qOAM, interestingly receives non-zero qOAM contributions.

Now that we have specified the overlap representation to the three quark case and to the objects of our interest, and we know how to extract the LFWFs from a general three quark matrix element from the literature, we turn to modeling such a matrix element in order to perform such extractions.

9.5 . The Diquark Model

This work focuses on modeling nucleon properties using a quark-diquark approach, treating the diquark as a composite two-body system rather than

a point-like entity, which allows for the inclusion of diquark internal p-wave correlations often neglected in simpler models [103]. The analysis herein employs Bethe-Salpeter formalism and Faddeev equations [96] to characterize nucleon states and extends Euclidean space results to the lightcone through Mellin moments. This method involves constructing Light-Front Wave Functions (LFWFs) by addressing the complexities of translating models from Euclidean space (model Fadeev amplitudes) to the lightcone (as LFWFs).

9.5.1 . Mellin Reconstruction

To transform Faddeev amplitudes computed in Euclidean space into Light-Front Wave Functions (LFWFs) defined on the lightcone, we need to manage the transition of lightcone time arguments to zero. This involves integrating over specific parameters to handle momentum fractions and projections. In Minkowski space, the LFWF is given by:

$$\Psi(x_1, \vec{k}_{1\perp}; x_2, \vec{k}_{2\perp}) \quad = \quad N \int \mathrm{d}k^-_{1;M} \mathrm{d}k^-_{2;M} \chi(k_{1;M}, k_{2;M}), \tag{9.9}$$

where N is a normalization constant. Since computations are in Euclidean space, we use the Mellin transform to avoid complex contour integrations. The Mellin moment of a function $f(x)$ of order m is:

$$\int \mathrm{d}x\, x^m f(x), \tag{9.10}$$

with bounds $0 \leq x \leq 1$. Two functions with identical Mellin moments are equivalent [113]:

$$\int \mathrm{d}x\, x^m f(x) \quad = \quad \int \mathrm{d}x\, x^m g(x), \quad \forall m \in \mathbb{N} \tag{9.11}$$

$$\Rightarrow f(x) \quad = \quad g(x). \tag{9.12}$$

The longitudinal momentum fraction x_i in Euclidean variables is:

$$x_i^{m_i} \quad \equiv \quad \frac{(k_{E;i} \cdot n_E)^{m_i}}{(P_E \cdot n_E)^{m_i}}, \tag{9.13}$$

where $n_E^2 = 0$ ensures projection onto the $+$ lightcone component. Using Mellin moments, we reconstruct the $x_{1,2}$ dependence of LFWFs with:

$$\begin{aligned} & \int_0^1 \mathrm{d}x_1 \int_0^{1-x_1} \mathrm{d}x_2 x_1^{m_1} x_2^{m_2} \Psi(x_1, \vec{k}_{1\perp}; x_2, \vec{k}_{2\perp}) \\ \equiv \; & \text{Normalization} \int \mathrm{d}k^3_{1;E} \mathrm{d}k^4_{1;E} \mathrm{d}k^3_{2;E} \mathrm{d}k^4_{2;E} \frac{(k_{E;1} \cdot n_E)^{m_1}}{(P_E \cdot n_E)^{m_1}} \frac{(k_{E;2} \cdot n_E)^{m_2}}{(P_E \cdot n_E)^{m_2}} \\ & \mathrm{Tr}_{\text{Dirac}} \left\{ \Gamma_{\text{Proj.}} \chi(k_{1;E}, k_{2;E}) \right\}, \end{aligned} \tag{9.14}$$

where $\Gamma_{\text{Proj.}}$ is a Dirac structure used for extracting contributions. This method is discussed in [112].

9.5.2 . Identification of Mellin Variables

To compute fundamental contributions to the six LFWFs, a Euclidean quark-diquark correlation model of the nucleon is used. Tensorial structures are introduced, contracted, and Mellin moments are calculated to extract contributions to the LFWFs. Define the quark propagator as:

$$S(p) = [-i\gamma\cdot p + M_q]\, D_{M_q}(p^2), \tag{9.15}$$

$$D_M(s) = \frac{1}{s+M^2}, \tag{9.16}$$

and the Nakanishi representation of the simplest tensorial contribution to the diquark vertex using the basis l and q:

$$\eta_0\Gamma^0_\mu C^\dagger = i\gamma_5\int_{-1}^{1}\mathrm{d}z\rho_\nu(z)D_{\Lambda_q}(q_z), \tag{9.17}$$

with $q_z = q + \frac{z}{2}\left(\frac{2}{3}P - \ell\right)$ and $\rho_\nu(z)$ a Nakanishi weight function taken to be a polynomial. The diquark propagator in terms of diquark momentum K and a Nakanishi representation of the simplest tensorial contribution to the quark-diquark correlation are given respectively by:

$$\Delta^{0+}(K) = \frac{1}{K^2+\widetilde{M^2}}, \tag{9.18}$$

$$s_1 = i\eta\int_{-1}^{1}\mathrm{d}z\,\tilde{\rho}(z)\left[\frac{1}{(\ell_z^2+\Lambda_N^2)}\right]^3. \tag{9.19}$$

Here, P is defined as $(0,0,0,iM_N)$ and quark momenta are:

$$k_i \equiv \frac{P}{3}+\ell, \tag{9.20}$$

$$k_j \equiv \frac{P}{3}-\frac{\ell}{2}+q, \tag{9.21}$$

$$k_k \equiv \frac{P}{3}-\frac{\ell}{2}-q. \tag{9.22}$$

where q is the diquark internal momentum difference and l is another variable crafted to be real. The projected Faddeev amplitude when quark 1 is not included in the diquark (bystander) is:

$$\chi^{\uparrow,\downarrow,\uparrow}_{\alpha_3;\sigma} = S(k_2)_{\alpha_2\alpha_2'}[\Gamma^0(q,K)]_{\alpha_2'\alpha_3'}S(k_3)_{\alpha_3\alpha_3'}\Delta_0 S^T(k_1)_{\alpha_1'\alpha_1}s_{1\alpha_1',\sigma}. \tag{9.23}$$

Which can then be projected onto the quark helicity projections contributing to auxiliary function $\psi^{1,-1}$, the simplest qOAM$=0$ auxiliary function

$$\chi^{h_1,h_2,h_3}_{\alpha_1\alpha_2\alpha_3;\sigma} = (\not{n}L^\uparrow_{\alpha_3'\alpha_3}S_{\alpha_3\lambda}(k_3)\Gamma^{0T}_{\lambda\lambda'}S^T_{\lambda'\alpha_2}(k_2) \tag{9.24}$$

$$\times(L^\downarrow\not{n}^T(C^\dagger)^TL^\uparrow)_{\alpha_2\alpha_1}S_{\alpha_1\alpha_1'}(k_1)s_{1\alpha_1'\sigma}\Delta(k_2+k_3). \tag{9.25}$$

Projecting on γ^ν for the leading twist operator:

$$\frac{1}{4}\gamma_\nu \mathsf{Tr}[\gamma^\nu \not{n} L^\uparrow S(k_3)\Gamma^{0T} S^T(k_2)(L^\downarrow \not{n}^T (C^\dagger)^T L^\uparrow S(k_1)\mathcal{S}]\Delta(k_2+k_3)$$
$$= \frac{1}{2}\gamma_\nu n^\nu \mathsf{Tr}[S(k_3)\Gamma^{0T} S^T(k_2) L^\downarrow C^\dagger \not{n} L^\uparrow]\sigma_S(k_1) s_1(\ell, P_E)\mathsf{Tr}[\gamma^\nu \not{n} L^\uparrow \Delta(k_2+k_3)].$$

The essential approach for extraction is to compute the Mellin moments of the quark-diquark correlation model and use them to directly extract LFWFs. This avoids the complications of particularly messy contour integrations and leverages the integral moments to obtain LFWFs.
To combine the denominators of all of the structures of our model we use the Feynman parametrization, introducing quite a few variables over which to integrate. We can then identify the Mellin moments of the auxiliary function $\psi^{1,-1}$ as

$$\begin{aligned}
&\int_0^1 \mathrm{d}x_1 \int_0^{1-x_1} \mathrm{d}x_2 x_1^{m_1} x_2^{m_2} \psi^{1,-1}(x_1, \vec{k}_{1\perp}; x_2, \vec{k}_{2\perp}) \\
= &\int_0^1 \mathrm{d}\bar{\alpha} \int_0^{1-\bar{\alpha}} \mathrm{d}\beta' \int_0^{\beta'} \mathrm{d}v' \int_{\beta'}^{1-\bar{\alpha}} \mathrm{d}u' \int_0^{\bar{\alpha}} \mathrm{d}a_{34} \qquad (9.26)\\
&\int_{\bar{\alpha}}^1 \mathrm{d}\bar{a}_1 \int_0^{a_{34}} \mathrm{d}a_3 \\
&\bar{\alpha}^{m_1}\beta'^{m_2} \frac{g(\bar{\alpha}, \beta', u', v', a_{34}, \bar{a}_1, a_3, \vec{k}_{1\perp}, \vec{k}_{2\perp})}{h(\bar{\alpha}, \beta', u', v', a_{34}, \bar{a}_1, a_3, \vec{k}_{1\perp}, \vec{k}_{2\perp})} \\
\to &\ \psi^{1,-1}(x_1, \vec{k}_{1\perp}; x_2, \vec{k}_{2\perp}) \\
= &\int_0^{x_2} \mathrm{d}v' \int_{x_2}^{1-x_1} \mathrm{d}u' \int_0^{x_1} \mathrm{d}a_{34} \int_{x_1}^1 \mathrm{d}\bar{a}_1 \int_0^{a_{34}} \mathrm{d}a_3 \\
&\frac{g(x_1, x_2, u', v', a_{34}, \bar{a}_1, a_3, \vec{k}_{1\perp}, \vec{k}_{2\perp})}{h(x_1, x_2, u', v', a_{34}, \bar{a}_1, a_3, \vec{k}_{1\perp}, \vec{k}_{2\perp})} \qquad (9.27)
\end{aligned}$$

While we must perform a 5D integral over Feynman parameters to compute $\psi^{1,-1}$ at a single point, we now have an expression we can use. In the next section we show an example plot of zero transverse quark momentum.

9.6 . Results

Here we show a contour plot of the $x_{1,2,3}$ dependence of the auxiliary function $\psi^{1,-1}$. There is a noticeable symmetry between the momentum fractions $x_{2,3}$. Although there is some clear numerical instability, the longitudinal momentum fraction x_1, corresponding to the bystander quark (the one which does not participate in the diquark), carries in general a preferentially high portion of the longitudinal momentum.

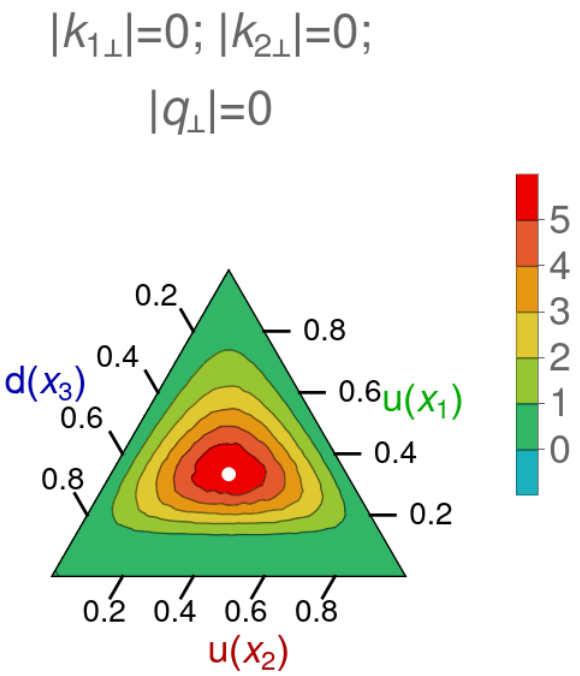

Figure 9.3: A Plot of the function $\psi^{1,-1}$ for $|\vec{k}_{1\perp}| = |\vec{k}_{2\perp}| = 0$ is shown. This plot is a contour plot, given on a triangular domain due to the momentum conservational constraint $1 = \sum_{i=1}^{3} x_i$. The normalization has not been set due to any physical constraints, and is consistent among all of the LFWF plots given in this document. The normalization is calculated by computing the largest value of $\psi^{1,-1}$ among all of the computed values, and scaling all plots such that that maximum value becomes 6, in order to align with the color scales of these plots. We remind the reader that the transverse momenta are given in units of the nucleon mass M_N.

9.6.1 . The PDF

To compute contributions of various Light-Front Wave Functions (LFWFs) to GPDs and their limits, we must first compute their overlaps. Starting with the function $\psi^{1,-1}$:

$$\begin{aligned}
\psi^{1,-1} \quad = \quad & \tilde{N}(\nu,\sigma)\int [df]\tilde{\rho}\rho_\nu(\bar{a}_1 - a_{34})^{\sigma-2}(a_{34}-a_3)^{\nu}(1-x_2)^{\nu+2}M_N^{-2(\sigma+2+\nu)} \\
& \times\Big[\frac{\ell_\perp^2}{M_N^2} + (1-\bar{a}_1)(\frac{M^2}{M_N^2}-\frac{1}{9}) + (\bar{a}_1 - a_{34})(\frac{\Lambda_N^2}{M_N^2}-\lambda) + a_3(\frac{\widetilde{M}^2}{M_N^2}-\frac{4}{9}) \\
& +(a_{34}-a_3)(\frac{M_{\text{eff}}^2+(q_\perp^{\text{eff}})^2}{M_N^2}-\frac{4}{9}) + (x_2-\frac{1}{3})^2\Big]^{-(\sigma+2+\nu)} \\
& \times[x_1(v'(x_1-2(1-x_2))+x_1(1-x_2)) + \bar{u}'(v'(1-x_2)-(x_1)^2)]^{-\nu-1} \\
& (\bar{u}'-v')^{2\nu-1}, \qquad (9.28)
\end{aligned}$$

Here, $\tilde{N}(\nu,\sigma)$ is a normalization factor. To calculate the contribution of this function's overlap with itself to the GPD H when quark 1 is active, we start with the transverse momentum dependent term, using a new Feynman parametrization:

$$\begin{aligned}
&\Big[(1+\frac{a_{34}-a_3}{(x_2-1)^2}x_1^2)k_{1\perp}^2+(a_{34}-a_3)k_{2\perp}^2 \\
&+2\frac{a_{34}-a_3}{-1+x_2}x_1\vec{k}_{1\perp}\cdot\vec{k}_{1\perp}+\hat{M}^2\Big]_{in}^{-(\sigma+2+\nu)}\Big[(1 \\
&+\frac{a_{34}-a_3}{(x_2-1)^2}x_1^2)k_{1\perp}^2+(a_{34}-a_3)k_{2\perp}^2+2\frac{a_{34}-a_3}{-1+x_2}x_1\vec{k}_{1\perp}\cdot\vec{k}_{1\perp} \\
&+\hat{M}^2\Big]_{out}^{-(\sigma+2+\nu)} \\
= &\int_0^1 dh\Big[A_1\bar{k}_{1\perp}^2+A_2\bar{k}_{2\perp}^2+A_3\Delta_\perp^2+A_4\bar{k}_{1\perp}\cdot\bar{k}_{2\perp} \\
&+A_5\bar{k}_{1\perp}\cdot\Delta_\perp+A_6\bar{k}_{2\perp}\cdot\Delta_\perp+A_7]^{-2(\sigma+2+\nu)},
\end{aligned} \tag{9.29}$$

where $\hat{M}$ includes non-transverse-momentum terms. By shifting the transverse momenta:

$$\begin{aligned}
\tilde{k}_{1\perp} &\equiv \bar{k}_{1\perp}+\frac{A_4}{2A_1}\bar{k}_{2\perp}+\frac{A_5}{2A_1}\Delta_\perp \\
\tilde{k}_{2\perp} &\equiv \bar{k}_{2\perp}+\tilde{A}_6\Delta_\perp,
\end{aligned} \tag{9.30}$$

we redefine for convenience:

$$\begin{aligned}
\tilde{A}_2 &\equiv A_2-\frac{A_4^2}{4A_1} \\
\tilde{A}_6 &\equiv A_6-\frac{A_4A_5}{2A_1} \\
\tilde{A}_3 &\equiv A_3-\frac{\tilde{A}_6^2}{2\tilde{A}_2}.
\end{aligned} \tag{9.31}$$

The expression simplifies to:

$$\int_0^1 dh\Big[A_1\tilde{k}_{1\perp}^2+\tilde{A}_2\tilde{k}_{2\perp}^2+\tilde{A}_3\Delta_\perp^2+A_7\Big]^{-2(\sigma+2+\nu)}. \tag{9.32}$$

Integrating over both $\tilde{k}_{1,2}$ gives:

$$\begin{aligned}
&\Big[\tilde{N}(\nu,\sigma)\int[df_{in}]\tilde{\rho}\rho_\nu(\bar{a}_1-a_{34})^{\sigma-2}(a_{34}-a_3)^\nu(1-x_2)^{\nu+2} \\
&\times[x_1(v'(x_1-2(1-x_2))+x_1(1-x_2)) \\
&+\bar{u}'(v'(1-x_2)-(x_1)^2)]^{-\nu-1}(\bar{u}'-v')^{2\nu-1}\Big]_{\text{in}} \\
&\Big[\tilde{N}(\nu,\sigma)\int[df_{in}]\tilde{\rho}\rho_\nu(\bar{a}_1-a_{34})^{\sigma-2}(a_{34}-a_3)^\nu(1-x_2)^{\nu+2} \\
&\times[x_1(v'(x_1-2(1-x_2))+x_1(1-x_2)) \\
&+\bar{u}'(v'(1-x_2)-(x_1)^2)]^{-\nu-1}(\bar{u}'-v')^{2\nu-1}\Big]_{\text{out}} \\
&\times\frac{\pi^2}{2}\int_0^1 dh\Big[\tilde{A}_3\Delta_\perp^2+A_7\Big]^{-2(\sigma+1+\nu)}\Big[A_1\tilde{A}_3(\sigma+\nu+1)(3+2\sigma+2\nu)\Big]^{-1}.
\end{aligned} \tag{9.33}$$

In order to compute the GPD (or PDF) at a given point we must therefore compute a 13-dimensional numerical integral, as we must integrate over the 11 Feynman parameters as well as the inactive longitudinal momentum fraction x_2 and the transverse momentum angle θ_{12}. This large dimensional integration involves some noisiness, especially if we would like to compute such integrals efficiently. We chose to use Adaptive Monte-Carlo integration, and not Gauss-Kronrod, which is more accurate but less efficient [118, 117].
We therefore show the contributions of the auxiliary function $\psi^{1,-1}$ to the PDF. While noisy, there is a clear non-zero signal. Further, the large x_1 tail reflects the previously mentioned tendency for the longitudinal momentum to be held by the bystander quark, u_1. In addition, as previously mentioned, there is an approximate u_2-d_3 symmetry, as they are the diquark participants.

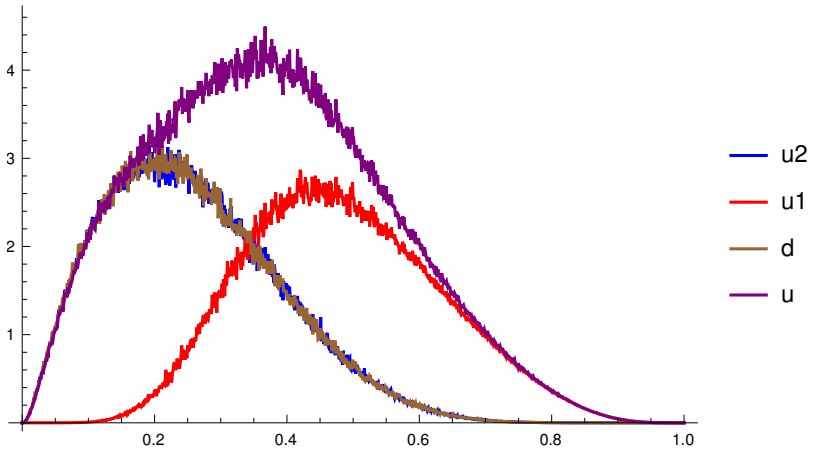

Figure 9.4: The results for the forward limit of $\Psi^{1,-}$ self overlaps (PDFs) are shown. The red curve corresponds to that of the bystander quark $u1$, the blue to the participant quark $u2$, the brown to the participant quark $d(3)$, and the purple to the total u quark contribution. This result has been computed using Adaptive Monte-Carlo integration with 1001 points along the x axis, and is extremely noisy. Even so, there is a clearly visible signal which is not compatible with zero.

9.7 . Conclusion and Outlook

GPDs are essential for making experimental predictions in processes such as DVCS and DVMP, due to their universal nature ensured by factorization proofs. However, extracting GPDs from experimental data is complex due to convolutions with calculable kernels. Practical constraints on GPDs should incorporate inputs from lattice QCD computations and other techniques for comparison with experiments.

Bayesian reweighting of ANN GPD candidates using lattice data can significantly reduce uncertainty, provided the data's correlation is known. Complementary lattice data can address the limitations of the perturbative kernel in experimental data, offering insights into otherwise inaccessible regions.

Polarized and unpolarized DGLAP region GPDs can be represented through LFWFs of definite qOAM, contributing to the GPD H even in the forward limit, linking polarized PDFs to qOAM contributions via the Ji sum rules. A simple model for such LFWFs demonstrates computation from tensorial structures.

To align these models with experimental data, extending DGLAP GPDs to the ERBL region and evolving them to experimental scales is necessary. Further efforts in modeling, including systemizing tensorial structures and integrating complex plane methods with a running mass, are crucial for a more intimate understanding of definite qOAM contributions to the nucleon.

10 - Résumé détaillé en Français

10.1 . Introduction

Dans les années 1960, Gell-Mann a proposé un modèle de quarks pour expliquer un large spectre de valeurs de spin et de charge [4]. Il a introduit trois saveurs de quarks de spin-$\frac{1}{2}$: "up" (u), "down" (d) et "strange" (s), avec des charges de $\frac{2}{3}$, $-\frac{1}{3}$, et $-\frac{1}{3}$, respectivement. Les spins des quarks étaient contraints de s'(anti)aligner pour correspondre aux spins des baryons. La particule Δ^{++}, avec trois quarks u et une charge totale de $+2$, posait problème en raison du principe d'exclusion. Pour résoudre cela, [5, 6] ont introduit un groupe de jauge "couleur", SU(3), ajoutant un nombre quantique appelé "charge de couleur" avec trois valeurs. Cela permettait à chaque quark u dans la Δ^{++} d'avoir une couleur différente, satisfaisant ainsi le principe d'exclusion. Le groupe de jauge non abélien SU(3) avait des conséquences significatives pour la force forte, conduisant à la Chromodynamique Quantique (QCD). La densité lagrangienne de l'Électrodynamique Quantique (QED) décrit les particules de spin-1/2 (par exemple, les électrons) et les champs électromagnétiques, incluant des termes pour le champ fermionique ψ, la dérivée covariante de jauge D_μ, le tenseur de champ électromagnétique $F_{\mu\nu}$ et la masse du fermion m. La densité lagrangienne de la QCD décrit les quarks et les gluons, incluant des termes pour le champ de quarks ψ, la dérivée covariante de jauge D_μ avec la constante de couplage forte g_s, le tenseur de champ de gluons $G^a_{\mu\nu}$, et la masse du quark m. Les fonctions β de la QED et de la QCD déterminent la dépendance à l'échelle de leurs constantes de couplage. En QED, le couplage augmente avec l'échelle d'énergie, menant au pôle de Landau. En QCD, le couplage diminue à hautes énergies (liberté asymptotique) et augmente à basses énergies, menant à la confinement. Cela implique que seuls les états neutres en couleur sont observables, une propriété connue sous le nom de confinement de couleur.

10.1.1 . Comparaison avec l'Expérience

Pour comparer les résultats expérimentaux avec les prédictions théoriques, les calculs théoriques doivent être structurés pour correspondre aux observables expérimentales. Les interactions expérimentales et leurs probabilités sont répertoriées sous forme de sections efficaces, calculées à partir de sommes d'amplitudes d'interaction. La théorie des perturbations est une méthode pour exprimer ces amplitudes théoriquement. En Électrodynamique Quantique (QED), la constante de couplage e permet des développements perturbatives utiles à des échelles d'énergie basses, le pôle de Landau de la QED ne posant pas de problème pratique pour les calculs correspondant aux expéri-

ences actuelles. Cependant, en Chromodynamique Quantique (QCD), le pôle de Landau se produit à une échelle d'énergie relativement basse Λ_{QCD}, rendant la QCD perturbative (pQCD) inefficace seule pour comprendre la sous-structure du nucléon.
La Diffusion Inélastique Profonde (DIS) est un processus révélant la structure du nucléon. La factorisation, le processus de séparation de la section efficace en parties calculables perturbativement et parties inaccessibles perturbativement, a été prouvée pour la DIS, permettant des prédictions basées sur les Distributions des Partons (PDFs). Cependant, extraire ces PDFs des données expérimentales pose des défis en raison de la convolution impliquée, ce qui rend difficile la séparation des contributions dues aux différentes saveurs de quarks.
La Collaboration Européenne des Muons (EMC) a "découvert" la crise du spin du nucléon, révélant des contributions inattendues au spin du nucléon provenant des états de la QCD au-delà des quarks de valence, inspirant des recherches sur les Distributions Généralisées des Partons (GPDs) pour comprendre davantage la structure du nucléon. La diffusion Compton à grande virtualité (DVCS) et la production de mésons à grande virtualité (DVMP) sont des processus expérimentaux permettant de sonder la sous-structure partonique des cibles nucléoniques. La DVCS implique une sonde leptonique entrante interagissant avec une cible nucléonique, résultant en un nucléon non brisé dans l'état final ainsi qu'un second photon et un lepton dans l'état final. La DVMP, quant à elle, produit un méson dans l'état final à la place du photon de l'état final de la DVCS. Les deux processus sont factorisables, où les contributions des parties molles et dures de l'interaction sont séparées. Les Distributions Généralisées des Partons (GPDs) des nucléons, notées $H(x, \xi, t)$ et $E(x, \xi, t)$, décrivent les corrélations de la fraction moyenne d'impulsion partonique x pour le parton actif, le paramètre de coup de cône de lumière ξ, appelé la skewness, et le t, le transfert d'impulsion carré du nucléon dans l'interaction. Elles sont données en termes d'éléments de matrice impliquant les champs de quarks et de gluons. Elles satisfont diverses contraintes, telles que la parité paire par rapport à ξ et les propriétés de polynomialité. Ces GPDs contribuent aux Facteurs de Forme de Compton (CFFs), qui sont des convolutions de GPDs avec une fonction noyau. Ces CFFs sont utilisés dans l'expression de la section efficace expérimentale. De plus, les GPDs sont liées aux Facteurs de Forme Électromagnétiques (EFFs), qui décrivent la structure interne des nucléons. Le moment angulaire total porté par les quarks est lié aux premiers moments de Mellin des GPD des quarks et est connu sous le nom de règle de somme de Ji. De plus, les Distributions des Paramètres d'Impact (IPDs) et les distributions du temps d'Ioffe fournissent des représentations alternatives des GPDs dans l'espace position-impulsion et l'espace impulsion-spatial (longitudinal-transversale), respectivement.

De plus, dans les années à venir, en plus des données expérimentales, nous nous attendons à ce que la QCD sur réseau fournisse des données utiles.

10.2 . Repondération

10.2.1 . Réseaux de Neurones Artificiels

Dans un effort continu pour distinguer parmi la myriade de candidats pour les Distributions Généralisées des Partons (GPDs) de manière impartiale tout en garantissant le respect de toutes les contraintes théoriques nécessaires, les réseaux de neurones artificiels (ANNs) ont été utilisés pour modéliser les GPDs. Un exemple est le travail de Dutrieux et al. [69], où les pseudo-données GPD du modèle Goloskokov-Kroll (GK) ont été utilisées pour entraîner les ANNs. Ces ANNs ont été conçus pour produire des fonctions candidates satisfaisant la plupart des propriétés des GPDs. Pour évaluer davantage la discrimination parmi les fonctions candidates, des données fictives de QCD sur réseau, systématiquement variées pour être compatibles avec les fonctions candidates, ont été introduites.
Les réseaux de neurones consistent en des couches de nœuds. Les réseaux de neurones à action directe, comme ceux utilisés dans cette étude, ont des connexions uniquement entre les couches adjacentes. La sortie de chaque nœud j dans la couche $i > 1$ est calculée en utilisant des fonctions d'activation et des sommes pondérées des entrées de la couche précédente. Les théorèmes d'approximation universelle garantissent que des réseaux suffisamment grands peuvent approximer toute fonction continue sur un ensemble compact. Les fonctions d'activation, souvent des fonctions sigmoïdes, interpolent entre 0 et 1. Notamment, dans les modèles ANN utilisés ici, les arguments de la fonction d'activation présentent une non-linéarité dans les variables d'entrée α et β pour garantir le respect de certaines propriétés des GPDs.
Les neurones de la couche cachée de l'ANN effectuent des calculs spécifiques pour reproduire certaines propriétés des GPDs. Trois extractions de GPDs utilisant des pseudo-données générées avec le modèle GK ont été réalisées, avec différents ensembles de données d'entraînement et contraintes. L'algorithme génétique a été utilisé pour la minimisation des paramètres, avec une régularisation utilisée pour éviter des résultats biaisés dus au surajustement. La régularisation par dropout a été utilisée, éliminant aléatoirement une fraction prédéfinie de neurones à chaque itération de l'algorithme de minimisation pour empêcher la fixation sur les détails des données d'entraînement. Cette section se concentre sur la modélisation de la GPD $H(x, \xi, t)$, avec t fixé à zéro pour examiner exclusivement le plan $x - \xi$. Représenté en termes de la transformée de Radon d'une Double Distribution (DD), les modèles ANN discutés ici visent à modéliser les DDs correspondant à H. Spécifiquement, la combinaison impaire $H^{q(+)}(x, \xi, 0) = H^q(x, \xi, 0) - H^q(-x, \xi, 0)$, représen-

tant la GPD des quarks de mer, est étudiée. Pour obtenir de la flexibilité et reproduire les limites connues, le modèle DD comprend trois termes : F_C, F_S et F_D. F_C est conçu pour reproduire la limite avancée et modéliser la ligne $x = \xi$, F_S vise à reproduire l'incertitude de déconvolution et disparaît à certaines lignes, et F_D modélise le terme D. F_C est défini pour assurer la réduction correcte à la limite avancée et la flexibilité pour modéliser la ligne $x = \xi$. F_S vise à reproduire l'incertitude de déconvolution et est écrit comme la différence de deux fonctions de profil. Enfin, F_D fournit de la flexibilité pour modéliser le terme D, crucial pour caractériser la matière partonique.
Au lieu d'utiliser des données expérimentales appropriées, les pseudo-données Goloskokov-Kroll (GK) ont été employées comme preuve de concept pour la mise en œuvre de l'architecture du réseau utilisée dans la modélisation des GPDs. Le modèle GK, initialement développé pour la DVMP, a réussi à reproduire les mesures expérimentales. Les pseudo-données GK sont limitées par les hypothèses inhérentes au modèle GK.

10.2.2 . Analyse

Des techniques statistiques telles que la médiane de la déviation absolue (MAD) sont discutées comme méthode d'estimation de l'incertitude, en particulier lorsque définir des valeurs aberrantes dans le jeu de données est difficile. MAD fournit une estimation robuste de l'écart type sans avoir besoin de définir explicitement des valeurs aberrantes, ce qui le rend adapté à l'analyse des jeux de données où la définition des valeurs aberrantes peut être arbitraire. La comparaison entre l'écart type et MAD illustre la robustesse de MAD dans l'estimation de la dispersion des jeux de données, en particulier en présence de valeurs aberrantes. Comprenant maintenant à la fois l'origine des répliques GPD (fonctions candidates) et un estimateur statistique important à utiliser plus tard dans le chapitre correspondant, il est nécessaire de jeter un coup d'œil au raisonnement pour lequel et la méthode par laquelle des données de réseau fictives ont été générées pour l'étude d'impact à venir de son effet discriminant par rapport aux répliques ANN GPD. Ces deux points sont également délimités.

10.2.3 . Données de Réseau Fictives

Le choix d'utiliser des données de réseau fictives pour cette étude d'impact est informé par deux points clés. La première de ces raisons est un manque d'accès aux données de réseau. La seconde, qui est un avantage plutôt qu'un inconvénient de l'utilisation de données fictives, est la capacité à contrôler systématiquement l'accord des données fictives avec l'ensemble des répliques GPD considérées. Ce contrôle systématique a été réalisé via l'utilisation de paramètres contrôlant la précision et la corrélation des données de réseau fictives. Basé sur des études réelles de réseau telles que celle citée, on en conclut que les extractions actuelles de GPD sur réseau à la pointe de la tech-

nologie ne sont pas également facilitées dans toutes les plages cinématiques. Les données GPD de réseau sont généralement présentées dans l'espace-temps Ioffe, car les calculs se déroulent sur un réseau dans l'espace des coordonnées, plutôt que dans l'espace des impulsions. Cependant, il convient de noter que les données de réseau après lesquelles les données de réseau fictives générées dans cette étude ont été modélisées ne sont pas appariées au cône de lumière, mais existent le long de certaines directions Euclidiennes. Par conséquent, une étude appropriée comparant les répliques aux données de réseau fictives n'aurait pas eu lieu sur le cône de lumière, mais hors du cône de lumière. Par conséquent, tous les calculs comparant et combinant les répliques ANN GPD aux données de réseau fictives sont effectués dans l'espace-temps Ioffe. Comme la GPD singulet ajustée ANN, H, du nucléon est celle traitée ici, sa parité impaire dans la fraction d'impulsion longitudinal x permet de limiter les études correspondantes à l'espace-temps Ioffe à la partie imaginaire de H. Cette méthode génère des données de réseau fictives qui sont en général compatibles avec la valeur centrale de la bande de répliques dans la précision générée par la fonction g. Cependant, jusqu'à présent, la génération de données traite tous les points de données de réseau fictives comme non corrélés. Pour en tenir compte dans notre étude d'impact, des données de réseau fictives sont générées dans trois régions distinctes de l'espace-temps Ioffe, où la corrélation intracollaboration est fixée à $0 \leq c < 1$, et la corrélation intercollaboration est fixée à zéro. La fig. 10.1 illustre un jeu de données de réseau fictives superposé aux répliques générées par notre modèle GPD. Avec une méthode pour générer des données de réseau fictives contrôlées systématiquement en termes de précision et d'adhérence à l'ensemble des répliques GPD, et la corrélation entre toutes ces données générées en main, il est maintenant possible d'influencer l'incertitude associée de la bande de répliques en utilisant ces données de réseau fictives pour évaluer la capacité discriminante potentielle des données de réseau. Dans l'étude discutée ici, une procédure de repondération bayésien utilisant les données de réseau fictives comme a priori a été choisie, visant à enquêter sur l'incertitude résultante de l'ensemble des répliques GPD sans ajustements coûteux. Jusqu'à présent, la discussion a largement ignoré la déformation de la GPD, se concentrant sur l'analyse en x et ν. Dans les sections finales, les discussions sur la déformation joueront un rôle important, nécessitant un aperçu de la procédure de repondération bayésien utilisée. La procédure précise délimite l'attribution de poids à chaque réplique en fonction de leur accord avec les données de réseau fictives, conduisant à une médiane repondérée et à un écart type de l'ensemble des répliques. Ces quantités fournissent une mesure de la réduction de l'incertitude sur la bande de répliques.

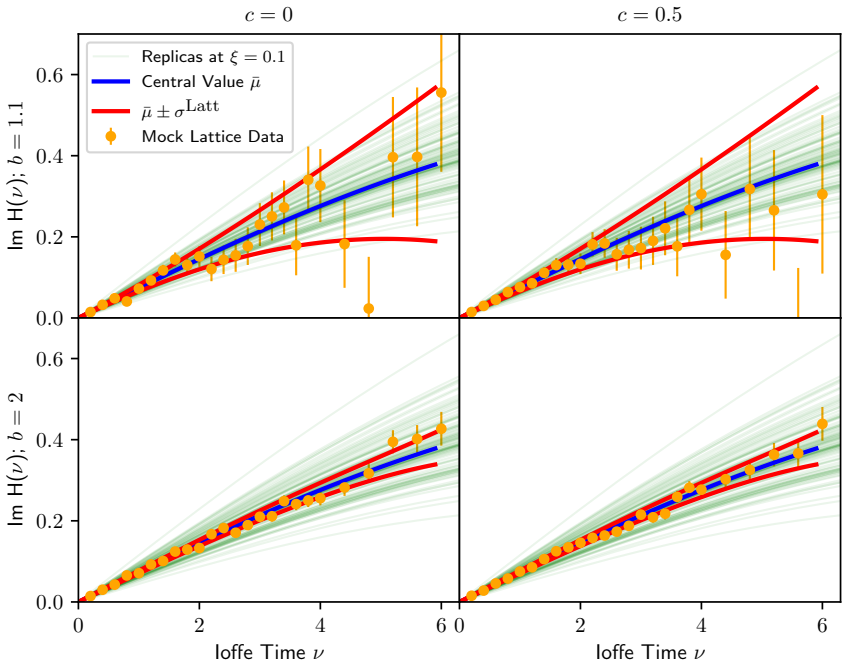

Figure 10.1: Il est montré l'ensemble des répliques des GPD couvrant les temps d'Ioffe de $\nu = 0$ à $\nu = 6$ à $\xi = 0.1$ (indiqués en vert), avec leur médiane (en bleu) et la bande à 1σ (en rouge), correspondant à $b = 1.1$ (en haut) et $b = 2$ (en bas). De plus, l'ensemble de données de réseau fictif généré en conséquence avec $c = 0$ (à gauche) et $c = 0.5$ (à droite) est représenté en orange.

	Données			Résultats		
$\xi_{\text{Utilisé}}$	Précision	Corrélation	$\xi_{\text{Affiché}}$	τ	r_ν	$r_{\ln x}$
0.1	Basse	Basse	0.1 / 0.5	0.47	0.25 / 0.92	0.82 / 1.24
0.1	Basse	Haute	0.1 / 0.5	0.83	0.85 / 0.93	1.02 / 1.15
0.1	Haute	Basse	0.1 / 0.5	0.30	0.16 / 0.90	0.78 / 1.08
0.1	Haute	Haute	0.1 / 0.5	0.46	0.23 / 0.91	0.82 / 1.23
0.5	Basse	Basse	0.5	0.36	0.44	0.67
0.5	Basse	Haute	0.5	0.52	0.58	0.64
0.5	Haute	Basse	0.5	0.11	0.25	0.54
0.5	Haute	Haute	0.5	0.37	0.51	0.77
0.1 0.2 0.3	Basse	Basse	0.5	0.30	0.62	0.95
0.1 0.2 0.3	Basse	Haute	0.5	0.77	0.82	1.00
0.1 0.2 0.3	Haute	Basse	0.5	0.10	0.34	0.54
0.1 0.2 0.3	Haute	Haute	0.5	0.30	0.61	0.73
0.1 0.2 0.3 0.4 0.5	Basse	Basse	0.5	0.16	0.19	0.66
0.1 0.2 0.3 0.4 0.5	Basse	Haute	0.5	0.57	0.65	0.75
0.1 0.2 0.3 0.4 0.5	Haute	Basse	0.5	0.03	0.13	0.45
0.1 0.2 0.3 0.4 0.5	Haute	Haute	0.5	0.18	0.25	0.77

Table 10.1: Résultats en fonction des paramètres de repondération. Basse Corrélation: $c = 0$, Haute Corrélation: $c = 0.5$, Basse Précision: $b = 1.1$, Haute Précision: $b = 2$. $r_{\ln x}$: Maintien moyen de l'incertitude en x, r_ν: Maintien moyen de l'incertitude en ν, τ: Fraction effective des répliques retenues après repondération.

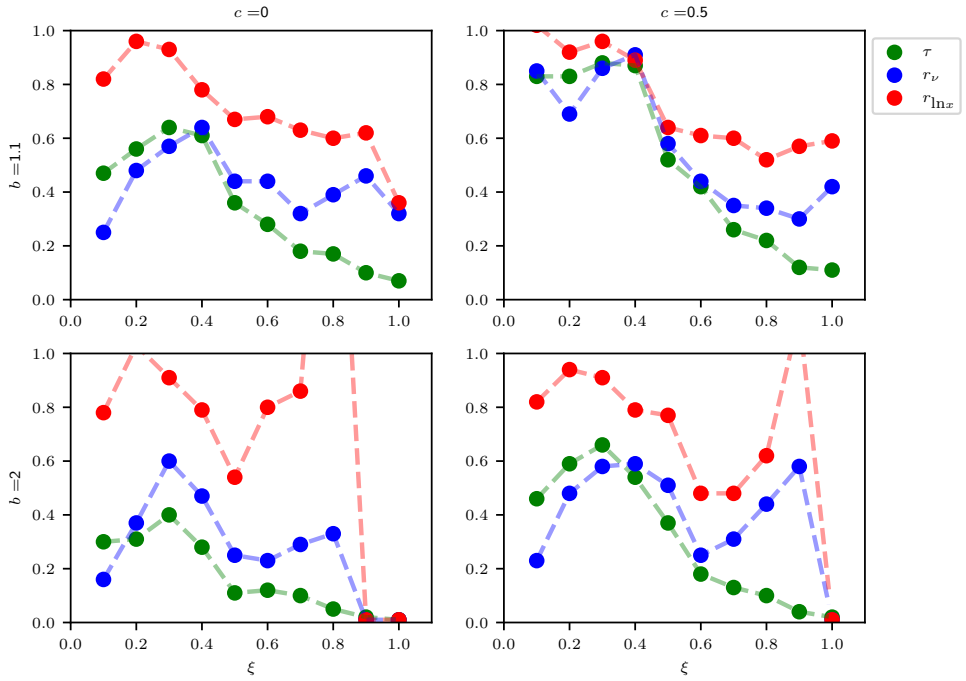

Figure 10.2: La fraction effective des répliques retenues après repondération τ (illustrée par la courbe verte), préservation de l'incertitude en temps loffe (montrée par la courbe bleue), et en espace d'impulsion (représentée par la courbe rouge) pour diverses combinaisons de bruit élevé et faible (désigné comme $b = 1.1$ et 2 respectivement) et de corrélation faible et élevée (indiquée comme $c = 0$ et 0.5 respectivement).

Nous comparons les maintiens de l'incertitude résultant de différentes quantités de données de réseau fictives à des niveaux d'obliquité bas à moyens ($\xi \in 0.1$, $\xi \in 0.1, 0.2, 0.3$, $\xi \in 0.1, 0.2, 0.3, 0.4, 0.5$) avec ceux observés dans la section précédente à des niveaux de déformation purement moyens. Les principales conclusions incluent:

- Le repondération avec de grandes incertitudes et une faible précision ($b = 1.1$) et des données corrélées ($c = 0.5$) réduit significativement l'incertitude en temps loffe à $\xi = 0.5$.

- L'ajout de données à $\xi = 0.1$ améliore le maintien de l'incertitude à $\xi = 0.5$, mais l'inclusion supplémentaire de données à $\xi \in 0.1, 0.2, 0.3$ et $\xi \in 0.1, 0.2, 0.3, 0.4, 0.5$ resserre le maintien de l'incertitude à $\xi = 0.5$. Cependant, le repondération direct à $\xi = 0.5$ avec $b = 2$ et $c = 0.5$ donne de meilleurs résultats.

De plus, nous présentons une Table (10.1) illustrant l'impact de différents niveaux de bruit et de corrélation sur les processus de maintien. En outre,

nous utilisons la Fig. 10.2 pour comparer les effets du repondération à diverses valeurs de ξ en présentant la fraction effective des répliques retenues (τ) et le maintien de l'incertitude à la fois en temps Ioffe et en espace d'impulsion. En examinant la Fig. 10.2, nous observons qu'à des niveaux de déformation moyens, la fraction effective des répliques retenues après repondération (τ) est à peu près égale dans les scénarios de faible corrélation et de faible précision ainsi que de haute corrélation et de haute précision. Cette relation compensatoire entre précision et corrélation pourrait guider les praticiens du réseau dans l'allocation efficace des ressources informatiques.
Il est important de noter qu'en utilisant une approche bayésienne pour fusionner les connaissances expérimentales et celles du réseau sur les GPD, prouvant efficace lorsque les données du réseau s'alignent bien avec le modèle a priori, a permis de réduire d'environ 40% l'incertitude à des niveaux de déformation moyens. Néanmoins, notre étude souligne la nécessité de traiter les corrélations au sein des données de réseau pour une extraction conjointe, car les données réelles du réseau présentent souvent des degrés élevés de corrélation et des effets systématiques qui nécessitent une gestion soigneuse pour éviter les biais dans l'évaluation de l'incertitude.

10.3 . Techniques du Continuum pour la Modélisation des GPD

L'analyse poursuivie ici des distributions de partons généralisées des nucléons implique le développement des éléments de matrice en utilisant des fonctions d'onde sur le cône de lumière (LFWFs). Cette approche éclaire la connexion entre les états nucléoniques et les amplitudes définies sur le cône de lumière, offrant des aperçus sur les contributions définies du moment angulaire orbital (OAM) des quarks aux GPD et objets connexes. En examinant le développement de Fock des états nucléoniques dans lesquels les LFWFs apparaissent comme des fonctions de coefficient dépendantes des impulsions et des nombres quantiques, on peut tronquer de manière cohérente de telles développements de Fock pour des calculs pratiques, au prix de limiter la cinématique du calcul à $|x| > |\xi|$. Cela permet à la représentation des GPD d'être exprimée en termes de recouvrements de LFWFs, en incluant uniquement les contributions des quarks de valence.
L'élément de matrice utilisé pour caractériser les états de Fock à trois quarks contribuant à un état nucléon $|P; h\rangle$ (avec $h = +\frac{1}{2}$) implique un opérateur qui crée un état à trois quarks neutre en couleur. Dans l'espace des impulsions, nous représentons cet élément de matrice en termes de diverses structures tensoriales que nous projetons ensuite sur des états de projection de hélicité des quarks définis, correspondant à des valeurs définies de qOAM. Les composantes de cette base tensorielle, dotées de fonctions de coefficient correspondantes appelées fonctions auxiliaires dont certaines combinaisons

linéaires donnent les fonctions d'onde sur le cône de lumière, fournissent alors un moyen d'extraire ces LFWFs d'un modèle donné pour cet élément de matrice via des traces de Dirac sélectives. En réduisant la base tensorielle employée en un ensemble plus petit de tenseurs en appliquant la symétrie des quarks u et la symétrie isospin, les LFWFs peuvent être identifiées comme cela a été fait dans la littérature [90].

10.4 . Représentation par recouvrements des GPD

Pour caractériser les contributions des états à trois quarks aux Distributions de Partons Généralisées (GPD) et objets connexes, nous pouvons tirer parti de la représentation par recouvrements des GPD [34]. Cette approche clarifie quelles paires d'états de Fock à trois quarks contribuent aux GPD en utilisant leurs recouvrements. Avant de commencer cette section, nous définissons les coordonnées de cône de lumière:

$$v = (v^+ \equiv \frac{v^0 + v^3}{\sqrt{2}}, \vec{v}_\perp \equiv (v_1, v_2), v^- \equiv \frac{v^0 - v^3}{\sqrt{2}}). \tag{10.1}$$

10.4.1 . Formule de recouvrement

Les impulsions initiaux et finaux de l'état du quark actif reflètent le transfert d'impulsion dû à l'interaction avec le photon. Pour voir quelles combinaisons d'états de Fock entrants et sortants contribuent, examinons les nombres quantiques impliqués. Les nombres quantiques collectifs $\mathcal{Q}_l$ pour le l-ième quark sont définis comme suit :

- **Impulsion** : $\kappa_l = (x_l, \vec{k}_{l\perp})$,
- **Hélicité** : λ_l,
- **Couleur** : c_l,
- **Saveur** : f_l,

La formule de recouvrement pour l'amplitude dépendante de l'hélicité $\mathcal{H}^{\hat{f}}_{h'h}(\bar{x}, \xi, t)$ est donnée par :

$$\mathcal{H}^{\hat{f}}_{h'h}(x, \xi, t) = \frac{1}{2\sqrt{1-\xi^2}} \sum_{\hat{c}} \int \frac{dz^-}{2\pi} e^{ix\bar{P}^+ z^-} \langle P', h' | \bar{q}^{\hat{c}}_{\hat{f}}(-\frac{z}{2}) \gamma^+ q^{\hat{c}}_{\hat{f}}(\frac{z}{2}) | P, h \rangle \tag{10.2}$$

$$\equiv \mathcal{O}^{\hat{f}} \left[\varphi_{\hat{\mathbb{S}}_{\mathbb{A}}(\mathcal{Q}');h'}, \varphi_{\mathcal{Q};h} \right] (x, \xi, t), \tag{10.3}$$

où $\hat{f}$ est la saveur du quark actif, $\hat{c}$ est un indice de couleur, $P(')$ et $h(')$ sont les impulsions et les hélicités des nucléons entrants (sortants), $z = (z^+ = 0, \vec{z}_\perp = \vec{0}_\perp, z^-)$ est un vecteur spatial dans la direction moins, $\bar{P}^+$ est l'impulsion plus

moyen du nucléon, $\bar{q}^{\hat{c}}_{\hat{f}}(-\frac{z}{2})\gamma^{+}q^{\hat{c}}_{\hat{f}}(\frac{z}{2})$ est un champ de quark bilocal bilinéaire, et $\hat{\mathbb{S}}_{\mathbb{A}}$ est la $\mathbb{A}$-ième permutation du groupe de permutations S_3 sur lesquelles nous faisons la somme.
Ici, $\mathcal{O}^{\hat{f}}\left[\varphi',\varphi\right]$ représente la fonction de recouvrement entre les LFWFs des états initiaux et finaux.

10.4.2 . Formule maîtresse du recouvrement: GPDs et Sous-Résultats

Les GPDs $H^{\hat{f}}$ et $E^{\hat{f}}$ sont exprimés en termes des amplitudes dépendantes de l'hélicité :

$$H^{\hat{f}} = \mathcal{H}^{\hat{f}}_{\frac{1}{2},\frac{1}{2}} + \frac{\xi^2 2M_N|\vec{\Delta}_\perp|}{(\Delta_1+i\Delta_2)\sqrt{1-\xi^2}\sqrt{\frac{4\xi^2m^2}{\xi^2-1}-t}}\mathcal{H}^{\hat{f}}_{-\frac{1}{2},\frac{1}{2}} \tag{10.4}$$

$$E^{\hat{f}} = \frac{2M_N|\vec{\Delta}_\perp|\sqrt{1-\xi^2}}{(\Delta_1+i\Delta_2)\sqrt{\frac{4\xi^2M_N^2}{\xi^2-1}-t}}\mathcal{H}^{\hat{f}}_{-\frac{1}{2},\frac{1}{2}}, \tag{10.5}$$

Nous pouvons représenter les amplitudes dépendantes de l'hélicité en termes de recouvrements de LFWF, où nos LFWFs Ψ_{h,λ_Σ} sont étiquetées par l'hélicité correspondante du proton h et la projection totale du moment angulaire des quarks λ_Σ telle que qOAM=$h-\lambda_\Sigma$. En termes de nos LFWFs définis par le moment angulaire orbital (qOAM), nous avons :

$$\begin{aligned}\mathcal{H}^{\hat{f}}_{\frac{1}{2},\frac{1}{2}} = \quad & \Big(\mathcal{O}^{\hat{f}}(\Psi_{\frac{1}{2},\frac{1}{2}},\Psi_{\frac{1}{2},\frac{1}{2}}) + \mathcal{O}^{\hat{f}}(\Psi_{\frac{1}{2},-\frac{1}{2}},\Psi_{\frac{1}{2},-\frac{1}{2}}) \\ & + \mathcal{O}^{\hat{f}}(\Psi_{\frac{1}{2},\frac{3}{2}},\Psi_{\frac{1}{2},\frac{3}{2}}) + \mathcal{O}^{\hat{f}}(\Psi_{\frac{1}{2},-\frac{3}{2}},\Psi_{\frac{1}{2},-\frac{3}{2}})\Big)\end{aligned} \tag{10.6}$$

$$\mathcal{H}^{\hat{f}}_{-\frac{1}{2},\frac{1}{2}} = \quad \Big(\mathcal{O}^{\hat{f}}(\Psi_{-\frac{1}{2},-\frac{3}{2}},\Psi_{\frac{1}{2},\frac{3}{2}}) + \mathcal{O}^{\hat{f}}(\Psi_{-\frac{1}{2},\frac{3}{2}},\Psi_{\frac{1}{2},-\frac{3}{2}})\Big). \tag{10.7}$$

Tandis que l'amplitude conservant l'hélicité reçoit uniquement des contributions diagonales en qOAM, l'amplitude de changement d'hélicité reçoit uniquement des contributions hors-diagonales. Cela ne viole pas nos attentes, car cela signifie que le GPD de changement d'hélicité E, qui reçoit des contributions uniquement de l'amplitude de changement d'hélicité $\mathcal{H}_{-\frac{1}{2},\frac{1}{2}}$, reçoit uniquement des contributions hors-diagonales en qOAM. De plus, la PDF, qui est liée à la probabilité de trouver un parton (quark ici) d'une saveur particulière portant une fraction particulière de l'impulsion longitudinale du nucléon, est donnée dans la limite avant de l'expression pour le GPD H comme

$$\begin{aligned}f^{\hat{f},\mathbb{P}}(x_{\mathsf{BJ}}) \quad = \quad & H^{\hat{f},\mathbb{P}}|_{t=\xi=0} = \\ & \Big(\mathcal{O}^{\hat{f},\mathbb{P}}(\Psi_{\frac{1}{2},\frac{1}{2}},\Psi_{\frac{1}{2},\frac{1}{2}}) + \mathcal{O}^{\hat{f},\mathbb{P}}(\Psi_{\frac{1}{2},-\frac{1}{2}},\Psi_{\frac{1}{2},-\frac{1}{2}}) \\ & + \mathcal{O}^{\hat{f},\mathbb{P}}(\Psi_{\frac{1}{2},\frac{3}{2}},\Psi_{\frac{1}{2},\frac{3}{2}}) + \mathcal{O}^{\hat{f},\mathbb{P}}(\Psi_{\frac{1}{2},-\frac{3}{2}},\Psi_{\frac{1}{2},-\frac{3}{2}})\Big)|_{t=\xi=0},\end{aligned} \tag{10.8}$$

qui, bien qu'il reçoive uniquement des contributions diagonales en qOAM, reçoit intéressamment des contributions non nulles en qOAM.

Maintenant que nous avons spécifié la représentation par recouvrement au cas des trois quarks et aux objets de notre intérêt, et que nous savons comment extraire les LFWFs d'un élément de matrice général à trois quarks à partir de la littérature, nous nous tournons vers la modélisation d'un tel élément de matrice afin de réaliser ces extractions.

10.5 . Le Modèle Diquark

Ce travail se concentre sur la modélisation des propriétés des nucléons en utilisant une approche quark-diquark, en traitant le diquark comme un système composite à deux corps plutôt que comme une entité ponctuelle, ce qui permet l'inclusion de corrélations internes en onde p du diquark souvent négligées dans des modèles plus simples [103]. L'analyse ici utilise le formalisme de Bethe-Salpeter et les équations de Faddeev [96] pour caractériser les états nucléoniques et étend les résultats de l'espace euclidien au cône de lumière à travers les moments de Mellin. Cette méthode implique la construction des Fonctions d'Onde sur le cône de lumière (LFWFs) en abordant les complexités de la traduction des modèles de l'espace euclidien (modèle d'amplitudes de Faddeev) au cône de lumière (comme LFWFs).

10.5.1 . Reconstruction de Mellin

Pour transformer les amplitudes de Faddeev calculées dans l'espace euclidien en Fonctions d'Onde sur le cône de lumière (LFWFs) définies sur le cône de lumière, nous devons gérer la transition des arguments de temps du cône de lumière à zéro. Cela implique d'intégrer sur des paramètres spécifiques pour traiter les fractions d'impulsion et les projections. Dans l'espace Minkowskien, la LFWF est donnée par :

$$\Psi(x_1, \vec{k}_{1\perp}; x_2, \vec{k}_{2\perp}) \quad = \quad N \int \mathrm{d}k^-_{1;M} \mathrm{d}k^-_{2;M} \chi(k_{1;M}, k_{2;M}), \tag{10.9}$$

où N est une constante de normalisation. Étant donné que les calculs sont dans l'espace euclidien, nous utilisons la transformation de Mellin pour éviter les intégrations complexes en contour. La impulsion de Mellin d'une fonction $f(x)$ d'ordre m est:

$$\int \mathrm{d}x\, x^m f(x), \tag{10.10}$$

avec des bornes $0 \leq x \leq 1$. Deux fonctions ayant des moments de Mellin identiques sont équivalentes [113]:

$$\int \mathrm{d}x\, x^m f(x) \quad = \quad \int \mathrm{d}x\, x^m g(x), \quad \forall m \in \mathbb{N} \tag{10.11}$$

$$\Rightarrow f(x) \quad = \quad g(x). \tag{10.12}$$

La fraction de l'impulsion longitudinale x_i en variables euclidiennes est:

$$x_i^{m_i} \equiv \frac{(k_{E;i}\cdot n_E)^{m_i}}{(P_E\cdot n_E)^{m_i}}, \tag{10.13}$$

où $n_E^2 = 0$ assure la projection sur le composant $+$ du cône lumineux. En utilisant les moments de Mellin, nous reconstruisons la dépendance $x_{1,2}$ des LFWFs avec:

$$\begin{aligned}
&\int_0^1 \mathrm{d}x_1 \int_0^{1-x_1} \mathrm{d}x_2 x_1^{m_1} x_2^{m_2} \Psi(x_1, \vec{k}_{1\perp}; x_2, \vec{k}_{2\perp}) \\
\equiv\ & \text{Normalisation} \int \mathrm{d}k_{1;E}^3 \mathrm{d}k_{1;E}^4 \mathrm{d}k_{2;E}^3 \mathrm{d}k_{2;E}^4 \frac{(k_{E;1}\cdot n_E)^{m_1}}{(P_E\cdot n_E)^{m_1}} \frac{(k_{E;2}\cdot n_E)^{m_2}}{(P_E\cdot n_E)^{m_2}} \\
& \mathrm{Tr}_{\text{Dirac}} \left\{ \Gamma_{\text{Proj.}} \chi(k_{1;E}, k_{2;E}) \right\},
\end{aligned} \tag{10.14}$$

où $\Gamma_{\text{Proj.}}$ est une structure de Dirac utilisée pour extraire les contributions. Cette méthode est discutée dans [112].

10.5.2 . Identification des Variables de Mellin

Pour calculer les contributions fondamentales aux six LFWFs, un modèle de corrélation quark-diquark euclidien du nucléon est utilisé. Les structures tensoriales sont introduites, contractées, et les moments de Mellin sont calculés pour extraire les contributions aux LFWFs. Définir le propagateur de quark comme:

$$S(p) = [-i\gamma\cdot p + M_q]\, D_{M_q}(p^2), \tag{10.15}$$

$$D_M(s) = \frac{1}{s+M^2}, \tag{10.16}$$

et la représentation de Nakanishi de la contribution tensorielle la plus simple au vertex diquark en utilisant la base l et q :

$$\eta_0 \Gamma_\mu^0 C^\dagger = i\gamma_5 \int_{-1}^1 \mathrm{d}z \rho_\nu(z) D_{\Lambda_q}(q_z), \tag{10.17}$$

avec $q_z = q + \frac{z}{2}\left(\frac{2}{3}P - \ell\right)$ et $\rho_\nu(z)$ une fonction de poids de Nakanishi donnée comme un polynôme. Le propagateur diquark en termes de l'impulsion du diquark K et une représentation de Nakanishi de la contribution tensorielle la plus simple à la corrélation quark-diquark sont donnés respectivement par :

$$\Delta^{0+}(K) = \frac{1}{K^2 + \widetilde{M^2}}, \tag{10.18}$$

$$s_1 = i\eta \int_{-1}^1 \mathrm{d}z\, \tilde{\rho}(z) \left[\frac{1}{(\ell_z^2 + \Lambda_N^2)}\right]^3. \tag{10.19}$$

Ici, P est défini comme $(0,0,0,iM_N)$ et les impulsions des quarks sont :

$$k_i \equiv \frac{P}{3} + \ell, \tag{10.20}$$

$$k_j \equiv \frac{P}{3} - \frac{\ell}{2} + q, \tag{10.21}$$

$$k_k \equiv \frac{P}{3} - \frac{\ell}{2} - q. \tag{10.22}$$

où q est la différence de l'impulsion interne du diquark et l est une autre variable façonnée pour être réelle. L'amplitude projetée de Faddeev lorsque le quark 1 n'est pas inclus dans le diquark (témoin) est:

$$\chi^{\uparrow,\downarrow,\uparrow}_{\alpha_3;\sigma} = S(k_2)_{\alpha_2\alpha'_2}[\Gamma^0(q,K)]_{\alpha'_2\alpha'_3} S(k_3)_{\alpha_3\alpha'_3} \Delta_0 S^T(k_1)_{\alpha'_1\alpha_1} s_{1\alpha'_1,\sigma}. \tag{10.23}$$

Ce qui peut ensuite être projeté sur les projections d'hélicité du quark contribuant à la fonction auxiliaire $\psi^{1,-1}$, la fonction auxiliaire la plus simple avec qOAM$= 0$:

$$\chi^{h_1,h_2,h_3}_{\alpha_1\alpha_2\alpha_3;\sigma} = (\not{n} L^{\uparrow}_{\alpha'_3\alpha_3} S_{\alpha_3\lambda}(k_3) \Gamma^{0T}_{\lambda\lambda'} S^T_{\lambda'\alpha_2}(k_2) \tag{10.24}$$

$$\times (L^{\downarrow} \not{n}^T (C^{\dagger})^T L^{\uparrow})_{\alpha_2\alpha_1} S_{\alpha_1\alpha'_1}(k_1) s_{1\alpha'_1\sigma} \Delta(k_2+k_3). \tag{10.25}$$

En projetant sur γ^ν pour l'opérateur de twist principal:

$$\frac{1}{4}\gamma_\nu \mathsf{Tr}[\gamma^\nu \not{n} L^{\uparrow} S(k_3) \Gamma^{0T} S^T(k_2) (L^{\downarrow} \not{n}^T (C^{\dagger})^T L^{\uparrow} S(k_1) \mathcal{S}] \Delta(k_2+k_3)$$
$$= \frac{1}{2}\gamma_\nu n^\nu \mathsf{Tr}[S(k_3)\Gamma^{0T} S^T(k_2) L^{\downarrow} C^{\dagger} \not{n} L^{\uparrow}] \sigma_S(k_1) s_1(\ell, P_E) \mathsf{Tr}[\gamma^\nu \not{n} L^{\uparrow} \Delta(k_2+k_3)].$$

L'approche essentielle pour l'extraction est de calculer les moments de Mellin du modèle de corrélation quark-diquark et de les utiliser pour extraire directement les LFWFs. Cela évite les complications des intégrations en contour particulièrement difficiles et utilise les intégrales définissant les moments pour obtenir les LFWFs.
Pour combiner les dénominateurs de toutes les structures de notre modèle, nous utilisons la paramétrisation de Feynman, introduisant un grand nombre de variables sur lesquelles intégrer. Nous pouvons alors identifier les

moments de Mellin de la fonction auxiliaire $\psi^{1,-1}$ comme

$$
\begin{aligned}
& \int_0^1 \mathrm{d}x_1 \int_0^{1-x_1} \mathrm{d}x_2 x_1^{m_1} x_2^{m_2} \psi^{1,-1}(x_1, \vec{k}_{1\perp}; x_2, \vec{k}_{2\perp}) \\
= \; & \int_0^1 \mathrm{d}\bar{\alpha} \int_0^{1-\bar{\alpha}} \mathrm{d}\beta' \int_0^{\beta'} \mathrm{d}v' \int_{\beta'}^{1-\bar{\alpha}} \mathrm{d}u' \int_0^{\bar{\alpha}} \mathrm{d}a_{34} \\
& \int_{\bar{\alpha}}^1 \mathrm{d}\bar{a}_1 \int_0^{a_{34}} \mathrm{d}a_3 \\
& \bar{\alpha}^{m_1} \beta'^{m_2} \frac{g(\bar{\alpha}, \beta', u', v', a_{34}, \bar{a}_1, a_3, \vec{k}_{1\perp}, \vec{k}_{2\perp})}{h(\bar{\alpha}, \beta', u', v', a_{34}, \bar{a}_1, a_3, \vec{k}_{1\perp}, \vec{k}_{2\perp})}
\end{aligned} \tag{10.26}
$$

$$
\begin{aligned}
\rightarrow \; & \psi^{1,-1}(x_1, \vec{k}_{1\perp}; x_2, \vec{k}_{2\perp}) \\
= \; & \int_0^{x_2} \mathrm{d}v' \int_{x_2}^{1-x_1} \mathrm{d}u' \int_0^{x_1} \mathrm{d}a_{34} \int_{x_1}^1 \mathrm{d}\bar{a}_1 \int_0^{a_{34}} \mathrm{d}a_3 \\
& \frac{g(x_1, x_2, u', v', a_{34}, \bar{a}_1, a_3, \vec{k}_{1\perp}, \vec{k}_{2\perp})}{h(x_1, x_2, u', v', a_{34}, \bar{a}_1, a_3, \vec{k}_{1\perp}, \vec{k}_{2\perp})}
\end{aligned} \tag{10.27}
$$

Bien que nous devons effectuer une intégrale 5D sur les paramètres de Feynman pour calculer $\psi^{1,-1}$ à un point donné, nous avons maintenant une expression que nous pouvons utiliser. Dans la section suivante, nous montrons un exemple de tracé pour une impulsion transverse nul des quarks.

10.6 . Résultats

Ici, nous montrons un graphique de contour de la dépendance de $x_{1,2,3}$ de la fonction auxiliaire $\psi^{1,-1}$. Il y a une symétrie notable entre les fractions d'impulsion $x_{2,3}$. Bien qu'il y ait une certaine instabilité numérique claire, la fraction d'impulsion longitudinalee x_1, correspondante au quark témoin (celui qui ne participe pas au diquark), porte généralement une portion préférentiellement élevée d'impulsion longitudinalee.

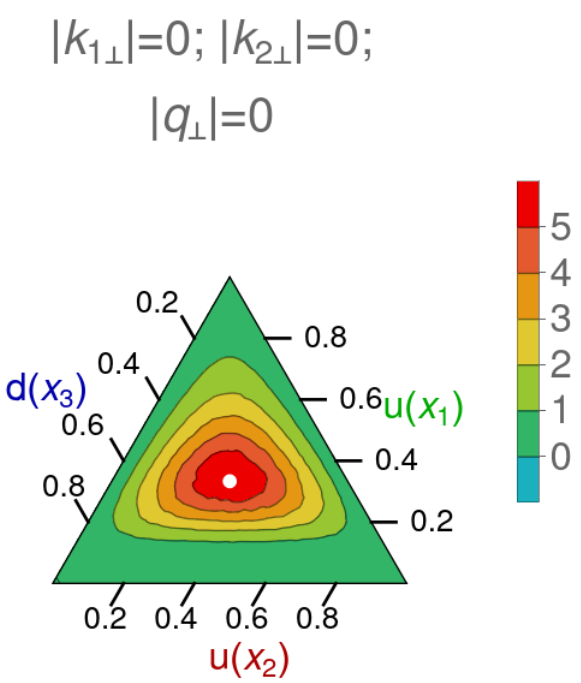

Figure 10.3: Un graphique de la fonction $\psi^{1,-1}$ pour $|\vec{k}_{1\perp}| = |\vec{k}_{2\perp}| = 0$ est montré. Ce graphique est un graphique de contour, donné sur un domaine triangulaire en raison de la contrainte de conservation de l'impulsion $1 = \sum_{i=1}^{3} x_i$. La normalisation n'a pas été définie en raison de contraintes physiques, et est cohérente parmi tous les graphiques de LFWF donnés dans ce document. La normalisation est calculée en déterminant la plus grande valeur de $\psi^{1,-1}$ parmi toutes les valeurs calculées, et en mettant à l'échelle tous les graphiques de manière à ce que cette valeur maximale devienne 6, afin de s'aligner avec les échelles de couleurs de ces graphiques. Nous rappelons au lecteur que les impulsions transverses sont donnés en unités de la masse du nucléon M_N.

10.6.1 . La PDF

Pour calculer les contributions des diverses Fonctions d'Onde sur le cône de lumière (LFWFs) aux GPDs et leurs limites, nous devons d'abord calculer

leurs recouvrements. En commençant par la fonction $\psi^{1,-1}$:

$$\begin{aligned}\psi^{1,-1} &= \tilde{N}(\nu,\sigma)\int [df]\tilde{\rho}\rho_\nu(\bar{a}_1-a_{34})^{\sigma-2}(a_{34}-a_3)^\nu(1-x_2)^{\nu+2}M_N^{-2(\sigma+2+\nu)}\\ &\times\Big[\frac{\ell_\perp^2}{M_N^2}+(1-\bar{a}_1)(\frac{M^2}{M_N^2}-\frac{1}{9})+(\bar{a}_1-a_{34})(\frac{\Lambda_N^2}{M_N^2}-\lambda)+a_3(\frac{\widetilde{M}^2}{M_N^2}-\frac{4}{9})\\ &+(a_{34}-a_3)(\frac{M_{\rm eff}^2+(q_\perp^{\rm eff})^2}{M_N^2}-\frac{4}{9})+(x_2-\frac{1}{3})^2\Big]^{-(\sigma+2+\nu)}\\ &\times[x_1(v'(x_1-2(1-x_2))+x_1(1-x_2))+\bar{u}'(v'(1-x_2)-(x_1)^2)]^{-\nu-1}\\ &(\bar{u}'-v')^{2\nu-1}, \end{aligned} \tag{10.28}$$

Ici, $\tilde{N}(\nu,\sigma)$ est un facteur de normalisation. Pour calculer la contribution de ce recouvrement de fonction avec elle-même au GPD H lorsque le quark 1 est actif, nous commençons par le terme dépendant de l'impulsion transverse, en utilisant une nouvelle paramétrisation de Feynman :

$$\begin{aligned}&\Big[(1+\frac{a_{34}-a_3}{(x_2-1)^2}x_1^2)k_{1\perp}^2+(a_{34}-a_3)k_{2\perp}^2 \\ &+2\frac{a_{34}-a_3}{-1+x_2}x_1\vec{k}_{1\perp}\cdot\vec{k}_{1\perp}+\hat{M}^2\Big]_{in}^{-(\sigma+2+\nu)}\Big[(1\\ &+\frac{a_{34}-a_3}{(x_2-1)^2}x_1^2)k_{1\perp}^2+(a_{34}-a_3)k_{2\perp}^2+2\frac{a_{34}-a_3}{-1+x_2}x_1\vec{k}_{1\perp}\cdot\vec{k}_{1\perp}\\ &+\hat{M}^2\Big]_{out}^{-(\sigma+2+\nu)}\\ =\ &\int_0^1 dh\Big[A_1\bar{k}_{1\perp}^2+A_2\bar{k}_{2\perp}^2+A_3\Delta_\perp^2+A_4\bar{k}_{1\perp}\cdot\bar{k}_{2\perp}\\ &+A_5\bar{k}_{1\perp}\cdot\Delta_\perp+A_6\bar{k}_{2\perp}\cdot\Delta_\perp+A_7]^{-2(\sigma+2+\nu)},\end{aligned} \tag{10.29}$$

où $\hat{M}$ inclut des termes non transversaux-impulsion. En décalant les moments transverses :

$$\begin{aligned}\tilde{k}_{1\perp} &\equiv \bar{k}_{1\perp}+\frac{A_4}{2A_1}\bar{k}_{2\perp}+\frac{A_5}{2A_1}\Delta_\perp\\ \tilde{k}_{2\perp} &\equiv \bar{k}_{2\perp}+\tilde{A}_6\Delta_\perp,\end{aligned} \tag{10.30}$$

nous redéfinissons pour la commodité:

$$\begin{aligned}\tilde{A}_2 &\equiv A_2-\frac{A_4^2}{4A_1}\\ \tilde{A}_6 &\equiv A_6-\frac{A_4A_5}{2A_1}\\ \tilde{A}_3 &\equiv A_3-\frac{\tilde{A}_6^2}{2\tilde{A}_2}.\end{aligned} \tag{10.31}$$

L'expression se simplifie en:

$$\int_0^1 dh\Big[A_1\tilde{k}_{1\perp}^2+\tilde{A}_2\tilde{k}_{2\perp}^2+\tilde{A}_3\Delta_\perp^2+A_7\Big]^{-2(\sigma+2+\nu)}. \tag{10.32}$$

L'intégration sur les deux $\tilde{k}_{1,2}$ donne :

$$\begin{aligned}
&\Big[\tilde{N}(\nu,\sigma)\int [df_{in}]\tilde{\rho}\rho_{\nu}(\bar{a}_1-a_{34})^{\sigma-2}(a_{34}-a_3)^{\nu}(1-x_2)^{\nu+2} \\
&\times[x_1(v'(x_1-2(1-x_2))+x_1(1-x_2)) \\
&+\bar{u}'(v'(1-x_2)-(x_1)^2)]^{-\nu-1}(\bar{u}'-v')^{2\nu-1}\Big]_{\text{in}} \\
&\Big[\tilde{N}(\nu,\sigma)\int [df_{in}]\tilde{\rho}\rho_{\nu}(\bar{a}_1-a_{34})^{\sigma-2}(a_{34}-a_3)^{\nu}(1-x_2)^{\nu+2} \\
&\times[x_1(v'(x_1-2(1-x_2))+x_1(1-x_2)) \\
&+\bar{u}'(v'(1-x_2)-(x_1)^2)]^{-\nu-1}(\bar{u}'-v')^{2\nu-1}\Big]_{\text{out}} \\
&\times\frac{\pi^2}{2}\int_0^1 dh\Big[\tilde{A}_3\Delta_{\perp}^2+A_7\Big]^{-2(\sigma+1+\nu)}\Big[A_1\tilde{A}_3(\sigma+\nu+1)(3+2\sigma+2\nu)\Big]^{-1}.
\end{aligned} \tag{10.33}$$

Afin de calculer la GPD (ou PDF) à un point donné, nous devons donc calculer une intégrale numérique de 13 dimensions, car nous devons intégrer sur les 11 paramètres de Feynman ainsi que la fraction de l'impulsion longitudinalee inactive x_2 et l'angle de l'impulsion transverse θ_{12}. Cette grande intégration dimensionnelle implique un certain bruit, surtout si nous souhaitons calculer ces intégrales de manière rapide. Nous avons choisi d'utiliser l'intégration de Monte-Carlo adaptative, et non Gauss-Kronrod, qui est plus précise mais plus lente [118, 117]. Nous montrons donc les contributions de la fonction auxiliaire $\psi^{1,-1}$ à la PDF. Bien que bruité, il y a un signal non nul clairement visible. De plus, la grande taille de x_1 reflète la tendance mentionnée précédemment pour que l'impulsion longitudinale soit détenu par le quark témoin, u_1. En outre, comme mentionné précédemment, il y a une symétrie approximative u_2-d_3, car ce sont les participants au diquark.

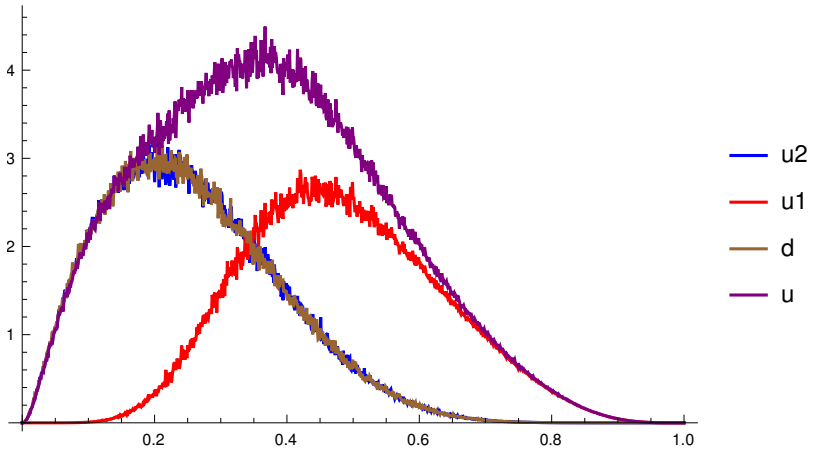

Figure 10.4: Les résultats pour la limite en avant des recouvrements de $\Psi^{1,-}$ (PDFs) sont montrés. La courbe rouge correspond à celle du quark témoin $u1$, la bleue au quark participant $u2$, la brune au quark participant $d(3)$, et la violette à la contribution totale du quark u. Ce résultat a été calculé en utilisant l'intégration de Monte-Carlo adaptative avec 1001 points le long de l'axe x, et est extrêmement bruité. Néanmoins, il y a un signal clairement visible qui n'est pas compatible avec zéro.

10.7 . Conclusion et Perspectives

Les GPDs sont essentielles pour faire des prévisions expérimentales dans des processus tels que la DVCS et la DVMP, en raison de leur nature universelle assurée par les preuves de factorisation. Cependant, extraire les GPDs des données expérimentales est complexe en raison des convolutions avec des noyaux calculables. Les contraintes pratiques sur les GPDs devraient incorporer des entrées provenant des calculs sur réseau QCD et d'autres techniques pour la comparaison avec les expériences. Le repondération bayésienne des candidats GPD ANN en utilisant les données sur réseau peut réduire considérablement l'incertitude, à condition que la corrélation des données soit connue. Les données sur réseau complémentaires peuvent résoudre les limitations du noyau perturbatif dans les données expérimentales, offrant des perspectives sur des régions autrement inaccessibles. Les GPDs polarisées et non polarisées de la région DGLAP peuvent être représentées à travers des LFWFs de qOAM défini, contribuant au GPD H même dans la limite en avant, reliant les GPDs aux contributions de qOAM via les règles de somme de Ji. Un modèle simple pour de telles LFWFs démontre le calcul à partir de structures tensorielles. Pour aligner ces modèles avec les données expérimentales, il est nécessaire d'étendre les GPDs DGLAP à la région ERBL et de les faire évoluer vers les échelles expérimentales. Des efforts supplémentaires dans la modélisation, y compris la systématisation des structures

tensorielles et l'intégration des méthodes du plan complexe avec une masse variable, sont cruciaux pour une compréhension plus intime des contributions qOAM définies au nucléon.

Bibliography

[1] R. Hofstadter, H. R. Fechter, and J. A. McIntyre. High-energy electron scattering and nuclear structure determinations. *Phys. Rev.*, 92:978–987, 11 1953. doi: 10.1103/PhysRev.92.978. URL https://link.aps.org/doi/10.1103/PhysRev.92.978.

[2] I. Estermann and O. Stern. "Über die magnetische Ablenkung von Wasserstoffmolekülen und das magnetische Moment des Protons. II". *Zeitschrift für Physik*, 85(1):17–24, 1933. ISSN 0044-3328. doi: 10.1007/BF01330774.

[3] R. F. Hudson, E. W. Hughes, and Ralph K. Nesbet. The magnetic moment of the proton. *Physical Review*, 78(4):287, 1950. doi: 10.1103/PhysRev.78.287.

[4] M. Gell-Mann. A schematic model of baryons and mesons. *Physics Letters*, 8(3):214–215, 1964. ISSN 0031-9163. doi: https://doi.org/10.1016/S0031-9163(64)92001-3. URL https://www.sciencedirect.com/science/article/pii/S0031916364920013.

[5] O. W. Greenberg. Spin and unitary-spin independence in a paraquark model of baryons and mesons. *Phys. Rev. Lett.*, 13:598–602, 1964. doi: 10.1103/PhysRevLett.13.598. URL https://link.aps.org/doi/10.1103/PhysRevLett.13.598.

[6] M. Y. Han and Y. Nambu. Three-triplet model with double SU(3) symmetry. *Phys. Rev.*, 139:B1006–B1010, 1965. doi: 10.1103/PhysRev.139.B1006. URL https://link.aps.org/doi/10.1103/PhysRev.139.B1006.

[7] Paul A. M. Dirac. The quantum theory of the emission and absorption of radiation. *Proceedings of the Royal Society of London. Series A, Containing Papers of a Mathematical and Physical Character*, 114(767):243–265, 1927.

[8] K. G. Wilson. Non-lagrangian models of current algebra. *Physical Review*, 179(5):1499–1512, 1969.

[9] David J. Gross and Frank Wilczek. Ultraviolet behavior of non-abelian gauge theories. *Physical Review Letters*, 30(26):1343–1346, 1973. doi: 10.1103/PhysRevLett.30.1343.

[10] H. David Politzer. Reliable perturbative results for strong interactions? *Phys. Rev. Lett.*, 30:1346–1349, 06 1973. doi: $10.1103/\mathrm{PhysRevLett.}30.1346$. URL https://link.aps.org/doi/10.1103/PhysRevLett.30.1346.

[11] Rafael S. de Souza and Julien Lesgourgues. Landau poles in the standard model with scalar dark matter. *Journal of Cosmology and Astroparticle Physics*, 2014(05):013, 2014. doi: $10.1088/1475\text{-}7516/2014/05/013$.

[12] J. D. Bjorken. Applications of the chiral $u(6) \bigotimes u(6)$ algebra of current densities. *Phys. Rev.*, 148:1467–1478, Aug 1966. doi: $10.1103/\mathrm{PhysRev.}148.1467$. URL https://link.aps.org/doi/10.1103/PhysRev.148.1467.

[13] George Sterman. *An Introduction to Quantum Field Theory*. Cambridge University Press, 1993. ISBN 978-0521312067.

[14] Sasha Glazov. Measurement of dis cross section at hera. *Brazilian Journal of Physics - BRAZ J PHYS*, 37, 06 2007. doi: $10.1590/\mathrm{S0103}\text{-}97332007000500030$.

[15] C. Adloff et al. Deep inelastic inclusive e p scattering at low x and a determination of alpha(s). *Eur. Phys. J. C*, 21:33–61, 2001. doi: $10.1007/\mathrm{s100520100720}$.

[16] C. Adloff et al. Measurement and QCD analysis of neutral and charged current cross-sections at HERA. *Eur. Phys. J. C*, 30:1–32, 2003. doi: $10.1140/\mathrm{epjc/s2003}\text{-}01257\text{-}6$.

[17] S. Chekanov, D. Krakauer, S. Magill, B. Musgrave, J. Repond, R. Yoshida, M. C. K. Mattingly, P. Antonioli, G. Bari, M. Basile, L. Bellagamba, D. Boscherini, A. Bruni, G. Bruni, G. Cara Romeo, L. Cifarelli, F. Cindolo, A. Contin, M. Corradi, S. De Pasquale, P. Giusti, G. Iacobucci, A. Margotti, R. Nania, F. Palmonari, A. Pesci, G. Sartorelli, A. Zichichi, G. Aghuzumtsyan, D. Bartsch, I. Brock, J. Crittenden, S. Goers, H. Hartmann, E. Hilger, P. Irrgang, H.-P. Jakob, A. Kappes, U. F. Katz, R. Kerger, O. Kind, E. Paul, J. Rautenberg, R. Renner, H. Schnurbusch, A. Stifutkin, J. Tandler, K. C. Voss, A. Weber, D. S. Bailey, N. H. Brook, J. E. Cole, B. Foster, G. P. Heath, H. F. Heath, S. Robins, E. Rodrigues, J. Scott, R. J. Tapper, M. Wing, M. Capua, A. Mastroberardino, M. Schioppa, G. Susinno, J. Y. Kim, Y. K. Kim, J. H. Lee, I. T. Lim, M. Y. Pac, A. Caldwell, M. Helbich, X. Liu, B. Mellado, Y. Ning, S. Paganis, Z. Ren, W. B. Schmidke, F. Sciulli, J. Chwastowski, A. Eskreys, J. Figiel, K. Olkiewicz, K. Piotrzkowski, M. B.

Przybycień, P. Stopa, L. Zawiejski, L. Adamczyk, T. Bołd, I. Grabowska-Bołd, D. Kisielewska, A. M. Kowal, M. Kowal, T. Kowalski, M. Przybycień, L. Suszycki, D. Szuba, J. Szuba, A. Kotański, W. Słomiński, L. A. T. Bauerdick, U. Behrens, K. Borras, V. Chiochia, D. Dannheim, M. Derrick, G. Drews, J. Fourletova, A. Fox-Murphy, U. Fricke, A. Geiser, F. Goebel, P. Göttlicher, O. Gutsche, T. Haas, W. Hain, G. F. Hartner, S. Hillert, U. Kötz, H. Kowalski, G. Kramberger, H. Labes, D. Lelas, B. Löhr, R. Mankel, M. Martínez, I.-A. Melzer-Pellmann, M. Moritz, D. Notz, M. C. Petrucci, A. Polini, A. Raval, U. Schneekloth, F. Selonke, B. Surrow, H. Wessoleck, R. Wichmann, G. Wolf, C. Youngman, W. Zeuner, A. Lopez-Duran Viani, A. Meyer, S. Schlenstedt, G. Barbagli, E. Gallo, C. Genta, P. G. Pelfer, A. Bamberger, A. Benen, N. Coppola, H. Raach, M. Bell, P. J. Bussey, A. T. Doyle, C. Glasman, S. Hanlon, S. W. Lee, A. Lupi, G. J. McCance, D. H. Saxon, I. O. Skillicorn, I. Gialas, B. Bodmann, T. Carli, U. Holm, K. Klimek, N. Krumnack, E. Lohrmann, M. Milite, H. Salehi, S. Stonjek, K. Wick, A. Ziegler, Ar. Ziegler, C. Collins-Tooth, C. Foudas, R. Gonçalo, K. R. Long, F. Metlica, D. B. Miller, A. D. Tapper, R. Walker, P. Cloth, D. Filges, M. Kuze, K. Nagano, K. Tokushuku, S. Yamada, Y. Yamazaki, A. N. Barakbaev, E. G. Boos, N. S. Pokrovskiy, B. O. Zhautykov, H. Lim, D. Son, F. Barreiro, O. González, L. Labarga, J. del Peso, I. Redondo, J. Terrón, M. Vázquez, M. Barbi, A. Bertolin, F. Corriveau, A. Ochs, S. Padhi, D. G. Stairs, M. St-Laurent, T. Tsurugai, A. Antonov, P. Danilov, B. A. Dolgoshein, D. Gladkov, V. Sosnovtsev, S. Suchkov, R. K. Dementiev, P. F. Ermolov, Yu. A. Golubkov, I. I. Katkov, L. A. Khein, I. A. Korzhavina, V. A. Kuzmin, B. B. Levchenko, O. Yu. Lukina, A. S. Proskuryakov, L. M. Shcheglova, N. N. Vlasov, S. A. Zotkin, C. Bokel, M. Botje, J. Engelen, S. Grijpink, E. Koffeman, P. Kooijman, E. Maddox, A. Pellegrino, S. Schagen, E. Tassi, H. Tiecke, N. Tuning, J. J. Velthuis, L. Wiggers, E. de Wolf, N. Brümmer, B. Bylsma, L. S. Durkin, J. Gilmore, C. M. Ginsburg, C. L. Kim, T. Y. Ling, S. Boogert, A. M. Cooper-Sarkar, R. C. E. Devenish, J. Ferrando, G. Grzelak, T. Matsushita, M. Rigby, O. Ruske, M. R. Sutton, R. Walczak, R. Brugnera, R. Carlin, F. Dal Corso, S. Dusini, A. Garfagnini, S. Limentani, A. Longhin, A. Parenti, M. Posocco, L. Stanco, M. Turcato, E. A. Heaphy, B. Y. Oh, P. R. B. Saull, J. J. Whitmore, Y. Iga, G. D'Agostini, G. Marini, A. Nigro, C. Cormack, J. C. Hart, N. A. McCubbin, C. Heusch, I. H. Park, N. Pavel, H. Abramowicz, A. Gabareen, S. Kananov, A. Kreisel, A. Levy, T. Abe, T. Fusayasu, S. Kagawa, T. Kohno, T. Tawara, T. Yamashita, R. Hamatsu, T. Hirose, M. Inuzuka, S. Kitamura, K. Matsuzawa, T. Nishimura, M. Arneodo, N. Cartiglia, R. Cirio, M. Costa, M. I. Ferrero, S. Maselli, V. Monaco, C. Peroni, M. Ruspa, R. Sacchi, A. Solano, A. Staiano, R. Galea, T. Koop, G. M. Levman, J. F. Martin, A. Mirea, A. Sabetfakhri, J. M. Butterworth, C. Gwen-

lan, R. Hall-Wilton, T. W. Jones, M. S. Lightwood, J. H. Loizides, B. J. West, J. Ciborowski, R. Ciesielski, R. J. Nowak, J. M. Pawlak, B. Smalska, J. Sztuk, T. Tymieniecka, A. Ukleja, J. Ukleja, A. F. Żarnecki, M. Adamus, P. Plucinski, Y. Eisenberg, L. K. Gladilin, D. Hochman, U. Karshon, D. Kçira, S. Lammers, L. Li, D. D. Reeder, A. A. Savin, W. H. Smith, A. Deshpande, S. Dhawan, V. W. Hughes, P. B. Straub, S. Bhadra, C. D. Catterall, S. Fourletov, S. Menary, M. Soares, and J. Standage. Zeus next-to-leading-order qcd analysis of data on deep inelastic scattering. *Phys. Rev. D*, 67:012007, Jan 2003. doi: $10.1103/\mathrm{PhysRevD.67.012007}$. URL https://link.aps.org/doi/10.1103/PhysRevD.67.012007.

[18] Richard D. Ball et al. Parton distributions for the LHC Run II. *JHEP*, 04: 040, 2015. doi: $10.1007/\mathrm{JHEP04(2015)040}$.

[19] Michele Arneodo, A. Arvidson, B. Badelek, Maarten Ballintijn, Günter Baum, J. Beaufays, I. G. Bird, Peter Björkholm, Michiel Botje, C. Broggini, W. Brückner, Annelise Brüll, William Jerome Burger, Jacek Ciborowski, R. vanDantzig, Anna Dyring, H. Engelien, M. I. Ferrero, L. Fluri, Ulrike Gaul, Thierry Granier, Matthias Grosse-Perdekamp, D. vonHarrach, M. Vanderheijden, Clemens A. Heusch, Q. Ingram, M. deJong, E. Kabuß, Ralf Kaiser, T. Ketel, F. J. de Klein, Sven O. Kullander, Krzysztof Kurek, Ulrich Landgraf, T. Lindqvist, Gerhard Mallot, Chiara Mariotti, G. vanMiddelkoop, Alain Milsztajn, Yoshiyuki Mizuno, Arndt Mücklich, Jan Pawel Nassalski, Dustin J Nowotny, J. E. J. Oberski, Alan Paic, Cristiana Peroni, Bogdan Povh, Kjell Prytz, Robert Rieger, Klaus Rith, K. Röhrich, Ewa Rondio, Leszek Ropelewski, Andrzej Sandacz, David A. Sanders, Christoph Scholz, Rudi Seitz, Franc Sever, Toshi aki Shibata, M. Siebler, A. Simón, Amedeo Staiano, Michal Szleper, Wieslaw Tlaczala, Y. Tzamouranis, M. Virchaux, J-L. Vuilleumier, T. Walcher, Roland Windmolders, Andre Witzmann, Krzysztof Zaremba, and Frank Zetsche. The a dependence of the nuclear structure function ratios. *Nuclear Physics B*, 481:3–22, 1996. URL https://api.semanticscholar.org/CorpusID:15490964.

[20] Stephen B. Libby and George Sterman. Mass divergences in two-particle inelastic scattering. *Phys. Rev. D*, 18:4737–4745, 12 1978. doi: $10.1103/\mathrm{PhysRevD.18.4737}$. URL https://link.aps.org/doi/10.1103/PhysRevD.18.4737.

[21] European Muon Collaboration (EMC). Spin Structure of the Nucleon. *Nuclear Physics B*, 328:1–45, 1989. doi: $10.1016/0550\text{-}3213(89)90011\text{-}7$.

[22] Xiang-Dong Ji. Deeply virtual Compton scattering. *Phys. Rev. D*, 55:7114–7125, 1997. doi: $10.1103/\mathrm{PhysRevD.55.7114}$.

[23] Maxime Defurne. *Photon and π electroproduction at Jefferson Laboratory-Hall A*. PhD thesis, Orsay, 2015.

[24] John C. Collins and Andreas Freund. Proof of factorization for deeply virtual Compton scattering in QCD. *Phys. Rev. D*, 59:074009, 1999. doi: $10.1103/\mathrm{PhysRevD.59.074009}$.

[25] Xiang-Dong Ji and Jonathan Osborne. One loop corrections and all order factorization in deeply virtual Compton scattering. *Phys. Rev. D*, 58: 094018, 1998. doi: $10.1103/\mathrm{PhysRevD.58.094018}$.

[26] A. V. Radyushkin. Nonforward parton distributions. *Phys. Rev. D*, 56: 5524–5557, 1997. doi: $10.1103/\mathrm{PhysRevD.56.5524}$.

[27] John C. Collins, Leonid Frankfurt, and Mark Strikman. Factorization for hard exclusive electroproduction of mesons in qcd. *Phys. Rev. D*, 56: 2982–3006, 09 1997. doi: $10.1103/\mathrm{PhysRevD.56.2982}$. URL https://link.aps.org/doi/10.1103/PhysRevD.56.2982.

[28] Fatma Aslan, Matthias Burkardt, Cédric Lorcé, Andreas Metz, and Barbara Pasquini. Twist-3 generalized parton distributions in deeply-virtual compton scattering. *Phys. Rev. D*, 98:014038, 07 2018. doi: $10.1103/\mathrm{PhysRevD.98.014038}$. URL https://link.aps.org/doi/10.1103/PhysRevD.98.014038.

[29] Xiang-Dong Ji. Gauge-Invariant Decomposition of Nucleon Spin. *Phys. Rev. Lett.*, 78:610–613, 1997. doi: $10.1103/\mathrm{PhysRevLett.78.610}$.

[30] Stephan Meissner, Andreas Metz, and Marc Schlegel. Generalized parton correlation functions for a spin-1/2 hadron. *JHEP*, 08:056, 2009. doi: $10.1088/1126\text{-}6708/2009/08/056$.

[31] Barbara Pasquini and Cédric Lorcé. The multidimensional nucleon structure. *EPJ Web Conf.*, 129:00044, 2016. doi: $10.1051/\mathrm{epjconf}/201612900044$.

[32] B. Pasquini and C. Lorce'. The partonic structure of the nucleon from generalized transverse momentum-dependent parton distributions. In *Advanced Studies Institute on Symmetries and Spin*, 4 2013.

[33] Xiangdong Ji. Deeply Virtual Compton Scattering. *Phys. Rev. D*, 55:7114–7125, 1997. doi: $10.1103/\mathrm{PhysRevD.55.7114}$.

[34] M. Diehl, T. Feldmann, R. Jakob, and P. Kroll. The overlap representation of skewed quark and gluon distributions. *Nucl. Phys. B*, 596:33–65, 2001. doi: $10.1016/\mathrm{S0550\text{-}3213(00)00684\text{-}2}$. [Erratum: Nucl.Phys.B 605, 647–647 (2001)].

[35] A. V. Radyushkin. Generalized parton distributions. 10 2000. doi: 10.1142/9789812810458_0027.

[36] G. Altarelli and G. Parisi. Asymptotic freedom in parton language. *Nuclear Physics B*, 126(2):298–318, 1977. ISSN 0550-3213. doi: https://doi.org/10.1016/0550-3213(77)90384-4. URL https://www.sciencedirect.com/science/article/pii/0550321377903844.

[37] Yu.L. Dokshitzer. Calculation of the structure functions for deep inelastic scattering and e+ e- annihilation by perturbation theory in quantum chromodynamics. 1977. URL https://api.semanticscholar.org/CorpusID:123025524.

[38] V.N. Gribov and L.N. Lipatov. Deep inelastic electron scattering in perturbation theory. *Physics Letters B*, 37(1):78–80, 1971. ISSN 0370-2693. doi: https://doi.org/10.1016/0370-2693(71)90576-4. URL https://www.sciencedirect.com/science/article/pii/0370269371905764.

[39] Anatoly V. Efremov and Anatoly V. Radyushkin. Asymptotic behavior of the pion form factor in quantum chromodynamics. *Theoretical and Mathematical Physics*, 42:97–110, 1980. URL https://api.semanticscholar.org/CorpusID:120300498.

[40] G. Peter Lepage and Stanley J. Brodsky. Exclusive processes in quantum chromodynamics: Evolution equations for hadronic wavefunctions and the form factors of mesons. *Physics Letters B*, 87(4):359–365, 1979. ISSN 0370-2693. doi: https://doi.org/10.1016/0370-2693(79)90554-9. URL https://www.sciencedirect.com/science/article/pii/0370269379905549.

[41] Xiangdong Ji. Off-forward parton distributions. *Journal of Physics G: Nuclear and Particle Physics*, 24(7):1181, 07 1998. doi: 10.1088/0954-3899/24/7/002. URL https://dx.doi.org/10.1088/0954-3899/24/7/002.

[42] A. V. Radyushkin. Symmetries and structure of skewed and double distributions. *Phys. Lett. B*, 449:81–88, 1999. doi: 10.1016/S0370-2693(98)01584-6.

[43] Dieter Müller, D. Robaschik, B. Geyer, F. M. Dittes, and J. Hořejši. Wave functions, evolution equations and evolution kernels from light ray operators of QCD. *Fortsch. Phys.*, 42:101–141, 1994. doi: 10.1002/prop.2190420202.

[44] Maxim V. Polyakov and C. Weiss. Skewed and double distributions in pion and nucleon. *Phys. Rev. D*, 60:114017, 1999. doi: 10.1103/PhysRevD.60.114017.

[45] B. L. G. Bakker, E. Leader, and T. L. Trueman. A Critique of the angular momentum sum rules and a new angular momentum sum rule. *Phys. Rev. D*, 70:114001, 2004. doi: 10.1103/PhysRevD.70.114001.

[46] E. Leader and C. Lorcé. The angular momentum controversy: What's it all about and does it matter? *Phys. Rept.*, 541(3):163–248, 2014. doi: 10.1016/j.physrep.2014.02.010.

[47] M. V. Polyakov. Generalized parton distributions and strong forces inside nucleons and nuclei. *Phys. Lett. B*, 555:57–62, 2003. doi: 10.1016/S0370-2693(03)00036-4.

[48] Maxim V. Polyakov and Peter Schweitzer. Forces inside hadrons: pressure, surface tension, mechanical radius, and all that. *Int. J. Mod. Phys. A*, 33(26):1830025, 2018. doi: 10.1142/S0217751X18300259.

[49] Cédric Lorcé, Hervé Moutarde, and Arkadiusz P. Trawiński. Revisiting the mechanical properties of the nucleon. *Eur. Phys. J. C*, 79(1):89, 2019. doi: 10.1140/epjc/s10052-019-6572-3.

[50] H. Dutrieux, C. Lorcé, H. Moutarde, P. Sznajder, A. Trawiński, and J. Wagner. Phenomenological assessment of proton mechanical properties from deeply virtual Compton scattering. *Eur. Phys. J. C*, 81(4):300, 2021. doi: 10.1140/epjc/s10052-021-09069-w.

[51] Stanley J. Brodsky, Dae Sung Hwang, Bo-Qiang Ma, and Ivan Schmidt. Light cone representation of the spin and orbital angular momentum of relativistic composite systems. *Nucl. Phys. B*, 593:311–335, 2001. doi: 10.1016/S0550-3213(00)00626-X.

[52] Peter Lowdon, Kelly Yu-Ju Chiu, and Stanley J. Brodsky. Rigorous constraints on the matrix elements of the energy-momentum tensor. *Phys. Lett. B*, 774:1–6, 2017. doi: 10.1016/j.physletb.2017.09.050.

[53] Cédric Lorcé and Peter Lowdon. Universality of the Poincaré gravitational form factor constraints. *Eur. Phys. J. C*, 80(3):207, 2020. doi: 10.1140/epjc/s10052-020-7779-z.

[54] M. Diehl. Generalized parton distributions in impact parameter space. *Eur. Phys. J. C*, 25:223–232, 2002. doi: 10.1007/s10052-002-1016-9. [Erratum: Eur.Phys.J.C 31, 277–278 (2003)].

[55] Matthias Burkardt. Impact parameter dependent parton distributions and off forward parton distributions for zeta —> 0. *Phys. Rev. D*, 62: 071503, 2000. doi: 10.1103/PhysRevD.62.071503. [Erratum: Phys.Rev.D 66, 119903 (2002)].

[56] B.L. Ioffe. Space-time picture of photon and neutrino scattering and electroproduction cross section asymptotics. *Physics Letters B*, 30(2):123–125, 1969. ISSN 0370-2693. doi: https://doi.org/10.1016/0370-2693(69)90415-8. URL https://www.sciencedirect.com/science/article/pii/0370269369904158.

[57] V. Braun, P. Gornicki, and L. Mankiewicz. Ioffe - time distributions instead of parton momentum distributions in description of deep inelastic scattering. *Phys. Rev. D*, 51:6036–6051, 1995. doi: 10.1103/PhysRevD.51.6036.

[58] G. C. Wick. Properties of bethe-salpeter wave functions. *Phys. Rev.*, 96:1124–1134, 11 1954. doi: 10.1103/PhysRev.96.1124. URL https://link.aps.org/doi/10.1103/PhysRev.96.1124.

[59] G. C. Rossi and M. Testa. Note on lattice regularization and equal-time correlators for parton distribution functions. *Phys. Rev. D*, 96(1):014507, 2017. doi: 10.1103/PhysRevD.96.014507.

[60] Anatoly Radyushkin. Quasi-PDFs and pseudo-PDFs. QCDEV2017:021, 2017. doi: 10.22323/1.308.0021.

[61] Xiangdong Ji. Parton Physics on a Euclidean Lattice. *Phys. Rev. Lett.*, 110:262002, 2013. doi: 10.1103/PhysRevLett.110.262002.

[62] Colin Egerer, Robert G. Edwards, Christos Kallidonis, Kostas Orginos, Anatoly V. Radyushkin, David G. Richards, Eloy Romero, and Savvas Zafeiropoulos. Towards high-precision parton distributions from lattice qcd via distillation. *JHEP*, 11:148, 2021. doi: 10.1007/JHEP11(2021)148. URL https://link.springer.com/article/10.1007/JHEP11(2021)148.

[63] A. Accardi, L. T. Brady, W. Melnitchouk, J. F. Owens, and N. Sato. Constraints on large-x parton distributions from new weak boson production and deep-inelastic scattering data. *Phys. Rev. D*, 93(11):114017, 2016. doi: 10.1103/PhysRevD.93.114017.

[64] A. D. Martin, W. J. Stirling, R. S. Thorne, and G. Watt. Heavy-quark mass dependence in global PDF analyses and 3- and 4-flavour parton distributions. *Eur. Phys. J. C*, 70:51–72, 2010. doi: 10.1140/epjc/s10052-010-1462-8.

[65] Eric Moffat, Wally Melnitchouk, T. C. Rogers, and Nobuo Sato. Simultaneous Monte Carlo analysis of parton densities and fragmentation functions. *Phys. Rev. D*, 104(1):016015, 2021. doi: 10.1103/PhysRevD.104.016015.

[66] Richard D. Ball et al. Parton distributions from high-precision collider data. *Eur. Phys. J. C*, 77(10):663, 2017. doi: 10.1140/epjc/s10052-017-5199-5.

[67] J. Bringewatt, N. Sato, W. Melnitchouk, Jian-Wei Qiu, F. Steffens, and M. Constantinou. Confronting lattice parton distributions with global QCD analysis. *Phys. Rev. D*, 103(1):016003, 2021. doi: 10.1103/PhysRevD.103.016003.

[68] Constantia Alexandrou, Krzysztof Cichy, Martha Constantinou, Kyriakos Hadjiyiannakou, Karl Jansen, Aurora Scapellato, and Fernanda Steffens. Unpolarized and helicity generalized parton distributions of the proton within lattice QCD. *Phys. Rev. Lett.*, 125(26):262001, 2020. doi: 10.1103/PhysRevLett.125.262001.

[69] Hervé Dutrieux, Oskar Grocholski, H. Moutarde, and P. Sznajder. Artificial neural network modelling of generalised parton distributions. 12 2021.

[70] S. V. Goloskokov, P. Kroll, and B. Postler. Leptoproduction of vector mesons at small x(Bj) and generalized parton distributions. In *11th International Workshop on Deep Inelastic Scattering (DIS 2003)*, pages 243–248, 8 2003.

[71] S. V. Goloskokov and P. Kroll. Vector meson electroproduction at small Bjorken-x and generalized parton distributions. *Eur. Phys. J. C*, 42:281–301, 2005. doi: 10.1140/epjc/s2005-02298-5.

[72] S. V. Goloskokov and P. Kroll. The Role of the quark and gluon GPDs in hard vector-meson electroproduction. *Eur. Phys. J. C*, 53:367–384, 2008. doi: 10.1140/epjc/s10052-007-0466-5.

[73] S. V. Goloskokov and P. Kroll. An Attempt to understand exclusive pi+ electroproduction. *Eur. Phys. J. C*, 65:137–151, 2010. doi: 10.1140/epjc/s10052-009-1178-9.

[74] George V. Cybenko. Approximation by superpositions of a sigmoidal function. *Mathematics of Control, Signals and Systems*, 2:303–314, 1989. URL https://api.semanticscholar.org/CorpusID:3958369.

[75] V. Bertone, H. Dutrieux, C. Mezrag, H. Moutarde, and P. Sznajder. Deconvolution problem of deeply virtual Compton scattering. *Phys. Rev. D*, 103(11):114019, 2021. doi: 10.1103/PhysRevD.103.114019.

[76] Melanie Mitchell. *An Introduction to Genetic Algorithms*. MIT Press, Cambridge, MA, USA, 1998. ISBN 0262631857.

[77] Nitish Srivastava, Geoffrey Hinton, Alex Krizhevsky, Ilya Sutskever, and Ruslan Salakhutdinov. Dropout: A simple way to prevent neural networks from overfitting. *Journal of Machine Learning Research*, 15(56):1929–1958, 2014. URL http://jmlr.org/papers/v15/srivastava14a.html.

[78] K. Goeke, J. Grabis, J. Ossmann, M. V. Polyakov, P. Schweitzer, A. Silva, and D. Urbano. Nucleon form-factors of the energy momentum tensor in the chiral quark-soliton model. *Phys. Rev. D*, 75:094021, 2007. doi: 10.1103/PhysRevD.75.094021.

[79] Peter Kroll, Herve Moutarde, and Franck Sabatie. From hard exclusive meson electroproduction to deeply virtual Compton scattering. *Eur. Phys. J. C*, 73(1):2278, 2013. doi: 10.1140/epjc/s10052-013-2278-0.

[80] Carl Friedrich Gauss. Bestimmung der genauigkeit der beobachtungen. *Abhandlungen zur Methode der kleinsten Quadrate, 1887*, 1816.

[81] Simon J. D. Prince. *Computer Vision: Models, Learning, and Inference*. Cambridge University Press, USA, 1st edition, 2012. ISBN 1107011795.

[82] Joseph Karpie, Kostas Orginos, Alexander Rothkopf, and Savvas Zafeiropoulos. Reconstructing parton distribution functions from Ioffe time data: from Bayesian methods to Neural Networks. *JHEP*, 04:057, 2019. doi: 10.1007/JHEP04(2019)057.

[83] Herve Dutrieux. *Phenomenology of generalised parton distributions from deeply virtual Compton scattering*. PhD thesis, IRFU, Saclay, 2022.

[84] C. E. Shannon. A mathematical theory of communication. *The Bell System Technical Journal*, 27(3):379–423, 1948. doi: 10.1002/j.1538-7305.1948.tb01338.x.

[85] Stanley J. Brodsky. The Light cone Fock representation in QCD. *Nucl. Phys. B Proc. Suppl.*, 90:3–13, 2000. doi: 10.1016/S0920-5632(00)00863-X.

[86] José Manuel Morgado Chavez, Valerio Bertone, Feliciano De Soto Borrero, Maxime Defurne, Cédric Mezrag, Hervé Moutarde, José Rodríguez-Quintero, and Jorge Segovia. Pion generalized parton distributions: A path toward phenomenology. *Phys. Rev. D*, 105(9):094012, 2022. doi: 10.1103/PhysRevD.105.094012.

[87] N. Chouika, C. Mezrag, H. Moutarde, and J. Rodríguez-Quintero. A Nakanishi-based model illustrating the covariant extension of the pion

GPD overlap representation and its ambiguities. *Phys. Lett. B*, 780:287–293, 2018. doi: 10.1016/j.physletb.2018.02.070.

[88] N. Chouika, C. Mezrag, H. Moutarde, and J. Rodríguez-Quintero. Covariant Extension of the GPD overlap representation at low Fock states. *Eur. Phys. J. C*, 77(12):906, 2017. doi: 10.1140/epjc/s10052-017-5465-6.

[89] Barbara Pasquini, Simone Rodini, and Simone Venturini. Valence quark, sea, and gluon content of the pion from the parton distribution functions and the electromagnetic form factor. *Phys. Rev. D*, 107 (11):114023, 2023. doi: 10.1103/PhysRevD.107.114023.

[90] Xiang-dong Ji, Jian-Ping Ma, and Feng Yuan. Three quark light cone amplitudes of the proton and quark orbital motion dependent observables. *Nucl. Phys. B*, 652:383–404, 2003. doi: 10.1016/S0550-3213(03)00010-5.

[91] V. Braun, R. J. Fries, N. Mahnke, and E. Stein. Higher twist distribution amplitudes of the nucleon in QCD. *Nucl. Phys. B*, 589:381–409, 2000. doi: 10.1016/S0550-3213(00)00516-2. [Erratum: Nucl.Phys.B 607, 433–433 (2001)].

[92] Walter Greiner. *Quantum Mechanics: Symmetries*. Springer, 1994. ISBN 978-3-540-58080-5.

[93] Jose F. Nieves and Palash B. Pal. Generalized Fierz identities. *Am. J. Phys.*, 72:1100–1108, 2004. doi: 10.1119/1.1757445.

[94] Jack S. Goldstein. Properties of the Salpeter-Bethe Two-Nucleon Equation. *Phys. Rev.*, 91:1516–1524, 1953. doi: 10.1103/PhysRev.91.1516.

[95] A. B. Henriques, B. H. Kellett, and R. G. Moorhouse. General Three Spinor Wave Functions and the Relativistic Quark Model. *Annals Phys.*, 93:125, 1975. doi: 10.1016/0003-4916(75)90209-2.

[96] E. E. Salpeter and H. A. Bethe. A Relativistic equation for bound state problems. *Phys. Rev.*, 84:1232–1242, 1951. doi: 10.1103/PhysRev.84.1232.

[97] Gernot Eichmann, Helios Sanchis-Alepuz, Richard Williams, Reinhard Alkofer, and Christian S. Fischer. Baryons as relativistic three-quark bound states. *Prog. Part. Nucl. Phys.*, 91:1–100, 2016. doi: 10.1016/j.ppnp.2016.07.001.

[98] Si-Xue Qin and Craig D. Roberts. Resolving the Bethe–Salpeter Kernel. *Chin. Phys. Lett.*, 38(7):071201, 2021. doi: 10.1088/0256-307X/38/7/071201.

[99] Daniele Binosi, Lei Chang, Joannis Papavassiliou, Si xue Qin, and Craig D. Roberts. Symmetry preserving truncations of the gap and bethe-salpeter equations. *Physical Review D*, 93:096010, 2016. URL https://api.semanticscholar.org/CorpusID:73525173.

[100] Si-xue Qin. A systematic approach to sketch Bethe-Salpeter equation. *EPJ Web Conf.*, 113:05024, 2016. doi: 10.1051/epjconf/201611305024.

[101] Si-Xue Qin, Lei Chang, Yu-Xin Liu, Craig D. Roberts, and Sebastian M. Schmidt. Practical corollaries of transverse Ward-Green-Takahashi identities. *Phys. Lett. B*, 722:384–388, 2013. doi: 10.1016/j.physletb.2013.04.034.

[102] Arturo Amor-Quiroz, William Focillon, Cédric Lorcé, and Simone Rodini. Energy–momentum tensor in the scalar diquark model. *Eur. Phys. J. C*, 83(11):1012, 2023. doi: 10.1140/epjc/s10052-023-12190-7.

[103] Barbara Pasquini, Simone Rodini, and Alessandro Bacchetta. Revisiting model relations between T-odd transverse-momentum dependent parton distributions and generalized parton distributions. *Phys. Rev. D*, 100(5):054039, 2019. doi: 10.1103/PhysRevD.100.054039.

[104] M. Burkardt and B. Pasquini. Modelling the nucleon structure. *Eur. Phys. J. A*, 52(6):161, 2016. doi: 10.1140/epja/i2016-16161-7.

[105] B. Pasquini, S. Cazzaniga, and S. Boffi. Transverse momentum dependent parton distributions in a light-cone quark model. *Phys. Rev. D*, 78:034025, 2008. doi: 10.1103/PhysRevD.78.034025.

[106] Stanley J. Brodsky, Barbara Pasquini, Bo-Wen Xiao, and Feng Yuan. Phases of Augmented Hadronic Light-Front Wave Functions. *Phys. Lett. B*, 687:327–330, 2010. doi: 10.1016/j.physletb.2010.03.049.

[107] C. Lorce and B. Pasquini. On the Origin of Model Relations among Transverse-Momentum Dependent Parton Distributions. *Phys. Rev. D*, 84:034039, 2011. doi: 10.1103/PhysRevD.84.034039.

[108] Yang Yu, Peng Cheng, Hui-Yu Xing, Fei Gao, and Craig D. Roberts. Contact interaction study of proton parton distributions. 2 2024.

[109] Jorge Segovia, Ian C. Cloet, Craig D. Roberts, and Sebastian M. Schmidt. Nucleon and Δ elastic and transition form factors. *Few Body Syst.*, 55:1185–1222, 2014. doi: 10.1007/s00601-014-0907-2.

[110] Dirk Schlingemann. From Euclidean field theory to quantum field theory. *Rev. Math. Phys.*, 11:1151–1178, 1999. doi: 10.1142/S0129055X99000362.

[111] Gernot Eichmann, Eduardo Ferreira, and Alfred Stadler. Going to the light front with contour deformations. *Phys. Rev. D*, 105(3):034009, 2022. doi: 10.1103/PhysRevD.105.034009.

[112] Cédric Mezrag, Jorge Segovia, Minghui Ding, Lei Chang, and Craig D. Roberts. Nucleon Parton Distribution Amplitude: A scalar diquark picture. *Springer Proc. Phys.*, 238:773–781, 2020. doi: 10.1007/978-3-030-32357-8_122.

[113] N. I. Akhiezer and Nicholas Kemmer. The classical moment problem and some related questions in analysis. 2020. URL https://api.semanticscholar.org/CorpusID:118961639.

[114] Noboru Nakanishi. Partial-Wave Bethe-Salpeter Equation. *Phys. Rev.*, 130:1230–1235, 1963. doi: 10.1103/PhysRev.130.1230.

[115] Paul Butzer and François Jongmans. P. l. chebyshev (1821-1894). *J. Approx. Theory*, 96(1):111–138, jan 1999. ISSN 0021-9045. doi: 10.1006/jath.1998.3289. URL https://doi.org/10.1006/jath.1998.3289.

[116] RA Brewster and JD Franson. Generalized delta functions and their use in quantum optics. *Journal of Mathematical Physics*, 59(1), 2018.

[117] William H Press, Saul A Teukolsky, William T Vetterling, and Brian P Flannery. *Numerical Recipes in C: The Art of Scientific Computing*. Cambridge University Press, 1992. ISBN 978-0521431088.

[118] Milton Abramowitz and Irene A. Stegun, editors. *Handbook of Mathematical Functions: with Formulas, Graphs, and Mathematical Tables*. Dover Publications, 1964. ISBN 978-0486612720.

[119] Hideo Fusaoka and Yoshio Koide. Updated estimate of running quark masses. *Phys. Rev. D*, 57:3986–4001, 1998. doi: 10.1103/PhysRevD.57.3986.

[120] P. Dall'Olio, F. De Soto, C. Mezrag, J. M. Morgado Chávez, H. Moutarde, J. Rodríguez-Quintero, P. Sznajder, and J. Segovia. Unraveling generalized parton distributions through Lorentz symmetry and partial DGLAP knowledge. *Phys. Rev. D*, 109(9):096013, 2024. doi: 10.1103/PhysRevD.109.096013.

[121] A. V. Belitsky and A. V. Radyushkin. Unraveling hadron structure with generalized parton distributions. *Phys. Rept.*, 418:1–387, 2005. doi: 10.1016/j.physrep.2005.06.002.

[122] R. P. Feynman. Space-time approach to quantum electrodynamics. *Phys. Rev.*, 76:769–789, 09 1949. doi: $10.1103/\mathrm{PhysRev.76.769}$. URL https://link.aps.org/doi/10.1103/PhysRev.76.769.